DEVELOPMENT OF A ROCK MASS CHARACTERISTICS MODEL FOR TBM PENETRATION RATE PREDICTION

GONG QIUMING

SCHOOL OF CIVIL AND ENVIRONMENTAL ENGINEERING
NANYANG TECHNOLOGICAL UNIVERSITY
2006

DEVELOPMENT OF A ROCK MASS CHARACTERISTICS MODEL FOR TBM PENETRATION RATE PREDICTION

GONG QIUMING
B. Eng., M. Eng.

SCHOOL OF CIVIL AND ENVIRONMENTAL ENGINEERING

NANYANG TECHNOLOGICAL UNIVERSITY

A THESIS SUBMITTED TO THE NANYANG TECHNOLOGICAL UNIVERISITY
IN FULFILLMENT OF THE REQUIREMENT FOR THE DEGREE OF
DOCTOR OF PHILOSOPHY

2006

ACKNOWLEDGEMENTS

The author would like to express gratitude to his supervisor, Dr. Zhao Jian, for his invaluable guidance, constructive suggestions and encouragement throughout the study. The author is very grateful to the review panel for questions and comments during his first-year-PhD confirmation presentation in 2003.

The author would like to thank all the staff in the Division of Geotechnics and Transportation for their comments and encouragement. The author wishes to express his gratitude to the laboratory engineers and technicians who have provided invaluable help during the laboratory experiments.

The author deeply appreciates the help and cooperation of the Philipp Holzmann-Sembcorp Joint Venture during the field tests and data collection. Without its help, it is impossible for the author to finish the study. The author would like to extend his sincere thanks to many individuals who spent their time, and shared data and comments during the course of this study. Special thanks are extended to Mr. Tay Ching Khiang, Mr. Teo Tiong Yong, Dr. Jiang Yusheng, Dr. Amund Bruland, Dr. Olav Torgeir Blindhein, Mr. Tsang Chao Liang, Mr. Sucri Sebastian, Dr. Ernst Buchi, Dr. Ulrich Klotz, Mr. Hasfini Cen, and Mr. Dong Zhuangyuan, Prof. Wang Sijing, Prof. Zhang Zaiming, and Prof. Shen Xiaoke.

The author also would like to extend his gratitude to his colleagues in the Underground Technology and Rock Engineering Program: Dr. Jiao Yuyong, Ms. Bian Haiying, Mr. Zhang Xihu, Dr. Cai Jungang, Dr. Zhao Xiaobao and Ms. Liang Xiaodan, for their helpful discussions and suggestions.

Most importantly, thanks are due to my wife, Li Weiwei, who provided the unbounded quantities of help and moral support that encouraged me to go across a long and winding road. Thanks are due to my two years old son, who grows with this research and always makes me happy.

TABLE OF CONTENTS

SUMMARY

With the advances of technology, TBMs are becoming more versatile and TBM tunneling has become a common tunneling method. During project planning, the prediction of TBM performance is a key factor for selection of tunneling methods and preparation of project schedules. During the construction, TBM performance need to be evaluated based on the encountered rock mass conditions and the machine parameters. A suitable prediction and evaluation model is required by the developer, contractors and TBM manufacturers. The objectives of this research are to study rock mass fragmentation mechanism induced by TBM cutters, and to develop a TBM penetration rate prediction model based on in situ measurements and laboratory tests.

The rock breakage process under TBM rolling cutters can be divided into two stages. The first stage is the rock indentation, followed by the chip formation between two cuts. The process was simulated by using Universal Distinct Element Code (UDEC). The simulation results showed that rock indentation process consists of three stages: formation of a crushed zone, formation of minor crack zone and major cracks propagation. The crack initiation and propagation mainly grows along the frontier of the tensile failure zones. When the side cracks initiated from the crushed zone of two neighboring cutters propagate towards each other and coalesce, a chip is formed. The chip formation is greatly dependent on the cutter spacing and the critical cutter load. The optimal cutter spacing was also analyzed, taking the Bukit Timah granite as an example.

The main rock mass properties, which influence rock mass breakage process and hence the penetration rate, include rock compressive strength, rock brittleness index, joint spacing and joint orientation. The effect of these rock mass parameters on the rock mass breakage process was analyzed by using UDEC modeling. These parameters influence not only the cracks initiation and propagation, but also the rock chipping model. Due to the existence of joint in rock mass, the stress field is changed. This resulted in the variation of the rock chipping model with different joint patterns. The simulation results showed the existence of two modes of crack initiation and propagation. One mode is the crack initiated from the joint plane propagates towards free surface. The other is the crack initiated from the crushed zone propagates towards the joint plane. The existence of joints makes the rock chipping process easier, and thus improves the penetration rate.

The in situ shield friction and penetration tests were performed to analyze the rock mass breakage mechanism at various thrust levels. The TBM penetration curve, the results of muck sieve tests and large muck shape analysis showed that when the cutter load is more than the critical value, the TBM cutterhead breaks rock mass efficiently. A specific rock mass boreability index was proposed to express the rock mass boreability.

Extensive site data collection and laboratory tests were conducted to obtain rock mass properties, TBM performance data and machine parameters. A database was then established. It includes the predominant rock mass characteristic parameters, the corresponding machine performance data, namely the specific rock mass boreability index and the machine parameters. A rock mass characteristics (RMC) model for the TBM penetration rate was obtained through a nonlinear statistical analysis by using a commercial software NLREG. Then, parametric studies were carried out to investigate the effect of rock mass properties on penetration rate based on the new model. The results were analyzed and compared with the numerical simulation results. The results are in good agreement with each other. The advantages and disadvantages of the new model were also discussed. It has potential applications in the tunnel industry.

LIST OF SYMBOLS

A_c	Cylinder area
B	Brittleness
BI	Boreability Index
Bi	Brittleness Index
C_c	Cutting coefficient
C_s	Correction factor for skew
c_c	Cutter constant (relevant to cutter diameter)
c, ϕ	Cohesion and Friction angle
D	Cutter diameter
d	Diameter of the rock sample
F_D	Drag force
E	Modulus of elasticity
e	Efficiency of the motor
F_r	Rolling force per cutter
F_n	Normal force per cutter
$F_{earthpressure}$	Force from earth pressure
$F_{frontshield}$	Friction force of front shield
F_{rock}	Force acted on rock mass by cutterhead
$F_{steering}$	Total force of steering cylinder
$F_{support}$	Force supporting the shield by the tunnel invert
G_{IC}	Critical energy release rate
H_A	Abrasion hardness
H_R	Rebound hardness
H_T	Total hardness
I_s	Point load test strength
I_{s50}	Point load test strength of equivalent sample diameter at 50 mm
J_o	Joint orientation

J_v	Volumetric joint count
J_a	Joint alteration number
J_r	Joint roughness number
J_n	Joint set number
J_{si}	Joint spacing in meters for the joint set
J_w	Joint water reduction factor
k_D	Correction coefficient of cutter diameter
k_s	Correction factor for average cutter spacing
k_{si}	Fracturing factor for joint set number i
k_{DRI}	Correction factor for DRI of the rock
k_{por}	Correction factor for porosity of the rock
k_{ekv}	Equivalent fracturing factor
k_{s-tot}	Total fracturing factor
M_{ekv}	Equivalent thrust
N_m	Number of motors in use
N	Total number of cutters
N_r	Number of random joints
n	Porosity
P	Penetration
$P^{'}$	Base pressure
P_w	Power consumed by each motor per minute
P_p	Propel pressure
$PRev$	Penetration per revolution
Q	Q system value
Q_{TBM}	Q_{TBM} system value
q	Quartz content in percent
R	Cutter radius
R_f	Field penetration rate
R_a^2	Adjusted coefficient of multiple determination

R^2	Coefficient of multiple determination
R_w	The weighted average cutter rotation radius
S	Cutter spacing
S_k	Cutting constant
s	Size reduction factor
SSE	Error sum of squares
SST	Total sum of squares
t	Thickness of the specimen
w_t	Cutter tip width
$W_{frontshield}$	Weight of the front shield
α	Angle between the tunnel axis and the joint plane
σ_c	Compressive strength
ε_{1i}	Irreversible longitudinal strain at failure
σ_t	Tensile strength
β	Angle between the cutter rolling direction and the joint outcrop
φ	Angle of the arc of contact
ϕ	Cutter tip angle
ψ	Dilation angle
ν	Poisson's ratio
λ	The mean discontinuity frequency of a large discontinuity population
σ^2	Variance
σ_θ	Tangential stress
σ_{c50}	Compressive strength with a sample diameter 50 mm
σ_{cd}	Compressive strength with a sample diameter d mm
σ_1, σ_3	Principal Stress

LIST OF ABBREVIATIONS

AR	Advance Rate
BI	Boreability Index
BT	Brizilian Tensile Strength
CAI	Cerchar Abrasivity Index
CLI	Cutter Life Index
CSM	Colorado School of Mines
CW	Completely Weathered
DEM	Discrete Element Method
DRI	Drilling Rate Index
DTSS	Deep Tunnel Sewerage System
EPB	Earth Pressure Balance
F	Fresh
FDM	Finite Difference Method
FEM	Finite Element Method
HW	Highly Weathered
GSI	Geological Strength Index
IMS	Integrated Mass System
ISRM	International Society for Rock Mechanics
JII	Joint Impact Index
LCM	Linear Cutting Machine
MRT	Mass Rapid Transit
MW	Moderately Weathered
NATM	New Austrian Tunnelling Method
NLREG	Nonlinear Regression
NTNU	Norwegian University of Science and Technology
PR	Penetration Rate
PRev	Penetration per Revolution
RMBI	Rock Mass Boreability Index
RMC	Rock Mass Characteristics
RMCR	Rock Mass Classification for Coal Measures Rocks
RMi	Rock Mass Index

RMR	Rock Mass Rating
RPM	Revolution per Minute
RQD	Rock Quality Designation
RS	Residual Soil
RSR	Rock Structure Rating
SRF	Stress Reduction Factor
SRMBI	Specific Rock Mass Boreability Index
SW	Slightly Weathered
TBM	Tunnel Boring Machine
U	Utilization
UCS	Uniaxial Compressive Strength
UDEC	Universal Distinct Element Code

LIST OF FIGURES

LIST OF TABLES

Chapter 1 Introduction

1.1 TBM Tunneling

The use of tunnel boring machine (TBM) can be dated back to 19th century. In 1851, an American engineer Charles Wilson invented a tunnelling machine, which is generally considered as the first successful continuous borer for rock (Askilsrud, 1998). However, TBMs were not adopted practically until 1950s when James S Robbins redesigned a TBM for tunnels. Since the mid 1950s, the development of TBMs has made great progress. At present, the level of mechanization and automation of TBMs has been improved significantly, and TBMs can be designed to excavate tunnels with different shapes in various ground conditions (Robbins, 1982; Nilsen and Ozdemir, 1993; Hanamura, 1995; Askilsrud, 1998; Ishii, 2000; Herrenknecht and Bappler, 2002; Imai et al., 2002; Girmscheid and Schexnayder, 2003). The types of TBM are becoming more versatile. TBM tunnelling has become a common and popular tunnelling method.

With remarkably high advance rates, many long tunnels have been excavated by TBMs throughout the world, for example, Qinling Tunnel in China (Liu and Liang, 2000), Tolo Tunnel in Hong Kong (Mcfeat-Smith and Askilsrud, 1993), Frasnadello and Antea Tunnels in Italy (Barla, 2000), Kelinchi Transfer Tunnel in Malaysia (Sundaram et al., 1998), Pinglin Tunnel in Taiwan (Tseng et al., 1998) and so on. In Singapore, a total of 23.5 km tunnels for the Changi Airport Line (3.5 km) and the North East Line (20 km) MRT have been constructed by TBMs recently. Started in Year 2001, the Deep Tunnel Sewerage System (DTSS) Phase one with a total of approximately 48 km of main tunnels and many subsidiary link tunnels has employed TBMs and micro-TBMs for excavation.

TBM performance relies on the machine design, the geological conditions encountered, and the competence of the contractor, engineers and tunneling crew. In order to design and manufacture a TBM that is suitable for the encountered geological conditions, the interaction between the machine and rock mass, e.g. the rock mass fragmentation mechanisms, need to be well understood. The geological conditions at the site should be correctly interpreted. The main rock mass parameters that affected the TBM performance ought to be obtained during site investigation.

The site geological conditions are the fundamental factors. The machine optimal design and project planning according to the TBM performance prediction are totally based on the site geological conditions. The impacts of site geological condition on TBM performance are twofold. Firstly, the penetration rate is affected by rock mass properties, such as intact rock strength, rock brittleness index, joint spacing and joint orientation. Secondly, the TBM utilization is also affected by the geological conditions. For instance, tunnel support installation, dewatering system, muck conveyors, etc, which are related to utilization, strongly depend on the site geological characteristics. Of course, the response of the tunnelling crew and the flexibility of the machine to changing geology are also of significant impact.

There are many successful cases of TBM excavations, for example, the Meraker project in Norway, a 10 km of tunnel completed in 12 months (Johannessen et al., 1998). The success is attributed to the comprehensive site investigation, proper TBM selection and optimal design, project planning based on TBM performance prediction, and the experienced contractor and crew. However, the TBM performance was less than expected in many tunneling projects. As a result, tunnelling contracts ended up with major disputes and claims. Some of these disputes were due to the unexpected ground conditions, such as high ground water inflow and fault zone. Another type of dispute arises from a lower than anticipated performance based on the information provided in the geotechnical interpretation report (Cheema, 1999). The former may be avoided by combining multiple types of investigation methods to interpret the site engineering conditions, such as core drilling, seismic refraction and reflection at the surface and at the tunnel face. Some precautionary measures can be adopted to avoid these disputes. In addition, an experienced tunneling crew is also an important factor to reduce the risk. Generally, an agreement can be reached to compensate the contractor for the losses of time and extra costs incurred by investigating the special sections where problems are likely to occur. However, the latter is usually very difficult to be resolved. So, the rock mass fragmentation mechanism by the TBM cutters needs to be well understood. The existing TBM performance prediction models also need to be updated with improved tunneling technology and various rock mass conditions.

Laughton and Nelson (1996) pointed out that the natural variation in tunnelling quality that occurs over extended distances in most rock masses continues to be difficult to define quantitatively on the basis of site investigation data. Even though rock mass conditions are fully interpreted from site investigations, the TBM response to and performance achieved within the rock mass conditions are seldom accurately predicted. Many studies have been carried out on the prediction of the TBM performance, as it is particularly important to both clients and contractors of underground construction projects.

1.2 TBM Performance Prediction

Over the years, many prediction models of TBM performance have been developed. These include a series of single factor prediction models (Graham, 1976; Farmer and Glossop, 1980; Nelson, 1983; Hughes, 1986; O’Rourke et al., 1994), CSM (Colorado School of Mines) semi-theoretical model (Rostami and Ozdemir, 1993; Rostami, 1997; Cheema, 1999), NTNU (Norwegian University of Science and Technology) empirical model (Bruland et al., 1995; Bruland, 1998; Blindheim and Bruland, 1988), probabilistic model (Nelson et al., 1999), Q_{TBM} rock mass classification model (Barton, 1999 and 2000; Barton and Jhun, 2000), neuro-fuzzy model (Grima et al., 2000; Bruines, 2001; Benardos and Kaliampakos, 2004). All the models contributed to the understanding of TBM tunneling in one way or another. Each model was developed under certain assumptions, and has some limitations depending on the basis used for their development. This is due to the very complex nature of the problem that involves a wide range of parameters including rock mass properties, TBM specifications and its operational parameters, and tunnel geometries. The interaction between TBM and rock mass controls the rock mass breakage process. Rock mechanical properties affect rock failure and chipping, crack initiation and propagation. Discontinuities in rock mass also affect the penetration rate by changing the failure mode and reducing the crack propagation distance. TBM specifications and its operational parameters such as cutter spacing, cutter diameter, total thrust, torque, revolution per minute (RPM), affect the efficiency of TBM.

Due to the complex interaction between TBM and rock mass, a practical and concise prediction model based on rock mass parameters and machine parameters, which can be easily obtained and commonly used, is more feasible than an “accurate and complex” prediction model. Because many uncertainties are involved when considering a rock mass, a reasonable estimate of TBM performance is good enough to provide reference for the design of TBM and its back-up system, and planning of the project.

1.3 Objectives and Scopes

The objectives of this study are to investigate rock mass fragmentation mechanism induced by TBM cutters, to identify the factors influencing rock mass breakage process, and then to develop a TBM penetration rate prediction model based on field measurements and laboratory tests.

The scopes of the study are as follows:

- To examine the rock fragmentation process induced by TBM cutters using a numerical method.
- To study the effect of relevant rock mass parameters on TBM penetration rate.
- To study the relevant TBM factors influencing TBM penetration rate.
- To obtain the rock mass property data in the tunnel face and TBM performance data at the site.
- To analyze the rock mass boreability index based on the field test results.

- To conduct the laboratory tests to obtain rock strength parameters.
- To develop a prediction model of TBM penetration rate based on the rock mass parameters and TBM parameters using statistical methods.

1.4 Layout of Thesis

The thesis is organized with the intention to provide a logical sequence for reviewing the issues and developing solutions. In Chapter 1, a general introduction to TBM tunneling and a brief review of TBM performance prediction models are presented. The objectives and scopes of the research work are also stated.

In Chapter 2, the pertinent literature is reviewed, including the hard rock TBM system, TBM boring process and its performance parameters, the forces acting on the cutters that cause the rock mass fragmentation, and the existing TBM performance prediction models. The applicability of rock mass classification systems on TBM performance prediction is also discussed and summarized.

In Chapter 3, the rock breakage process is simulated by using UDEC. The rock breakage process includes the rock indentation and the chip formation between two neighboring cutters. The effect of cutter line spacing on rock breakage process is also analyzed.

In Chapter 4, the effects of rock mass properties on rock mass breakage process are analyzed by numerical simulations. These rock mass properties include rock compressive strength, rock brittleness index, joint spacing and joint orientation.

In Chapter 5, the process of establishing a database including rock mass properties and TBM performance is described. This Chapter covers the introduction of the T05 and T06 tunnels of DTSS project, the acquirement of rock mass parameters at the site and in the laboratory, collection and analysis of TBM data.

In Chapter 6, the shield friction and penetration tests conducted in T05 and T06 tunnel sites of DTSS project are described in detail. The test results are analyzed and summarized. A specific rock mass boreability index is proposed to express the rock mass boreability.

In Chapter 7, the rock mass characteristics model for TBM penetration rate prediction is obtained by using nonlinear statistical analysis method. The effect of each rock mass parameter on TBM penetration rate is analyzed. The results are compared with those of the numerical simulations in Chapter 4. The limitations of the model are identified. Compared with other models, the advantages and shortcomings of this new model are analyzed.

Conclusions of the research work and recommendations for further research are presented in Chapter 8.

Chapter 2 Hard Rock Tunnel Boring and Performance Prediction

2.1 Hard Rock TBM

A typical hard rock TBM is composed of many sub-systems, such as cutterhead, propulsion sub-system, torque sub-system, rock mass support sub-system, material conveyance sub-system and explorer sub-system. The cutterhead, propulsion sub-system and torque sub-system are the key components that affect the penetration rate. They are directly related to the rock mass breakage process and machine efficiency. In this section, the cutterhead, propulsion sub-system and torque subsystem will be discussed.

2.1.1 Cutterhead

The cutterhead directly contacts the rock mass to be excavated. The cutter arrangement, cutter diameter and shape, cutterhead shape and system rigidity are important to rock mass breakage. Peripheral cutters are termed gauge cutters that are used to control tunnel shape, cutters at the center of the cutterhead are termed center cutters and the rest are known as face cutters, as shown in Figure 2.1.

The cutting tool is a crucial component of any mechanical excavation system. It performs the actual rock penetration under certain amount of thrust and torque exerted by the machine. The cutting tool most commonly used in full-face TBMs is the single disc cutter. This cutter is composed essentially of a ring, or disc, on a hub connected to a central shaft. It is mounted to a steel saddle, which is bolted to the cutterhead face. Figure 2.2 shows the sketch of a single disc cutter and its support. Over the years, with the development and utilization of more resistant materials and steel alloys, the cutter technology has experienced a dramatic evolution. The cutter diameter changes from 11", 12", 14", $15\frac{1}{2}$", $16\frac{1}{2}$", 17", 19", and up to 20" (500 mm) with average individual rated loads increasing steadily from 80 through 133, 178, 222, 245, 267, and 311 kN respectively (Askisrud, 1998). Individual cutter may undergo three to five times load of the average rated load in hard rock TBMs. In early times, disc cutters were V-shape which resulted in rapid loss of efficiency due to the tip wear. In the late 1970’s, V-shape ring profiles were gradually replaced with constant cross-section profiles which is able to maintain approximately the same cutting efficiency even if the tip worn out. Figure 2.3 shows the cutters with constant cross-section profile used in T05, DTSS project, Singapore.

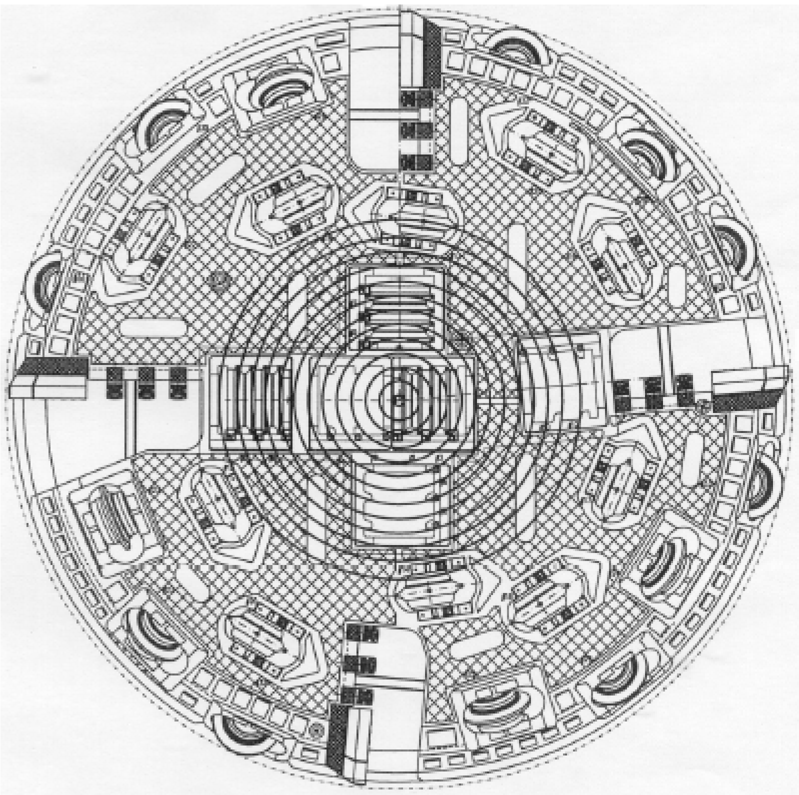

Figure 2.1 Cutterhead

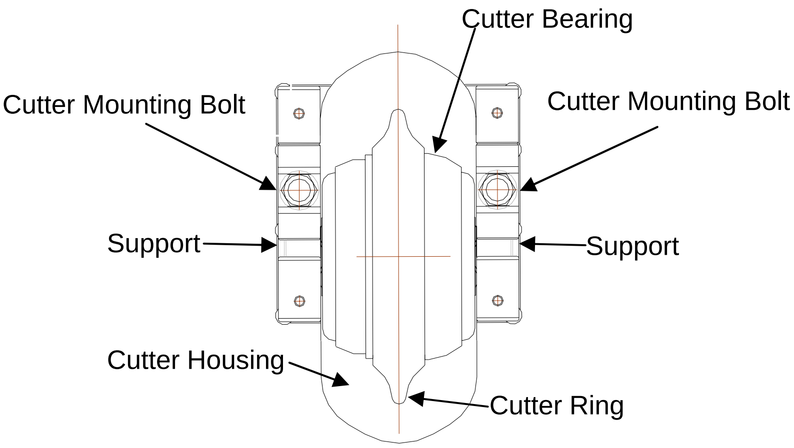

Figure 2.2 Sketch of a single disc cutter

Figure 2.3 Photo of cutters used in T05

As the cutterhead rotates, each cutter indents and traces a circle on the rock face. The cutter arrangement on the cutterhead is designed to facilitate rock chipping between concentric indentations. The position of cutters on a flat cutterhead can be described by two parameters, angular spacing and line spacing (Roxborough, 1978). The line spacing is the distance between two adjacent concentric circles shown in Figure 2.1. The line spacing of cutters is an important factor affecting rock chipping formation, chip size and machine efficiency. Snowdon et al. (1983a) performed a series of tests to ascertain the optimum cutter line spacing based on the specific energy for fragmenting the rock with single pass chipping model. The optimum ratio of line spacing to penetration is generally about 7-20. Average spacing between adjacent cutter grooves is generally about 65-80 mm (Nelson, 1993). The angular spacing is the angle difference of two adjacent cutters in polar coordinates. The objective in selecting a suitable angular spacing is to obtain as close as possible a balanced thrust force on the cutterhead. Optimization of angular spacing is more difficult to achieve than that of line spacing, but fortunately it is a less critical factor on the cutting efficiency. The cutter layout should be designed in such a way that each cutter more or less breaks the rock to a free face created by a preceding cutter on one side. If possible, cutting into rock without any relief on either side of the cutter should be avoided, because this would result in high loads on individual cutter. The cutter layout should also provide the best balancing of the cutterhead in order to minimize the cutter vibrations during the boring process. Cutterhead vibrations not only accelerate cutter wear, but also adversely affect the boring performance. It results in premature failure of various machine components, in particular the main bearing (Cheema, 1999).

2.1.2 TBM Propulsion Sub-system

Hydraulic cylinders, located adjacent and parallel to the main beam, are generally designed to provide the cutterhead thrust that pushes the machine forward. Each hydraulic cylinder is rated by its manufacturer to operate at a maximum level. During the tunnelling process, two forces can reduce the effective thrust. One is the drag force (friction force) acting on shield elements or stabilizers in contact with the tunnel sidewalls. The other is the towing force of back-up sub-system. The total amount of friction and tow forces is generally 10 to 15 percent of the total thrust force recorded (Nelson et al., 1985b). The average normal force acting on the cutter is the effective total thrust force divided by the number of cutters, as shown in Equation 2.1:

$$F_n = \frac{(P_p A_c C_s) - F_D}{N} \tag{2.1}$$

where F_n is average normal force per cutter; P_p is the propel pressure; A_c is the cylinder area; C_s is the correction factor for skew; F_D is the drag force used to advance TBM and trailing gear with no face contact; N is the number of cutters.

When the thrust cylinders deviate from the direction of mining, adjustments to the calculation are required. Because the gauge cutters are installed at an angle with regard to the tunnel axis, they carry fewer loads than the face cutters. Cheema (1999) proposed an equivalent number of cutters to replace the total number of cutters in order to accurately estimate average thrust of cutters. The equivalent number of cutters is the number of cutters that, at loads equal to face cutters, would require the same net thrust.

The drag tests in the field for the open mode TBM are found to be useful to estimate the magnitude of the drag force. The common procedure to perform a drag test is to pull the cutterhead back from the face, set the propel pressure to zero and then push the machine towards the face. While the machine starts moving forward, the measured push force is equivalent to the drag force. During the period of tests, it should avoid additional friction caused by cutters contacting the walls and damages to gauge cutters.

2.1.3 TBM Torque Sub-system

The cutterhead is rotated by motors that are anchored to a frame at the back of the cutterhead. Motors typically allow for variation of torque and RPM. Torque is transmitted through pinion gears that connect with a relatively large diameter bull gear, causing rotation of the cutterhead around the main bearing. The torque system is mainly composed of motors rated in terms of amperage which stands for the power consumed by cutterhead. If the motors draw too much amperage, they will overheat and lead to an internal damage. Each motor is rated by its manufacturer to operate at a suitable level. During excavation, the operator can make adjustments to keep the amperage near the maximum rating or keep the thrust near the maximum rating in accordance with the machine performance and rock mass condition.

The torque can be estimated from the number of operating motors, power consumption per motor and mechanical efficiency of the electro-mechanical system, often estimated at approximately 85 percent (Nelson, 1983). The average rolling force per cutter may be approximately calculated from the gross torque according to the Equation 2.2.

$$F_r = \frac{N_m P_w e}{N 2\pi (RPM) R_w} \tag{2.2}$$

where F_r is the average rolling force per cutter; N_m is the number of motors in use; P_w is the power consumed by each motor per unit time; e is the efficiency of the motor and drive train assembly; N is the number of cutters; RPM is revolution per minute; R_w is the weighted average cutter rotation radius.

In such calculations, the weighted average cutter rotation radius can be calculated for a specific cutter layout. Alternatively, an approximate value of 0.59 multiplying the cutterhead radius is commonly adopted (Laughton, 1998). While TBM is in operation, the peripheral friction and muck related losses should be taken into consideration. Commonly, the impact of muck lodged in the buckets may be estimated. However, the torque losses are difficult to evaluate while mining in the soft or highly jointed rock mass due to the friction between the tunnel face and the cutterhead plate.

2.1.4 TBM System Rigidity

System rigidity plays a key role in the achievable machine performance. Snowdon et al. (1983a) studied the effect of system rigidity on the mechanical cutting characteristics of rocks by laboratory experiments performed in a linear rig (Snowdon et al., 1981). The results showed lower values of specific energy occured at higher stiffness values. The most efficient ratio of cutter spacing to penetration tends to be smaller as the system stiffness decreases. The mean rolling and normal force decrease linearly with increasing stiffness, whilst the peak to mean force ratios increase linearly with the increasing stiffness. The cutting system should incorporate as high stiffness as possible to minimize energy losses and to maximize the boring performance. A stiff cutting system also mitigates cutter wear by reducing the vibrations and shock loads experienced by the cutters during boring. Higher system stiffness also allows for wider cutter spacing.

2.2 TBM Boring Process and Performance Parameters

2.2.1 Boring Cycle

Two types of TBMs are usually used for rock tunnel excavation. One is unshielded TBM (usually called hard rock TBM) and the other is shielded TBM, which is of two basic types – the open face TBM and the closed face (EPB or bentonite) TBM. The boring cycle is different for each type.

Figure 2.4 shows a typical boring cycle for unshield MK TBM (Askilsrud, 1998). At the beginning of the cycle, the anchoring section with grippers is engaged against the tunnel sidewalls and the front lift leg is in contact with the rock in the invert. The invert scraper is in floating contact with the rock in the invert and the hydraulically operated rear support legs have been pulled up from the invert. With the cutterhead rotating, the thrust cylinders are activated to push the cutterhead and the working section forwards the full stroke.

At the end of the forward stroke, cutterhead rotation is stopped. The rear lift legs are lowered against the invert, and the invert scraper is brought from the floating mode,

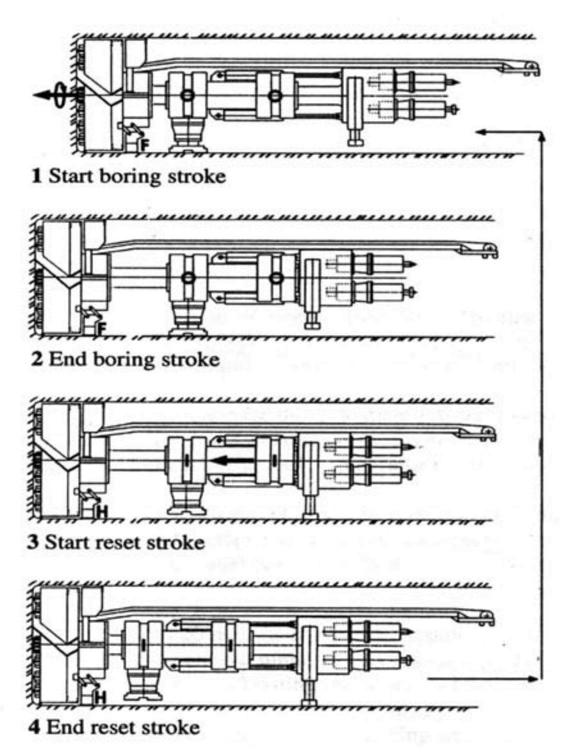

F = Invert scraper floating   O = Gripper out
H = Invert scraper holding   I = Gripper in

Figure 2.4 A complete boring cycle for MK TBM – step by step (Askilsrud, 1998)

which is the normal mode for boring, to the supporting mode in order to carry the weight of the front part of the machine.

With the TBM supported at both ends, the grippers and the front lift leg are retracted. The anchoring section becomes free for resetting which is realized by retracting the thrust cylinders.

The shielded TBM includes single shielded TBM and double shielded TBM. The single shielded TBM is equipped with an open shield. During boring, the thrust force for a single shielded TBM is provided by the hydraulic jacks acting against segment lining. When the machine is stopped and the hydraulic jacks are retracted, concrete segments are assembled inside the tailskin. The hydraulic jacks then push against the ring which was just installed and the next boring cycle can be started.

The double shielded TBM consists of a telescope zone between two shields. During the boring period the telescoping zone between the two shields is expanding but remains closed to avoid rock caving from outside. The thrust required to push the cutterhead in front shield is provided by grippers set in the rear shield or the ring installed in rear shield. The capacity of grippers is given by the bearing capacity of the rock, which could be calculated and predicted. When the boring cycle and ring erection are completed, the rear shield is retracted toward the front shield by closing the telescope section. When the machine works in competent rock masses, it can continuously mine without stopping for ring installation. In case that the machine goes through a zone of very bad ground condition, the grippers cannot provide sufficient thrust for the cutterhead. Thus, the boring process is the same as the single shield machine.

The boring operation relies directly on the capacity of the mucking system to continuously remove muck from the cutterhead to outside of the tunnel. Various materials handling systems have been used to perform this task (Frobenius, 1989). For rock tunnelling, conveyor belt combinations have most commonly been used for “From-face” conveyance and one of three transport systems including single-track rail, double-track rail and conveyor for in-tunnel muck transport. Usually hoist or conveyor systems are used to transport the muck from the in-tunnel.

The maintenance and availability of mucking system in course of TBM excavation can contribute significantly to the overall downtime accumulated during a mining shift (Nelson et al., 1985b). Usually shaft haulage will add to the challenge of the mucking system. Sometimes the limitation of the mucking system is an important factor affecting the performance of TBMs (Johannessen et al., 1998).

2.2.2 TBM Performance Parameters

Generally, four parameters, namely penetration rate, advance rate, utilization and cutter wear are used to evaluate the TBM performance. Penetration rate primarily reflects the machine efficiency in rock breakage. The advance rate and utilization are mainly related to the suitability among the machine, the rock mass and the project management. Cutter wear not only depends on the rock mineral composition and texture, tunnel face variation, such as mixed face, but also on the characteristics of cutters and the operating factors.

Penetration Rate

Penetration rate (PR) is the excavation distance of TBM per boring unit time. PR is generally expressed in meters per hour (m/h). PR is a parameter indicating the interaction between rock mass and TBM. It also indicates whether the selection of TBM in a project is suitable or not.

Penetration per revolution (PRev) is the excavation distance per cutterhead revolution, which is also defined as the basic penetration rate (Bruland, 1998). It is another parameter that is usually used to express the excavation efficiency.

Based on the statistical data (Laughton, 1998), the average penetration rate values that can be achieved range from 0.5 to 7 m/h, corresponding to penetration per revolution of 2 to 20 mm for the same data set.

The penetration rate depends on the levels of thrust and torque delivered to the face for a given rock mass. In order to develop correlations with rock mass properties, a field penetration index was recommended to normalize PRev with regard to cutter thrust (kN/mm) (Hamilton and Dollinger, 1979; Wanner and Aeberli, 1979). Sundin and Wanstedt (1994) proposed a boreability index, which is the reciprocal of the field penetration index. These indexes will be discussed in details in Chapter 6.

Utilization

Utilization (U) is the percentage of available shift time during which excavation, or rock penetration occurs (Nelson, 1983). U is a comprehensive factor that provides insight to suitability of TBM operating in rock masses, construction management and adverse incident. U is affected by lots of uncertainties. In the excavation of sub-horizontal rock masses, U ranged between 15 to 65 percent (Laughton, 1998).

Advance Rate

Advance rate (AR) is the excavation distance of TBM per unit time, which is equal to the product of the penetration rate and the machine utilization. It is an important parameter to express TBM tunnelling. It is usually applied to evaluate the applicability of TBMs. AR can be calculated during a week, one month, one year or the construction period of a whole tunnel. AR values range from 0.3 to 3.3 meters per hour in the excavation of sub-horizontal rock tunnels (Laughton, 1998).

Cutter Wear

Cutter wear is actually a time-dependent abrasion of the cutter ring. It can be defined with respect to working time (h/cutter) or rolling distance (km/cutter). The cutter life in hours is combined with the net penetration rate (m/h) and the TBM diameter to calculate the cutter life in m/cutter and m^3/cutter. When the cutter wear is expressed in m^3/cutter, it indicates the excavation efficiency of cutter.

A cutter is required to be replaced either because of abrasion usually when the radius loss reaches a value of about 20 mm (Grandori et al., 1990), or as a result of failure of the discs or their supports. It is very useful to differentiate the normal cutter wear and abnormal cutter breakage, because the breakage of cutter ring, cutter bearing and cutter support is not subjected to a normal operating condition. Normally, site geological conditions and TBM operating factors have significant effects on cutter wear.

2.3 Forces Acting on the Cutters

As the TBM cutterhead cuts through the rock mass, the cutters roll concentrically on the tunnel face. There are three forces acting on the cutter, namely the normal force (F_n), the rolling force (F_r) and the side force. Figure 2.5 shows these force components on a disc cutter. Normal forces determine the thrust requirement and rolling forces decide the torque and power requirements of the machine. Side forces are usually random. Snowdon et al. (1983a) found that the rolling cutter experienced the maximum side force while chips formed in the linear cutting experiments. The exception is that the side forces on the center and gauge cutters (installed at an angle) act outwards toward the periphery of the tunnel (Cheema, 1999). These cutters often experience significant side forces.

Over the years, the forces acting on disc cutters and the relationship between the normal force and rolling force have been extensively studied. These forces and their relationship are used to optimize the cutterhead layout and overall machine design in order to achieve the maximum TBM performance. Furthermore, they are used to predict the machine performance and evaluate the applicability of TBMs. Different approaches have been used to study the cutting forces. One approach was to study the rock fragmentation mechanism by many indentation tests with different indenters, and then to identify the relative factors affecting the cutting forces. The other approach involved numerous cutting tests conducted on individual cutters with various geometries to measure the cutting forces, the relationships between these forces and the effect of rock properties. The third approach was to conduct field studies and to observe the relationships between the influencing parameters.

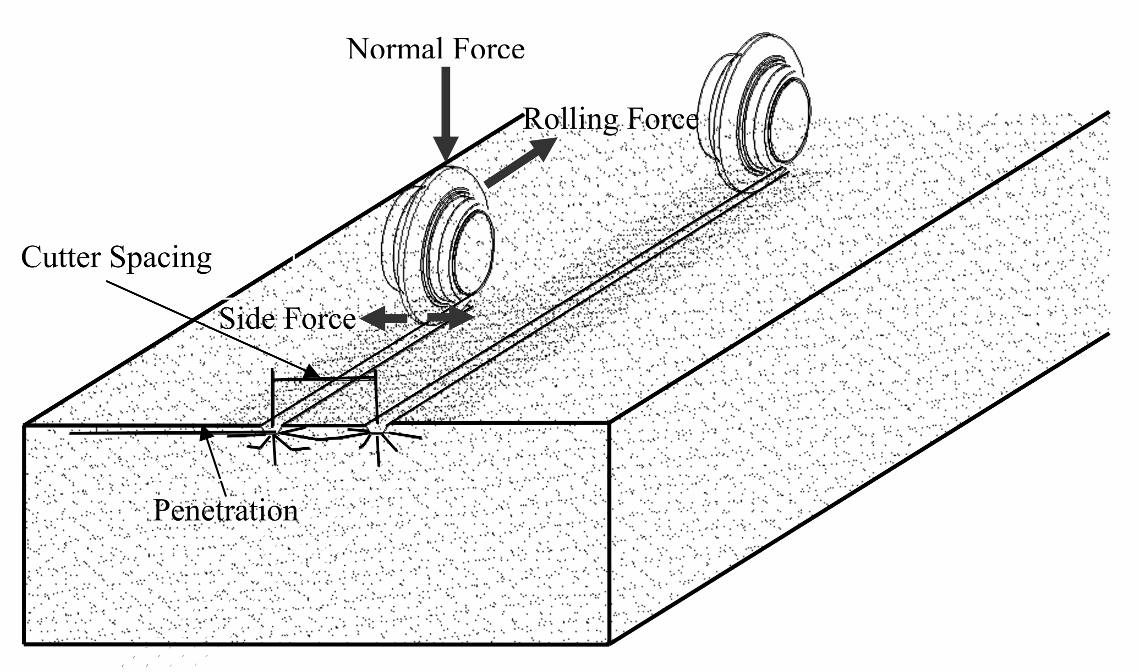

Figure 2.5 Forces acting on the rolling cutter and geometry for kerf cutting

2.3.1 Rock Indentation

Based on the experimental evidence, Reichmuth (1963) proposed there is a crushed zone under the wedge indenter. He assumed that the crushed zone is a triaxial compression region that generates tangential tensile stress field. The material behaves elastically and the tensile failure criterion is applied. The maximum tangential tensile stress is generated immediately underneath the cutter tip. The stress estimation formulas for cracks initiation and propagation to the surface were developed. In his equation, the penetration was not taken into consideration.

Paul and Sikarskie (1965) assumed that the wedge indenter directly loads to brittle isotropic rocks and causes shear failure. The occurrence of crushed zone was not considered. The continuous chipping process is obtained. The chipping forces are derived from Mohr-Coulomb failure criterion assuming a uniform shear and normal stress distribution along the potential failure line. The theory was extended to bedded brittle rocks by Benjuma and Sikarskie (1969). The corresponding force levels are known to be overestimated (Pang et al., 1989; Cheema, 1999).

Pang et al. (1989) developed a force deformation model for localized loading of brittle rocks. In the model, the force-penetration equations were proposed for conical and wedge shape indenters. The model shows that the force-indentation relation during crushing is linear for a wedge indenter and quadratic for a conical indenter. The force indentation behavior mainly depends on the geometry of the indenter rock contact area. The model results are in good agreement with the experimental results. Stacey (1981) proposed an extension strain criterion, such that "fractures in a brittle rock will initiate when the total extension strain (ε_{et}) in the rock exceeds a critical value (ε_{ec}), which is characteristic of the rock type". By applying this criterion, Pang and Goldsmith (1990) deduced theoretical functions of crack propagation scope for three types of indenters, namely, conical indenter, wedge indenter and hemispherical indenter. Subsequently, the static and dynamic indention tests were conducted. The test results showed that the cracks induced by maximum tensile strain with their directions were predicted reasonably by the theory.

The rock fragmentation process based on the numerical simulation on rock indentation was also studied (e. g. Cook et al. 1984; Pang and Goldsmith, 1990; Chiaia, 2001; Liu et al., 2002). The relevant parameters influencing rock fragmentation were also analyzed. The details are depicted in Chapter 3.

The analytical solutions based on the indention tests offer an explanation for the force penetration behavior. The force analysis results show that the rock fragmentation process is mainly dominated by tensile failure, rather than shear failure, which is consistent with the rock indentation observation and numerical modeling results. When an indenter penetrates the rock, a crushed zone is developed immediately under the indenter. The zone is composed of fine material, which in turn transfers the loads to the surrounding area. Median and radial cracks are created around the crushed zone. With the increase of the loads in the zone, these cracks propagate downwards and sidewards to free surfaces. The forces increase until a chip is formed.

2.3.2 Linear Cutting Tests and Disc Cutter Theories

The above mentioned rock indentation process is under static loading on one point. The rock fragmentation process under TBM cutters is a continuous loading process along cutter kinetic circle in the tunnel face. The formation of chips depends on both the rock indentation and the interaction between the two adjacent cuts. The operating relationship between the normal force and the rolling force is also very important to the overall TBM design.

Roxborough et al. (1975, 1978) proposed a simple mathematical model to describe the performance of TBMs with V-shape cutters. The geometry of a symmetrical disc of radius R, edge angle ϕ and operating at a penetration P is shown in Figure 2.6. The friction between rock mass and rolling cutters is neglected. Thus, the resultant force F must pass through the center of rotation O. The stress acting along

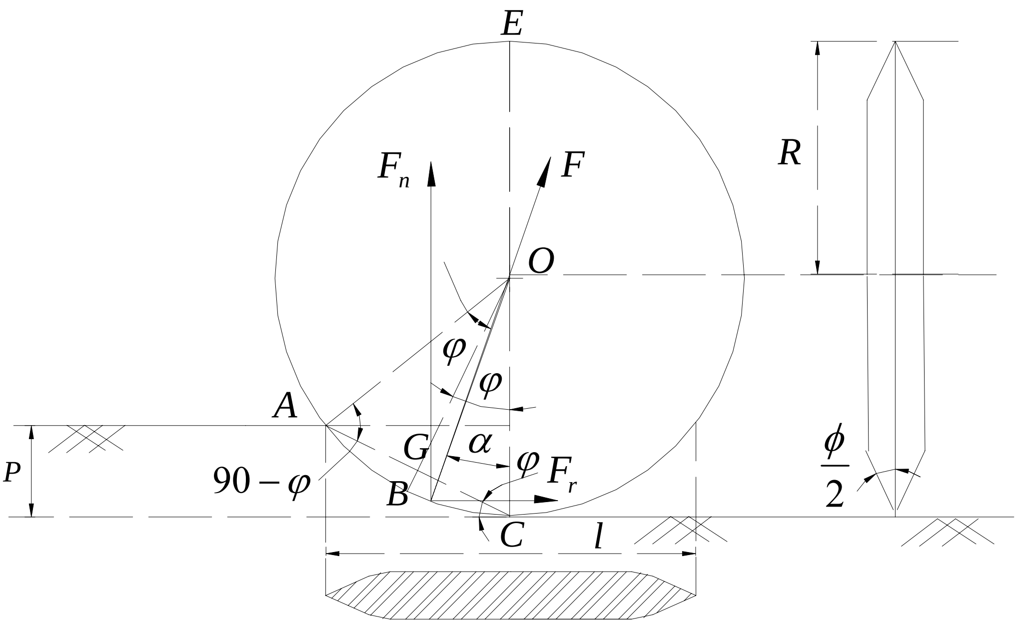

Figure 2.6 Geometry of disc penetration (after Roxborough, 1978)

the arc of disc contact AC is assumed to be constant. When the penetration is small, the value of φ is also small, then

$$\sin\varphi \to \varphi,\ C_c = \frac{F_r}{F_n} = \cot\varphi = \sqrt{\frac{P}{D-P}} \tag{2.3}$$

where C_c is cutting coefficient and is defined as the ratio of average cutter rolling force to average cutter normal force, D is the diameter of the rolling cutter and P is penetration.

The above equation shows that the relationship between normal and rolling forces is dependent only on disc diameter and depth of penetration and is irrelevant to rock properties and other geometrical features of the disc.

Roxborough and Phillips (1975) assumed the thrust force F_n would be the projected area of disc contact zone (Figure 2.6) multiplied by the compressive strength (σ_c) of the rock. For the sake of simplicity, the width of disc contact is taken to be constant along the contact length. Then, the normal force and the rolling force may be written as follows:

$$F_n = 4\sigma_c \tan\frac{\varphi}{2}\sqrt{DP^3 - P^4} \tag{2.4}$$

$$F_r = 4\sigma_c P^2 \tan\frac{\varphi}{2} \tag{2.5}$$

Phillips (1975) recalculated the contact area of the disc cutter and modified above functions as follows,

$$F_n' = \frac{8}{3}\sigma_c \tan\frac{\varphi}{2}\sqrt{DP^3 - P^4} \tag{2.6}$$

$$F_r' = \frac{8}{3}\sigma_c P^2 \tan\frac{\varphi}{2} \tag{2.7}$$

Equations 2.5 and 2.7 indicate the rolling force is independent of disc diameter. The model did not include the effect of cutter spacing. From the assumption of rock shear failure between two adjacent cuts, Roxborough (1978) concluded the optimal ratio of penetration to cutter spacing is equal to the ratio of rock shear strength to compressive strength.

Ozdemir et al. (1977) and Wanner and Aeberli (1979) proposed a theoretical model for predicting the cutting forces acted on the V-shape cutter. They assumed that a crushed zone existed under the cutter, the ridge between two cuts was a shear failure, and the rock was isotropic and brittle.

Howarth (1981) studied the impact of spacing and infill of a set of joints on TBM performance using rock cutting rig in the laboratory. The experimental results showed that the larger the infill width and the smaller the spacing, the less is the thrust force required to penetrate a certain depth. Experiments by Howarth (1981) and Sanio (1985) indicated that the angle between the tunnel axis and joint plane has an obvious effect on the cutting force. With increase of the angle, the normal force increases.

Sanio (1985) proposed a cutting force model based on the rock tensile failure on the rock breakage process under the action of V-shape TBM cutter. As the cutter tip loads on the rock, the rock first crushed in a zone right below the cutter. An approximate hydrostatic stress state exists within this crushed zone that causes tangential tensile stresses to be generated in the surrounding undamaged rock. Tensile cracks develop and extend radially from the cutting edge when the tensile stresses reach the tensile strength. Sanio used a solution derived by Ouchterlony (1974) for the normal cutter force, which is the correlation among the length of the cracks, the radius of the hole and stress for a pressurized hole (blasting) with pressureless radial cracks in an infinite plate. The equations are as follows:

$$F_n = S_k \cdot \sqrt{D \cdot S \cdot P} \cdot \tan\left(\frac{\varphi}{2}\right) \tag{2.8}$$

$$C_c = \frac{4}{5} \cdot \sqrt{\frac{P}{D}} \tag{2.9}$$

where, S_k is defined to be the cutting constant (in N/m$^{1.5}$) which depends on the rock strength, the geometry of the crushed zone and the number of radial cracks. D is the cutter diameter, S is the cutter spacing and P is penetration. φ is the cutter tip angle. C_c is cutting coefficient.

S_k can only be obtained by tests. The S_k value is strongly dependent on the degree and orientation of existing strength anisotropy. It reflects the effect of rock anisotropy on rock indentation.

Rostami and Ozdemir (1993) assumed that a pressure distribution along the periphery of the disc cutter (within rock-cutter interacting area) could be written as

Equation 2.10 and shown in Figure 2.7 in a longitudinal cross-section (along the cut). Force elements could be integrated to obtain normal and rolling forces. Side forces can be neglected, because side force is caused by chip formation on one side of the cutter and the unbalanced pressure on the other side.

$$P = P'\left(1-\frac{\theta}{\varphi}\right)^{\psi} \tag{2.10}$$

where P' = Base pressure; θ = Angle from the normal to face, ranging from 0 to φ.

When the base pressure distribution is linear, the cutting coefficient can be estimated by:

$$C_c = \frac{1-\cos\varphi}{\varphi-\sin\varphi} \tag{2.11}$$

The general form of the cutting coefficient is derived by Rostami et al. (1993) as follows:

$$C_c = \tan\beta = \tan(\varphi-\gamma) \tag{2.12}$$

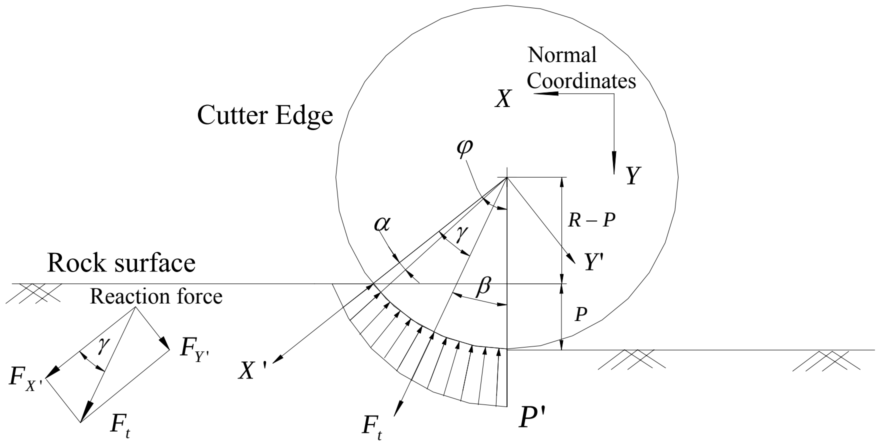

Figure 2.7 General shape of pressure distribution with power function (after Rostami et al., 1993)

$$\gamma = \tan^{-1}(\frac{F_{Y'}}{F_{X'}}) \tag{2.13}$$

$$F_{X'} = \sum_{1}^{n}(-1)^{i-1}\frac{\varphi^{2i+\psi}}{(2i+\psi)(2i-2)!} \tag{2.14}$$

$$F_{Y'} = \sum_{0}^{n}(-1)^{i-1}\frac{\varphi^{2i-1+\psi}}{(2i-1+\psi)(2i-2)!} \tag{2.15}$$

Here, n is the number of iterations needed to reach the desired degree of accuracy in numerical estimation. Usually, n with a value of more than 5 is enough. In general, the value of ψ depends on the shape of cutter tip. The value is close to 1 for V-shape disc cutter. For constant cross section cutters and worn cutters, ψ is close to zero and decreases with increasing tip width. The base pressure is assumed to be uniform. The cutting coefficient is the same as the result by Roxborough (1978), which is shown in Equation 2.3.

Rostami (1997) proposed a prediction model of disc cutting forces using the database of the measured cutting forces by linear cutting experiments. The model is introduced in detail in Section 2.4.

The studies conducted by various researchers in the linear cutting tests confirmed that the following factors influence the cutting forces.

1. Intact rock properties
a) Uniaxial compressive strength
b) Brazilian tensile strength

2. Joints
a) Joint spacing
b) Joint orientation

3. Disc cutter geometry
a) Disc diameter
b) Disc tip width (Constant cross profile cutter) or tip angle (V-shape cutter)
4. Cutting geometry
a) Cutting spacing
b) Penetration

These studies also confirmed that the cutting coefficient mainly relies on the cutter diameter and penetration. The base pressure distribution with the constant cross section is nearly uniform.

2.3.3 Field Studies on TBM Performance

Although the laboratory linear cutting tests provide a valuable approach to measure the cutting forces and the effects of rock properties, cutter and cutting geometry, they are not good enough to represent the whole image of TBM performance. Compared with the linear cutting tests, the field studies have these advantages as follows:

a) Contain the complexity of the overall TBM system;
b) Consider the effects of the geological conditions, especially the rock mass structure, besides the rock physical and mechanical properties;
c) Take the operating factors into account.

Ideally, boring should take place at the rated level of both torque and thrust in order to maximize TBM efficiency. With change of rock mass conditions, TBM operation can be referred to as either thrust-limited or torque-limited with respect to its installed capacity of F_n and F_r respectively. The operating relationship between the normal force (F_n), rolling force (F_r) and penetration rate in different rock mass conditions is shown in Figure 2.8 (Laughton, 1998). From rock mass A to rock mass D, the operation model transits from torque-limited to thrust-limited. Generally, with increase of penetration per revolution, F_n and F_r are observed up to the point at which one of the installed force capacities is reached. When TBM operates in low strength rock mass and crushed rock mass, the limited torque is easily reached. On the contrary, when TBM operates in high strength and brittle rock mass, the limited thrust is likely to be reached first.

In reality, operators usually control the machine based on their experiences obtained from the previous tunneling operations. Because of the variation of geological conditions in the tunnel alignment, it is often very difficult to operate the machine in an optimum state. In some cases, due to the influence of the mucking capacity, machine vibration and tunnel face stability, the machine performance is impossible to reach the maximum value designed. In the field study, the effects of these factors on TBM performance can be analyzed.

Some previous studies have shown that the penetration rate decreases with the increase of rock uniaxial compressive strength or rock hardness (Farmer et al., 1979; Morimoto and Hori, 1986; Fukui & Okuubo, 1999). Because TBM performance is also affected by other factors including TBM specifications, the single function between penetration rate and rock strength or hardness is not likely to be convincing.

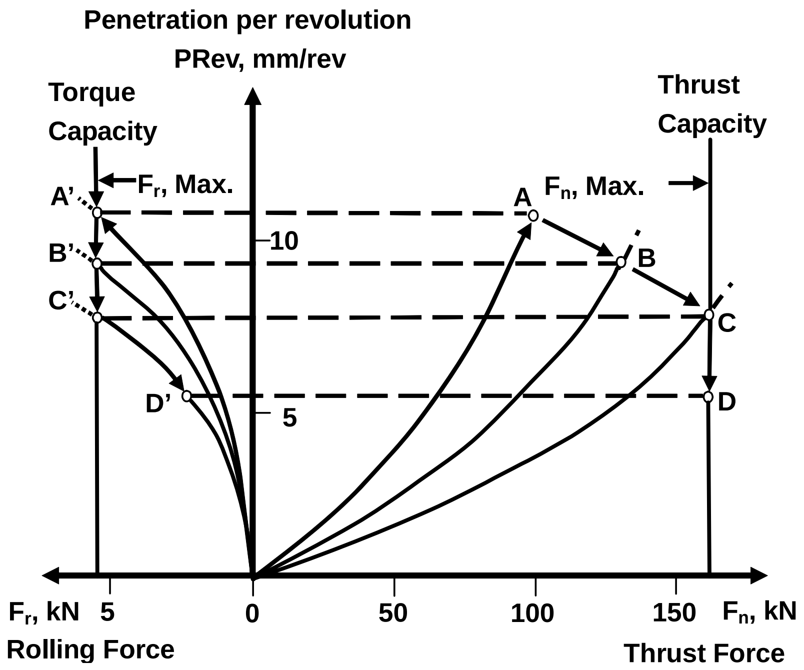

Figure 2.8 Interaction between F_n and F_r as a function of rock mass boreability (after Laughton, 1998)

The effects of rock brittleness on rock breakage or chipping have been investigated in various laboratory programs, as well as field measurements/observations (Snowdon et al., 1982 and 1983b; Bruland, 1998). The effects are summarized as follows:

a) Rocks with high brittleness have most crack formation and chipping to the sides. Rock cutting efficiency improves with increasing brittleness.
b) From the experimental results based on single-pass cutting (Snowdon et al., 1982 and 1983b), it is found that the ratio of penetration to cutter spacing decreases with increasing rock brittleness. At the same penetration rate, the effect zone of single-pass cutting also decreases with increasing rock brittleness. The main reason is that brittle rocks under rolling cutters are easy to yield radial tensile cracks, release strain energy and form small rock chips. Rocks exhibiting plastic behavior may absorb substantive strain energy and its effect zone is large. The formation of chips may be a combined result of tensile failure and shear failure.
c) Based on multiple-pass cutting in situ tests, together with the observations and analyses of the largest chips from a great number of TBM tunnels, Bruland (1998) concluded that when the rock brittleness is high, the chipping frequency (TBM penetration per revolution / average thickness of the largest chips) and kerf depth factor (kerf depth at chip forming / maximum chip thickness) is low. Larger cutter spacing can be employed for rocks of higher brittleness.

Nelson et al. (1985a) highlighted that rock fracture and chip formation is a process of consuming energy to create new surface area. They studied the correlation among the critical energy release rate (G_{Ic} (N/m)), field penetration index (R_f (kN/cutter/mm/revolution)), total hardness (H_T ($g^{-1/2}$)) which is calculated as an amount of the Schmidt hammer rebound hardness (H_R) and the square root of the modified Taber abrasion hardness (H_A). Based on the test observations from massive and brittle materials in different limestones and dolostones, the relationships among G_{Ic}, R_f and H_T are linear.

Howarth and Rowlands (1987a) introduced a texture coefficient to correlate with drillability and strength properties. The texture coefficient refers to grain-shape, orientation, degree of interlocking and relative proportion of grains and matrix. The texture coefficient is a measure of the resistance of a rock microstructure to crack propagation that may be inter or intra-granular. For example, fractures propagate through the weak phyllosilicate matrix in some sandstones, and it is an intra-granular fracture path in some igneous rocks. The fracture path was reported to affect the TBM performance to some extent (Gehring, 1994). The correlations between rock compressive strength, Brazilian tensile strength, static Young's modulus and the texture coefficient are almost linear. The effect of rock texture on the cutting forces includes two aspects. One is that the mineral composition and structures affect rock strength and fracture paths. The other is that due to presence of hard and abrasive minerals, the rolling cutter is worn easily and becomes blunt in a short time.

The effect of abrasive and hard minerals on cutter wear has been extensively studied with laboratory and field tests (Nelson and Kulhawy, 1984; Bruland, 1998). Generally, cutter wear influences full-face tunnel boring machine performance in several ways, including cutter displacement and repair, loss of production time, and reduction of penetration rate. The effect of hard and abrasive minerals on penetration rate is less than that on the advance rate. The effects of the rock abrasiveness on the cutter ring are twofold:

(a) The rock hardness determines the amount of crushed rock powder produced per pass and the size of the contact area between the cutter edge and the crushed powder.

(b) The hardness and abrasiveness of the crushed powder cause the abrasion on the cutter ring.

With the increase of quartz content and other hard minerals such as epidote and garnet, the cutter ring abrasion increases (Bruland, 1998). Nelson and Kulhway (1984) concluded that rolling distance per unit disc diameter loss had linear correlation with rock abrasiveness.

In light of the TBM performance in different rocks, Bruland (1998) found that with the increase of rock porosity, the penetration increases. Cheema (1999) also pointed out that higher porosity would increase rock boreability. From the rock breakage process, the porosity has dual effects on rock breakage. On one hand, higher porosity enhances the boring performance by making penetration of cutters easier. On the other hand, higher porosity may provide dilatation space and hinder crack propagation from one cut to another.

Laughton et al. (1994) studied the effect of joint spacing on the penetration. The penetration rate increases with decreasing joint spacing. However, if the joint spacing is too small, the face itself becomes unstable leading to “blocky condition”, resulting in a negative influence on penetration rate. Based on a large number of case histories, Bruland (1998) also concluded that the penetration rate increases with decreasing joint spacing. The maximum penetration rate in highly fractured rock mass can reach more than nine times the penetration rate in intact rock.

Experiments by Howarth (1981) and Sanio (1985) indicated that the angle (α) between the tunnel axis and joint plane has an obvious effect on the cutting force. Theoretically, the penetration rate is the largest with $\alpha = 90°$ (Rostami and Ozdemir, 1993). When the rolling cutter is perpendicular to the weakness planes, breakage may take place along the weakness planes and the fragmentation is optimal. The results of Bruland (1998) showed when the angle is equal to 60º, the penetration rate attains the maximum value.

The field studies on TBM performance also confirmed these parameters influencing the cutting forces or penetration rate similarly to those conducted in the laboratory. The physical and mechanical properties of rock primarily include the unaxial compressive strength and rock brittleness. The penetration rate decreases with increasing rock unaxial compressive strength. The penetration rate increases with increasing rock brittleness. Other rock parameters, such as rock hardness, texture and porosity are also known to influence the penetration rate. The rock hardness and texture are strongly relevant to the rock strength and brittleness. The porosity affects the penetration rate only in high porosity rocks. In the field studies, the joint properties were confirmed to greatly influence the penetration rate. These effects cannot be fully represented in the linear cutting tests due to the difficulty in sampling. The penetration rate generally increases with decreasing joint spacing. The penetration rate increases as the angle between the tunnel axis and joint plane increases, and reaches the maximum when the angle is equal to 60º, and then decreases with further increase of the angle. Other rock mass parameters, such as faults and mixed face encountered in the tunnel excavation, also have significant impact on the penetration rate. These parameters also greatly influence the advance rate and cutter wear. The machine parameters, such as cutter geometry and cutter spacing, have the same effect as discussed before. In the field study, the effect of cutter wear on penetration rate was taken into consideration. Due to the complexity of the TBM and variation of the rock mass conditions and operating factors, the prediction of the penetration rate is rather difficult.

Bruland (1998) derived an equation to calculate the cutting coefficient. Based on the actual TBM performance, it is relevant to the cutter diameter and the penetration rate.

$$C_c = c_c \cdot \sqrt{P} \tag{2.16}$$

where c_c is a constant relative to cutter diameter, which decreases with increasing cutter diameter; P is the basic penetration rate. The result is consistent with that conducted in the linear cutting tests.

Depending on the field studies, a series of prediction models for TBM performance have been proposed over the years. These models were set up under certain assumptions, which will be discussed in detail in Section 2.4.

2.4 Prediction of TBM Performance

Prediction of TBM performance in a given rock mass has been a hot and challenging research topic since the TBM is used as an excavation tool. The planning of tunnel projects and selection of construction methods require reasonably accurate prediction of TBM performance. Due to the complexity of the interaction between rock mass and TBM, it is not possible to predict the TBM performance theoretically. During the last 30 years, the prediction models have been developed from a single factor model (Graham, 1976; Farmer and Glossop, 1980; Nelson, 1983; Hughes, 1986; O'Rourke et al., 1994) to multi-factor model (Rostami, 1997; Bruland, 1998; Nelson et al., 1999; Barton, 2000; Grima et al., 2000; Bruines, 2001). Among the models, some are only based on laboratory tests and some based on practical tunnel construction data. Generally speaking, laboratory cutting tests on rocks are necessary, but they neither give a full picture of rock mass nor represent the full scale operation of the TBM. A realistic prediction model should combine the laboratory tests data and site geological and construction conditions.

2.4.1 Single Factor Prediction Model

During the early period of TBM application, some simple empirical equations were developed from data on rock strength tests and tunnel construction. The commonly used equations are discussed below.

Graham (1976) derived a prediction equation based on a predominantly hard rock (uniaxial compressive strength from 140 to 200 MPa) database:

$$P\,\mathrm{Re}\,v = 3940\, {}^{F_n}\!/_{\sigma_c} \tag{2.17}$$

where $P\,\mathrm{Re}\,v$ is penetration per revolution (mm/revolution); F_n is thrust force per cutter (kN); σ_c is uniaxial compressive strength of rock (kN/m^2).

Farmer and Glossop (1980), who established a database including mostly sedimentary rocks, derived the following equation:

$$P\operatorname{Re}v = 624\, {}^{F_n}\!/\!_{\sigma_t} \tag{2.18}$$

where σ_t is Brazilian tensile strength of rock (kN/m^2).

Hughes (1986) derived a relationship from coal mining as shown in Equation (2.19). It assumed only one disc track in each kerf groove, which is the normal practice for TBM design.

$$P\operatorname{Re}v = 1.667({}^{F_n}\!/\!_{\sigma_c})^{1.2}(\frac{2}{D})^{0.6} \tag{2.19}$$

where D is the disc diameter in millimeter.

Nelson (1983) derived a relationship from a comprehensive and detailed study on TBM performance in shale, sandstone, and limestone formations:

$$R_f = 5.95 + 0.18H_T \tag{2.20}$$

where R_f ((kN/cutter)/(mm/revolution)) is the field penetration index and H_T is total hardness, which is the product of the rebound hardness and square root of the abrasion hardness.

O'Rourke et al. (1994) derived a relationship mainly from hard metamorphic rock tunnel research:

$$R_f = 36 + 0.23H_T \tag{2.21}$$

Because these models originated from certain rock mass conditions and machine types, they can only be applicable to similar projects. In these models, only one of rock material strength parameters was taken into account. The joint system and its properties were omitted. Hence, these models can not reflect the whole image of rock mass properties. As a result, the penetration rate of the actual TBM in operation is usually more than the predicted penetration rate.

2.4.2 Multi-factor Prediction Model

CSM Model

Colorado School of Mines (CSM) developed a TBM performance prediction model, based on the database of measured cutting forces using disc cutters in different rock types (Rostami, 1997). The database was generated by the Linear Cutting Machine (LCM), and continuously updated. By running multiple variables regression analysis, the best-fit linear function was found as follows (the proportion of variance explained (R^2) is 78%). The equation is empirical and only the magnitude is considered.

$$F_n = -31620 + 2182S + 5538P + 2.6\sigma_t + 0.357\sigma_c + 71621w_t + 1162R \qquad (2.22)$$

where F_n denotes normal force (lbs.); S is cutter spacing (inch); P is penetration (inch/rev.); σ_t is rock tensile strength (psi); σ_c is rock uniaxial compressive strength (psi); w_t is cutter tip width (inch); R is cutter radius (inch).

Using the same database, logarithmic analysis was performed. The relationship among parameters is a power function instead of a linear function. The resultant function is as follows (the proportion of variance explained (R^2) is 86%):

$$F_n = 8.76 w_t^{0.797} R^{0.788} \varphi^{0.602} S^{0.28} \sigma_c^{0.629} \sigma_t^{0.195} \qquad (2.23)$$

where φ denotes the angle of the arc of contact.

After obtaining the normal force, the rolling force may be estimated by using the cutting coefficient (C_c), which is the ratio of the rolling force to the normal force discussed in Section 2.2.

$$C_c = \frac{F_n}{F_r} \quad \text{or} \quad F_r = F_n / C_c \tag{2.24}$$

Using the above equations, the required normal force and rolling force can be calculated. Then, the results are compared with the installed thrust and torque of machine, the achievable penetration rate may be estimated while thrust or torque reaches the maximum value. Nevertheless, the above model does not take into consideration the influence of discontinuities on the penetration rate.

Based on the above model, Cheema (1999) proposed a rock mass boreability index (RMBI) to substitute for rock uniaxial compressive strength in order to incorporate the effect of rock mass on the penetration rate. Three parameters, rock elasticity modulus, Poisson's ratio and the mass size reduction factor, was used to express the RMBI, as shown in Equations (2.25) and (2.26). The mass size reduction factor is derived from the Geological Strength Index (GSI) introduced by Hoek and Brown (1997).

$$RMBI = 8659 + 0.338E + 11614s - 434\upsilon \quad (\mathrm{R}^2\text{=73\%}) \tag{2.25}$$

$$RMBI = 26900 \cdot E^{0.097} \cdot s^{0.444} \cdot \upsilon^{-0.066} \quad (\mathrm{R}^2\text{=85\%}) \tag{2.26}$$

where $RMBI$ denotes rock mass boreability index (psi); E is elasticity modulus (kpsi); s is size reduction factor (equal to $\exp\left(\frac{GSI - 100}{9}\right)$); ν is the Poisson's ratio.

The original CSM model is derived from the linear cutting machine test results. The effect of machine parameters on penetration was fully taken into account. Due to the difficulty in sampling of jointed rock masses, only intact rocks were tested. The effect of joints in the rock mass cannot be reflected in the model. In the modified model, the rock uniaxial compressive strength was replaced by the rock mass boreablity index. The effect of joint orientation on penetration rate is still not included in this modified model. The joint orientation factor is regarded as one of important parameters that influence TBM penetration rate (e. g., Aeberli and Wanner, 1978; Sanio, 1985; Bruland, 1998; Thuro and Plinninger, 2003). It will be discussed in details in Chapter 4.

NTNU Model

The Norwegian University of Science and Technology (NTNU) developed a prediction model of TBM performance in the middle 1970's based on extensive laboratory tests, TBM performance data and geological mapping data. With the development of tunneling technology and the increasing knowledge, the model was periodically revised. Until now, the prediction model has been updated to its sixth revision.

The model can predict net penetration rate, cutter life, machine utilization and excavation cost step by step. In the sub-model for predicting the net penetration rate, the considered factors are listed in Table 2.1. In the sub-model for the cutter wear, the relevant impact factors are summarized in Table 2.2. The model combined the decisive rock mass parameters into one rock mass boreability parameter, the equivalent fracturing factor k_{ekv}, and the relevant machine parameters into one machine parameter, the equivalent thrust, M_{ekv}. The calculation of k_{ekv} is shown in Equation 2.27.

$$k_{ekv} = k_{s-tot} \cdot k_{DRI} \cdot k_{por} \tag{2.27}$$

where k_{ekv} is equivalent fracturing factor; k_{DRI} is correction factor for DRI of the rock; k_{por} is correction factor for porosity of the rock and k_{s-tot}, the total fracturing factor, can be calculated as follows.

$$k_{s-tot} = \sum_{i=1}^{n} k_{si} - 0.36(n-1) \tag{2.28}$$

where k_{si} is the fracturing factor for joint set number i (as indicated in Figure 2.9) and n is the number of fracturing sets.

The corrected factors of different rock mass properties are shown in Figure 2.9. In the model, the equivalent fracturing factor k_{ekv} takes the rock material properties and fracture properties into account. The rock properties include the rock drilling rate index and porosity from the laboratory tests. The fracture properties include the joint spacing and joint orientation. In this model, the systematic fractures are divided into fissures and joints. Joints are considered continuous and they may be followed all around the tunnel profile. Fissures are non-continuous joints and they may only be observed at some sections of the tunnel. Thus, joints and fissures are classified with respect to spacing as listed in Table 2.3. The impact of different class of fractures on TBM penetration is differentiated. In the newly revised prediction model (Bruland, 1998), the impact of single marked joint on the penetration rate is considered. A new correction factor for single marked joint was added to the original model. The equivalent thrust, M_{ekv}, considers the effect of cutter spacing and cutter diameter on TBM penetration rate. The calculation of the equivalent thrust is shown in Equation 2.29.

$$M_{ekv} = F_n \cdot k_D \cdot k_S \tag{2.29}$$

where M_{ekv} is the equivalent thrust; F_n denotes the normal force per cutter in kN/cutter; k_D is the correction factor for cutter diameter ($D \neq 483mm$); k_S is the correction factor for average cutter spacing ($S \neq 70mm$).

Based on the field data, the relationship between k_{ekv} and M_{ekv} is obtained, as shown in Figure 2.10.

Table 2.1 Machine and rock mass parameters influencing the net penetration rate (Bruland, 1998)

Rock Mass Parameters	Machine Parameters
Fracturing: frequency and orientation Drilling Rate Index, DRI Porosity	Cutter thrust Cutterhead revolution per minute Cutter spacing Cutter size and shape Torque

Table 2.2 Machine and rock mass parameters influencing the cutter wear (Bruland, 1998)

Rock Mass Parameters	Machine Parameters
Cutter Life Index, CLI Content of abrasive minerals	Cutter diameter Cutter type and quality Cutterhead diameters and shape Cutterhead RPM Number of cutters on the cutterhead

Table 2.3 Fracture classes for systematic fractured rock mass (Bruland, 1998)

Fracture Class Joints (Sp)(1) / Fissures (St)(2)	Distance between Planes of Weakness (mm)
0	-
0-I	1600
I	400
II	200
III	100
IV	50

(1)Joints (Sp): Include continuous joints that can be followed all around the tunnel profile. They can be open or filled with clay or weak minerals, e.g. calcite, chlorite or similar minerals.

(2)Fissures (St): Include non-continuous joints (can only be followed partly around the tunnel profile), filled joints with low shear strength and bedding plane fissures, e.g. as in mica schist or mica gneiss.

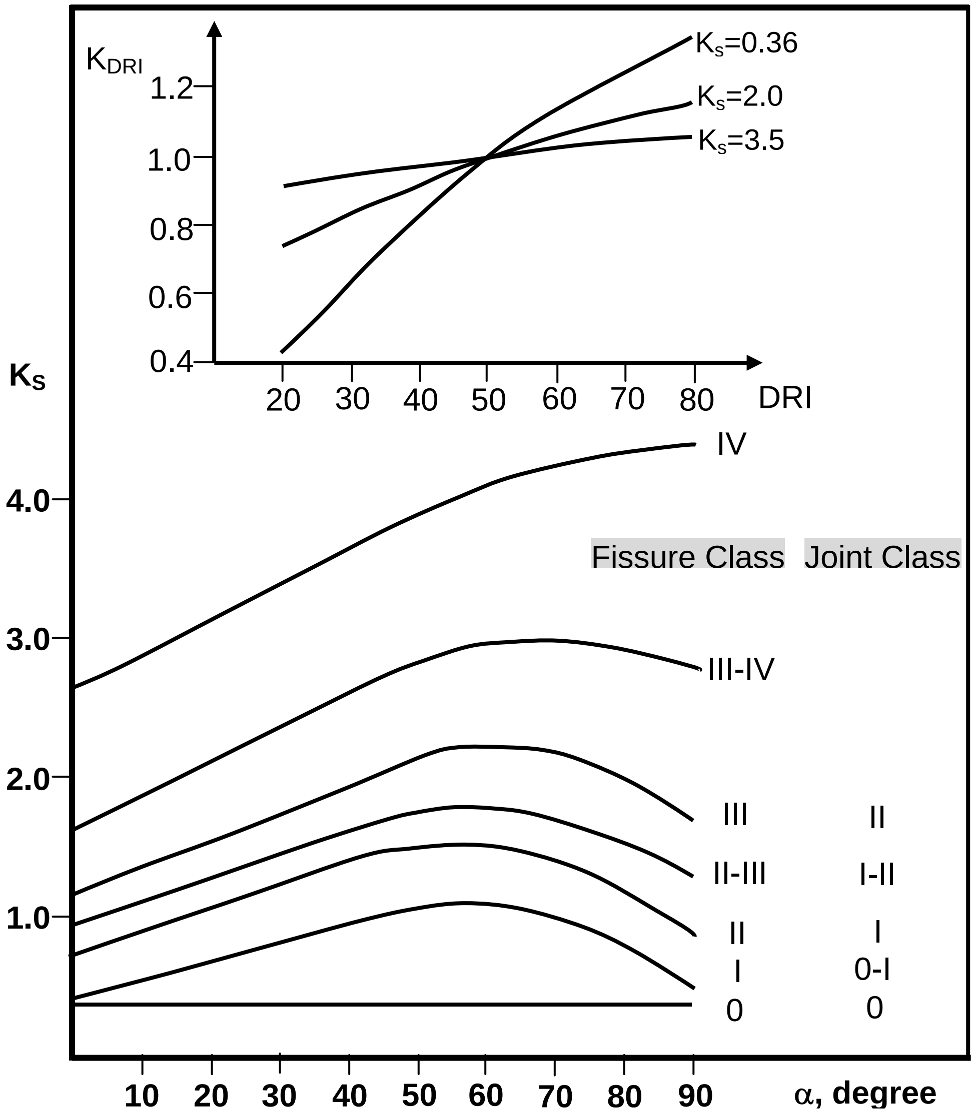

Figure 2.9 Fracturing correction factor for DRI ≠ 50

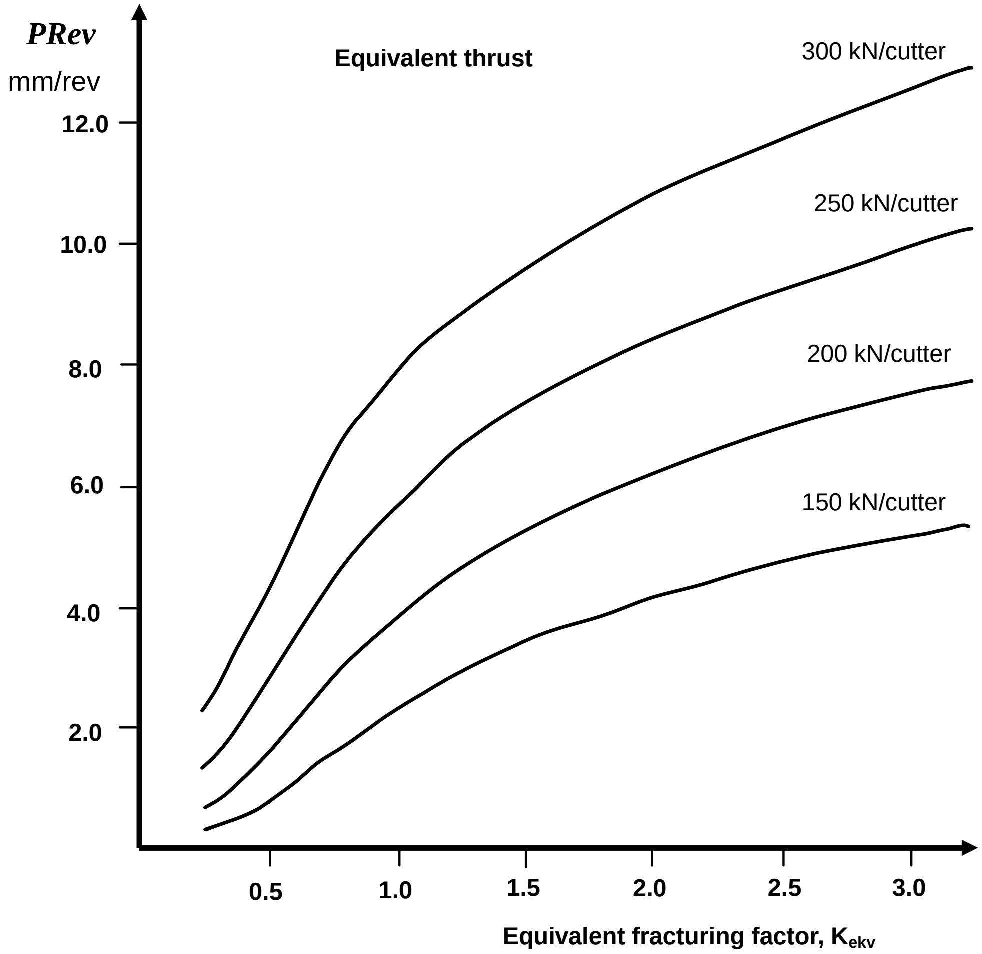

Figure 2.10 Basic penetration with cutter diameter 483 mm and cutter spacing 70 mm

The NTNU model is derived from the actual TBM performance on different rock mass conditions. The effect of machine parameters and rock mass parameters on penetration rate is fully reflected in this model. The thrust per cutter was modified by the machine parameters such as cutter diameter and cutter spacing. The rock mass parameters such as rock hardness and brittleness, the fracture spacing and its orientation are regarded as input factors. Furthermore, the model is updated by the development of the machine technology. So, it is extensively utilized to predict TBM performance including penetration rate, advance rate, cutter wear and cost. But, the laboratory tests that the model depends on were originally developed for prediction of drillability for percussive drilling. Because these tests are not the typical rock mechanical tests and are usually not available outside Norway, the application of the model is limited.

Q_{TBM} Model

Based on the Q-system and data from 145 tunnels totaling more than 1000 km in length, Barton (2000) modified the rock mass classification system – Q system into Q_{TBM} to predict TBM performance. Q_{TBM} adds some new parameters that take the interaction between TBM and rock mass into consideration. The components of Q_{TBM} are as follows:

$$Q_{TBM} = \frac{RQD_0}{J_n} \cdot \frac{J_r}{J_a} \cdot \frac{J_w}{SRF} \cdot \frac{SIGMA}{F_n^{10} / 20^9} \cdot \frac{20}{CLI} \cdot \frac{q}{20} \cdot \frac{\sigma_\theta}{5} \tag{2.30}$$

where RQD_0 is RQD interpreted in the tunnelling direction and RQD_0 is also used to evaluate the Q-value for rock mass strength estimation; J_n, J_r, J_a, J_w and SRF are the same as those in Q-system, except that J_r and J_a should refer to the joint set that mostly assists (or hinders) boring; F_n is average cutter load (ton) through the same zone, normalized by 20 ton; CLI is cutter life index originated from NTNU model; q is quartz content in percent; σ_θ is the induced biaxial stress on tunnel face (MPa) in the same zone, normalized to an approximate depth of 100 m; SIGMA is the rock mass strength estimation.

The meaning of the value of Q_{TBM} is illustrated schematically in Figure 2.11. The relative ease and difficulty for boring is shown at the top of this figure. The value of Q_{TBM} can range over twelve orders of magnitude, and both of the ends of the range are exceptionally unfavorable for advance rate.

Q_{TBM} model is a modified Q system. Since the Q system is a rock mass classification system originated from the tunnel stability evaluation, some parameters such as J_r, J_a, J_w and SRF have great effect on tunnel stability and are

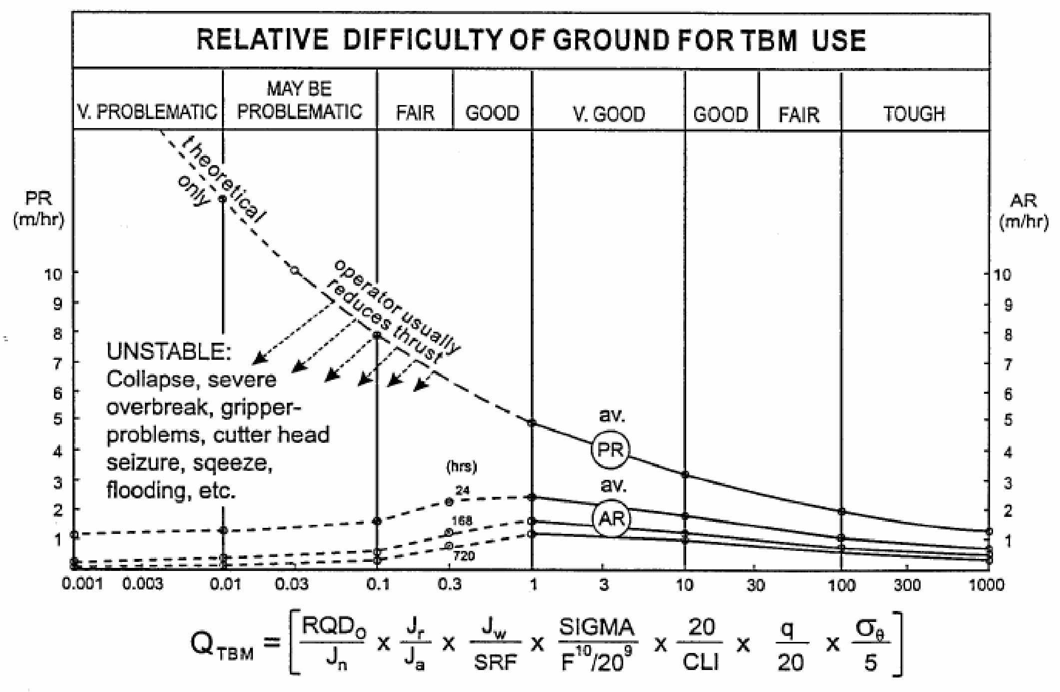

Figure 2.11 Suggested relation between PR, AR and Q_{TBM} (Barton, 2000)

not sensitive for TBM penetration rate (Sundaram et al. 1998). Some factors are overlapped in this model. Moreover, the effect of some important machine parameters such as cutter diameter and spacing on TBM performance is not reflected. In addition, this model includes too many parameters. It makes the model hard to apply.

Probabilistic Model

Due to the inherent uncertain nature of geological conditions surrounding tunnels and no accepted theoretical basis for predicting tunnel boring machine system performance, Nelson et al. (1999) proposed a probabilistic approach to simulate the TBM performance. The probabilistic prediction model is based on a large database of over 600 public-domain case histories.

The database is divided into four levels of data sets. The first level data set is composed of cursory and averaged project data over the length of a drive. The second and third levels contain the data sets over the length of a zone and a discrete unit cell respectively, as shown in Table 2.4. The last level contains all data in details including the performance of the TBM sub-systems and identifies fitted parametric probability density functions that describe the performance of the TBM sub-systems using time between failures and time to repair values. With regard to the different investigation program stage, the corresponding precision data can be obtained in the same database level by retrieving data through various statistical treatments to predict the construction time and construction costs and so on. The prediction results are represented as probabilistic distributions.

Especially, in order to consistently record and simulate the rock mass conditions in this model, Laughton (1998) applied the Rock Mass Condition Model shown schematically in Figure 2.12 to classify the rock mass conditions into 7 classes. Furthermore, Rock Mass Behavior classes were adopted to reflect the rock mass support level with regard to the consistently observed tunnel parameters as indicated schematically in Table 2.5. The two classification models are very useful to simulate the TBM performance of cells.

Table 2.4 Performance recording unit for data base level 1 through 3 (Nelson et al., 1999)

Data Base Level	Tunnel Drive Subdivision
1 Drive • Rock mass variation not recorded • Unique geological descriptor	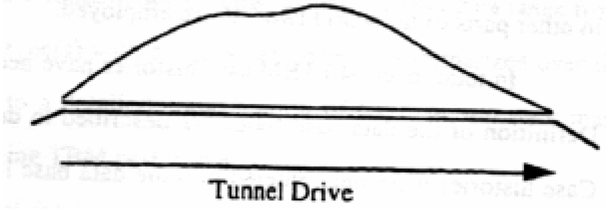
2 Zone • Rock mass variation characterized by zone parameters	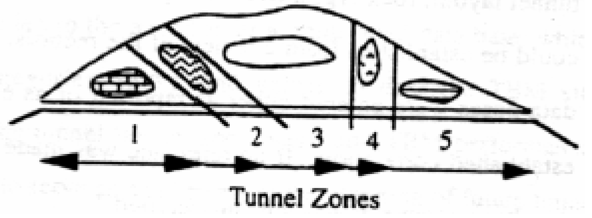
3 Unit Cell • Rock mass variation characterized by zone and unit cell parameters	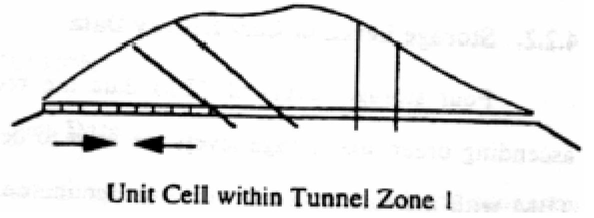

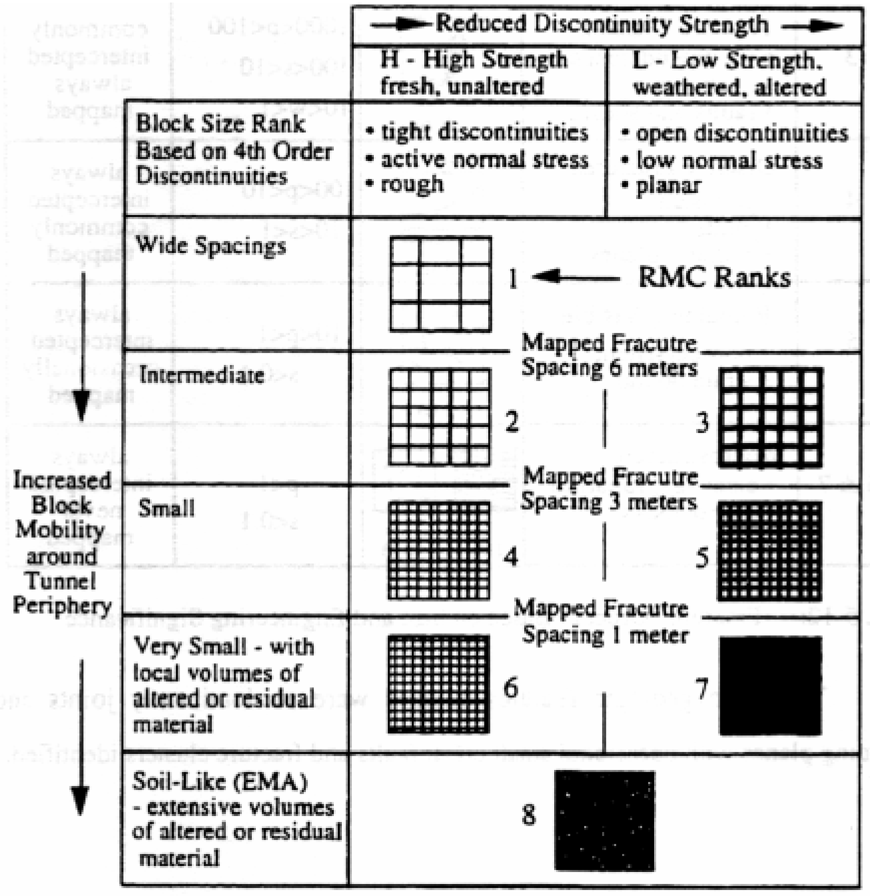

Figure 2.12 Rock mass condition model (Laughton, 1998)

Table 2.5 Rock mass behaviour classification based on fracture presence and overbreak (Laughton, 1998)

Behavoir-Classes	Evidence of Instability at the Heading	
I: Field-Massive	• Bedding only • No mapped joints	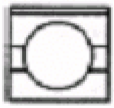
II: Fracture but Stable	• Mapped joints present • No overbreak	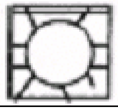
III: Local Fracture-Bound Overbreak	• Local overbreak • Limits of overbreak defined by planar fracture surfaces	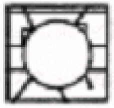
IV: Local Soil-Like Overbreak “Pockets”	• Local overbreak • Limits of overbreak defined by uneven weathered/altered surfaces	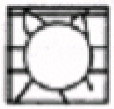
V: Extreme Mining Areas	• Extended overbreak length • Heavily fractured and/or altered/weathered materials	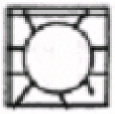

The probabilistic prediction model was developed from the case histories. Its predictions were derived from past performance. However, due to the uniqueness of the rock mass conditions for each project, TBM operation status and project management in different projects, the case history records may be affected by man-made factors. Furthermore, the tunnelling technology has been continuously improving over the years. Thus, it is difficult to simulate accurately the TBM performance based on the past project records. Nevertheless, it is still very useful in feasibility study, selecting viable project options, and predicting typical tunnel construction conditions and choosing construction methods.

Neuron-network Prediction

Grima et al. (2000) and Bruines (2001) emphasized that the interaction between TBM and rock mass is dynamic, uncertain, complex, non-linear and ill-defined, and rock masses, in most cases, behave anisotropically, non-linearly and are discontinuous. They applied the neuro-fuzzy model to predict TBM performance such as penetration rate and advance rate. The neuro-fuzzy model combines fuzzy logic and artificial neural network methods. Artificial neural network recognizes patterns and adapt themselves to cope with changing environment, and fuzzy logic can incorporate human knowledge to deal with uncertainty and imprecision, and to perform inference and decision-making. The final model (Grima et al., 2000) used five input parameters to predict penetration rate, which include the core fracture frequency, uniaxial compressive strength, RPM, thrust per cutter and cutter diameter, and seven input parameters to predict advance rate, which include rock mass parameters (geology, rock strength and strength deviation), geometry (diameter, length and shaft depth) and machine characteristics (TBM conditions). Moreover, the model only sets up a connection between input parameters and objects to be predicted. The prediction results depend strongly on the learning data used to establish the model.

Table 2.6 Penetration rate prediction models and the corresponding factors

Prediction value	Reference	Rock mass factors	Machine factors and tunnel geometry
PRev	Farmer and Glossop, 1980	σ_t	F_n
PRev	Graham, 1976	σ_c	F_n
PRev	Hughes, 1986	σ_c	F_n, cutter diameter
R_f (kN/cutter/mm/rev)	Nelson et al., 1983; O'Rourke et al., 1994	H_T (total hardness)	F_n
PRev	CSM (Rostami, 1997)	σ_c, σ_t	Cutter spacing, cutter tip width, cutter radius, F_n
PRev	Modified CSM (Cheema, 1999)	σ_t, RMBI (elasticity modulus, size reduction factor and possion's ratio)	Cutter spacing, cutter tip width, cutter radius, F_n
PR	NTNU model (Bruland, 1998)	Drilling rate index (DRI), fracture frequency and orientation, porosity	F_n, cutterhead RPM, cutter spacing, cutter size and shape, installed cutterhead power
PR, AR, U	Probabilistic model (Nelson et al., 1999)	The regional geological structure, rock type, quartz content, intact rock strength, the tunnel water conditions (level 2)	Maximum thrust, torque, cutterhead RPM, disc cutter number and diameter, TBM diameter, type of mucking system, tunnel length and gradient
PR, AR	Q_{TBM} (Barton, 2000)	RQD_0, J_n, J_r, J_a, J_w, SRF, the rock mass strength, CLI, quartz content, induced biaxial stress, porosity	Average cutter load, TBM diameter
PR	Neuro-fuzzy model (Grima et al., 2000)	The core fracture frequency, UCS	RPM, normal force per cutter, cutter diameter

2.4.3 Summary

From 1970's to now, a number of prediction models have been proposed, which include single factor and multi-factor prediction models, as summarized in Table 2.6.

The main factors of rock mass used to predict the PR include compressive strength and tensile strength of rock material, frequency and orientation of rock fractures. The machine factors applied to predict the PR include cutter spacing, cutter tip width, cutter radius, average thrust per cutter and RPM. At present, the extensively used models are the CSM model, the NTNU model, probabilistic model and Q_{TBM}. These models of course have their advantages and disadvantages because of their origin and background. The CSM model does not originally consider the influence of discontinuities on TBM performance. The modified CSM model only regards discontinuities as a factor that affects the rock mass strength. The NTNU model requires special experiments that are originated from the drilling. The tests are not commonly available outside Norway. The probabilistic model by Nelson et al. (1999) only takes into account the similarity of tunnels and neglects the interaction between TBM and rock mass. Q_{TBM} originates from Q system and includes too many parameters for actual application. In addition, some parameters are overlapped in this model.

2.5 Rock Mass Classification System and Applicability to Machine Tunnelling

A rock mass is composed of rock material and discontinuities. It is a complex geological unit, because there is great diversity both in the composition of the rock material and in the nature and extent of its discontinuities. Its formation and evolution are controlled by the surrounding geological environment. Its behavior is similar under similar geological and engineering characteristics. In order to improve engineering design and management, it is necessary for engineers to classify rock mass according to rock mass characteristics and engineering behavior. Bieniawski (1989) outlined the objectives of rock mass classification. It is still the guideline of rock mass classification for engineering applications.

Various classification systems have been employed in rock engineering since Terzaghi (1946) proposed the first one for tunnelling with steel support. Rock mass classifications have become the backbone of the empirical design approach. They are mainly applied to tunnel support design and slope stability analysis.

TBM is becoming a common tool for tunnel excavation. In order to predict and evaluate the TBM performance, rock mass classification systems are also used to correlate rock mass classes and TBM performance (e.g. Sapigni et al., 2002; Ribacchi and Fazio, 2005). The correlations between different rock mass classes in different rock mass classification schemes and TBM performance are reviewed in this section. The applicability of the existing rock mass classification schemes for TBM performance is discussed.

2.5.1 Rock Mass Classification Systems

The main classification and characterization systems are listed in Table 2.7. The corresponding expression form, application scopes and classification parameters of these classification systems are also listed in this table. The main expression form of rock mass classification includes numerical and descriptive form. Their applications are mainly on the design of support in tunnels and mine, general characterization and communication, assessment of excavatability. In all of the listed rock mass classification systems, the following parameters are most frequently applied: rock strength (rock compressive strength, tensile strength, shear strength, point load index and angle of internal friction), joint density (joint spacing or frequency and persistence, RQD and block size), joint conditions (joint infill and alteration), joint orientation, in situ stress, groundwater condition. Also, other features, such as weathering, swelling, geological structure, Young’s modulus, cone indenter index, Cerchar index, Shore scleroscope hardness and specific energy index are used in some rock mass classification systems.

Rock material strength, joint density and joint conditions are used to classify rock mass in almost all rock mass classification systems. It shows that these parameters are key rock mass characteristics. The various joint spacing and aperture classifications are shown in Figures 2.13 to 2.14 respectively. The rock strength classifications are compared in Figure 2.15. These parameters reflect the main intrinsic properties of rock mass which include the structure and components of rock mass. However, since the behavior of rock mass is estimated under the action of engineering conditions, the corresponding engineering factors may be incorporated into rock mass classification.

Table 2.7 Some of the main classification and characterization systems

Name of classification	Reference	Form	Main applications	Parameters
Rock load	Terzaghi, 1946	Descriptive and behavioristic form	For design of tunnels mainly supported with steel sets	Joint spacing or frequency, rock mass stress field and rock swelling (descriptive)
Stand-up time	Luffer, 1958	Description form	For design of support and excavation in tunnels	Rock strength, joint spacing and persistence (descriptive)
The new Austrian tunnelling method (NATM)	Rabcewicz and Golser, 1972; Muller, 1978	Descriptive and behaviouristic form Tunnelling concept	For design of support and excavation in tunnels	Rock strength, deformability and swelling, weathering, joint spacing and persistence, geological structure, rock stress condition and excavation dimensions (descriptive)
The rock quality designation	Deere and Deere, 1988	Numerical form	Core logging; used in other classification systems	RQD
The unified rock classification system	Williamson & Kuhn, 1988	Descriptive form	For use in communication	Weathering, strength, discontinuity, and density
Geotechnical description	ISRM, 1981	Descriptive form	For use in communication	Rock name, layer thickness and discontinuity spacing, the uniaxial compressive strength of the rock material and the angle of the friction of the fractures
The size-strength classification	Franklin,1986	Numerical form	Used mainly in mining	The strength of intact rock and the spacing of discontinuities
Classification of the rock mass structure	Hwong 1978	Descriptive form	For use in all geological engineering	Block size and shape, shear strength of discontinuities, strength of rock block (descriptive and numerical)
Rock structure rating (RSR) classification	Skinner, 1988	Numerical form	For design of tunnels mainly supported with steel sets	Rock type origin, rock hardness, geological structure, joint spacing, joint orientation, direction of tunnel drive, joint condition, and amount of water inflow
Rock mass rating system (RMR)	Bieniawski, 1973, 1989	Numerical form	For design of support in tunnels and mine	Uniaxial compressive strength of rock material, rock quality designation (RQD), spacing of discontinuities, condition of discontinuities, groundwater conditions, and orientation of discontinuities
Q system	Barton et al., 1974	Numerical form	For design of support in underground excavations	RQD, Number of joint sets, roughness of the unfavorable joint or discontinuity, degree of alteration or filling along the weakest joint, water inflow, and stress condition
Integrated mass system (IMS)	McFeat-Smith et al., 1986	Descriptive form	For design of support in underground excavation	Joint spacing, weathering grade and water inflows
JH method	Shinji et al., 2002	Numerical form	For design of support in underground excavation	Uniaxial compressive strength, weathering, spacing of joints, condition of joints, joint orientation, ground water, alteration by water
The geological strength index	Hoek and Brown, 1997	Numerical form	For general characterization, design of support	Joint surface roughness, filling and weathering, rock block size
The rock mass index (RMi) system	Palmstrom, 1995	Numerical form	For general characterization, design of support, TBM progress	Joint roughness, joint alteration, joint size and termination, density of joints, rock material strength
Rock mass classification for coal measures rocks (RMCR)	Yasar, 2001	Numerical form	For determining the cost and time for construction of coal mine and choosing excavation methods and support system	Mineral content index, uniaxial compressive strength, uniaxial tensile strength, young's modulus of elasticity, shear strength, cohesion of rocks, angle of internal friction, point load index, cone indenter index, Cerchar index, Shore scleroscope hardness and specific energy index
A classification system for the characterization of the excavatability of soils and rocks	Kirsten, 1988	Numerical form	For assessment of excavatability and selection of construction machines	Strength of the ground, RQD, joint set number, relative ground structure number, joint roughness rating and joint alteration rating

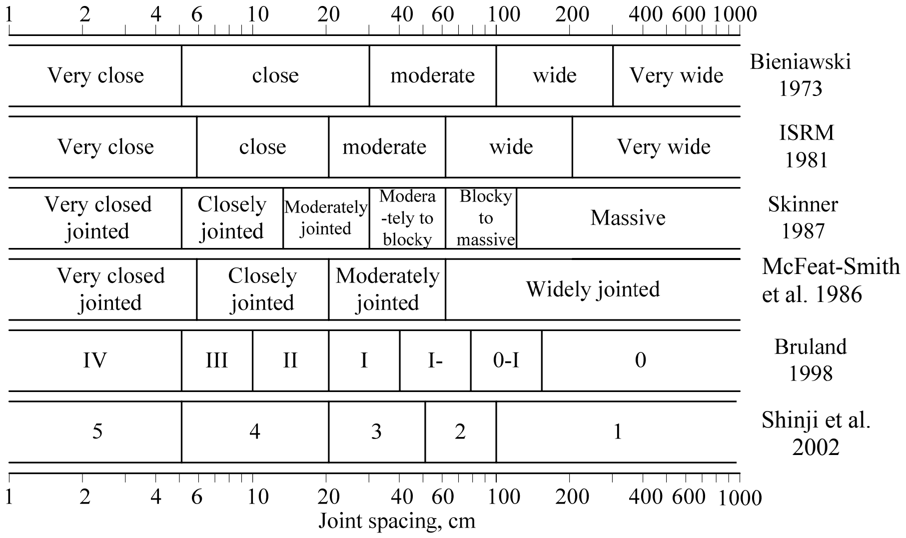

Figure 2.13 Various joint spacing classifications

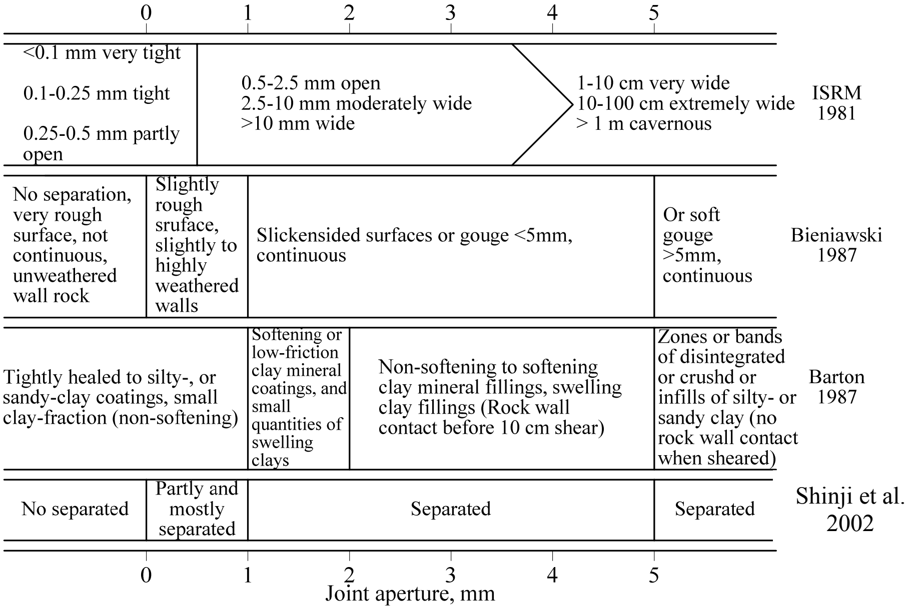

Figure 2.14 Various joint aperture classifications

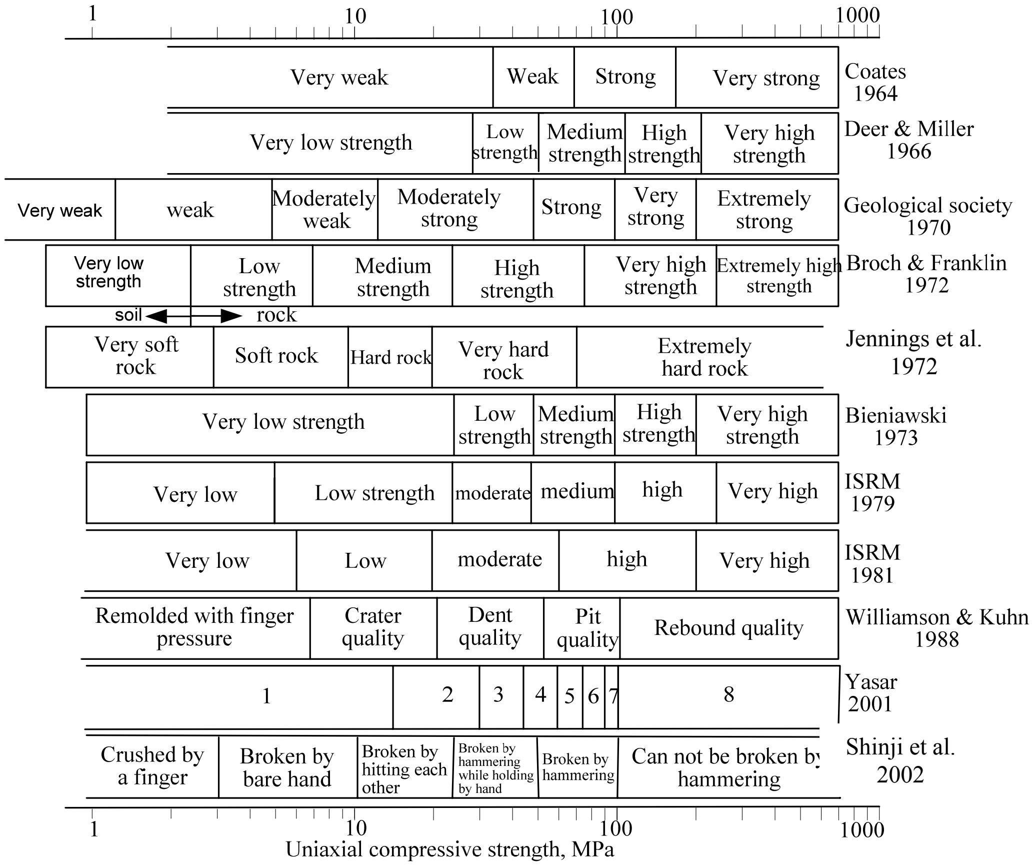

Figure 2.15 Various strength classifications for rock (after Bieniawski, 1989)

2.5.2 Applicability of Rock Mass Classification Systems to Machine Tunnelling

Morimoto and Hori (1986) assessed the effect of rock mass on TBM excavation rate for the headrace tunnel of the Hayakido Hydro Power Station. Rock masses composed of gneisses were divided into five classes. Although the results were considerably scattered, the trend of average excavation rate is obvious. The excavation rate at the medium rock mass classes was higher, and was lower at the good and poor rock mass classes.

Innaurato et al. (1991) utilized the uniaxial compressive strength (σ_c) and Rock Structure Rating (RSR) to predict TBM penetration rate. The analysis was based on 112 tunnel sections, which can be considered homogeneous with regard to TBM excavation. The correlations among the penetration rate (PR), σ_c and RSR are shown in Equation 2.31 and Figure 2.16.

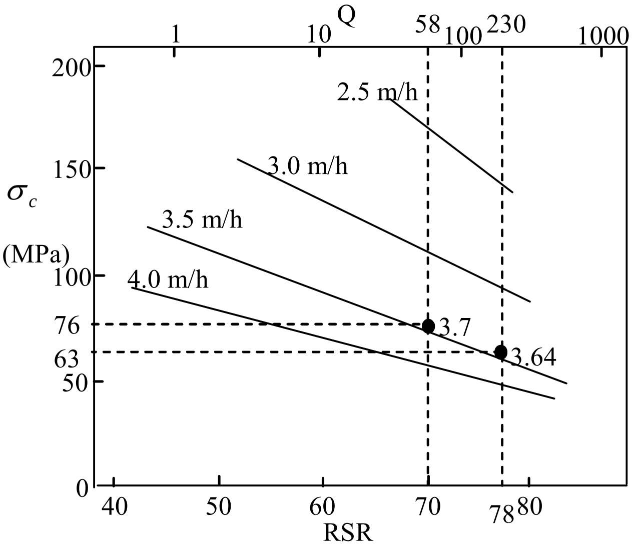

Figure 2.16 Equal penetration rate curves as function of σ_c, Q and RSR ratings for a 3.5m diameter tunnel (After Innaurato et al., 1991)

$$PR = \sigma_c^{-0.437} - 0.047 \cdot RSR + 3.15 \tag{2.31}$$

Laughton and Nelson (1996) classified rock masses into 36 classes, representing combinations of block size rank (four classes), degree of alteration or weathering (three classes), and level of water inflow at the heading (three classes). For penetration rate, combinations of block size and weathering are used to classify rock conditions. The impact of water inflow on penetration rate is not obvious. TBM Utilization is a function of rock mass class including the impact of water inflow and support class.

Based on the performance of TBMs used in the Frasnadello and Antea Tunnels, Barla (2000) pointed out that the penetration rate evaluated for the small diameter TBMs seems to be better related to the Rock Mass Rating (RMR) than observed for the large diameter TBMs. The direct correlation between the machine penetration rate and the Rock Mass Rating (RMR) was poor. TBM performance reached a maximum in RMR range of 40-70.

Sapigni et al. (2002) also found that slower penetration rate was experienced in both extremely bad and extremely good rock masses. Even considering the same machine and the same RMR class, lower penetration rates were experienced in strong rocks. The results show the rock mass rating only takes into account part of factors affecting TBM performance.

Alber (1996a and 2000) used rock mass strength (σ_{cm}) shown in Equation 2.32 to evaluate the specific penetration rate (mm/revolution/MN/cutter).

$$\sigma_{cm} = \sigma_c \cdot \sqrt{s} \tag{2.32}$$

where $s = \exp^{(RMR_{TBM} - 100)/9}$ and $RMR_{TBM} = 0.84 RMR + 21$.

The relationship between σ_{cm} and the specific penetration rate is that the specific penetration rate increases as the rock mass strength decreases down to a rock mass strength of about 15 MPa, and then decreases. Because rock masses with very low strength are often dominated by closely spaced discontinuities, the formation of rock chips between two discs may be hindered in those highly fractured rock masses. Single blocks may be ripped out of the face and reground.

Sundarm et al. (1998) studied the correlation between Q value and TBM performance in the Kelinchi Transfer Tunnel. The field penetration index (R_f, (kN/cutter)/(mm/revolution)) gave higher correlation with the RQD/J_n, and lower with J_r/J_a and lowest with J_w/SRF. For RQD > 75%, the breakage of the rock mass mainly depended on the material properties, and when RQD < 75%, the breakage is facilitated by the presence of discontinuities where crack propagation or rock mass failure takes place along the pre-existing weak planes. The field penetration index is sensitive to the spacing of discontinuities within the range of 6-20 cm.

Integrated Mass System (IMS) has been extensively applied to study correlation between TBM performance and rock mass classes in Hong Kong (McFeat-Smith and Askilsrud, 1993; McFeat-Smith, 1999; Gradnori et al., 1995). A basic trend is that with the increase of rock mass classes from 1 to 5, the predicted penetration rate increases, but the distribution overlaps to a large extent. When the penetration rate is normalized by thrust per cutter, the correlation is better, but it is still considerably scattered. McFeat-Smith (1999) found that reasonable relationships exist between IMS rock classes and machine utilization. Table 2.8 shows the machine utilization measured for each IMS rock class from six TBM excavated tunnels and a range of TBM types and sizes ranging from 3.35-9.8 m in diameter for igneous, metamorphic and sedimentary rock types.

Table 2.8 Machines utilization for IMS rock classes (after McFeat-Smith, 1999)

IMS	1	2	3	4	5
Utilization	45	40	30	20	15

2.5.3 Discussions and Conclusions

Rock mass classification, regarded as an empirical method, has become a backbone of support design for tunnels. Many rock mass classification systems have been proposed for tunnel support design, communication, and slope stability. In all these rock mass classification systems, rock strength, joint spacing or frequency and joint conditions were key parameters. These are the main intrinsic properties of rock mass that affect and control rock mass deformability and stability. These intrinsic properties were classified into different classes in different rock mass classification systems, as shown in Figures 2.13 to 2.15. The main reasons are that these classification systems originated from different case studies in different areas.

With the development of tunnel boring machine, TBM is now widely used to excavate rock tunnels. Extensive studies have been carried out to try to set up a relationship between rock mass quality and TBM performance. In these studies, the rock mass classification systems used to characterize rock mass quality mainly include RSR, RMR, Q system and IMS. The results show that with the increase of rock mass quality, the penetration rate generally decreases. However, very poor rock mass does not facilitate the penetration rate. Although the tendency is obvious, the TBM penetration rate distributes in a large range corresponding to rock mass classes. Even with the same rock mass classes and TBM specifications, the TBM performance is different (Innaurato et al. 1991, Sapigni et al. 2002). The correlation between rock mass classes and TBM penetration rate is poor. If one combines the rock mass classification with rock uniaxial compressive strength to predict the penetration rate, the results are better. The existing rock mass classification systems may either not include the parameters affecting the TBM performance or involve too many parameters that are not relevant to TBM performance. They cannot offer a complete solution to the rock mass fragmentation behavior during TBM boring.

By the study of McFeat-Smith (1999), the correlation between the rock mass IMS classes and TBM utilization is very good. With the increase of rock mass quality, TBM utilization increases. Because utilization is the percentage of available shift time during which excavation or rock penetration occurs, it is determined by the downtime. The downtime includes the time of TBM repair (cutter replacement, machine maintenance), backup system delay (portal operations and train delay), scheduled TBM maintenance, segment ring installation or restroke, delay due to ground conditions (rock jams, gripper bearing difficulty, clearance and rock support). The main factors influencing the variation of downtime are the cutter replacement time, temporary machine maintenance and ground conditions. The downtime is strongly related to rock mass quality and rock mass stability during excavation. Thus, the correlation between the rock mass classes and TBM utilization is better than that between the rock mass classes and TBM penetration rate. However, further studies are needed to confirm the relationship.

Rock strength, joint spacing and joint conditions are almost used in every classification system. They are the basic parameters expressing the structure and component of rock mass. Because these systems mainly originated from tunnel support design and stability evaluation, some parameters such as rock compressive strength and brittleness influencing the penetration rate are not included in some of the rock mass classification systems. Some classification systems include factors that are not related to the penetration rate. Furthermore, the machine parameters have not been taken into consideration with regard to the correlation between the rock mass classes and the penetration rate. Thus, the correlation between rock mass classes and TBM penetration rate is poor, while the correlation between the rock mass classes and TBM utilization is better.

2.6 Summary

TBM performance is determined by the machine efficiency on rock mass fragmentation, which depends on the machine parameters and rock mass characteristics. The rock breakage process consists of the rock indentation by the cutters and the chip formation between two neighboring cutters. The rock indentation process shows that the formation of the crushed zone immediately under the cutters and cracks initiation and propagation are heavily influenced by the rock uniaxial compressive strength, tensile strength or rock brittleness and cutter geometry. The chip formation is determined by the cracks propagation and cutter spacing. In order to efficiently fragment rock masses and maximize the penetration rate, sufficient thrust must be applied to cutters to crush the rock and propagate the cracks, and cutter spacing and layout need to be optimized for efficient boring.

The ratio of rolling force to normal force is termed the cutting coefficient. It is relevant to the cutter diameter and TBM penetration. It was confirmed by the linear cutting tests and field studies. In order to maintain TBM operation in high penetration rate, the suitable torque or capacity is required based on the rock mass conditions. Ideally, the TBM operates in a limited rate of both torque and thrust. In addition, the system rigidity plays an important role in TBM operation. Lower stiffness system needs more specific energy to break the rock. A stiff cutting system can reduce the machine vibrations and shock loads experienced by the cutters during boring, and then reduce the cutter wear and abnormal cutter failure.

Field studies confirmed that joint spacing and joint orientation greatly affected the penetration rate, which cannot be fully tested in the laboratory. The existing joints in rock masses reduce the distance of the cracks propagation, and speed up the rock chipping process. Due to the influence of the joint and its orientation, the chip size in jointed rock mass is larger than that in solid rock mass. With the increase of joint spacing, the penetration rate decreases. The maximum penetration rate occurred when the angle between the joint plane and tunnel axis is equal to 60º and decreases when the angle is less and more than 60º.

With the development of TBM technology, especially in automation and cutter capacity, it is extensively used to excavate tunnels. Based on the actual TBM performance, many TBM penetration prediction models were proposed. Some rock mass classification systems originated from the tunnel support and stability evaluation were used to predict the TBM penetration rate. In general, all the models and related researches are useful in identifying some of the influencing parameters. The disadvantages of these models are obvious.

As discussed earlier, the rock mass breakage process includes rock indentation and chip formation between two neighboring cutters. The rock mass fragmentation process is the interaction process between TBM and rock mass. The machine parameters and rock mass properties should be fully considered with regard to the prediction of the penetration rate. The aim of this thesis is to develop a model to predict the TBM penetration rate. The machine parameters influencing the penetration rate, such as thrust force, torque, cutter diameter, cutter tip width and cutter spacing are taken into account in the model. The main rock mass properties influencing the penetration rate, such as rock uniaxial compressive strength, rock brittleness, joint spacing and orientation, are also considered in the model.

Chapter 3 Numerical Modelling on Rock Breakage Process by TBM Cutters

3.1 Introduction

The rock breakage process under rolling cutters of TBM can be divided into two stages. The first is that the rolling cutter intrudes into the rock, and then generates the fragments of different sizes as well as internal cracks. This process is called indentation. The second stage is that cracks between two adjacent cutters propagate across the space between two cutters, and then large chips are formed between two cutters.

The response of rock to indentation by different shape indenters has been investigated by many researchers. Lawn and Swain (1975) studied the chipping formation process in brittle materials by using fracture mechanics principles. Cook et al. (1984) described the process of rock fragmentation induced by circular flat-bottom indenter using punch loading tests. Pang and Goldsmith (1990) predicted theoretically the crack extent and direction in the rock indentation process based on the maximum principle strain value and the associated extension strain criterion in a semi-infinite, homogeneous and isotropic solid. The prediction results showed good agreement with the experiments. During the past years, finite element method (FEM) has been used to simulate the rock material fragmentation by an indenter. Cook et al. (1984) employed a linear axisymmetric elastic finite element model to numerically investigate the fracture process in a strong, brittle rock by a circular, flat-bottomed punch. The results showed a good agreement with the laboratory experiment. Chiaia (2001) used a lattice model implemented in the FEM program to simulate the penetration process in heterogeneous material by a hard cutting indenter. He found that the indentation process characterized various interaction mechanisms, amongst them the dominant modes would be plastic crushing and brittle chipping. To reproduce the progressive process of rock fragmentation in indentation, Liu et al. (2002) presented a numerical code R-T^{2D} based on rock failure process analysis model in the simulation, where realistic crack pattern can be observed. In those studies, the force-penetration behavior was recorded and the formation of craters and cracks were examined. Those studies are useful for understanding rock fragmentation phenomena and establishing theories and models for rock breakage by mechanical tools. Also, those works provided phenomenological descriptions and some understandings of the processes under certain specific conditions.

The rock chipping process between two neighboring cutters has also been extensively studied. By linear cutting tests, Sonwdon et al. (1982) found that the optimal cutter spacing was determined by the rock properties and penetration per revolution. The rock brittleness greatly influences the optimal cutter spacing. Rostami and Ozdemir (1993) found out that rock chipping mode varied due to the different cutter spacing. Liu et al. (2002) represented the rock breakage process under the action of two cutters using the numerical code R-T^{2D}. Until now, there is still not a theoretical method available to be used in TBM design.

This chapter focuses on rock fragmentation process based on the above-mentioned interaction between rock and TBM cutterhead, and thereby finds out the rock breakage mechanisms and the main factors influencing the penetration rate, which include rock properties and machine parameters. The discrete element method (DEM), as a powerful numerical simulation method, can simulate conveniently the effect of joints on rock mass fragmentation process. Thus, DEM is adopted to simulate the above mentioned rock breakage process including single cutter indentation process, chip formation between two cuts in this chapter and jointed rock mass breakage process in next chapter. The optimization of cutter spacing is also simulated by UDEC in this chapter.

3.2 UDEC

Discrete element method (DEM), proposed by Cundall in 1971, is a discontinuous model to simulate fractured rock masses. In the DEM, a rock mass is treated as an assemblage of discrete blocks by discontinuities, namely rock joints. Individual block can be defined either as rigid or deformable by specifying the material models. The calculation conducted in the DEM alternates between a force-displacement law and an equation of motion. At the contact faces, interacting forces are governed by the force-displacement relationship; while at the centroid of each block, Newton's second law in central difference format is used to govern the motion of blocks. The solution scheme is identical to that used by the explicit finite difference method (FDM) for continuum analysis. The dynamic behavior is represented numerically by a temporal stepwise algorithm. By using the explicit dynamic approach, DEM is able to simulate large displacements across the discontinuities without encountering much numerical stability problems. The 2D DEM algorithm was coded and the commercial code UDEC (Universal Distinct Element Code) has been extensively applied in various fields such as quasi-static rock mass stability and dynamic response of rock mass under blasting/earthquake loading.

The explicit finite difference procedure is employed within blocks to account for the block deformation. To facilitate the code capability in analyzing irrestorable deformation, different plastic models can be incorporated. For the Mohr-Coulomb model which is available in UDEC and used in this study, a shear yield function and a non-associated shear flow rule are employed. This yield criterion is schematically illustrated in Figure 3.1. The yield function can be represented by the Mohr-Coulomb yield function and the tension yield function (Itasca, 1996):

$$\begin{aligned} f^s &= \sigma_1 - \sigma_3 N_\phi + 2C\sqrt{N_\phi} \\ f^t &= \sigma_t - \sigma_3 \end{aligned} \tag{3.1}$$

where $N_\phi = \dfrac{1+\sin\phi}{1-\sin\phi}$, C is the cohesion, σ_t is the tensile strength, ϕ is the friction angle.

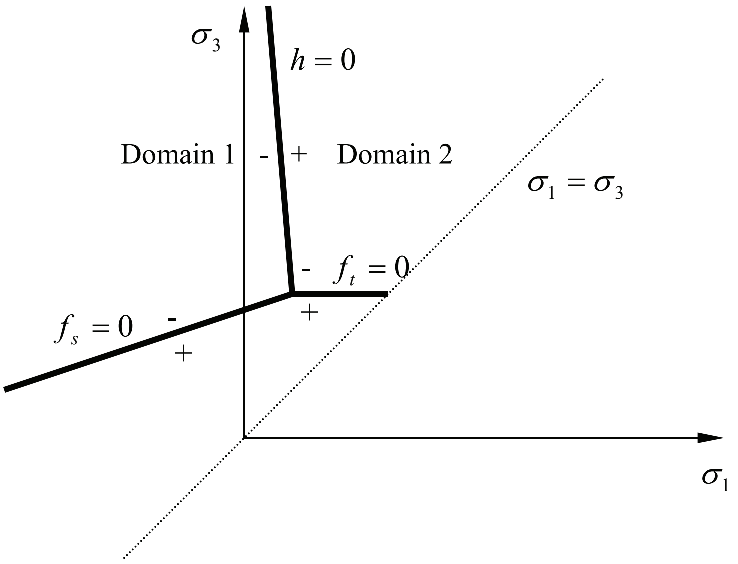

Figure 3.1 Mohr-Coulomb criteria in σ_1 - σ_3 plane

A non-associated flow rule is derived from the following functions:

$$\begin{aligned} g^s &= \sigma_1 - \sigma_3 N_\psi \\ g^t &= -\sigma_3 \end{aligned} \tag{3.2}$$

where $N_\psi = \dfrac{1+\sin\psi}{1-\sin\psi}$, ψ is the dilation angle.

To identify the shear failure and the tensile failure, a function defining the edge of the two areas is constructed:

$$h = \sigma_3 - \sigma_t + \alpha^P(\sigma_1 - \sigma^P) \tag{3.3}$$

where $\alpha^{\mathrm{P}} = \sqrt{1+N_\phi^2} + N_\phi$, $\sigma^{\mathrm{P}} = \sigma^t N_\phi - 2C\sqrt{N}$. As shown in Figure 3.1, when a stress point satisfies shear failure criteria, located in Domain 1, it will be brought back to $f^s = 0$ using a flow rule derived from the function g^s; Similary, a stress point located in Domain 2 will be brought back to $f^t = 0$ using a flow rule derived from g^t.

3.3 Numerical Simulation on Single Cutter Indentation

3.3.1 Overview

Cook et al. (1984) divided the loaded process of rock indentation into four stages based on the experiment, namely, building up of a stress field, formation of a crushed zone, formation of subsurface and surface chipping, and formation of crater as shown in Figures 3.2. At the beginning, the increasing load causes the closure of the pre-existing flaws in the rock. Then, with the increase of the load, the rock deforms in a linear elastic manner. Little damage to the rock occurs until the punch load exceeds about 45% of the peak punch load. At this point a conical, Hertzian crack is initiated at the punch corners. With the continuous increase of load, a crushed zone is formed immediately under the indenter. At this stage, movement and dilatation of rock fragments are restrained by the surrounding intact rock. In order to break the rock, the force must be further increased. This causes intense comminution of the rock fragments. The comminuted rock fragments are then partially recompacted under the combined action of the lateral confinement and the normal stress provided by the indenter. The moving and dilating tendency of rock fragments pushes the surrounding rock outwards and upwards, and therefore results in radial, median and side cracks. During the process of rock fracturing, the indenter gradually penetrates into the rock. When the side cracks reach the rock surface, the surrounding rock which offered the lateral confinement at the earlier stage, together with a part of the rock underneath the indenter, will quickly move away and form rock chips. Meanwhile, the strain energy stored in the rock will convert into the kinetic energy of the rock chips. The movement of the indenter has less resistance in this case. The force acting on the indenter is thus reduced to a lower value and the indenter penetrates the rock to a great depth within a short time. Lawn and Swain (1975) gave a different explanation on the rock indentation process, comparing with the above mentioned. After the formation of the crushed zone, cone cracks, penny-shaped median crack, and lateral cracks are formed. The lateral cracks could not extend to the surface because the surface is still under compression from the indenting load. These cracks would be free to propagate to the surface only during unloading. During the rock indentation process, the indenter shape, size and the confinement force affect the formation of the crushed zone and the internal cracks initiation and propagation (Wagner and Schumann, 1971; Cook et al., 1984; Mishnaevsky, 1995; Liu et al., 2002).

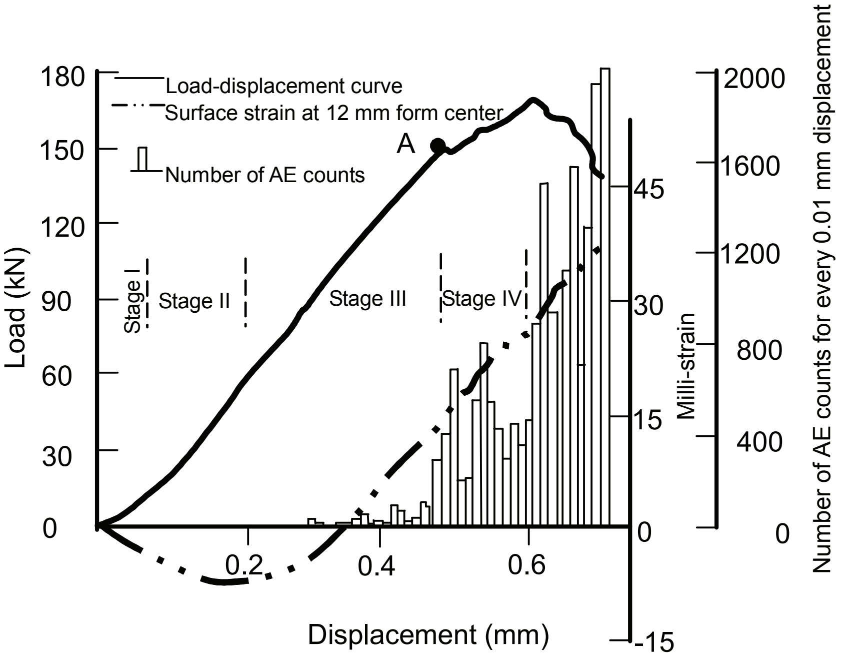

Figure 3.2 A typical loading cycle with corresponding acoustic emissions records using a 10 mm diameter flat-bottomed punch (after Cook et al., 1984)

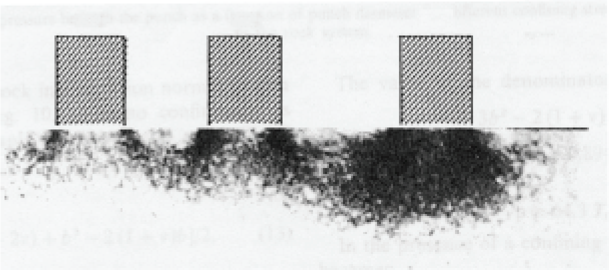

Figure 3.3 Crack and microcrack development in the rock specimen with increasing load (after Cook et al., 1984)

The crack initiation and propagation induced by a circular flat-bottom indenter in different static load are shown in Figure 3.3 (Cook et al., 1984). The crack pattern due to static loading with a wedge indenter is shown in Figure 3.4 (Pang and Goldsmith, 1990). Based on the rock indentation process and crack initiation and propagation, three different zones can be distinguished, as shown in Figure 3.5 (Lindquist and Lai, 1983; Cook et al., 1984, Pang and Goldsmith, 1990; Kou et al., 1998; Chiaia, 2001). Immediately below the indenter, a hydrostatic core develops, due to a high triaxial compressive stress induced beneath the indenter. Thus, this zone remains relatively intact. It may collapse only by crushing, resembling the effects of strong impacts or explosions. Outside the crushed zone, a surrounding zone of large strains develops due to the pushing action of the core. In this zone, the micro-cracks are pervasive. Tensile cracks are initiated from pre-existing flaws in the material. There are basically three types of cracks: median cracks, radial cracks and side cracks. Outside the crack zone, the material behaves elastically.

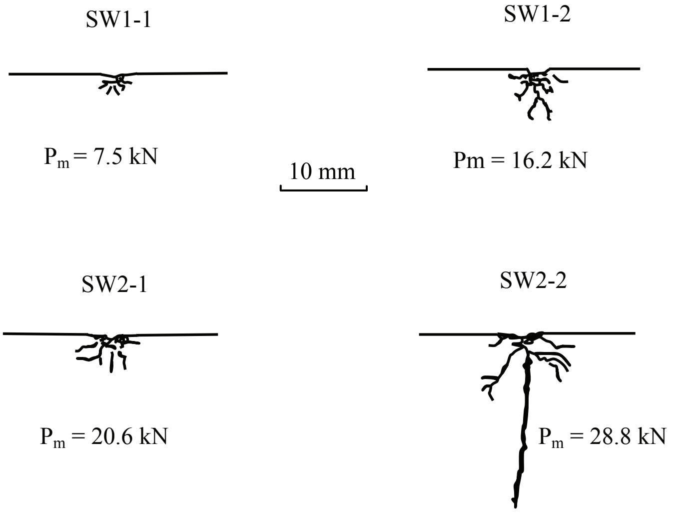

Figure 3.4 Crack pattern due to static loading with a wedge bit (SW1: 30º wedge; SW2: 60º wedge; P_m: peak force) (after Pang and Goldsmith, 1990)

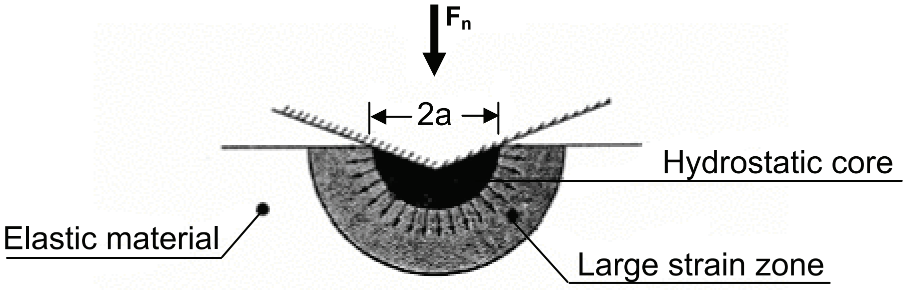

Figure 3.5 Indentation of brittle materials: formation of the hydrostatic core and the large-strain zone (after Chiaia, 2001)

Liu et al. (2002) pointed out that inside the crushed zone the rock fails in the ductile cataclastic mode. About 70% to 85% of energy is consumed by the formation of the crushed zone (Mishnaevsky, 1995). Outside the crushed zone, the rock fails in a tensile mode, resulting in internal cracks and rock chips. The energy needed for chipping is about 5-10% of overall energy needed for rock fragmentation (Mishnaevsky, 1995).

Some investigators (Nishimatsu, 1972, Roxborough, 1978, Pang et al., 1989) used a limit equilibrium approach to analyze the formation of chipping, with the assumption of a Mohr-Coulomb failure criterion. It was assumed that the chip formation occurred when the shear stress along an assumed failure plane exceeded the shear strength of the rock.

The above mentioned rock breakage process is a one cycle indentation process by an indenter. In the multi-pass cutting process, the penetration process by TBM cutters are composed of successive indentation cycles. Each indentation cycle consists of a crushing and chipping phase (Reichmuth, 1963; Lundberg, 1974; Pang et al., 1989). Crushing occurs when the indentation load exceeds the compressive strength of the rock. Chipping consists of the separation of rock segments and their ejection beneath the indenter. It involves a sudden release of strain energy when a critical stress state is reached.

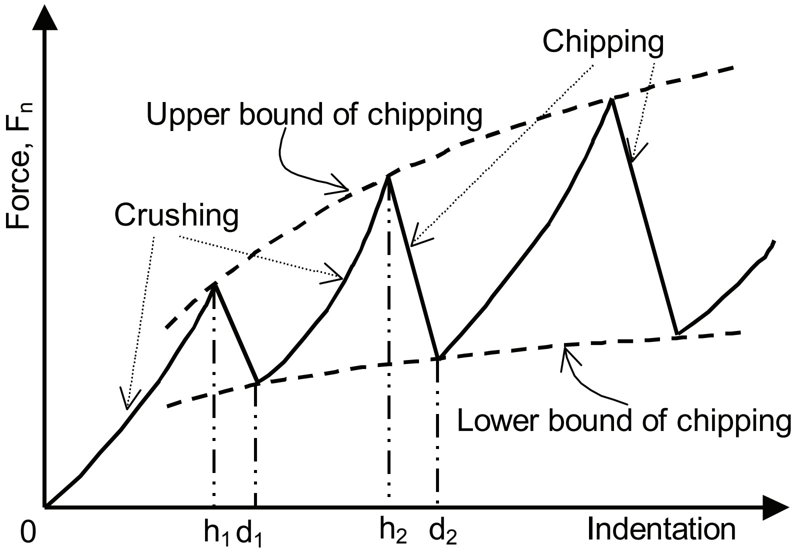

Figure 3.6 Force indentation curve for successive indentation cycle (after Pang et al., 1989)

The force-indentation process is shown in Figure 3.6. At the crushing stage, the resultant force normal to the free surface increases with indentation. At the chipping stage, the resultant force decreases with increasing indentation. The upper bound of chipping represents the end of the crushing process. The lower bound of chipping terminates chipping formation and initiates the next cycle until the final indentation is reached. In the process of chipping formation, the applied force is generally not reduced to zero, because not all the rock fragments are expelled from the region around the indenter.

In this section, only the rock indentation process by a single TBM cutter is simulated. The rock breakage process is described in details and the rock failure mechanism is analyzed.

3.3.2 Model Configuration

The configuration of the computational model is schematically shown in Figure 3.7. The dimension of the model was 0.6m×0.6 m. The cutter was modelled by a normal force applied at mid height of the left boundary through contact thickness of 15 mm. The upper, lower and right boundaries were regarded as fixed displacement boundaries. The rock block was discretized with fine finite difference meshes,

Table 3.1 Properties of intact granite

property	Value
Bulk density (kg/m3)	2600
Bulk modulus (GPa)	55
Shear modulus (GPa)	32
Cohesion (MPa)	66
Friction angle (°)	31
Tensile strength (MPa)	11.3
Dilation angle (°)	10

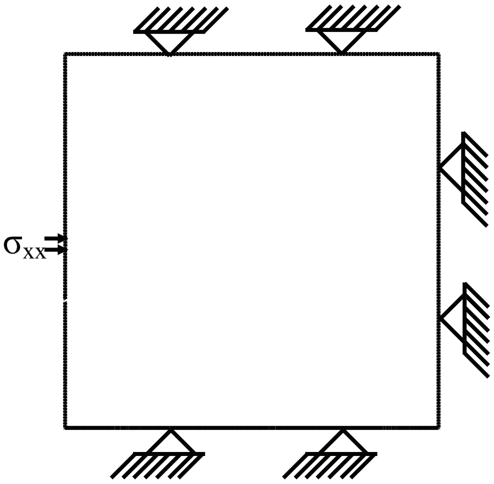

Figure 3.7 Numerical simulation model on a single cutter indentation

namely zones in UDEC. The zone size in the blocks was set to 5 mm and the damping value 0.1. The rock material modelled is typical granite found in Singapore (Wallace et al., 1995; Zhao, 1996). The intact granite is assumed to be the Mohr-Coulomb material and its properties are listed in Table 3.1.

3.3.3 Results Analysis

The crack pattern is shown in Figure 3.8. In the figure, the circle (black color) denotes tensile failure and the cross (red color) denotes compressive failure. In order to highlight the indentation process, the failure zones are zoomed in at different iteration steps, as shown in Figure 3.9. The crack initiation and propagation process can be divided into three stages, namely the formation of a crushed zone, formation of minor crack zone and propagation of major cracks. When a cutter first applies loads to the rock, a fan-shaped rock failure zone is formed as shown in Figure 3.9a. The frontier of the failure zone is governed by tensile failure. Immediately under the two corners of the cutter, a zone of Hertzian crack is initiated as shown in Figure 3.9a and b. An interesting phenomenon can be observed that immediately beneath the cutter the rock remains relatively intact because of the high confining pressure in this zone. It is the so-called hydrostatic compression state (Cook et al., 1984; Chiaia, 2001; Liu et al., 2002). As the penetration increases, the crushed zone that is directly located under the cutter is formed, as shown in Figure 3.9b. This zone is mainly composed of compression failure elements including numerous microcracks. The rock is comminuted to produce powder or extremely small particles (Pang and Goldsmith, 1990). With the increase of penetration, the minor crack zone is formed beneath the crushed zone, as shown in Figure 3.9c. The minor cracks including median and radial cracks are mainly initiated from the tensile failure zone and propagate along the tensile failure elements. In this stage, it is interesting to note that the crushed zone is symmetric as shown in Figures 3.9b and c. As the penetration continuously increases, the crushed zone and minor crack zone remain the same. The main cracks extend along certain directions, for example the median direction and side direction, as shown in Figures 3.9d, e and f. The crack propagation is induced by the element's tensile failure at the tip of the crack. The simulated indentation crack pattern shows good agreement with the experiment results conducted by Pang and Goldsmith (1990) with a wedge indenter (Figure 3.4).

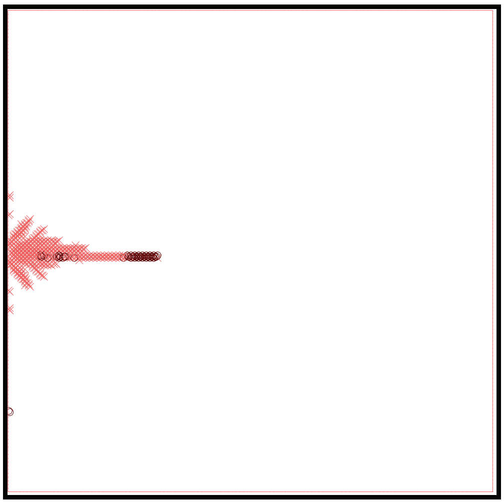

Figure 3.8 Crack pattern of a single cutter indentation (black circle denotes tensile failure, red cross denotes compressive failure)

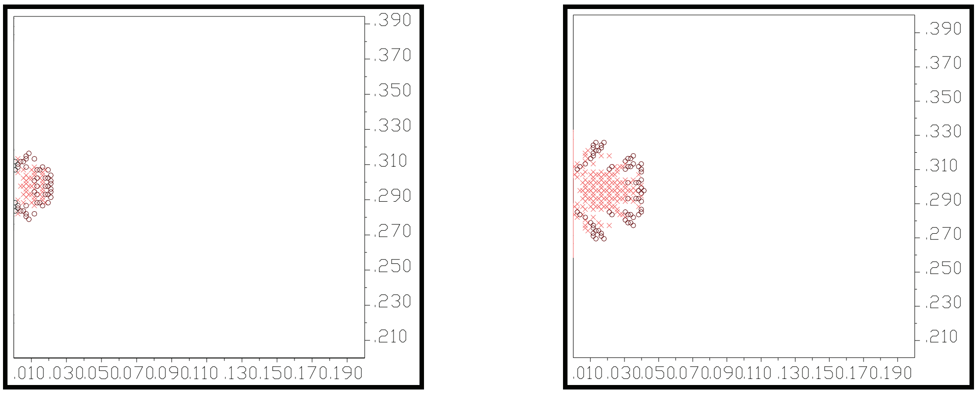

(a) Step:30 (b) Step:60

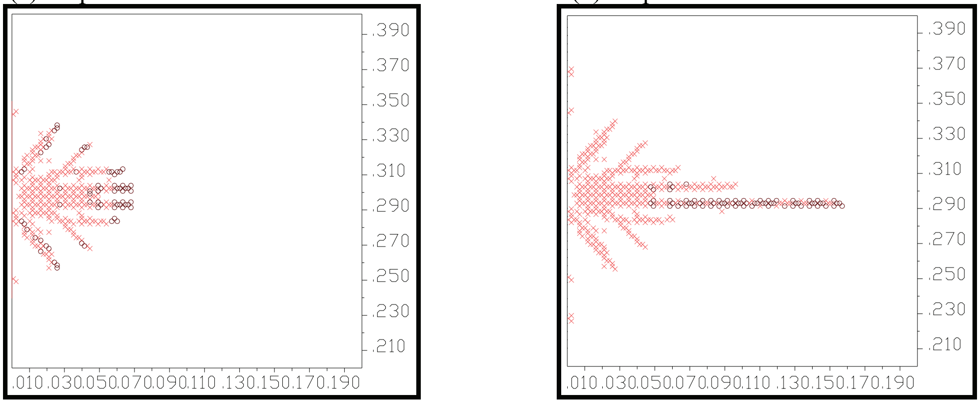

(c) Step:100 (d) Step:300

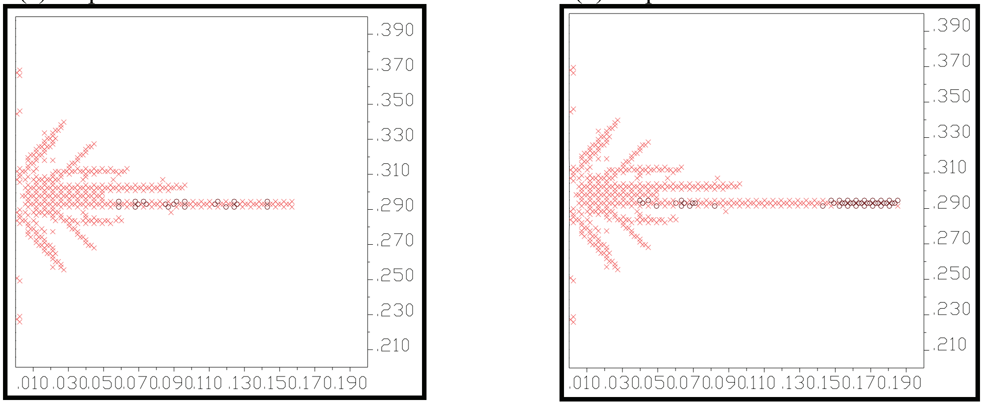

(e) Step:500 (f) Step:1000

Figure 3.9 A single cutter indentation process (black circle denotes tensile failure, red cross denotes compressive failure)

It is important for us to pay attention to the stress distribution that is mainly responsible for the crack initiation and propagation. When a normal point load acts on an isotropic, linear elastic half-space, the stress field was first given by Boussinesq in 1885, commonly known as the Boussinesq elastic field. When a smooth spherical indenter acts on an isotropic, linear elastic half-space, the stress field is known as the ideal Hertzian elastic field. Liu et al. (2002) simulated the quasi-photoelastic stress fringe pattern induced by a truncated indenter when the rock was considered as a homogeneous material. The stress distribution of a single cutter indentation is shown in Figure 3.10 when the rock is considered as a homogeneous material. The stress field is in agreement with the result obtained by Liu et al. (2002). The stress distribution is almost symmetrical. Immediately beneath the cutter and on either side of the cutter, an extremely high stress field is induced by the cutter loading. The stress decreases rapidly with the increasing distance from the cutter.

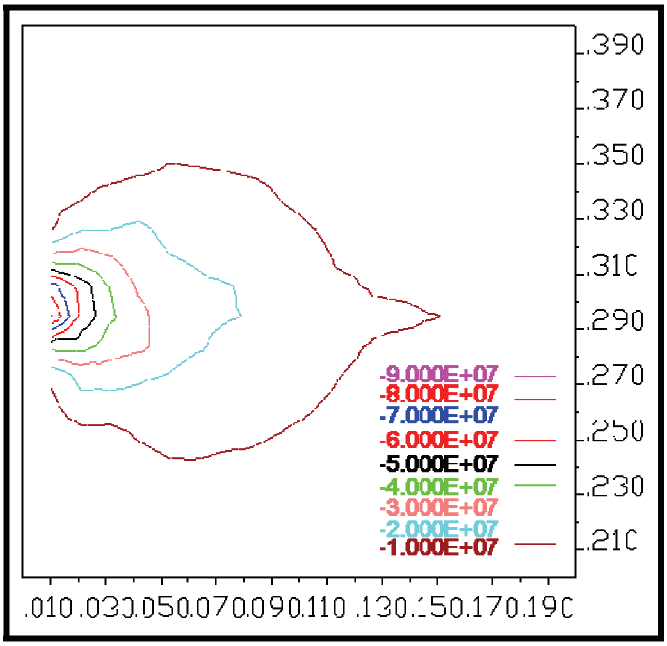

Figure 3.10 Major principal stress contour

3.4 Numerical Simulation on Chip Formation between Two Cuts

3.4.1 Overview

The previous section shows the indentation process of a single indenter/cutter acting on a point. For the tunnel excavation, when TBM cutters roll across the tunnel face, they continuously expand the crushed zone beneath themselves, and cracks are initiated and propagated. One or more cracks under the action of the rolling cutter may reach the free surface or propagate to meet the cracks of the neighboring cuts. In these two cases, chipping occurs. The first case is similar to the chip formation of a single indentation process. The latter is the interaction between two adjacent cuts. It is directly relevant to the design of TBM cutterhead and the efficiency of TBM excavation.

The interaction process is affected by the factors such as the acting loads, line spacing of two adjacent cutters, and rock properties that impact the angle and extension of cracks under the crushed zone. When the spacing between two cutters is too large, cracks develop toward cutting face, reach free surface and is followed by formation of small triangular chips. The material between two cutters is left intact. A ridge between the two cutters is formed, as shown in Figure 3.11a. When the spacing is too small or the load is too high, longer but ineffective cracks can develop inward and meet in a steep angle. A trough between the two cutters is formed, as shown in Figure 3.11b. For an optimum spacing, cracks ideally propagate towards the neighboring cuts through a relative straight line which would be the shortest distance for crack propagation and is approximately equal to half the spacing as shown in Figure 3.11c.

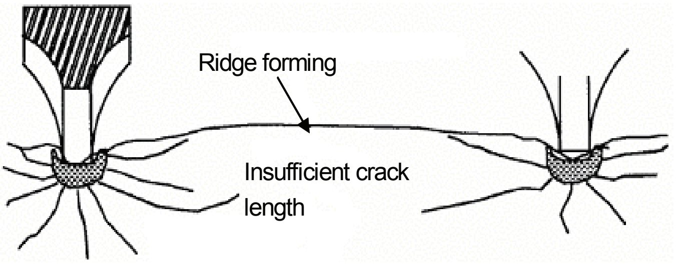

a. Ridge formation due to lack of pressure and length of cracks

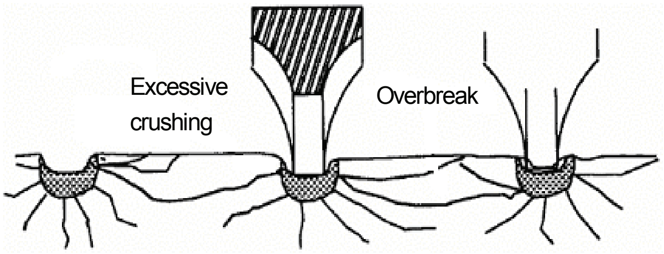

b. Over break due to excessive loading and longer cracks

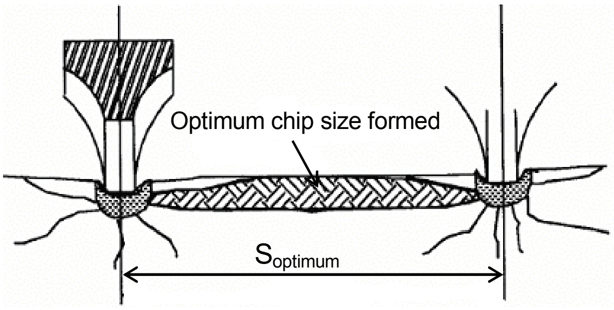

c. Normal cutting with optimum crack length and direction

Figure 3.11 Chip formation for different cutter spacing (after Rostami and Ozdemir, 1993)

In practice, two possible mechanisms are applicable to break the rock by rolling cutters. The first is the single pass cutting process, in which the spacing and penetration are such that interactive breakout occurs between adjacent cuts at each level in the tunnel face. The second is the multiple pass cutting process, in which a number of passes in the same groove is required before breakout to an adjacent groove occurs (Snowdon et al., 1983b). There are two reasons. One is that the cutter load is not enough to crush the rock and initiate and propagate the cracks. The other is that due to the rotation of the rolling cutter, the available time to create a stress field sufficient for crack initiation and crack propagation is limited. This process is highly influenced by energy input during the period when the cutter is in contact with rock. If it is not possible to achieve a level of energy transfer to make single pass chipping in the period available, only initial cracks are formed. The generated cracks cannot reach the critical length during the loading period. Therefore crack propagation does not become independent from applied stress. The state of fracture remains "undercritical" (Gehring, 1994). Single pass cutting mode almost occurs in all TBM excavated tunnels except those with very high rock strength.

The main advantages of single pass chipping are as follows (Lindquist and Ranman, 1980): (a) The surface of the cutting groove is more even. (b) Chip formation takes place more or less continuously. Therefore, the reactive load on the cutterhead can be balanced. (c) The required rolling distance of a disc cutter to produce a certain volume of muck is kept relatively short. On the contrary, multiple-pass chipping means higher cutterhead vibration, higher load variation on the cutters and higher cutter wear per excavated unit volume.

3.4.2 Model Configuration

The configuration of the computational model is schematically shown in Figure 3.12. The dimension of the model was 0.6m×0.6 m. The net distance between two cutters was set to 70 mm. The two cutters were modelled by two normal forces applied at mid height of the left boundary through contact thickness of 15 mm. The upper, lower and right boundaries were regarded as fixed displacement boundaries. The rock block was discretized with fine finite difference meshes, namely zones in UDEC. The zone size in the blocks was set to 5 mm and the damping value 0.1. The rock material modeled is typical granite found in Singapore (Wallace et al., 1995; Zhao, 1996). The intact granite is assumed to be the Mohr-Coulomb material and its properties are listed in Table 3.1.

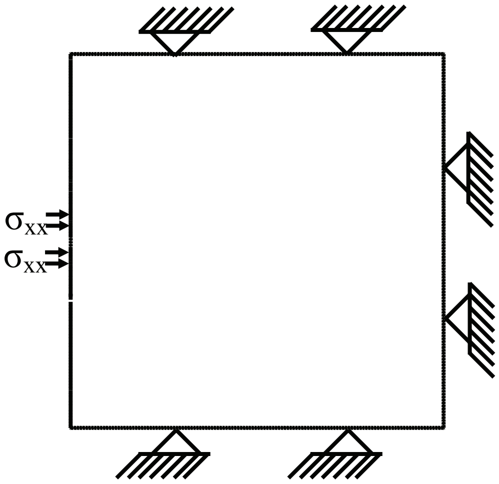

Figure 3.12 Numerical simulation model of chip formation between two cuts

3.4.3 Results Analysis

Figure 3.13 shows the crack pattern and chip formation between two cutters induced by the two cutters acting on the rock. Figure 3.14 shows the crack initiation and propagation process in the rock. At the beginning, each cutter acts on the rock independently. The stress field built up by each cutter is also independent. As shown in Figure 3.14a, two fan-shaped failure zones are formed beneath each cutter like that of a single cutter. The frontier of the failure zone is also governed by the tensile failure. Immediately beneath each cutter, an obvious intact rock zone exists because of the high confining pressure around this zone. The phenomenon is also observed in the single cutter indentation process. With the increase of the penetration, the Hertzian cracks under the two cutters are initiated as shown in Figure 3.14b. The crushed zones are formed immediately beneath the two cutters. These zones are mainly composed of compression failure elements that form numerous internal microcracks inside this zone. In the frontier of this zone, many microcracks are initiated and propagated outwards due to the rock tensile failure. As the penetration increases continuously, the crushed zone remains the same. Outside the crushed zone, the minor cracks including median and radial cracks continuously propagate. The most important is that the Hertzian cracks between two cutters change their extension direction and propagate toward each other due to the interaction between the two cutters. The chip is not formed until the two cracks coalesce in the middle of the two cutters, as shown in Figure 3.14c. The crack mainly propagates along the tensile failure elements. As the penetration increases, the minor cracks zone remains the same. The main cracks including median and side cracks develop continuously downwards and sideward due to the element tensile failure, as shown in Figures 3.14d and e. With the built-up of the stress field, the crack pattern is shown in Figures 3.14f, g and h.

Figure 3.15 shows the major principal stress contour. As can be seen, the stress field is symmetrical and the stress is extremely high immediately beneath the cutters and decrease rapidly with increasing distance from each cutter edge. A high stress zone is formed between the two cutters. Under the action of the high stress zone, the chip between the cutters is formed due to the tensile failure. When the depth beneath the cutters is more than 2.5 to 3.0 times of the cutter spacing, the major principal contour resembles that of the single cutter indentation.

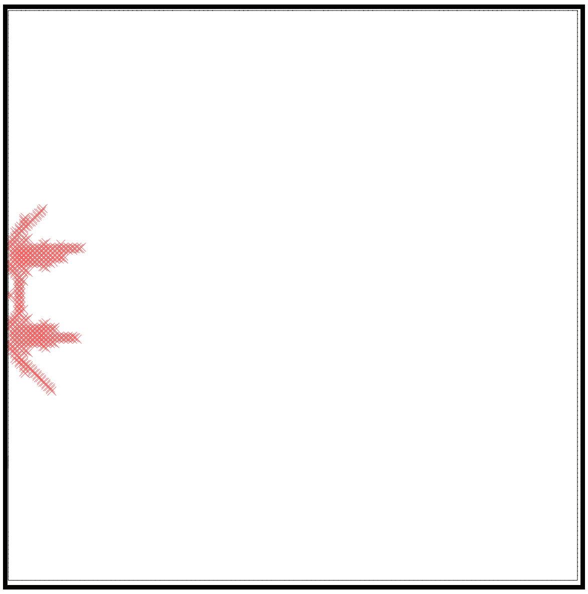

Figure 3.13 Crack pattern of two cutters indentation

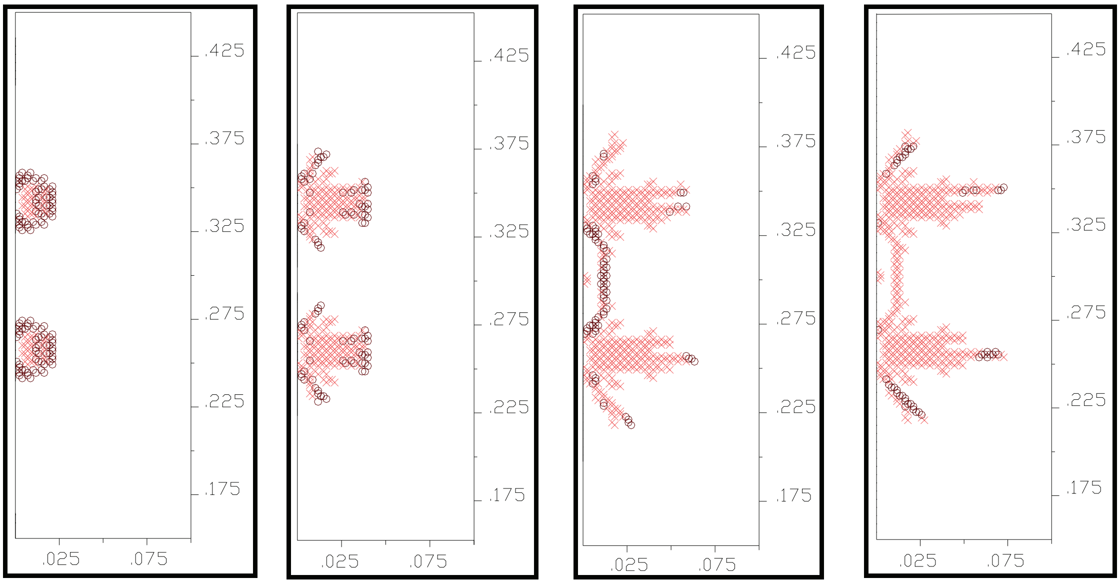

(a) Step:30 (b) Step:60 (c) Step:100 (d) Step:200

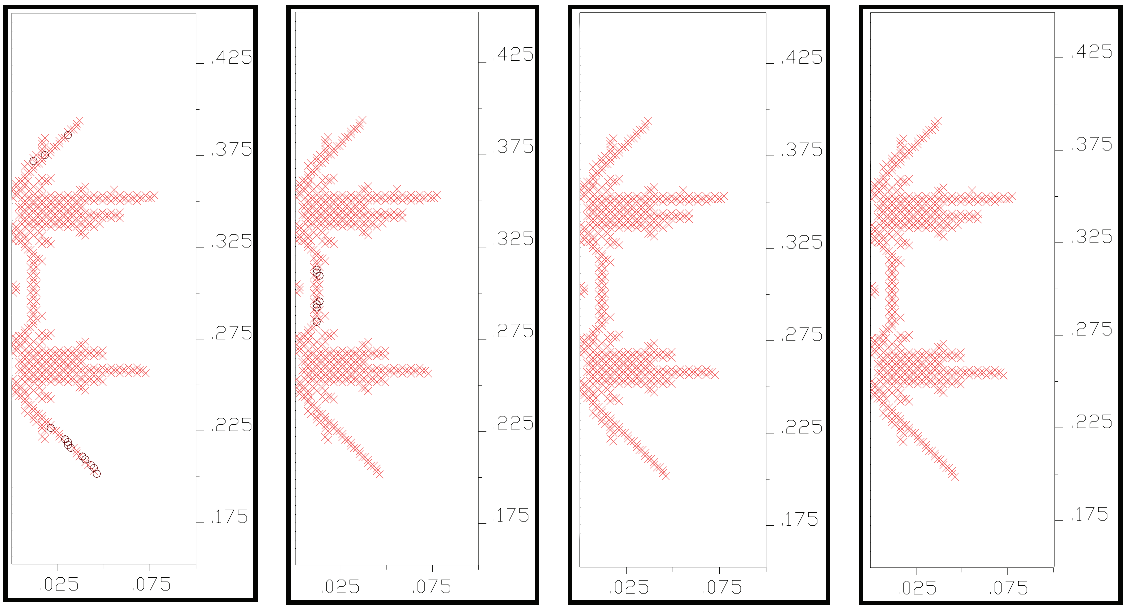

(e) Step:300 (f) Step:400 (g) Step:500 (h) Step:1000

Figure 3.14 Two cutters interaction process (black circle denotes tensile failure, red cross denotes compressive failure)

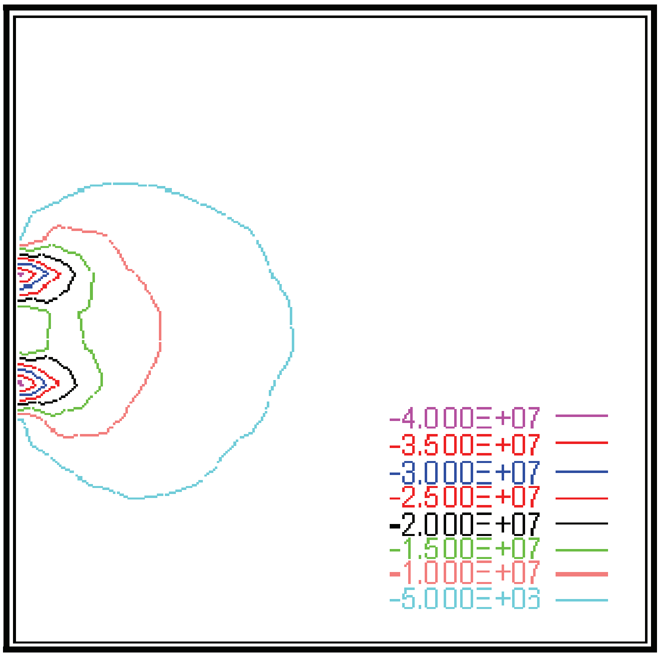

Figure 3.15 Major principal stress contour with two cutters indentation (MPa)

3.5 Optimal Spacing of Cutters

In light of the above mentioned indentation process by two cutters, the stress field interaction of two cutters is affected by the cutter spacing. Furthermore, the chipping size is also affected by the cutter spacing. Hence, the cutter spacing influences the machine's efficiency and production. Roxborough (1978) deduced an equation for the cutter spacing, in terms of the assumption of rock shear failure between two adjacent cuts. The ratio of cutter spacing to penetration is equal to the ratio of the uniaxial compressive strength to the shear strength. By utilizing the linear rock cutting rig, Snowdon et al. (1981, 1982) performed a series of liner cutting tests. The effects of the penetration and the ratio of cutter spacing to penetration on specific energy were analyzed. The correlation between cutter spacing and the three forces acting on the cutters was also studied. The optimum value of the ratio of cutter spacing to penetration for granite, dolerite and sandstone was found to be about 10 and that for the limestone was approximately 15. The optimum penetration was about 10 mm for granite, dolerite and sandstone.

In this study, the influence of the different cutter spacing on the penetration is simulated. The configuration of the computational model was the same with the previous section, as shown in Figure 3.12. The cutter spacing varied from 60 mm to 110 mm respectively. The properties of the modeled granite are shown in Table 3.1. The simulated rock chip formations at different cutter spacings are shown in Figure 3.16. As can be seen, the shape and thickness of the rock chips vary with the cutter spacing. The stress acting on the cutters was recorded and the chip thickness and chipping area were measured, as shown in Table 3.2. In this table, it is worth noting that the chip shape refers to the ratio of the chip width to chip thickness in the fifth column. The smaller the ratio, the closer the shape is to cubic and the efficiency of the TBM is higher. On the contrary, the bigger the ratio, the more frequently the chipping occurs in the tunneling process and the vibration of the cutterhead is low. The ratio of the chipping area to the chipping stress denotes the yield of rock chips per unit cutter force. It indirectly stands for the TBM penetration. The last column shows the ratio of P_{cs} to P_{60}, where P_{cs} denotes the penetration rate with the cutter spacing and P_{60} represents the penetration rate with the cutter spacing of 60 mm.

Table 3.2 Effect of the cutter spacing on the TBM penetration

Cutter spacing (mm)	Stress (MPa)	Chipping thickness (mm)	Chipping area (cm^2)	Chip width/ chip thickness	The ratio of chipping area to chipping stress (cm^2/MPa)	P_{cs}/P_{60}
60	160.00	13.08	5.73	4.59	0.0358	1.00
70	161.00	14.00	7.70	5.00	0.0478	1.34
80	165.00	17.60	10.14	4.55	0.0614	1.72
90	194.00	23.00	13.80	3.91	0.0711	1.99
100	210.00	24.00	18.00	4.17	0.0857	2.39
110	245.00	20.00	17.00	5.50	0.0694	1.94

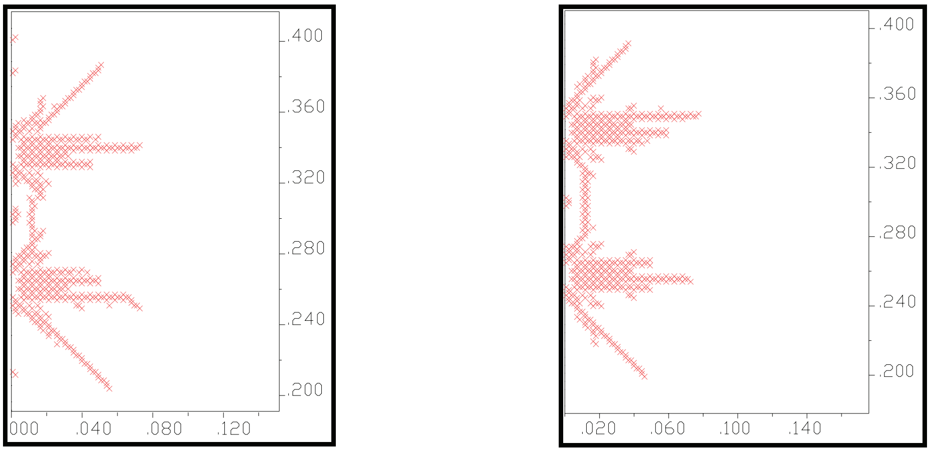

Cutter spacing: 60 mm

Cutter spacing: 70mm

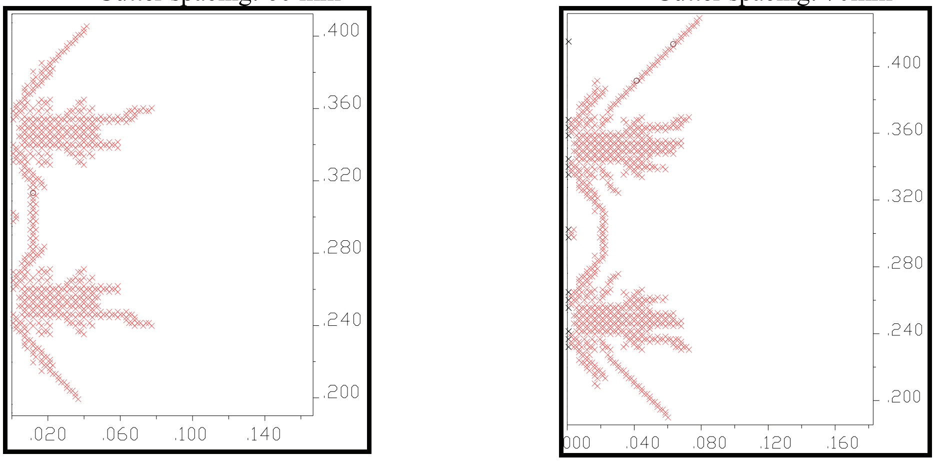

Cutter spacing: 80 mm

Cutter spacing: 90 mm

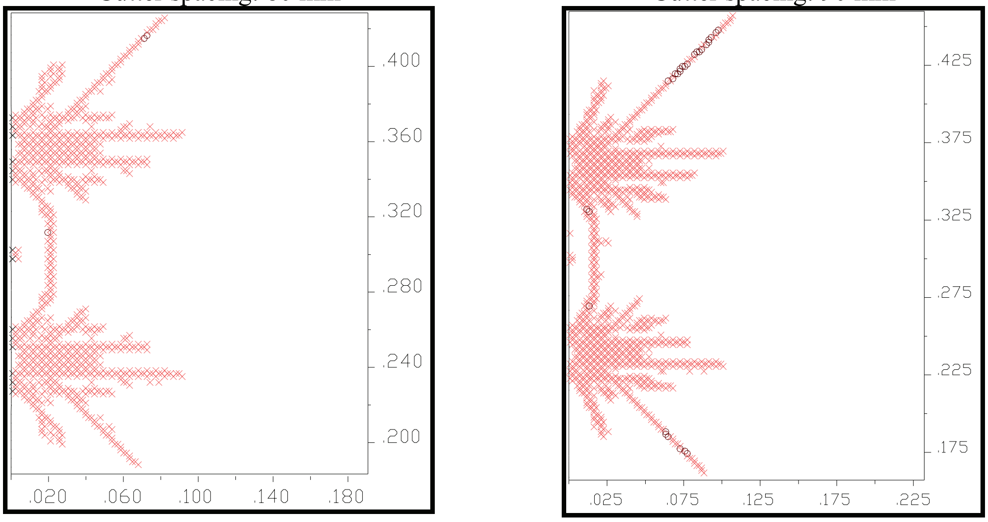

Cutter spacing: 100 mm

Cutter spacing: 110 mm

Figure 3.16 Chipping formation in different cutter spacings (black circle denotes tensile failure, red cross denotes compressive failure)

The relationships between the cutter spacing and the chip thickness, the chipping area are shown in Figure 3.17. When the cutter spacing is less than 100 mm, any increase in cutter spacing will result in the increase of the chip thickness and the chipping area. The chip thickness and the chipping area however decrease when the cutter spacing is more than 100 mm. The correlations between the ratio of chip width to chip thickness, P_{cs}/P_{60}, cutter stress and the cutter spacing are shown in Figure 3.18. As can be seen, the critical cutter stress required to chip the rock increases with increasing cutter spacing. The variation of the ratio of chip width to chip thickness is undulated with the increase of the cutter spacing. When the cutter spacing is between 90 mm and 100 mm, the ratio reaches the minimum value. The ratio of P_{cs} to P_{60} attains the largest value 2.39 when the cutter spacing is equal to 100 mm. The above results show that in this case, the optimal cutter spacing is 100 mm if the cutter load can attain the required critical value. It is interesting to note that the penetration is more than two times of that for the cutter spacing of 60 mm, when the cutter spacing is close to the optimal value.

Snowdon et al. (1981, 1982) used linear cutting machine (LCM) test to study the optimum cutter spacing in four selected British rocks. The tested granite is fresh coarse grained granite with uniaxial compressive strength of 174.2 MPa and Brazilian tensile strength of 9.96 MPa. The optimum ratio of cutter spacing to penetration is about 10 and the optimum penetration is about 10 mm for granite in the test. Thus, the optimum cutter spacing is also close to 100 mm. It is in good agreement with the experimental result.

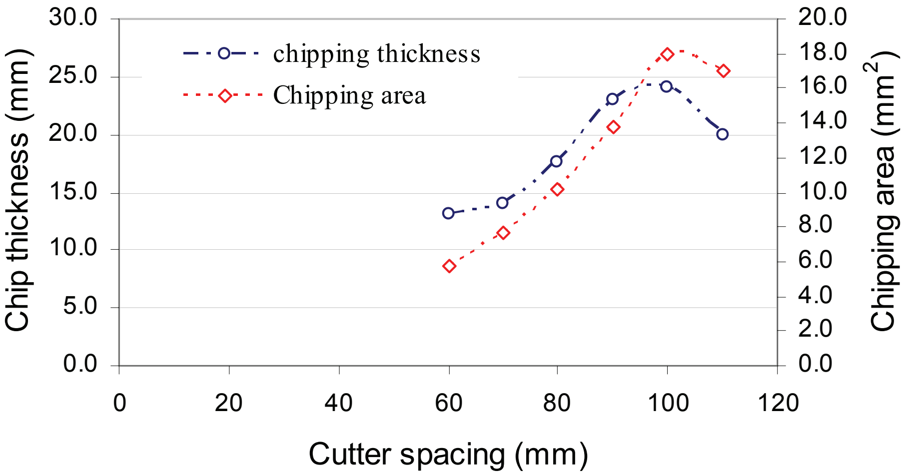

Figure 3.17 Variations of chip thickness and chipping area with the different cutter spacings

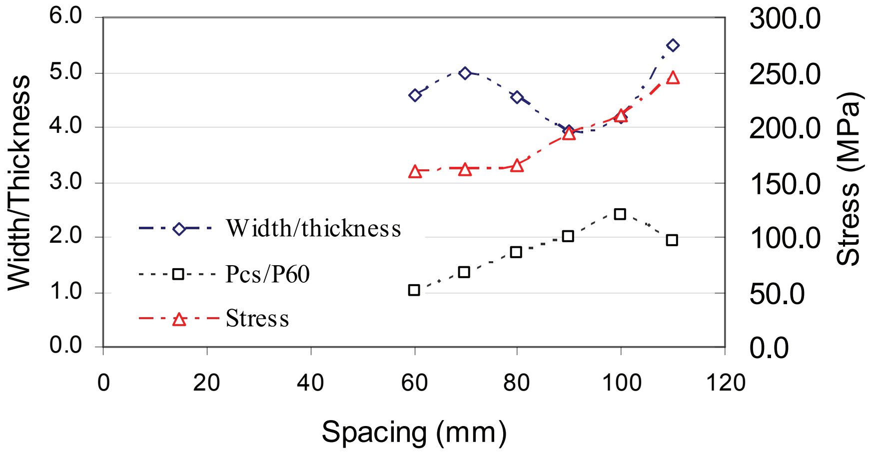

Figure 3.18 Variations of the ratio of chip width to chip thickness, P_{cs}/P_{60} and stress with the different cutter spacings

3.6 Conclusions

Rock indentation process by a single TBM cutter can be divided into three stages: the formation of a crushed zone, formation of minor crack zone and the propagation of major cracks. The crack initiation and propagation mainly grows along the frontier of the tensile failure zones. The stress distribution shows that immediately beneath the cutter and on either side of the cutter, an extremely high stress field is induced by the cutter load and the stress rapidly decreases with increasing distance from the cutter. The simulated cracking pattern shows good agreement with the experimental results.

Rock chipping process by two neighboring cutters was simulated by UDEC in this study. At the beginning, each cutter indents the rock independently and similarly to a single cutter indentation process. The stress field is also independent. After the formation of the crushed zone, cracks are initiated from this zone, and then the side cracks propagate along a certain direction due to the interaction of two cutters. With increasing penetration, the side cracks between two cutters propagate to each other and coalesce, and form the rock chip. The chip formation is greatly dependent on the cutter spacing and the critical cutter load.

The influence of different cutter spacing varying from 60 to 110 mm on TBM fragmentation efficiency in typical Singapore granite was simulated in this chapter. The critical cutter stress required for chipping increases with increasing cutter spacing. As long as the critical cutter load can be reached, the penetration rate will obtain the maximum value at a cutter spacing of 100 mm. This penetration rate is more than two times of that for the cutter spacing of 60 mm. As the cutter spacing is less than 100 mm, which is the optimum spacing, the increase in cutter spacing results in the increase in chip thickness and chipping area. The chip thickness and chipping area however decrease with the increase in cutter spacing if the spacing is greater than 100 mm. The result shows good agreement with the experimental results by Snowdon et al. (1981, 1982).

Chapter 4 Rock Mass Parameters Influencing TBM Penetration Process

4.1 Introduction

The rock fragmentation process under the action of TBM cutters was analyzed in the previous chapter. Because rock masses are composed of rock material and joints, the existing joint conditions affect greatly the initiation and propagation of cracks as well as rock mass breakage process. In practice, it has been well recognized that joints or fractures have an important effect on the TBM performance. From the viewpoint of either energy or fracture propagation, it is easy to understand that discontinuities can facilitate rock breakage, because rock mass with many discontinuities has more surface energy than that of the same volume of rock material and cracks may develop along the existing discontinuities. Up to now, it is still difficult to theoretically quantify the influence of discontinuities on TBM performance due to two reasons. Firstly, the system of joints and fractures is uncertain. Secondly, the breakage mechanisms of rock with discontinuities in different directions and sizes may change under the action of cutterhead of TBM with different design parameters.

This chapter, following the previous chapter, continues to analyze the influences of rock mass properties on the rock mass breakage mechanisms, and the TBM performance by UDEC modelling. The rock mass parameters mainly affecting the TBM penetration include rock uniaxial compressive strength, rock material brittleness index, joint spacing and orientation, as discussed in Chapter 2. Since the effect of rock uniaxial compressive strength on TBM penetration has been extensively studied, this chapter only reviews and summarizes the results. The rock material brittleness is discussed in this chapter. The influence of rock material brittleness on rock fragmentation process and TBM penetration is simulated by DEM modelling. The impacts of discontinuities spacing and orientation on rock mass breakage mechanisms are demonstrated by a series of two dimensional UDEC simulations. Furthermore, the effects of discontinuities spacing and orientation on TBM penetration are analyzed. The simulation results are compared with the in situ observational results.

4.2 Rock Material Strength

The main factor which affects the crushed zone and indentation depth during TBM cutting process is the rock behavior under compression. Exerted stress must exceed the rock strength in order to indent the rock. Thus, the rock compressive strength is directly related to the performance of TBM. This fact has also been proven by some models for predicting penetration rate (Graham, 1976; Hughes, 1986; Rostami and Ozdemir, 1993; O’Rourke et al., 1994).

Some previous studies have shown that the excavation rate decreases with the increase of rock uniaxial compressive strength or rock hardness (Farmer et al., 1979; Morimoto and Hori, 1986; Fukui & Okubo, 1999). Because TBM performance is also affected by other factors and TBM specifications, the simple function between penetration rate and rock strength or hardness is not likely to be convincing.

4.3 Rock Material Brittleness

Hucka and Das (1974) stated that the concept of brittleness was not yet made precise. But with higher brittleness, the following facts are observed, which include low values of elongation, fracture failure, formation of fines, high ratio of compressive to tensile strength, high resilience, higher angle of internal friction and formation of cracks during indentation. George (1995) defined rock brittleness as the ability of a rock material to deform continuously and perpetually without apparent permanent deformations along with the application of stress surpassing the necessary stresses for microcracking of the material. A general law with regard to brittleness is that a brittle rock breaks at very little deformation. Because the definition of brittleness only describes the behavior of rock deformation and failure subjected to the loading condition, the measurement of brittleness has not yet been standardized. The brittleness value can be calculated by strain, strain energy, rock internal friction, tensile and compressive strength, or special tests.

A) Measurement of brittleness by the strain

$B_1 = \varepsilon_{1i} \cdot 100\%$ (George, 1995). It is an absolute index based on the absolute irreversible longitudinal (parallel to σ_1) strain ε_{1i} until failure. From the view point of rock failure, rocks are classified as follows: $\varepsilon_{1i} < 3\%$ brittle; $3 < \varepsilon_{1i} < 5\%$ brittle-ductile; $\varepsilon_{1i} > 5\%$ ductile.

$B_2 = \frac{reversible \quad strain}{total \quad strain} = \frac{DE}{OE}$, as shown in Figure 4.1(Hucka and Das, 1974).

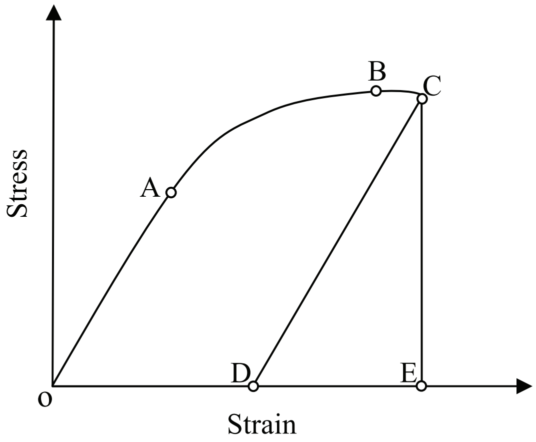

Figure 4.1 Measuerement of brittleness from stress-strain diagram (after Hucka and Das, 1974)

B) Measurement of brittleness by the percentage of reversible energy

$B_3 = \frac{reversible \quad energy}{total \quad energy} = \frac{Area \quad DCE}{Area \quad OABCE}$, as shown in Figure 4.1 (Hucka and Das, 1974; Vihtuk, 1998).

C) Measurement of brittleness by Mohr's envelope

$B_4 = \sin\varphi = \frac{\partial\tau/\partial\sigma_n}{(1+(\partial\tau/\partial\sigma_n)^2)^{1/2}}$ (Hucka and Das, 1974), determined from Mohr's envelope at $\sigma_n = 0$. φ is the angle of rock internal friction.

D) Measurement of brittleness by tensile and compressive strength

$B_5 = {\sigma_c}/{\sigma_t}$ (Hucka and Das, 1974; Kahraman, 2002; Altindag, 2002).

$B_6 = \frac{\sigma_c - \sigma_t}{\sigma_c + \sigma_t}$ (Hucka and Das, 1974; Kahraman, 2002; Kahraman and Altindag, 2004).

$B_7 = {\sigma_c \cdot \sigma_t}/{2}$ (Altinday, 2002; Kahraman and Altindag, 2004).

E) Measurement of brittleness by special tests

$B_8 = q\sigma_c$ (Protodyakonov, 1963), q is the percentage of fines formed in Protodyakonov impact test.

$B_9 = S_{20}$ (Blindheim and Bruland, 1998), S_{20} is the percentage of fines (<11.2 mm) formed in an impact test included in the Norwegian set of tests for TBM performance prediction.

Because brittleness based on tensile and compressive strength and brittleness based on the specialization tests are simply defined and easily obtained, they are often used in engineering analysis (Protodyakonov, 1963; Blindheim and Bruland, 1998; Kahraman 2002; Altindag, 2002). In terms of the correlation analysis, Kahraman (2002) concluded that the correlations among B_5, B_6 and TBM penetration rate, the penetration rate of rotary drills, B_8 and the penetration rate of percussive drills exist. On the contrary, there are no clear correlations among B_5, B_6 and the penetration rate of percussive drills, B_8 and the penetration rate of rotary drills. The correlation between B_7 and the penetration rate of rotary drills is good (Altindag, 2002). These are mainly due to the different rock breakage process in TBM penetration, rotary drilling and percussive drilling. Percussion is the dominant factor in percussive drilling and the process is similar to the impact test process. Thus, B_8 and B_9 are more suitable to correlate the penetration rate of percussive drills. The rock breakage process in TBM penetration and rotary drills is primarily composed of rock indentation by cutters or indenters, rock crushing, cracks initiation and propagation, rock chipping. The process is related to rock compressive and tensile strength. So, B_5, B_6, B_7 are more suitable to correlate the penetration rate of TBM and rotary drills.

In this study, the brittleness B_5 is adopted to analyze the influence of rock material brittleness on the cutter indentation and TBM penetration. It is believed that B_5 plays an important role in the failure process. Regrettably, at present, a quantitative scale does not exist yet, which, on the basis of B_5, could determine whether the rock is brittle or not. Generally, with the increase of B_5, rock brittleness increases. Hereafter, the brittleness index denotes the ratio of the uniaxial compressive strength to Brazilian tensile strength.

The computation model set up in the single cutter indentation was also used here. All of the parameters including the cutter force were the same in the simulation models except the rock brittleness index. The brittleness index of the Bukit Timah granite varied from 11.41 to 29.52, and correspondingly the rock tensile strength varied form 6.3 MPa to 16.3 MPa when the typical rock compressive strength was assumed to be 186 MPa (Zhao, 1996).

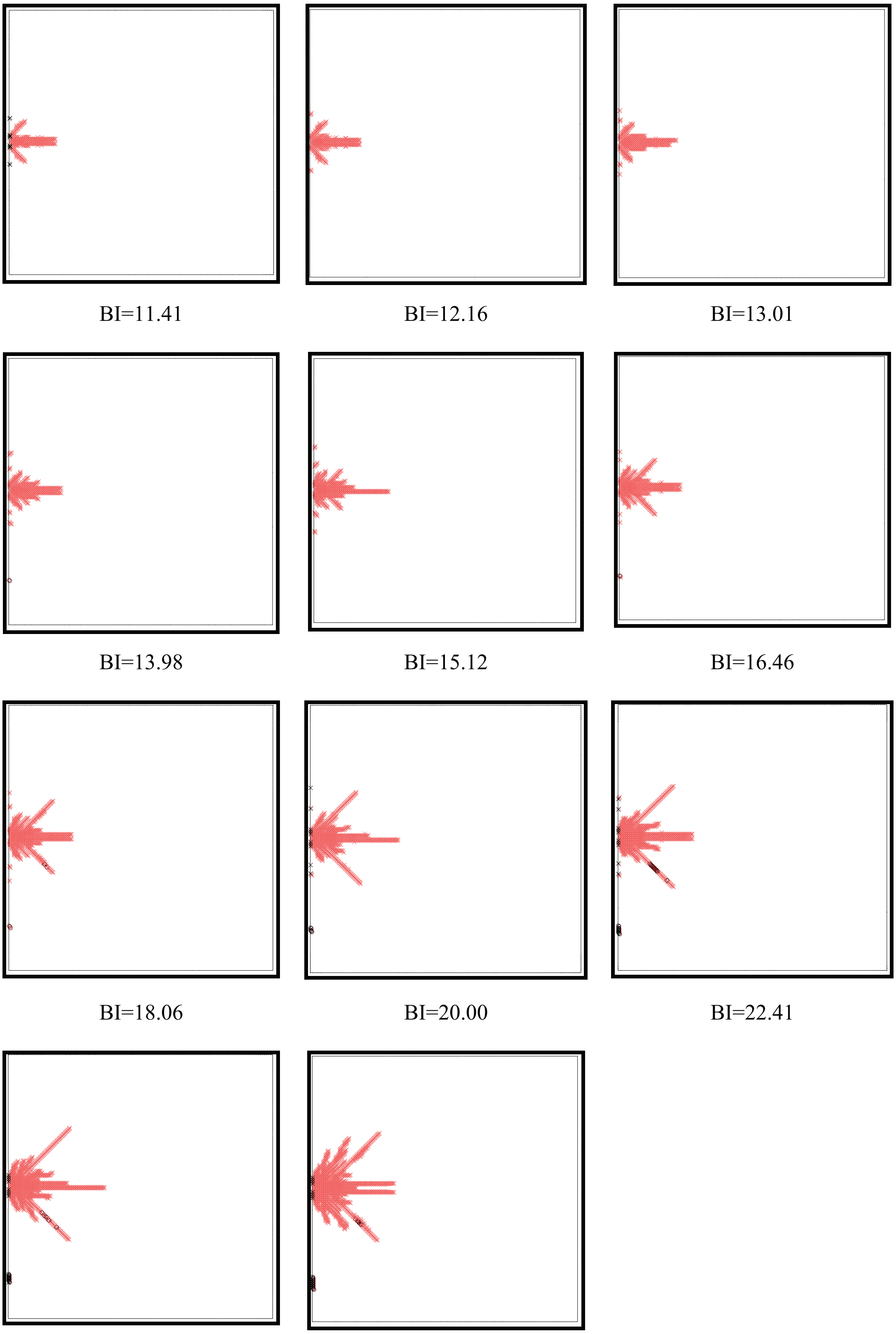

BI=11.41 BI=12.16 BI=13.01

BI=13.98 BI=15.12 BI=16.46

BI=18.06 BI=20.00 BI=22.41

BI=25.48 BI=29.52

Figure 4.2 Variation of failure zone at different rock brittleness index (black circle denotes tensile failure, red cross denotes compressive failure)

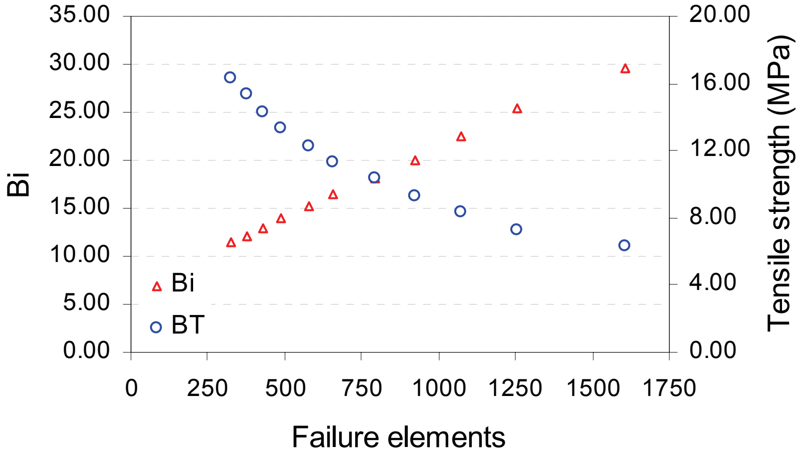

Figure 4.3 Variation of the failure elements at the different rock brittleness indices and the corresponding tensile strength

The crack patterns at the different brittleness indices are shown in Figure 4.2. With the increase of the brittleness index, the crushed zone increases and the number and length of the main cracks outside the crushed zone also increase. It is obvious that with the increase of the rock brittleness index the cutter indentation process is easier. In every case, the number of the failure element including compressive failure and tensile failure was recorded. The variation of the failure elements at the different rock brittleness indices and the corresponding tensile strength is plotted in Figure 4.3. With the increase of the brittleness index, the number of failure elements increases approximately linearly. Compared with the brittleness index, the number of failure elements decrease nonlinearly with the increase of the tensile strength. As a rock property, the brittleness index can express the rock indentation and chipping capacity better than the tensile strength.

4.4 Spacing of Discontinuities

4.4.1 Overview

Howarth (1981) studied the impact of spacing of a set of joints on TBM performance using rock cutting rig in the laboratory. In his study, the strike of the joint set was parallel to the axis of the tunnel. The spacing varied from 20 mm to 100 mm and the angle of cutting attack from 30° to 90°. The experimental results showed that the smaller the spacing, the less is the thrust force required to penetrate a fixed depth. Wanner and Aeberli (1979) studied the effects of different kinds of discontinuities on TBM performance. The total area of all joint planes per unit volume of excavated rock was used as a quantitative expression of joints in the rock mass. By field observations, it was found that tight joints and fissures produced by tensile stresses in rock mass did not improve the TBM performance. On the contrary, for joints caused by shear stresses with gauge material, mylonites and fractured rock zones, they lead to an increase of the penetration rate. Laughton et al. (1994) proposed a Joint Impact Index (JII) to evaluate the effect of joints on TBM performance. A length, which was equal to twice the tunnel diameter, was used as a survey unit cell length. Within the unit cell, eight scanlines perpendicular to the tunnel axis were used to quantify the cell's joint intensity. The total number of joint intercepts was counted for these eight scanlines, and the number of joint intercepts per bored diameter of scanline was reported as an average joint intensity. With the increase of JII, the penetration rate increases. When the JII ranges from 4 to 6, the penetration rate reaches the maximum. As the jointing becomes more extensive, the face itself becomes more unstable, and leads to "blocky condition", resulting in a negative influence on penetration rate. Bruland (1998) divided discontinuities into three types, namely, fissure, joint and single marked joint. Fissures and joints were then classified into four classes. Based on a large number of case histories, a fracturing factor was obtained according to the type and class of discontinuities. With decreasing joint spacing, the TBM penetration increases distinctly (Bruland, 1998).

Due to theoretical difficulties, numerical modelling methods have often been used to probe the mechanism of rock fragmentation. Amongst them, finite element method (FEM), finite difference method (FDM) and discrete element method (DEM) may be the most commonly applied approaches. As discussed in Chapter 3, the current numerical efforts mainly concentrate on the modeling of indentation in continua, and modelling of fragmentation in discontinua is limited. The DEM, which was originally developed for quasi-static problems (Cundall, 1971; Jiao et al., 2004), has been applied in rock dynamics recently (Chen and Zhao, 1998; Fan et al., 2004). In this section, the effects of joint spacing on indentation of rock mass are highlighted and modeled by using the 2D DEM code UDEC (Universal Distinct Element Code) (Itasca, 1996), and the obtained numerical results are compared with those from the field observations.

4.4.2 Model Configuration

As shown in Figure 4.4, the dimension of all the computational models was 0.6m×0.6m, and one set of vertical joints was included. The joint spacing varied from 10 mm to 500 mm. The dip direction of the joint set was assumed to be perpendicular to the cutter loading direction. The cutter was modelled by a normal force applied at mid height of the left boundary through contact thickness of 15 mm. Since it is 2D modeling, the rolling force acting on the cutter cannot be taken into consideration. The upper, lower and right boundaries were regarded as fixed displacement boundaries. The rock blocks between the set of joints were discretized with fine finite difference meshes, namely zones in UDEC. The zone size was 5 mm and the damping value 0.1. In order to compare with the in situ TBM penetration performance in granite rock mass in Singapore later, the rock mass modeled is typical granite distributed in Singapore. The rock material properties and joint properties were summarized by Zhao (1996) and Sharma et al. (1999). The intact granite is assumed to be the Mohr-Coulomb material and its properties are listed in Table 3.1, while all joints satisfy the Coulomb slip model with the properties summarized in Table 4.1.

Table 4.1 Properties of joints

property	value
Normal stiffness (GPa/m)	10
Shear stiffness (GPa/m)	5
Cohesion (MPa)	1.5
Friction angle (°)	25
Tensile strength (MPa)	0.04

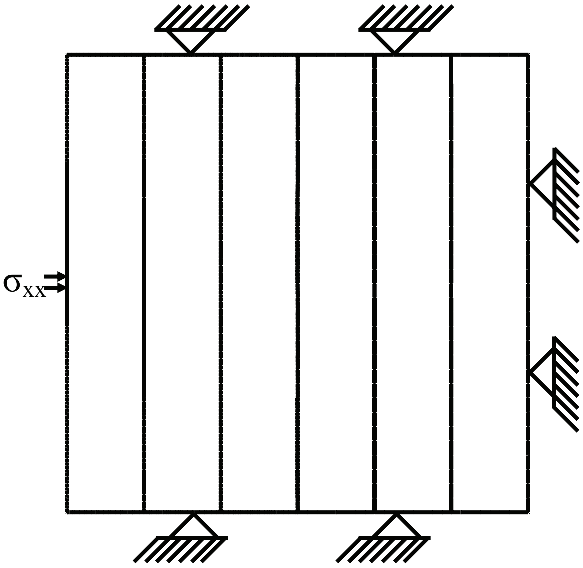

Figure 4.4 Numerical simulation model with joint spacing of 100 mm

4.4.3 Effect of Joint Spacing on Rock Mass Fragmentation

The simulated results show that there are two modes of rock crack initiation and propagation. One is that the crack initiates from the joint plane and propagates upward to the free surface when the joint spacing is equal to or less than 40 mm. The other is that the crack initiates from the crushed zone and propagates downwards to the joint plane when the joint spacing is more than 40 mm. Figure 4.5 shows the first mode of rock fragmentation process with the joint spacing of 30 mm under the action of the cutter. At the beginning of cutter loading, the tensile failure of some elements that are close to the joint plane under the cutter takes place due to the deformation of the joint plane, as shown in Figure 4.5a. With the increase of the penetration, the crack initiating from the joint plane propagates towards the free surface, as shown in Figure 4.5b. Then, due to the deformation of the joint, the tensile cracks emerge perpendicularly to the joint plane at two sides of the cutter, as shown in Figure 4.5c. The phenomenon resembles that of a load acting on a beam. When the penetration increases continuously, the lateral tensile cracks begin to initiate and propagate, making an angle of about 30° to the joint plane. The median crack passes through the rock block at last, as shown in Figures 4.5d, 4.5e and 4.5f. Figure 4.6 shows the second mode of crack initiation and propagation with the joint spacing of 100 mm. The crack initiation and propagation process resembles the single cutter indentation process in the rock mass without joints. Firstly, a fan-shaped rock failure zone appears, as shown in Figure 4.6a. Then the crushed zone is formed and the lateral cracks initiate. After that, the median and side cracks propagate, as shown in Figures 4.6b to 4.6f. The difference is that the growth of the median crack terminates at the joint plane, i.e., the rock fragmentation only occurs within the block immediately under the cutter. The crushed zone is smaller and the lateral cracks propagate longer than that of the single cutter indentation and the chipping angle is different.

The crack patterns at different joint spacings are shown in Figure 4.7. As can be seen, the median and lateral cracks reach the joint interface when the joint spacing is equal to or less than 80 mm. It is worth noting that with the increase of the joint spacing, the chipping angle increases, as listed in Table 4.2. When the joint spacing is more than 80 mm, the side cracks propagate obliquely towards the joint plane at the beginning, and then change the direction parallel to the joint plane. The side cracks can not pass through the rock block. In these cases, the chipping angle also increases with increase of the joint spacing, as listed in Table 4.2. The median crack can not reach the joint plane with the joint spacing more than 200 mm. When the joint spacing reaches 500 mm, the crack mode resembles that of the single cutter indentation on the rock material without joints. Therefore, the influence of the joint on the rock mass fragmentation is trivial. It is worth reiterating that the rock cracking pattern by the cutters, which can significantly influence the TBM performance, is closely related to the joint spacing. As illustrated, the favorable joint spacing for easy rock fragmentation may vary from 50 to 80 mm. Of course, this conclusion needs to be verified by further site work.

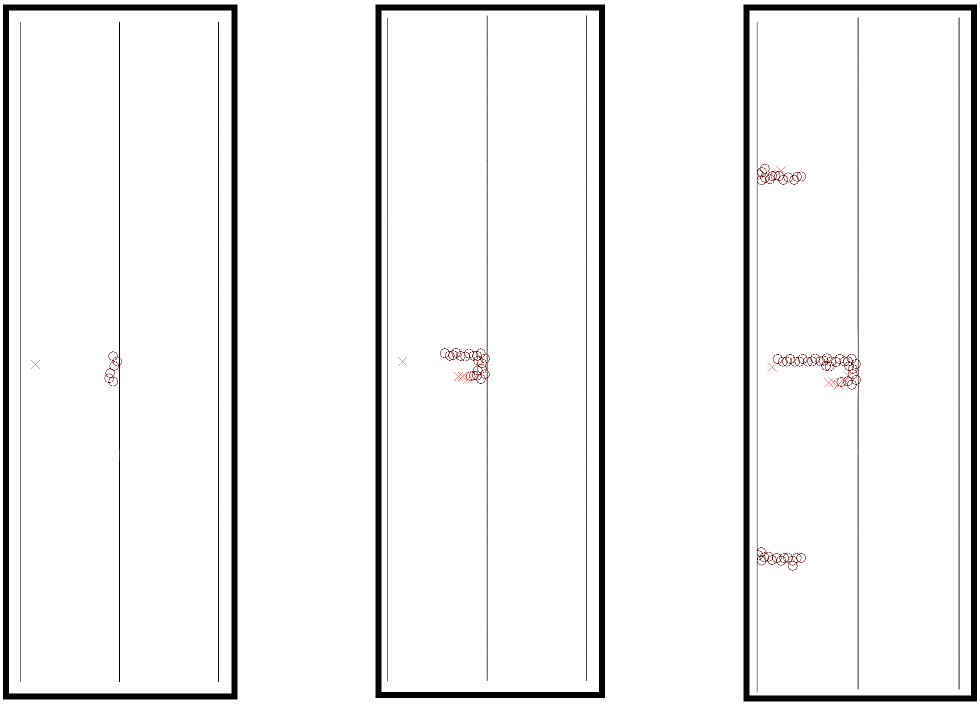

(a) Step: 60 (b) Step:100 (c) Step:300

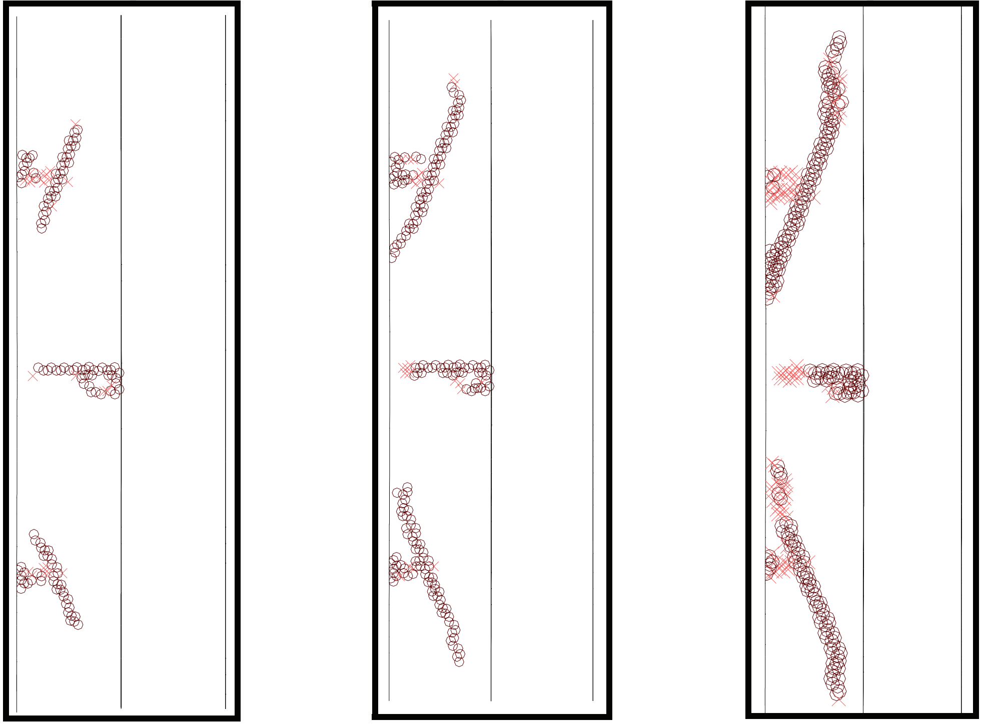

(d) Step:500 (e) Step:700 (f) Step:1000

Figure 4.5 Crack initiation and propagation with joint spacing 30 mm (black circle denotes tensile failure, red cross denotes compressive failure)

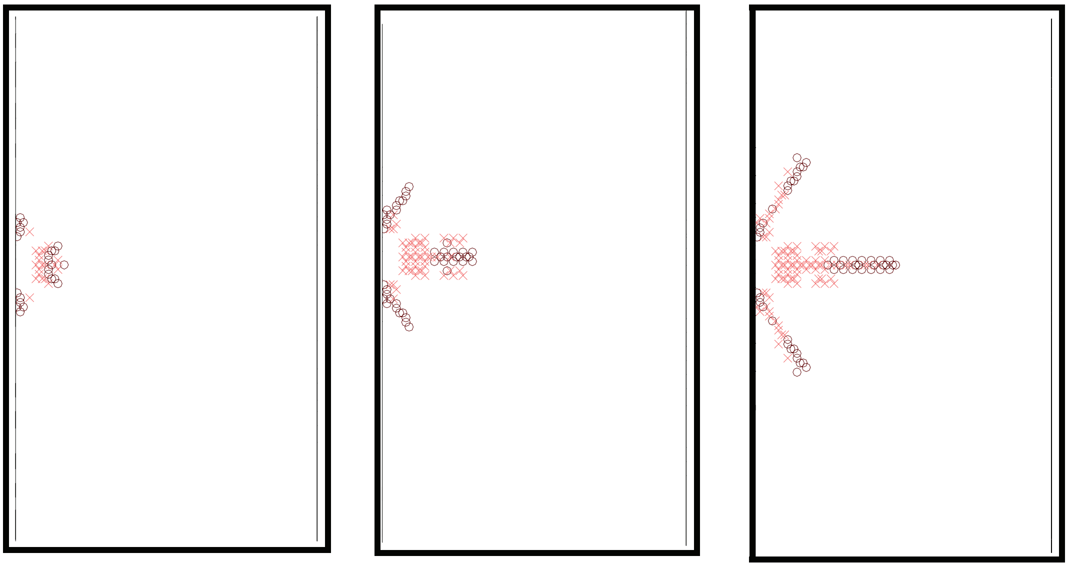

(a) Step: 30 (b) Step: 60 (c) Step: 100

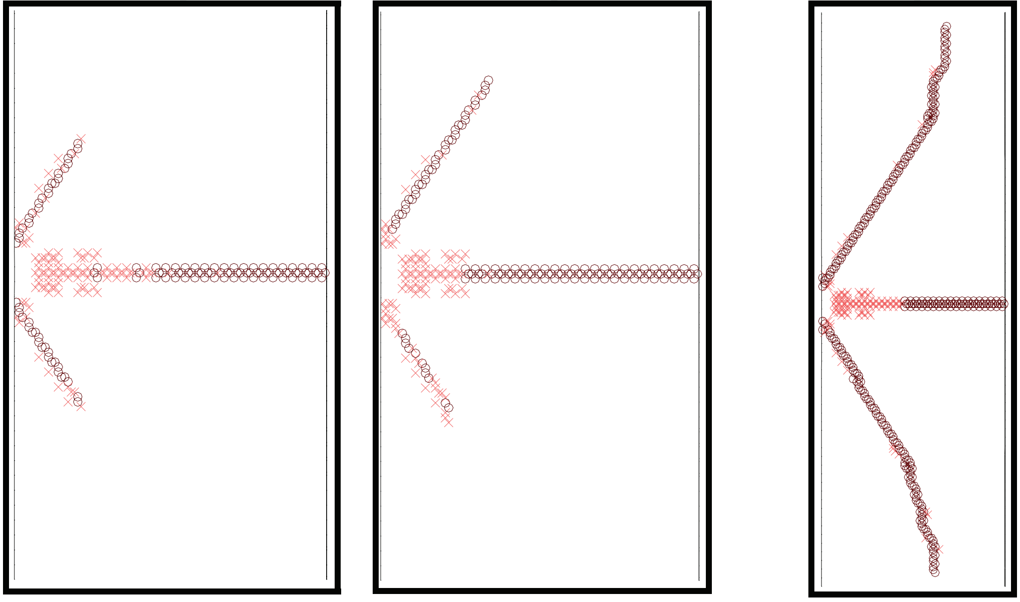

(d) Step: 300 (e) Step: 500 (f) Step: 1000

Figure 4.6 Crack initiation and propagation with joint spacing 100 mm (black circle denotes tensile failure, red cross denotes compressive failure)

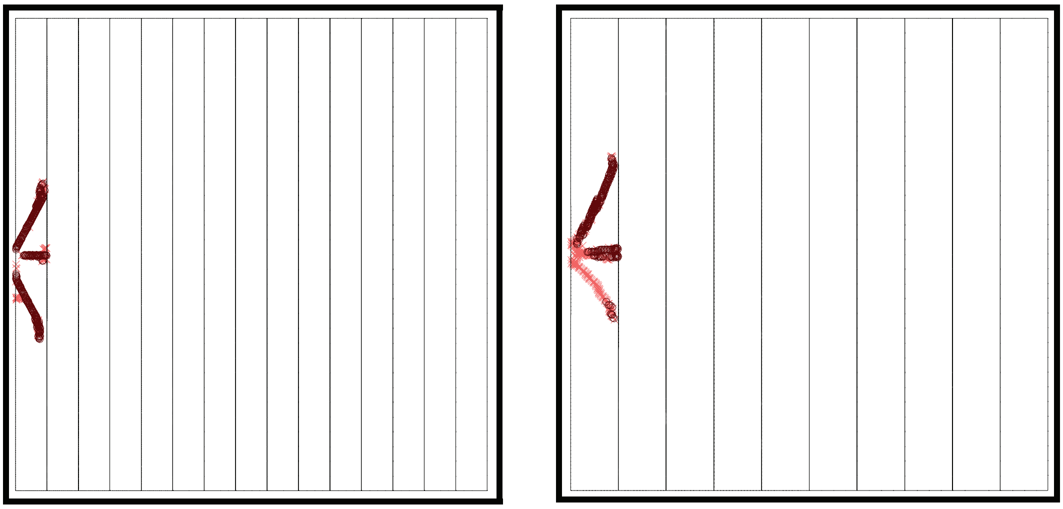

(a) Joint spacing: 40 mm

(b) Joint spacing: 60 mm

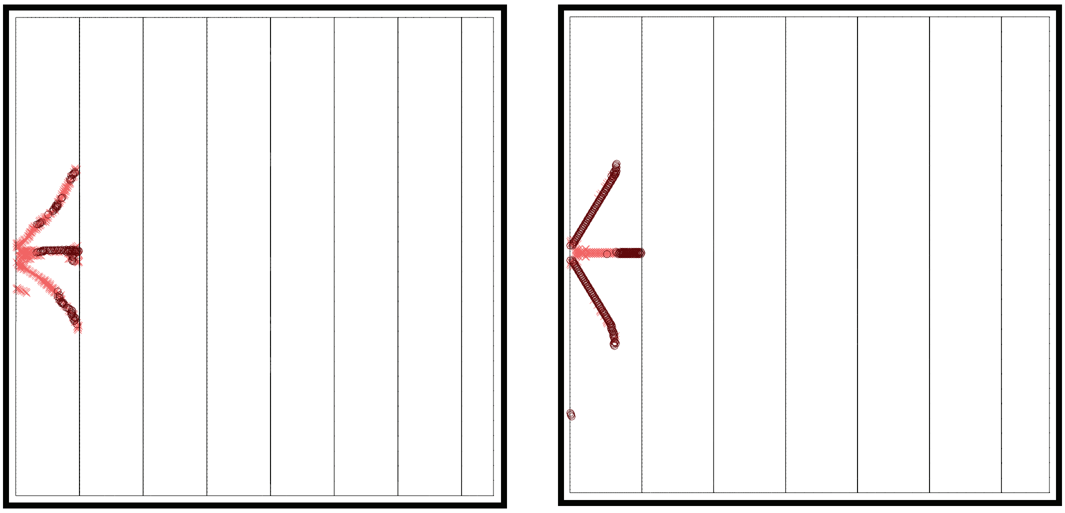

(c) Joint spacing: 80 mm

(d) Joint spacing: 90 mm

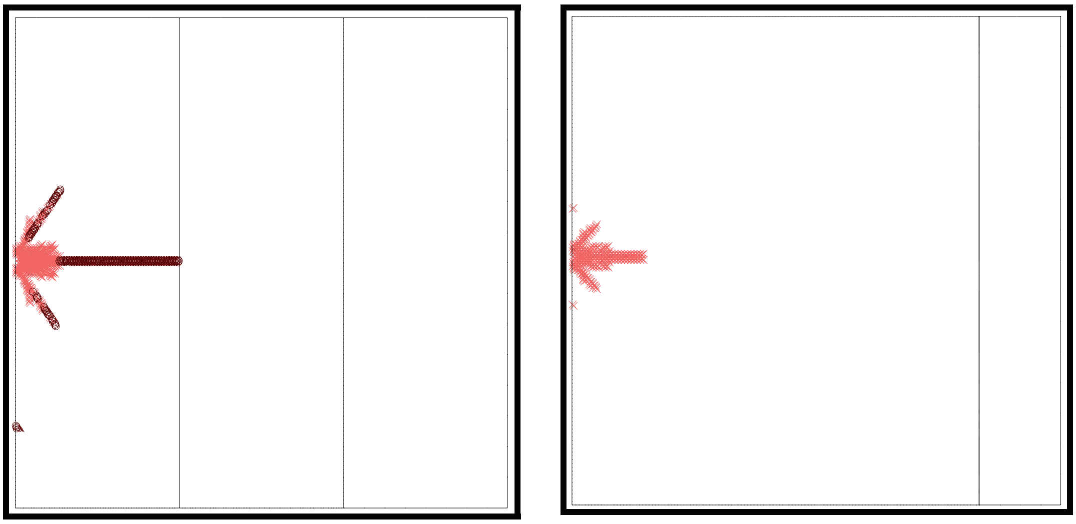

(e) Joint spacing: 200 mm

(f) Joint spacing: 500 mm

Figure 4.7 Crack pattern with different joint spacings (black circle denotes tensile failure, red cross denotes compressive failure)

4.4.4 Effect of Joint Spacing on Stress Field

The stress field induced by a single cutter indentation is studied in Chapter 3. The stress field is symmetrical and the stresses are extremely high close to the loading point and decrease rapidly with the increasing distance from the loading point. Figure 4.8 shows the stress fields with the joint spacing of 60 mm, 90 mm and 500 mm, respectively. As can be seen, high major principal stresses distribute in the vicinity of the loading point. But the principal stress contour extends to the two sides of the cutter parallel to the direction of the joint plane for the joint spacing less than 200 mm. The deflection of the stress field varies with the changes of the joint spacing. The deflection is getting larger with decrease of the joint spacing. The stress deflection is the main reason why the chipping angle changes with variation of the joint spacing. When the joint spacing reaches 500 mm, as shown in Figure 4.8c, the stress field resembles that of the single cutter indentation in the rock material without joints.

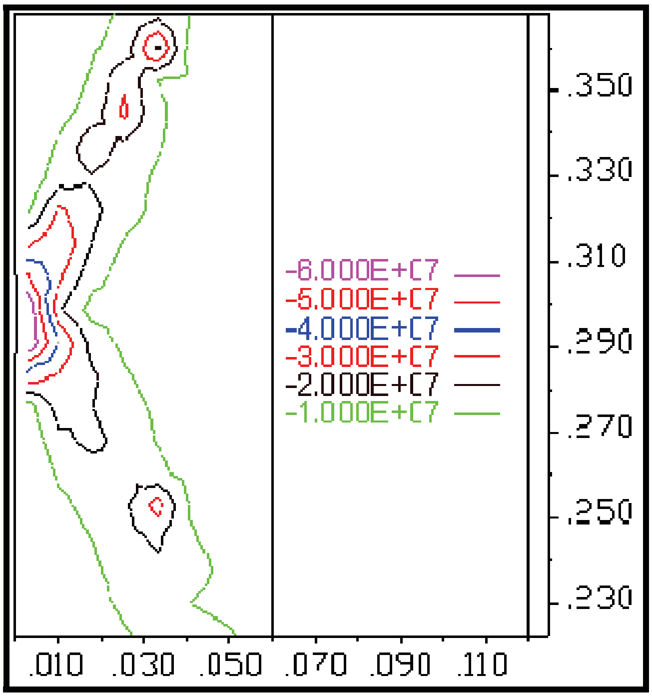

Figure 4.8a Major principal stress contour with different joint spacings (joint spacing: 60 mm)

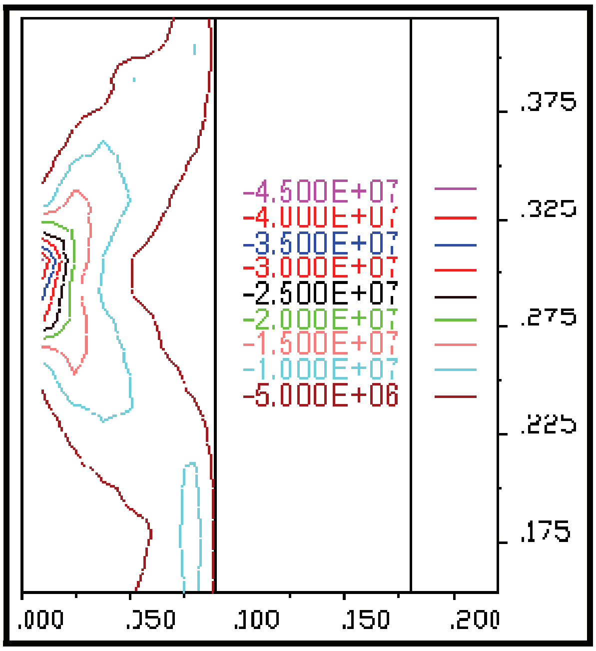

Figure 4.8b Major principal stress contour with different joint spacings (joint spacing: 90 mm)

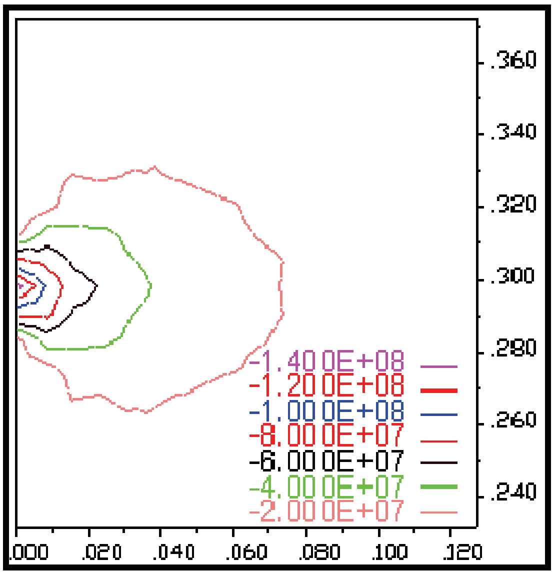

Figure 4.8c Major principal stress contour with different joint spacings (joint spacing: 500 mm)

4.4.5 Effect of Joint Spacing on the TBM Penetration

The simulation results are listed in Table 4.2. The first column is the joint spacing used in the computation. The second column is the chipping stress. It represents the threshold stresses for the cracks to initiate and propagate inside the rock. The third column is the chipping angle that is between the free surface and the lateral crack propagation direction. The fourth column is the chipping area. It is noteworthy that the net cutter spacing is assumed to be 80 mm. According to the crack mode and the chipping angle at different joint spacing, the chipping area is calculated. For example, when the joint spacing is equal to or less than 40 mm, the median crack is initiated from the joint interface. So, the chipping area is the cutter spacing times the joint spacing. Here, an exception is when the joint spacing is 10 mm, the cutter cuts through the first two joints and the area is 16 cm^2. The fifth column is the ratio of chipping area over chipping stress, which denotes the amplitude of rock chips per unit cutter force at different joint spacing. It indirectly stands for the TBM penetration rate. The last column is the ratio of P_s to P_{500}, where, P_s denotes the penetration rate with different joint spacings and P_{500} denotes the penetration rate with the joint spacing of 500 mm, respectively. With regard to the analysis of the major principal contour and crack mode, the effect of the joint spacing on the penetration rate is very small when the joint spacing is close to 500 mm. So, P_{500} is regarded as a base value to compare the effect of the joint spacing on the TBM penetration rate.

The chipping stress variation for different joint spacings is shown in Figure 4.9. The joint spacing of 200 mm is a critical point in the figure. For the joint spacing less than 200 mm, the chipping stress increases rapidly and approximately linearly with increasing joint spacing. For joint spacing more than 200 mm, the chipping stress increases slowly with increasing joint spacing. The correlation between joint spacing and the ratio of P_s/P_{500} is shown in Figure 4.10. The ratio of P_s/P_{500} decreases basically with the increase of joint spacing. While the joint spacing is equal to or less than 40 mm, the penetration rate is close to 9 times of that in the homogeneous rock. The main reason is owing to the different crack mode. As discussed before, the crack initiates from the joint interface and propagates upwards to the free surface. While the joint spacing varies from 50 mm to 80 mm, the penetration rate is close to 4 times of that of a rock mass without joints. It is also two times of the penetration rate at the joint spacing of 90 mm or 100 mm. The main reason is that, when the joint spacing is within 80 mm, the side cracks can propagate to the joint plane and improve the yield of rock chipping.

Based on the field observations and statistical analysis of over 250 km of TBM excavated tunnels in hard rock conditions for more than twenty years, Bruland (1998) divided the discontinuities into two sorts, namely joints (Sp) and fissures (St), and five classes as listed in Table 2.3. He summarized the effect of every fracture class and its orientation on the TBM penetration rate. For each discontinuity class and its orientation, he drew a fracturing factor graph. When the angle between the tunnel axis and the fracture plane is 90 degrees, the ratio of the penetration rate (P_s) with different fracture spacing to the penetration rate without fractures (P_0) based on that graph is shown in Figure 4.11. As mentioned earlier, when the joint spacing is 500 mm, its effect on the penetration rate is very small. It is assumed that P_{500} is equal to P_0. The simulated results are also plotted in Figure 4.11. In the graph, the simulated results are smaller than those from in situ measurements with fissure spacing. It is also much smaller than the measured results with joint spacing. But the trend of these curves is similar.

The simulation mainly focuses on explaining the mechanisms of rock fragmentation and its effect of the joint spacing on the TBM penetration rate. It only takes into account the rock mass fragmentation process during one revolution under the action of a single cutter. In practice, the TBM excavation is a continuous boring process during one stroke. The first revolution certainly influences the production of the second revolution and the penetration rate generally is more than the first one. Only if the tunnel face is pre-conditioned, does the penetration rate remain the same. Furthermore, the interaction between cutters also obviously affects the chipping process. This is the main reason why the simulation results are smaller than those from in situ measurements in rock masses with different fissure spacings. Furthermore, the effect on the penetration rate can not be simulated when the joint spacing is more than 300 mm, because the stress field is almost undisturbed even with the existence of the joints. In practical excavation, when the TBM is boring ahead continuously and close to the joint plane, the effect of the joint on the penetration rate can be observed. In this simulation, the joint aperture and joint filling are not taken into consideration. Thus, the simulation results are much smaller than the in situ measurements in rock masses with different joint spacings. In practice, the ratio of P_s/P_0 should be less than 9. When the joint spacing is too small, the tunnel face may not be stable during excavation. And in some cases, the capacity of the muck remove is limited or the torque is not enough. So, the penetration rate has to be reduced. Although the above mentioned factors are not considered and the simulation results are less than the actual results, the variation of the penetration rate with joint spacing shows agreement with the in situ measurements.

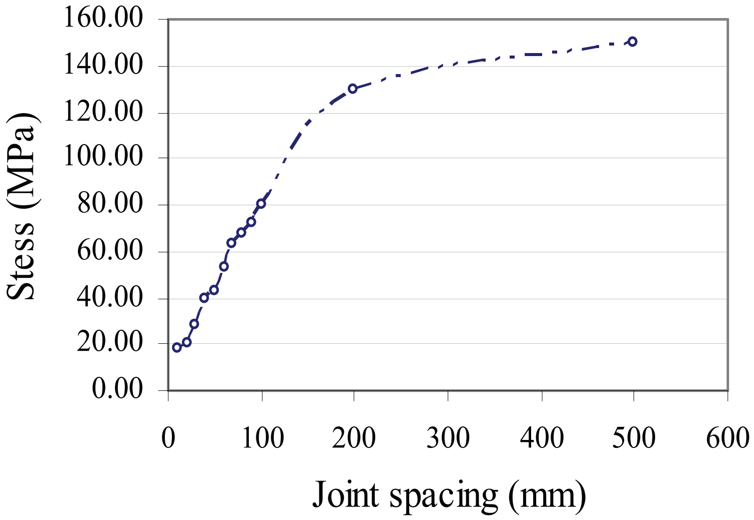

Figure 4.9 Chipping stress variation with different joint spacings

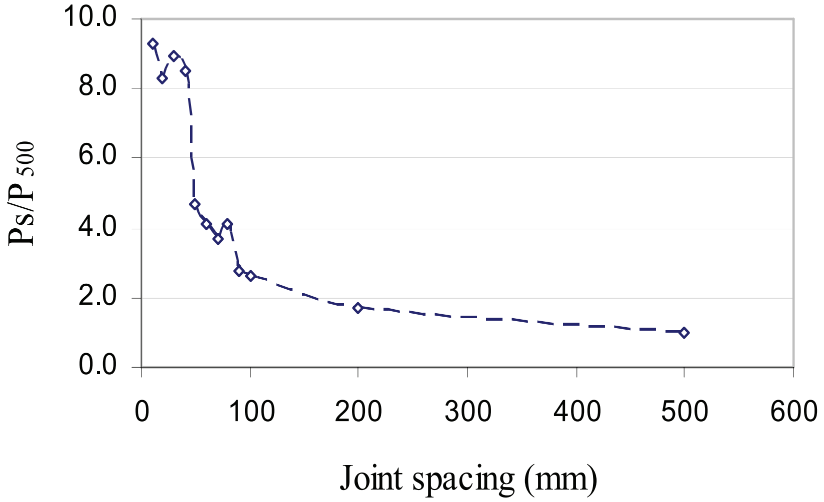

Figure 4.10 Effect of joint spacing on the penetration rate

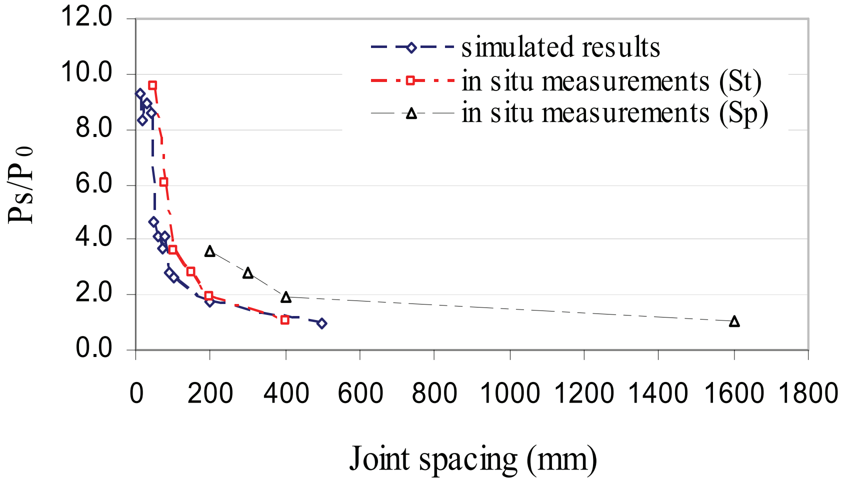

Figure 4.11 Comparison of effect of joint spacing on the penetration rate

Table 4.2 Effect of joint spacing on TBM penetration

Joint spacing (mm)	Chipping stress (MPa)	Chipping angle (°)	Chipping area (cm^2)	The ratio of chipping area to chipping stress (cm^2/MPa)	P_s/P_{500}
10	18.0		16.00	0.889	9.26
20	20.0		16.00	0.800	8.33
30	28.0	21	24.00	0.857	8.92
40	39.0	27	32.00	0.821	8.54
50	43.0	31	19.20	0.447	4.65
60	53.0	33	20.80	0.392	4.09
70	63.0	35	22.40	0.356	3.70
80	68.0	40	26.88	0.395	4.12
90	72.0	31	19.20	0.267	2.78
100	80.0	32	20.00	0.250	2.60
200	130.0	34	21.60	0.166	1.73
500	150.0	42	16.41	0.096	1.00

4.4.6 Conclusions

The simulation results show that there are two modes of crack initiation and propagation. One is that the crack initiates from the joint plane and propagates upward to the free surface. The other is that the crack initiates from the crushed zone and propagates towards to the joint plane. Due to the existence of the joint plane beneath the cutter, the principal stress field is deflected to two sides of the cutter. It leads to the variation of the rock chipping angle. The growth of cracks terminates at the joint interface which is in the way of the crack propagation.

Based on the simulated results and the field observations by Bruland (1998), the effect of joint spacing on TBM penetration rate is analyzed and compared. The simulated values are smaller than the in situ measured values in rock masses with different fissure spacings, and also much smaller than those from in situ measurements in rock masses with different joint spacings. The main reason is that in the numerical modeling, the fillings and aperture of the joints are not taken into account, and the simulation also does not consider the continuous boring process. But the trend of these curves is similar.

4.5 Orientation of Discontinuities

4.5.1 Overview

The influence of the joint orientation was observed in the earliest proposed comprehensive prediction model in 1976 by NTNU (Norwegian University of Science and Technology), but not quantified (Bruland, 1998). The 1979 edition of the model makes a first attempt to quantify the influence and the following updated editions considered the influence of the joint orientation based on the in situ measurements. In the recent models, the significance of joint spacing and orientation on TBM performance are emphasized and regarded as important factors influencing the TBM performance (Cheema, 1999; Barton, 2000). But, there seems to be a lack of complete understanding of the rock cutting process due to the very complex nature of the interaction of TBM cutters and rock masses (Rostami et al., 1996).

In situ measurements by Aeberli and Wanner (1978) in a homogeneous zone of schistose phyllite showed that the advance rate of TBM increases with the increase of the angle between TBM axis and the planes of schistosity. Similar phenomena were also observed by Thuro and Plinninger (2003) in phyllite and phyllite-carbonate-schist inter-stratification. Bruland (1998) summarized the in situ measurement results over 250 km of TBM tunnels. The effects of joint orientation were respectively obtained for different classes of joints. The same rule was observed. However, he noted that with the increase of joint spacing, the effect of joint orientation on TBM penetration decreases. A theoretical analysis of the interaction between cutter and rock with foliation by Sanio (1985) showed a similar trend. Although the above mentioned phenomenon was noticed, little research has been undertaken to explain the mechanism of rock fragmentation by TBM cutters in rock mass with different joint orientation. This may probably be due to the theoretical difficulty in simulating crack growth in discontinuous medium.

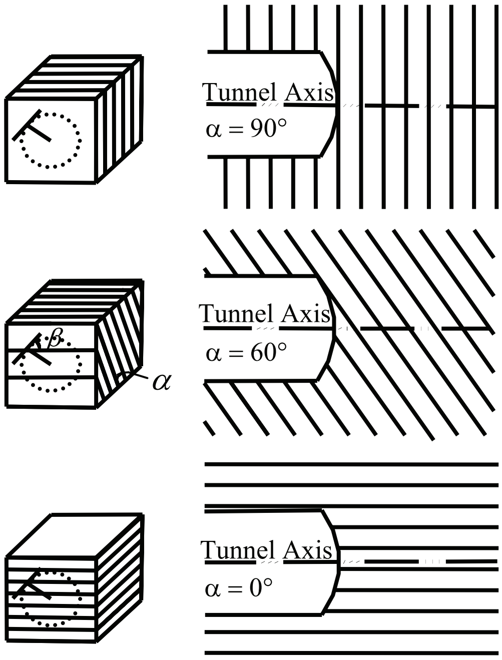

Figure 4.12 Influence of discontinuity orientation on TBM penetration

When a jointed rock mass is excavated by a TBM, the effect of joint orientation on the cutter penetration is shown in Figure 4.12. Cutter penetration may be affected by two angles: the angle α between the tunnel axis and the joint plane, and the attack angle β between the cutter rolling direction and the joint outcrop in the tunnel face. Experiments by Howarth (1981) and Sanio (1985) indicated that the influence of the angle β on the TBM performance was not obvious. The influence of the angle β can also be evaluated geometrically. As one joint outcrop moves across the tunnel face when the TBM advances, and the cutter moves in concentric circles, the effect of the angle β disappears. This study therefore focuses on the influence of the angle α by numerical modeling.

4.5.2 Model Configuration

The configuration of the computational model is schematically shown in Figure 4.13. The dimension of the model was 1.2m×1.2 m. The cutter is modelled by a normal force applied at mid height of the left boundary through contact thickness of 15 mm. The rolling force acting on the cutter was not taken into consideration in the two dimensional model. The upper, lower and right boundaries were regarded as fixed displacement boundaries. One joint set with a fixed spacing of 200 mm was included in the computation model. The dip direction of the joint set was assumed to be in the same direction as the cutting load, and the joint dip angle varies from 0°, 15°, 30°, 45°, 60°, and 75° to 90°. In all the models, the joint outcrop was at 80 mm above the contact point between the cutter and the rock. The rock blocks between the joint set were discretized with fine finite difference meshes, namely zones in UDEC. The zone size in the blocks was set to 10 mm and the damping value 0.1. The rock material modeled is typical granite found in Singapore (Wallace et al., 1995; Zhao, 1996). The intact granite is assumed to be the Mohr-Coulomb material and its properties are listed in Table 3.1, while all joints satisfy the Coulomb slip model with the properties summarized in Table 4.1.

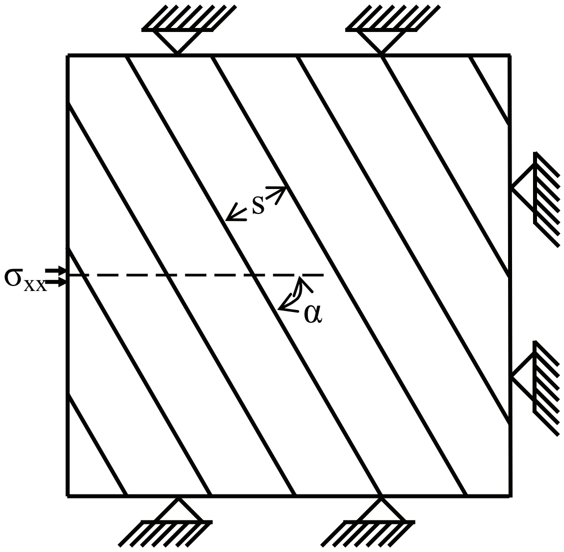

Figure 4.13 Numerical simulation model with fixed joint spacing of 200 mm

4.5.3 Rock Fragmentation at Different Joint Orientation

Figure 4.14 shows the pattern of the rock indentation and fracture formation by the cutter when the angle α is 45°. The plastic zones are plotted. In order to highlight the cutter indentation process, the zone of the cracks initiation and propagation immediately beneath the cutter is zoomed in at different iteration step while the angle α varies, as shown in Figures 4.15 to 4.21. As shown in the Figures, the indentation process can be divided into three stages, namely the formation of a crushed zone, cracks initiation and propagation, and chip formation.

When the cutter first acts on the rock, a fan-shaped rock failure zone is formed as shown in Figures 4.15a, 4.16a, 4.17a, 4.18a, and 4.21a. Immediately beneath the cutter is a zone of compressive failure. Further is a zone of tensile failure. At the cutter edge, a conical, Hertzian crack is initiated as shown in Figures 4.16a, 4.17a, 4.18a, and 4.21a. An interesting phenomenon can be observed that immediately beneath the cutter the rock remains relatively intact because of the high confining pressure in this zone. It is the so-called hydrostatic compression state (Cook et al., 1984; Chiaia, 2001; Liu et al., 2002). As the penetration increases, the crushed zone is formed including compression failure zone and tensile failure zone. This zone is directly located under the cutter and composed of numerous microcracks that comminute the rock to produce powder or extremely small particles (Pang and Goldsmith, 1990). The multiple cracks zone is also formed beneath the crushed zone. The median and radial cracks are initiated from the tensile zone as shown in Figures 4.15b, 4.16b, 4.17b, 4.18b, 4.18c, and 4.21b. The cracks mainly propagate along the tensile failure elements. In this stage, it is interesting to note that the crushed zone is asymmetric as shown in Figures 4.16b, 4.17b and 4.18c because of the influence of the joint. Subsequently, it causes the cracks initiating from the crushed zone to propagate asymmetrically as shown in Figures 4.16b, 4.17b and 4.18c. As the penetration continuously increases, the crushed zone remains the same. The cracks extend along certain directions, for example the median direction and side direction, as shown in Figures 4.15c, 4.16c, 4.17c, 4.18d, 4.18e, and 4.21c. The crack propagation is induced by the element tensile failure at the tip of the crack. As the cutter penetration increases to some extent, the side crack reaches to the joint plane, the chip is formed, as shown in Figures 4.15c, 4.16d, 4.17d, 4.18f, 4.19e and 4.20d.

When the angle α is 60° or 75°, the crack initiation and propagation show a completely different mode as shown in Figures 4.19 and 4.20. Due to the presence of the joint, the element closest to the joint plane is failed first, as shown in Figures 4.19a and 4.20a. As the penetration increases, the crack propagates along the intensity zone of tensile stress as shown in Figures 4.19b, 4.19c, 4.20b, and 4.20c. The tensile cracks are also initiated below the cutter edge because of the deformation of the rock immediately beneath the cutter. When the penetration continuously increases, the crack reaches to the free face. At the same time, the chip is formed, as shown in Figures 4.19d and 4.20e.

The above analysis on crack initiation and propagation shows that there are two possible chipping modes of rock fragmentation. One is that the crack initiates beneath the crushed zone and propagates downwards to the joint plane. The other is that the crack initiates from the joint plane and propagates upwards to the free surface.

It is worth noting that in all cases of different angle α, the growth of a crack terminates at the joint interface. In other words, fragmentation mainly occurs within the block immediately under the cutter. These phenomena are commonly observed at field excavation, as shown in Figure 4.22. It was taken from the TBM cutterhead chamber in a tunnelling project in the Bukit Timah granite in Singapore. When the cutter rolled over a joint set, the cracks directly propagate to the joint interface, and then the rock chips are formed.

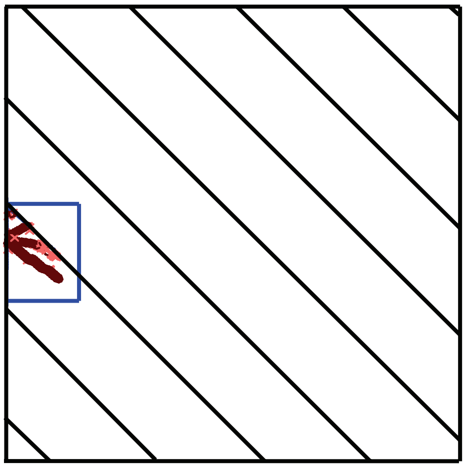

Figure 4.14 Rock failure pattern at α =45°

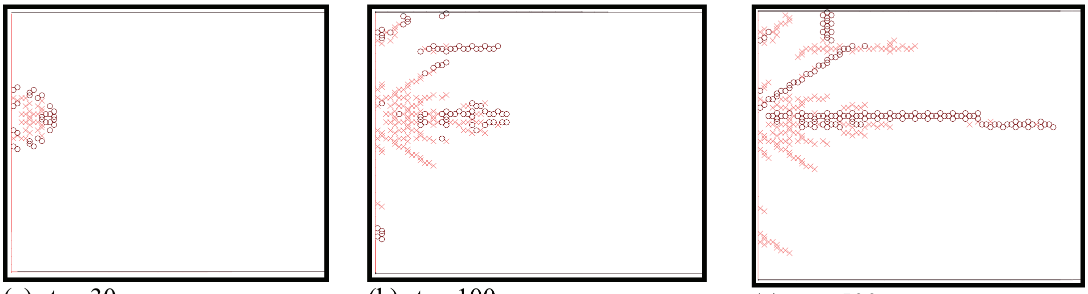

(a) step:30
(b) step:100
(c) step:500

Figure 4.15 Failure status of rock at selected steps at α =0° (circle denotes tensile failure, cross denotes compressive failure)

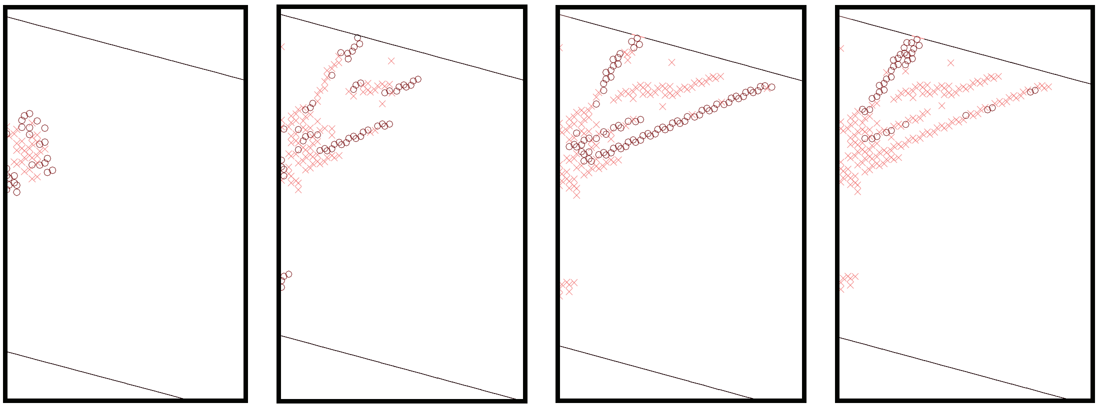

(a) step:30 (b) step:100 (c) step:500 (d) step:1000

Figure 4.16 Failure status of rock at selected steps at α =15° (circle denotes tensile failure, cross denotes compressive failure)

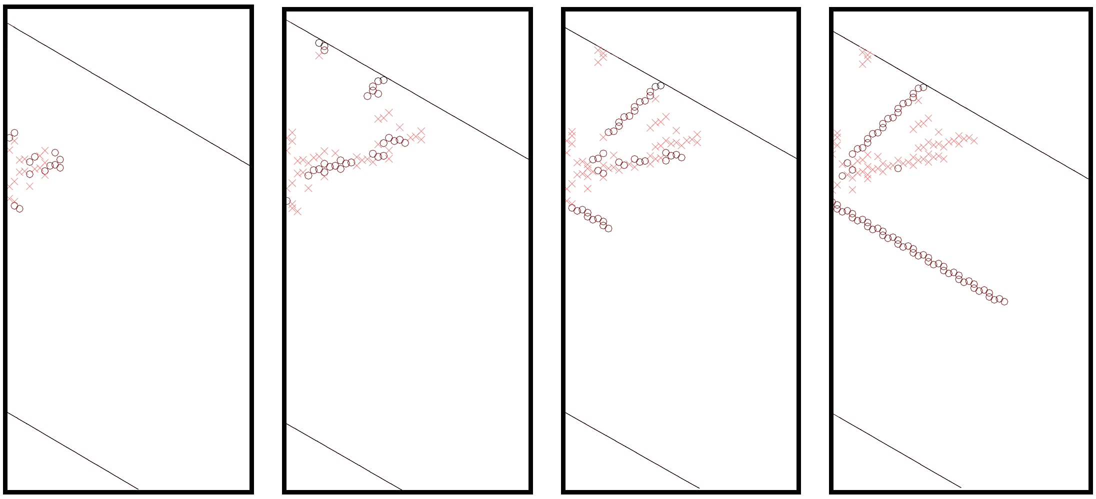

(a) step:30 (b) step:100 (c) step:300 (d) step:500

Figure 4.17 Failure status of rock at selected steps at α =30° (circle denotes tensile failure, cross denotes compressive failure)

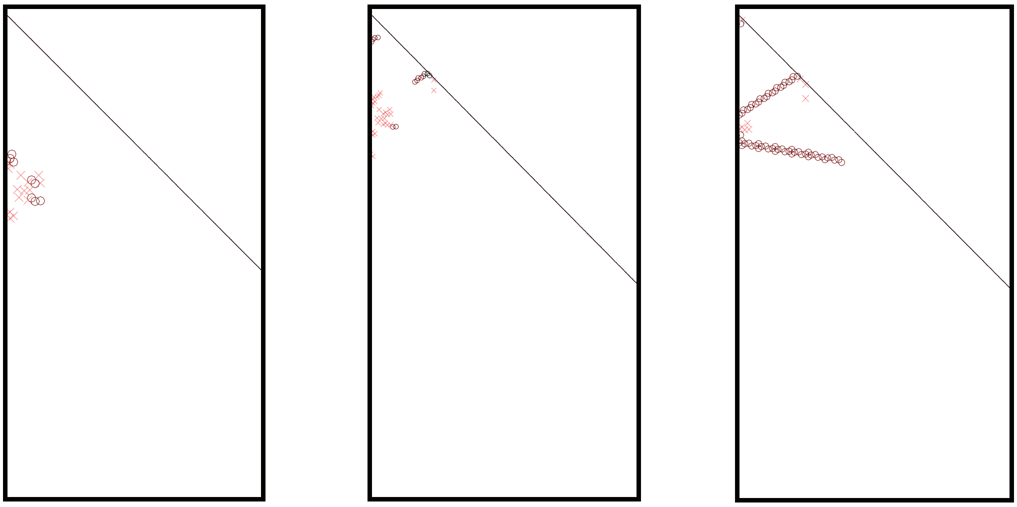

(a) step:30 (b) step:100 (c) step:300

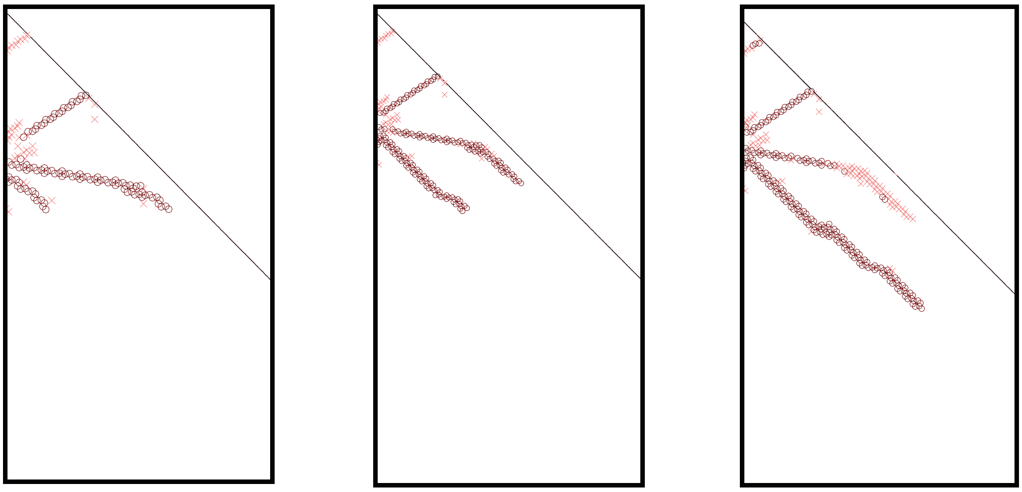

(d) step:500 (e) step:700 (f) step:1000

Figure 4.18 Failure status of rock at selected steps at α =45° (circle denotes tensile failure, cross denotes compressive failure)

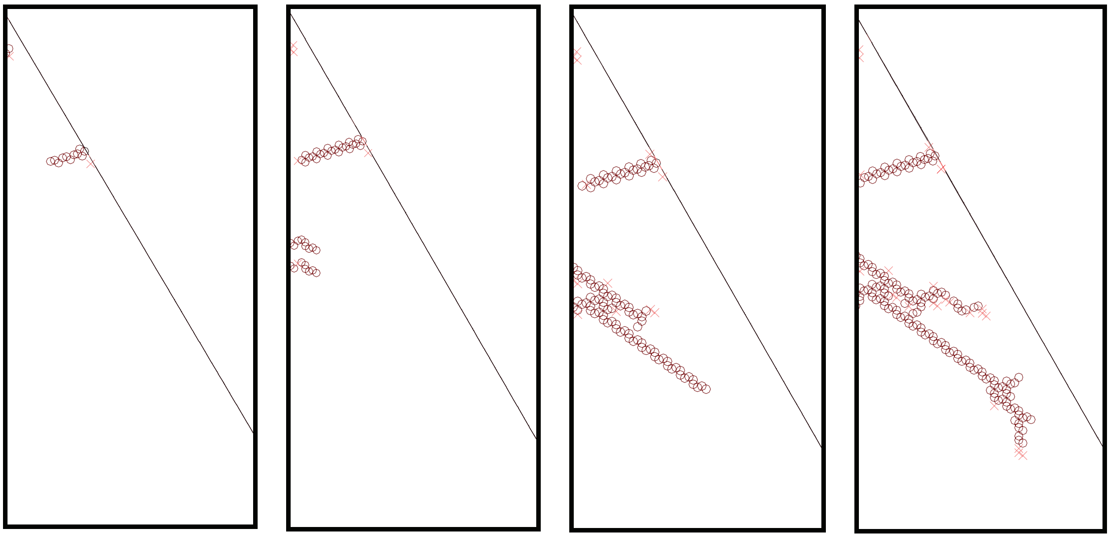

(a) step:100 (b) step:300 (c) step:500 (d) step:1000

Figure 4.19 Failure status of rock at selected steps at α =60° (circle denotes tensile failure, cross denotes compressive failure)

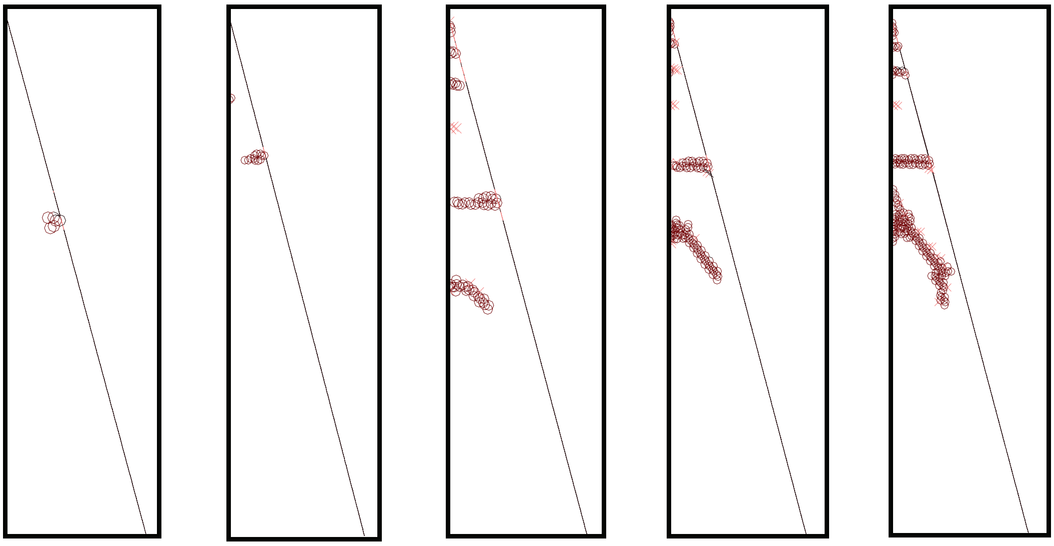

(a) step:60 (b) step:100 (c)step:300 (d) step:500 (e) step:1000

Figure 4.20 Failure status of rock at selected steps at α =75° (circle denotes tensile failure, cross denotes compressive failure)

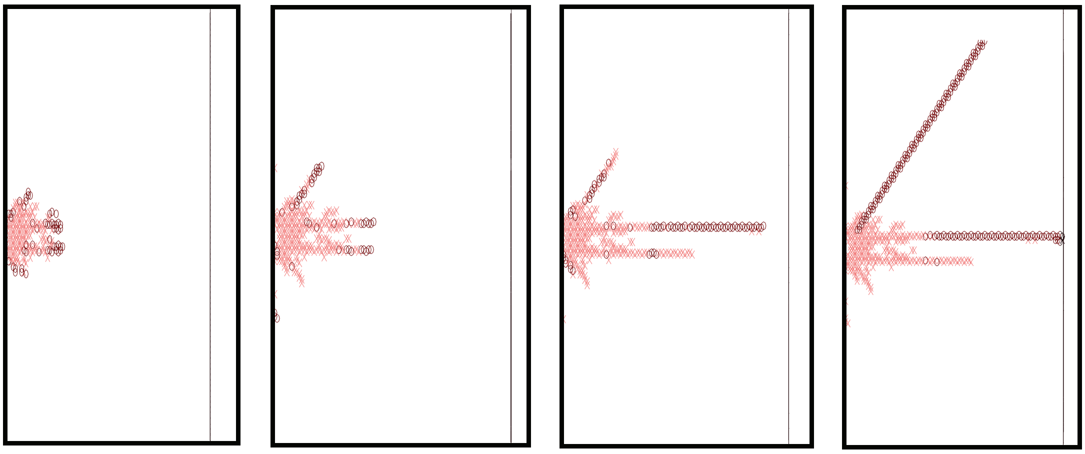

(a) step:60 (b) step:100 (c) step:300 (d) step:1000

Figure 4.21 Failure status of rock at selected steps at α =90° (circle denotes tensile failure, cross denotes compressive failure)

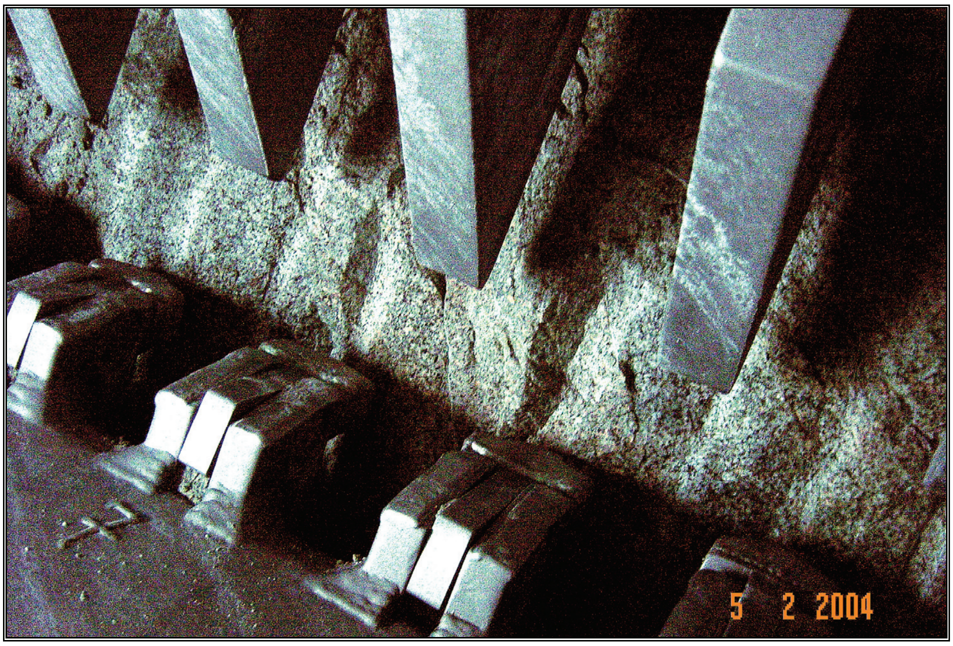

Figure 4.22 Effect of joint orientation on rock chipping formation

4.5.4 Effect of Joint Orientation on Rock Chipping Angle

Due to the influence of the joint and its orientation, the cracks induced by TBM cutters do not initiate and propagate symmetrically. Subsequently, the rock chipping angle between the tunnel face and the rock damage plane varies while the angle α changes as illustrated in Figure 4.23. With the increase of the angle α from 15° to 75°, the rock chipping angle also increases. When the angle α is 90°, the side crack propagation is not affected by the joint orientation and the chipping angle is about 30-35° that agrees with the Hertzian cone crack with the chipping angle 30°-40° (Chiaia, 2001). As the angle α is 0°, the chipping angle is about 56° which is greater than that at α=90°. The main reason of such phenomenon is that the influence of the near side joint deformation and the corresponding confinement stress decreases. It is worth noting that with the increase of the angle α, the rock breakage seems to be easier under the same cutting conditions.

4.5.5 Effect of Joint Plane on Stress Field

When a normal point load acts on an isotropic, linear elastic half-space, the stress field was first given by Boussinesq in 1885, commonly known as the Boussinesq elastic field. When a smooth spherical indenter acts on an isotropic, linear elastic half-space, the field stress is known as the ideal Hertzian elastic field. Liu et al. (2002) gave the simulated quasi-photoelastic stress fringe pattern induced by a single indenter when the rock is considered as a homogeneous material. Figure 3.10 also shows the stress field induced by single cutter acting on the rock material. The stress field is symmetrical and the stresses are extremely high close to the loading point and decrease rapidly with the increasing distance from the loading point. Figures 4.24, 4.25 and 4.26 show the major principal stress fields when the angle α is equal to 0°, 15°, and 90° respectively. As can be seen, the major principal stress contours are deflected to the joint plane, owing to the introduction of the joint set. The stress fields induced by the cutter in jointed rock mass are not symmetrical. Furthermore, the deflection of the stress field is different with the variation of the angle α. From this stress nature one can understand why the cracks initiate and propagate in an asymmetrical manner beneath the cutter, which also explains the variation of chipping angle at different α values.

It is interesting to note that the stress field induced by the cutter shows a discontinuous nature at joint interfaces. Due to the non-uniformity in stress transmission at the nearest joint interface, there is rare possibility for stress in the next block to reach failure. Therefore, the joint plane protects the neighboring rock block from damage. These phenomena are observed in all of the simulation results at different α, as shown in Figures 4.24 to 4.26. It is also observed in TBM tunneling site extensively, as in the example shown in Figure 4.22. The convincing results suggest that discrete element methods have the potential in reproducing the fragmentation process of jointed rock mass.

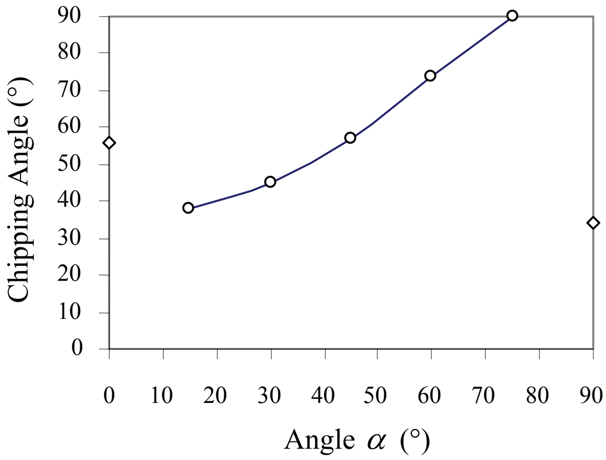

Figure 4.23 Chipping angle vs. the angle α

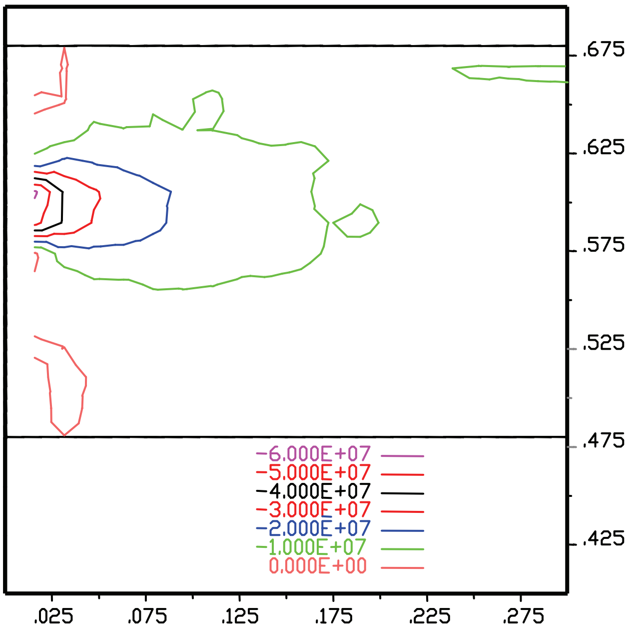

Figure 4.24 Major principal stress contour at α =0°

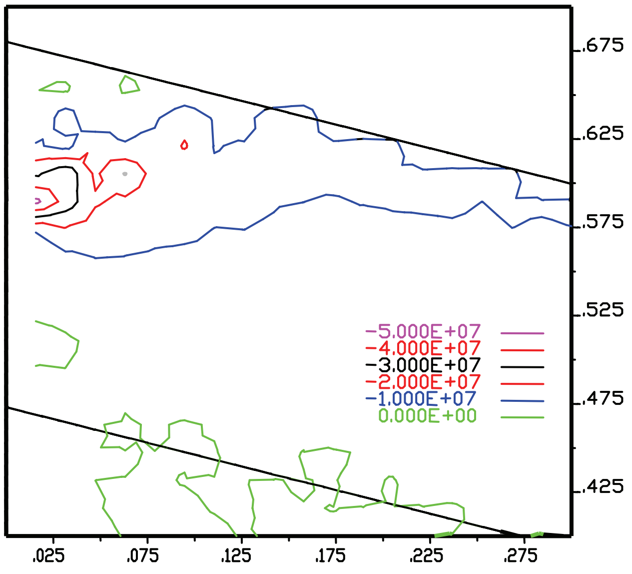

Figure 4.25 Major principal stress contour at α =15°

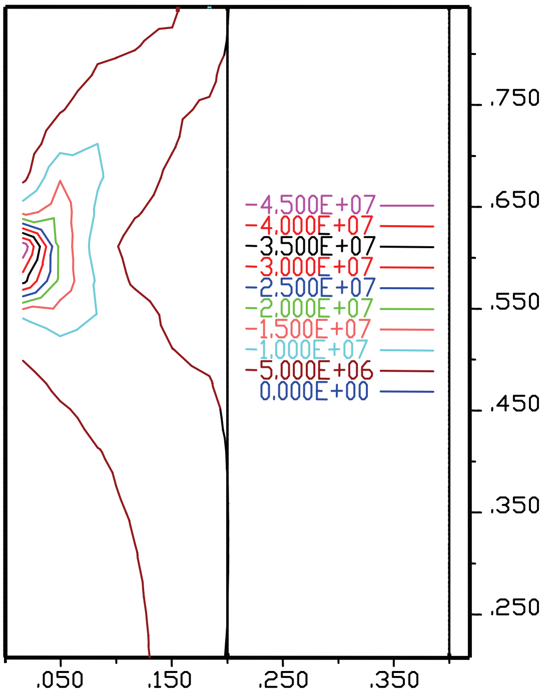

Figure 4.26 Major principal stress contour at α =90°

4.5.6 Comparisons with Field Observations

The comparisons present the correlation between the numerical simulation results and the observation results carried out in TBM tunneling projects. The simulated results are summarized in Table 4.3. The first column shows the variation of the angle α. The second column shows the stress on the cutter tip needed to fragment the rock. The third column shows the chipping zone area induced by the cutter. The fourth column shows the ratio of the chipping area to the chipping stress which denotes the yield of rock chips per unit cutter force at different α values and it indirectly stands for the TBM penetration. The fifth column shows the ratio of P_α/P_0, where, P_α denotes the penetration rate as the angle between the tunnel axis and the joint plane is equal to α and P_0 denotes the penetration rate at α = 0°. The simulated results are plotted in Figure 4.27 showing the influence of the angle α on the penetration rate. As the angle α increases, the penetration rate increases until α reaches 60°, then the penetration rate decreases with increasing α. When α is equal to 60°, the penetration rate achieves the maximum value that is more than double the penetration rate at α=0°.

Based on field studies and statistics from TBM tunneling in hard rock conditions over 250 km tunnel in more than twenty years, Bruland (1998) summarized the effects of joints including joint spacing and orientation on TBM penetration rate. The joints are divided into five classes according to the joint spacing. Then, the effects of joint orientation are given respectively for different classes of joints. When the joint spacing is equal to 200 mm that was used in the simulation, the effect of the joint orientation on the penetration rate is also plotted in Figure 4.27. As can be seen, the simulated P_α/P_0 ratio is more than 2.0 and also more than the observed results as a maximum, since it is not linear relationship between the P_α/P_0 ratio and penetration rate. But the trend of two curves is in good agreement.

Here, it should be noted that the observed results are the average values during TBM boring in a rock mass with the same average joint spacing at different angle α. The simulated results are only the instantaneous values when the cutter exerts loads on a rock mass, because the simulation mainly focuses on the mechanism of rock fragmentation induced by a TBM cutter. It does not consider the continuous boring process of the TBM and the interaction of the neighboring cutters. Moreover, the simulation is only conducted in granitic rock mass. The effects of the joint orientation on the TBM penetration should be further studied in terms of the numerical modelling of the interaction of neighboring cutters and physical modelling tests.

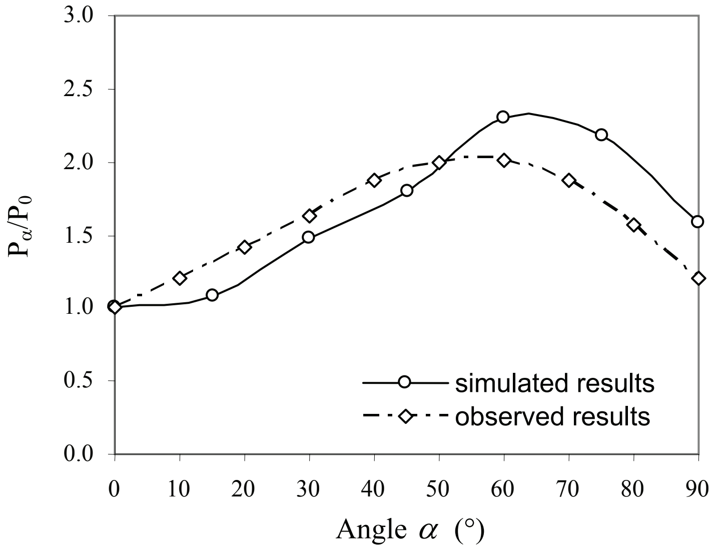

Figure 4.27 Effect of the angle α on the penetration

Table 4.3 Effect of the angle α on TBM penetration

α (°)	Chipping stress (MPa)	Chipping area (cm^2)	The ratio of chipping area to chipping stress (cm^2/MPa)	P_α/P_0
0	140	27.5	0.196	1.00
15	110	23.4	0.213	1.08
30	70	20.31	0.290	1.48
45	55	19.42	0.353	1.80
60	35	15.8	0.451	2.30
75	20	8.57	0.429	2.18
90	136	42.16	0.310	1.58

4.5.7 Conclusions

The rock chipping process induced by the TBM cutter is simulated by DEM modelling to examine the effect of joint orientation. The modelling results indicate that there are two modes of crack initiation and propagation in a jointed rock mass affected by the joint orientation. One mode is the rock fragmentation process induced by cutter indenter. As the cutter indentation increases continuously, stress is concentrated below the indenter, leading to the formation of crushed zone, initiating and propagating of cracks, chipping of rock. Because of the existence of the joint and its orientation, the crushed zones and the initiation and propagation of cracks are not symmetrical. The other mode is the occurrence of rock chipping induced by the tensile crack initiated from the joint plane. Furthermore, the joint and its orientation make the stress field deflecting to the joint plane, which leads to the variations of the rock chipping angle. The rock chipping angle increases as the angle between the tunnel axis and the joint plane increases, except when $\alpha=0°$ and 90°. The results also show that rock joint can act as a discontinuous interface for crack propagation and rock fragmentation. The modeling results conclude that the smaller the angle α, the easier the fragmentation of the rock mass occurs.

The simulated effect of the joint orientation on the TBM penetration is compared with the field observations. The variation tendency of the penetration rate due to the influence of joint orientation is in good agreement. As the angle α increases, the penetration rate increases until α reaches 60°, then the penetration rate decreases with the increase of α.

4.6 Evaluation of Effects of Rock Mass Properties on TBM Penetration Rate

The TBM penetration rate mainly depends on the rock fragmentation efficiency by TBM cutters. The rock breakage process is closely related to the machine parameters, such as the cutter line spacing, cutter diameter, total thrust and torque, and rock mass parameters, such as rock compressive strength, rock brittleness, joint spacing and orientation. The rock breakage process is composed of the rock indentation and chipping formation between the neighboring cutters. The cutter thrust, cutter spacing and diameter directly affect the rock breakage process. Only if the cutter thrust is more than the critical load, the effective rock breakage takes place. Only when the cutter spacing is optimum, the chipping formation is maximized, and then the penetration rate can reach the maximum. The machine should be designed based on the main rock mass conditions that are interpreted from the site investigation. Thus, the communications among the owner, the contractor and the manufacturer are very important for a successful project.

The numerical simulation results confirmed the rock mass properties greatly affect the rock mass fragmentation process. The rock compressive strength affects the crushed zone formation. The higher the rock strength, the larger is the required load on the cutter. Generally, with the increase of rock strength, the penetration rate decreases. The rock brittleness affects the crushed zone size and initiation and propagation of cracks in the rock indentation and formation of chips. With the increase of the rock brittleness, the failure elements increase almost linearly when the other conditions keep the same. The number of and length of cracks developed in the rock also increase. The penetration rate should increase with the rock brittleness. Due to the existence of joints in the rock mass, the stress field is changed while the rock mass is cut by TBM cutters. Furthermore, the chipping mode varies in different rock mass conditions. Thus, the joint spacing and joint orientation are very important factor influencing the penetration rate. With increasing joint spacing in the rock mass, the penetration rate decreases. The maximum penetration rate in a highly jointed rock mass is more than 9 times that in a rock mass without joints. As the angle α between tunnel axis and joint plane increases, the penetration rate increases until α reaches 60°, then the penetration rate decreases with increasing α.

The numerical simulation results are compared with the in situ measurements. The tendency shows good agreement. It is verified that the numerical simulation using UDEC correctly represents the rock mass fragmentation mechanisms by TBM cutters. Due to some limitations of the numerical simulation, the results only show the variation tendency of penetration rate in different rock mass conditions. The quantification of the effect of each rock mass parameter on the TBM penetration rate and the interaction between rock masses and TBM still needs more experimental studies and physical modeling and in situ measurements at the TBM construction site.

Based on the numerical simulation results, the main rock mass parameters influencing the TBM penetration rate are rock compressive strength, rock brittleness index, joint spacing and joint orientation. The four parameters of rock mass will be used to analyze the rock mass boreability and correlate the TBM penetration rate in the following chapters. The next chapter will introduce the collection process of the four rock mass parameters in the tunnel site and the corresponding TBM performance data. Then, a database of rock mass properties, TBM specifications, TBM operation parameters and TBM performance will be established. In Chapter 6, the rock mass boreability will be progressively analyzed. A specific rock mass boreability index is proposed to stand for the rock mass boreability. Then, a prediction model of TBM penetration rate is developed based on the database and rock mass boreability analysis. The effect of the four rock mass parameters on the penetration rate is quantified. Similarly, the actual results are also compared with the numerical results.

Chapter 5 Database of Rock Mass Properties and TBM Performance

5.1 Introduction

In Chapter 4, the influence of the main rock mass characteristics on the TBM penetration rate was summarized. A conceptual model of rock mass properties was proposed to stand for the rock mass boreability. To quantify and validate the conceptual model, significant efforts were made to collect field data from the ongoing projects, Contracts T05 and T06 of Deep Tunnel Sewerage System (DTSS), in Singapore. Furthermore, a database was established. The database includes three categories of data. The first is TBM specifications, such as TBM diameter, cutter number, cutter spacing, cutter size and shape, the designed total thrust and torque. The second is rock mass properties along the tunnel alignment, which include rock uniaxial compressive strength, rock brittleness index, joint spacing and joint orientation. The rock strength and brittleness index were obtained from laboratory tests. The joint spacing and joint orientation were derived from the tunnel face mappings performed during tunnel excavation. The third is the TBM operation and performance data corresponding to the recorded rock mass properties. These data include the applied thrust and torque, revolution per minute, penetration rate. They were automatically recorded by the TBM acquisition system.

In this Chapter, the DTSS project is summarized, with Contracts T05 and T06 highlighted. The geological conditions around T05 and T06 are described. The collection of rock mass parameters in different tunnel sections together with the TBM operation and performance information is presented.

5.2 Deep Tunnel Sewerage System Project

The Deep Tunnel Sewerage System (DTSS) project is a great ongoing infrastructure project. It is the long term solution to meet the island's needs in wastewater conveyance, treatment and disposal in Singapore. The deep tunnel intercepts the flows in existing gravity sewers, upstream of the pumping stations, and routes the flows entirely by gravity to two new centralized wastewater treatment plants located at the south-eastern and south-western coasts of Singapore. The treated effluent from the new treatment plants will be discharged through deep sea outfalls into the Straits of Singapore.

Phase one of the DTSS tunnels comprises the North tunnel and the Spur tunnel (Hulme and Burchell, 1999). The layout of DTSS is shown in Figure 5.1. The North tunnel is being constructed under five contracts (Contracts T-01 to T-05) and is approximately 38.5 km in length; with a finished diameter varying from 3.6 m to 6.0 m. Depth varies from 18 m to 50 m. The Spur tunnel (Contract T-06) is 9.6 km in length and discharges into the North tunnel. Depth of this 3.3 m finished diameter tunnel varies from 22 m to 41 m. From the geological map of Singapore shown in Figure 5.1, of all tunnels, only Contract T05, Kranji Tunnel, and Contract T06, Queensway Tunnel, which go through hard rock, will be studied.

Contract T05, Kranji Tunnel, is 12.6 km in length, with an internal diameter of 3.6 m. The Bukit Timah Granite of different weathering grades is found along the tunnel alignment, between Seletar and Kranji. It is being excavated by two EPB TBMs with a diameter of 4.82 m manufactured by Herrenknecht AG. The specifications of the machines would be introduced in Section 5.4. Precast segments are installed as initial ground support. A final concrete lining is required with a corrosion-resistant membrane.

Contract T06, Queensway Tunnel, is 9.6 km in length, with an internal diameter 3.3 m. The Bukit Timah granite of different weathering grades is found along most of the tunnel alignment. The Jurong Formation of interbedded, highly variable and mostly fractured mudstone, siltstone, sandstone, and conglomerate rocks is found in

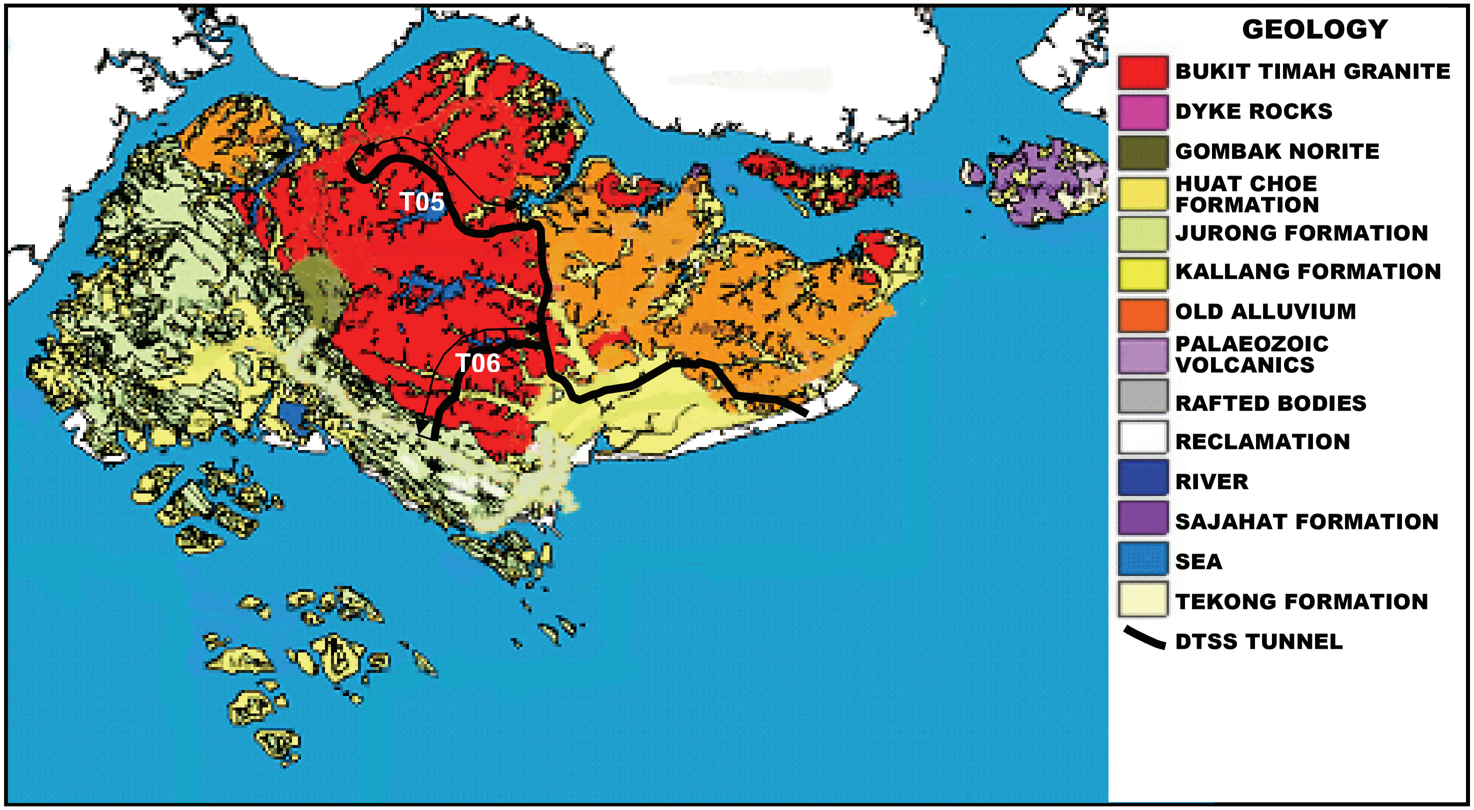

Figure 5.1 Layout of the DTSS project and a simple geological map of Singapore

a limited section (south end) of the tunnel. The Old Alluvium that consists of indistinctly bedded sandy clay or clayey sand with a very stiff to very dense consistency is found in the north end of the tunnel, as shown in Figure 5.1. It is constructed by two EPB TBMs also manufactured by Herrenknecht AG with a diameter of 4.45 m. The specifications of the machines would also be introduced in Section 5.4. Precast segments are also installed as initial ground support. A final concrete lining is required with a corrosion-resistant membrane.

5.3 Geological Conditions

5.3.1 Regional Geology

Singapore lies close to the southern extremity of the Eurasian tectonic plate and just north of the Java Trench which is part of the northerly termination of the Indian Plate. In the geological history, Singapore has come under the influence of this convergent plate boundary. But now it is migrating southwards, away from Singapore (Pitts, 1984a). Singapore is located at the southern tip of the Malay Peninsula and is structurally an integral part of it. The most common structural trend of the region is NW direction. It is indicated by the main fold axes and many of the faults in Jurong Formation and Bukit Timah granite (Zhao et al., 1995 and 1999). Results of the stress measurements in Bukit Timah granite show that the maximum horizontal in situ stress is in the direction of NNE-SSW (Zhao et al., 2005). This direction of maximum horizontal stress is in agreement with local geological setting. The ratio of $\sigma_v:\sigma_h:\sigma_H$ is approximately 1:2:3.

The strata of Singapore can be broadly divided into four main types: (a) the igneous rocks, consisting of the Bukit Timah granite and the Gombak norite in the north and central north; (b) the sedimentary rocks of the Jurong Formation in the west and southwest; (c) the Quaternary deposits of the Old Alluvium in the east; and (d) recent deposits of the Kallang Formation of the alluvium member, the transitional member and marine clay distributed throughout the island. Other less common geological formations in Singapore are: the Sajahat Formation consisting of well lithified quartzite, quartz sandstone, and argillite; the Tekong Formation consisting of a thin sequence of mainly sands and gravels of littoral and fluvial origin (PWD, 1976; Pitts, 1984b; Sharma et al., 1999). A simplified geological map is shown in Figure 5.1.

5.3.2 Geological Features around the Tunnel Site

The dominant bedrock in the T05 and T06 tunnel site includes the Bukit Timah granite and Jurong Formation. The Bukit Timah granite is an acidic igneous rock formed during the Triassic period. The Bukit Timah granite includes entire suite of acid rocks ranging from granite, adamellite and granodiorite. There is considerable hybridization resulting from the assimilation of basic rock within the formation. In some sites, the granodiorite was observed to be foliated. The granite is generally light grey and medium grained. The grain size ranges from 0.5 mm to 5 mm. Nevertheless the pink variety of orthoclase is also present. The main minerals include quartz, feldspar, biotite and hornblende. Quartz constitutes about 30% of the rock with a glassy grey appearance and a rough surface. Feldspar is the most abundant mineral and constitutes 60% to 65% of the rock. Its color commonly is cream with the more weathered ones being pale to brownish yellow (PWD, 1976).

Generally, there are three to four sets of joints in the granite rock masses with predominantly sub-vertical joint sets, accompanied by a sub-horizontal set. The strike of the dominant sub-vertical joint set is NNW-SSE, with secondary set at NNE-SSW and third set at NW-SE (Zhao et al., 1995; Zhao, 1996). The joints are widely spaced, and the surfaces of the joints are generally planar, closed and rough.

The weathering of the Bukit Timah granite was studied in details at Mandai area by Zhao et al. (1994a, 1994b). The weathering grades for Bukit Timah granite and rock mass are classified as shown in Table 5.1. The weathering is rapid and is primarily due to chemical decomposition under humid tropical climate in Singapore. The maximum depth of the residual soil at low lying areas is up to 70 m and in most areas the range is 20-50 m. Major penetration of weathering below the general zonal boundaries is usually limited to a few large joints and faults. The weathering of the Bukit Timah granite is mainly stratified and with a sharp boundary between the residual soil and the slightly to moderately weathered granite. The highly weathered layers are commonly left out (Zhao et al., 1994a and 1994b). However, the weathering profile found in the Mandai area is not necessary representative of other areas of the Bukit Timah granite. Core boulders were reported in the weathered granite during the construction of the Bukit Timah Expressway and also found in the Serangoon area (Shirlaw et al., 2000). The rock strength decreases significantly with increasing weathering. The moderately weathered granite loses 40-60% of its original strength. Due to variations in topography, the nature of the granite rock and structural features, uneven penetration of weathering can lead to very sudden changes in ground conditions, which can be particularly problematic for tunnelling. The weathered rock mass permeability values are much higher than the expected based on fines content (Shirlaw et al., 2000; Valle, 2001).

The age of Jurong Formation is deduced to be mid-Triassic to early Jurassic (PWD, 1976). The deposits are in part marine and in part terrestrial. The transitional nature of the depositional environments results in a wide variety of clastic sedimentary rock types from fine grained mudstone to coarse bouldery conglomerate, and carbonate rocks as well. Their bulk mineral composition includes quartz grains, clay minerals, feldspars and other altered igneous rock minerals. The Jurong Formation has undergone severe tectonism. A variety of folds developed in the Jurong Formation with the strike direction NE. Two sets of approximate perpendicular "thin-skin" faults were found in the Jurong Formation with the strike from NNE-SSW to NE-SW and NW-SE respectively. The weathering is intensive in Jurong Formation. Generally, the depth of the residual soils ranges from a few meters to 50 m. When assisted by a well-developed system of interconnecting fractures, the weathering depth can reach more than 100 m below surface (Zhao et al., 1999).

Table 5.1 Proposed weathering scheme for Bukit Timah granite material (After Zhao et al., 1994a)

Weathering class	Grade	Geological description of rock material from core Description of rock block	Strength indexes			
			σ_c	I_{s50}	S	P
Fresh granite (F)	I	All material constituents are sound. Feldspar cannot be scratched with knife. Material is fresh or slightly weathered. Many blows of geological hammer are required to fracture the rock. Surface of rock block is fresh or slightly weathered	>180	> 8	> 60	-
Slightly weathered (SW)	II	Plagioclases are occasionally slightly decomposed. Biotites are slightly decomposed, begin to stain the surrounding. Slightly weaker than the fresh rock. Rock block inner material is slightly weathered; block surface material is slightly or moderately weathered.	110~ 180	5~8	40~ 60	-
Moderately weathered (MW)	III	Most of plagioclases and some potash feldspars are moderately decomposed. Biotites are moderately decomposed, staining the surrounding. Feldspars can be scratched with a knife. Sample can be fractured by a single firm blow with a geological hammer. Core cannot be broken by hand. Considerably weaker than the fresh rock. Rock block inner material is moderately weathered; surface material is moderately or highly weathered, occasionally completely weathered.	50~ 110	2~5	20~ 40	-
Highly weathered (HW)	IV	All plagioclases are highly decomposed. Most potash feldspars are moderately decomposed. Biotites are highly decomposed staining most of the rock. Feldspars can be broken by hand with difficulty. Can be excavated with a spade with great difficulty. Significantly weaker than the fresh rock. Rock block inner material is highly weathered; surface material is highly or completely weathered, occasionally residual soil.	< 50	< 2	< 20	> 15
Completely weathered (CW)	V	All plagioclases and most of potash feldspars and biotites are completely weathered. Original texture present. Feldspars can be readily peeled by a knife. Can be excavated by hand with some effort. Cannot be indented by thumb. Very low strength compared with fresh rock. Most of rock block material completely weathered.	< 1	-	-	< 15
Residual soil (RS)	VI	Feldspars and biotites are completely decomposed (clayey). Original textures are absent. Samples can be indented by thumb with moderate effort. Can be easily excavated by hand. Very low strength compared with the fresh rock.	< 1	-	-	-

Note: σ_c denotes uniaxial compressive strength, MPa; S denotes Schmidt rebound hardness index; I_{s50} denotes point load index, MPa; P denotes hand penetrometer index.

5.3.3 Geotechnical Investigation

Both the geophysical method and boreholes were used to investigate the site geotechnical conditions. Seismic reflection survey was carried out to explore the thickness of the overburden layers and the subsurface structures along the T05 and T06 tunnel alignment. Electric resistivity survey was locally performed to confirm the existence of some faults and fractured zones. A total number of 49 and 43 boreholes were respectively drilled to provide the site information in T05 and T06 besides the geotechnical data obtained from the vicinity project sites. These boreholes are approximately evenly distributed along the tunnel alignment.

The T05 tunnel goes through Bukit Timah granite with different weathering grades and its residual soil. In order to conveniently apply to rock engineering, the weathering grades of granite are simply divided into four grades in site investigation in Singapore, as listed in Table 5.2. Along the whole 12.5 km length of the tunnel alignment, the predominant ground is fresh to slightly weathered granite (G1). It covers 47 percent of the total tunnel length. Approximately 3.2 m is in completely weathered granite to residual soil (G4), 1.9 km in mixed face ground where the hard rock and soil emerge in the same tunnel face and 1.6 km in moderately to highly weathered granite (G2), as shown in Figure 5.2.

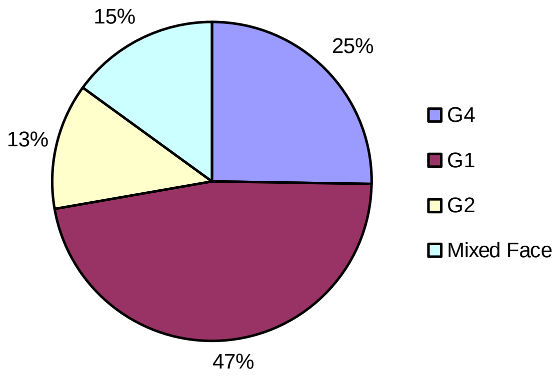

Figure 5.2 Ground condition along T05 tunnel alignment

Along the whole 9.6 km length of the T06 tunnel alignment, the predominant geological formation is the Bukit Timah granite with different weathering grades, as shown in Figure 5.3. Approximately 77% or 7.45 km of the tunnel is located in this formation. Of this section, 3.33 km is in moderately fractured and slightly weathered to fresh granite (G1) or highly fractured and highly to moderately weathered granite (G2), 3.05 km in completely weathered granite to residual soil (G4). The remainder 1.07 km is located in mixed face ground. About 0.91 km of the last southern section of the tunnel is located in multilayer sedimentary rock (Jurong Formation) consisting of interbedded sandstone, siltstone and mudstone, residual soil to completely weathered rock and mixed face ground. About 1.1 km of the last north section of the tunnel is located in the weathered to unweathered Old Alluvium.

Table 5.2 Granite rock and soil types

Geological formation	Rock and soil type	General description
Bukit Timah Granite	G1	Fresh to slightly weathered, fair to moderately fractured rock mass. (Weathering Grade I & II)
	G2	Moderately to highly weathered, highly fractured rock mass. (Weathering Grades III & IV)
	G3	Bouldery soil: Boulders of variable size and weathering within completely weathered material or residual soil
	G4	Completely weathered rock or residual soil. (Weathering Grades V & VI)

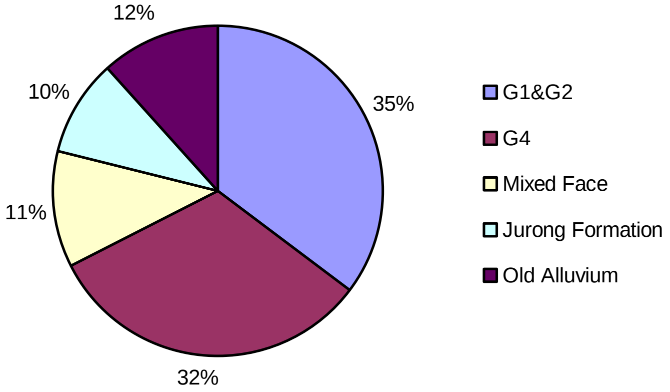

Figure 5.3 Ground condition along T06 tunnel alignment

It is necessary to note that tunneling in mixed face conditions of granite and soil like material, particularly in soil of high silt content, can present difficulties of the TBM in terms of ground water ingress, soil erosion and subsequent localized surface settlement troughs.

The mineralogical content of granite and diorite was analyzed based on the core sample for each rock type. The results are summarized in Table 5.3. The granite content is consistent with the previous experiment results conducted by PWD (1976). The Cerchar abrasivity index (CAI) of the granite is summarized in Table 5.4 based on the rock core samples. All the results show that the CAI is more than 4.0, and the rock is classified as extremely abrasive in accordance to the Cerchar definition. The rock samples were also taken to conduct the strength tests. The test results are summarized in Table 5.5. The rock strength varies in a large range in weathering grades I and II. The results are not consistent with the general granite weathering classification in Singapore (Zhao et al., 1994a). It shows that the rock classification at the site is too rough or the rock may fail along weak planes in the rock strength test.

Table 5.3 Mineralogy of the Bukit Timah granite

Mineral type	Diorite (dark grey fine grained)	Granite (light grey coarse grained)
Feldspar	57.1% (plagioclase)	57.8-64.5% (plagioclase + k-feldspar)
Amphibole (green hornblende)	22.4%	0.6-4.1%
Quartz	10.3%	26.4-29.2%
Mica (biotite & some chlotite)	8.8%	5.3-7.0%
Calcite (mostly vein)		0.2-6.4%
Others	1.4%	0.2-5.0%

Table 5.4 Results of abrasivity testing on the Bukit Timah granite

Borehole No.	Depth (m)	Geotechnical unit	Rock type	RQD	Cerchar abrasivity index (CAI)
NR-8 (T06)	40.5	G1	Granite	95	4.78
NR-8 (T06)	43.6	G1	Granite	43	5.24
NR-9 (T06)	51.0	G1/G2	Granite	27	4.72
G-106 (T05)	25.0	G1	Diorite	100	4.53
H-108 (T05)	53.75	G1	Granite	100	4.44

*the rock classified as extremely abrasive in accordance to the Cerchar definition.

Table 5.5 Laboratory rock strength test results of cored samples

Rock type	Geotechnical unit	Fracture index*	RQD	UCS (MPa)		Point Load test (I_{s50}, MPa)	
				Range	Ave.	Range	Ave.
Bukit Timah granite	G1	>32~2	0~94	19~209	85	1.2~14.5	7
	G2	>16	0~25	-	51	0.7~5.1	1.8
Jurong Formation	Siltstone, shale and Mudstone (Fresh to highly weathered)	6~16	10~59	17~28	23	0.6~1.2	1.0

*Fracture index is defined by the number of discontinuities per meter.

A number of faults and fractured zones have been identified in the seismic reflection profiling. The locations of these faults and fractures are listed in the following.

CH52+800 and 54+800, Nee Soon Fault

CH58+000, Sembawang Fault

CH58+900, Un-named Fault

CH61+000, Un-named Fault

CH78+100–Local fractured zone (along Farrer Road, near location of the HDB flat)

CH77+300–Fault (along Farrer Road, near to Bukit Timah junction)

CH74+525–Fault (along Lornie Road, in the vicinity of Access Shaft R3)

CH73+200–Local fractured zone (near Lornie Road / Marymount junction)

CH72+350–Local fractured zone (along Braddell Road, well below tunnel alignment)

The site investigation gave us an overall image of the ground condition along the tunnel alignment. The detailed rock mass properties cannot be interpreted from the geotechnical investigation reports due to the nature of granite weathering in the tropical weather. The rock head is generally a few meters below the ground surface. The joint system developed in the rock mass cannot be observed in the outcrops. In order to establish an elaborate database for the penetration rate prediction, and study the effect of rock mass properties on the TBM penetration rate, a comprehensive program for obtaining the joint properties and rock strength parameters was performed during the tunnel construction.

5.4 TBM Specifications

5.4.1 TBMs for T05

TBMs used in T05, Kranji Tunnel, are two hard rock type shield machines manufactured by Herrenknecht AG, as shown in Figure 5.4. They can be operated in earth pressure balanced mode (EPB mode). The outer diameter of the TBMs is 4880 mm with a total length of 110 m. The maximum tunneling speed is 90 mm/min. The shield comprises three main sections, namely front shield, center and airlock shield, and tail shield. The length of the three sections is 2950 mm, 5335 mm and 3900 mm respectively. Two articulations are designed for steering, one between the front shield and the center shield, another between center shield and rear skin. To prevent vibration during open mode excavation, stabilizers are provided in the front shield. For stabilization of the rear shield, gripper pads are installed in the center shield. Table 5.6 summarizes machine dimensions, components and operating characteristics.

Because the TBM cutterhead is designed for hard rock cutting and soft ground scraping, it is equipped with hard rock single and double cutters and soft ground drag bits, as shown in Figure 5.5. Disc cutters and ripper teeth are exchangeable and all cutting tools can be installed and changed inside the cutterhead chamber. The line spacing of the face cutter is about 100 mm. The cutterhead is driven by 5 motors with variable speed of rotation in both directions. 2×10 thrust jacks acting on concrete lining segments provide a total thrust up to 26600 kN. The propulsion cylinders with a stroke of 2300 mm can be operated individually or in groups. The screw conveyor transports the muck from the excavation chamber to the discharge point. In open mode operation, it has to handle granite chips. The screw spiral of the screw conveyor is equipped with wear plates which can be changed quickly if required. Then, the conveyor belt system transports the mucks from the discharge point of the screw conveyor to the loading point of the muck cars at the end of the backup system. The backup system consists of portal trailers, running on the segment and self aligning wheel bogies with vulculan wheel sets supporting the individual units. The backup equipment is towed by the TBM through hydraulic cylinders. The free space of the portal cars allows the trains to enter into the backup section and unload the segments and the grout tank.

All important operation parameters of the TBM can be monitored by an acquisition and recording system. Data readout and data reporting are carried out by a computer. Some of the major parameters recorded are:

- Face pressure;
- Thrust force;
- Steering force;
- Backup towing loads;
- Revolution per minute;
- Advance speed;
- Time for advance;
- Volume of excavated material via belt weighter;
- Segment placing and standby/stoppage;
- Some other system operating data.

Table 5.6 Summary of dimensions, components, and operating characteristics of the T05 S170, S171 TBMs

Manufacturer	Herrenknecht AG	
Model Number	S170, S171	
Tunnelling system	Max. operation pressure	4.5 bar
	Outside diameter of the shield	4,880 mm
	Outside length incl. back-up	110 m
	Total weight	430 ton
	Max. tunneling speed	90 mm/min
Shield	Total shield length without cutter head	12,185 mm
	Total weight shield	Ca. 250 Ton
Front shield	Outside diameter without hard facing	4,880 mm
	Length of front shield	ca. 2,950 mm
Tailskin	Outside diameter	4,850 mm
	Length	ca. 3,900 mm
Cutterhead	Diameter	4,930 mm
	Weight	ca. 50.0 ton
	Number of cutter tools	12 pcs
	Number of single cutter discs	23 pcs
	Number of double cutter discs	6 pcs
	Track distribution of the cutter discs	33 tracks
	Track distance	100 mm
	Diameter of cutter discs	17 inch
	Width cutter discs	¾ inch
	Max. load per cutter disc	25 ton
Thrust system	Thrust cylinders	220/180 mm
	Thrust cylinder stroke	2,300 mm
	Number of thrust cylinders	2*10 pcs
	Steering cylinders	280/200 mm
	Cylinder stroke	300 mm
	Number of cylinders	2*4 pcs
	Force per cylinder	2,150 kN
	Total tensile force (at 350 bar)	17,230 kN
Torque system	Installed power (6*250 kW)	1500 kW
	Available power	1350 kW
	Speed range	0-10.19 U/min
	Starting torque/initial breakaway torque	3137 kNm

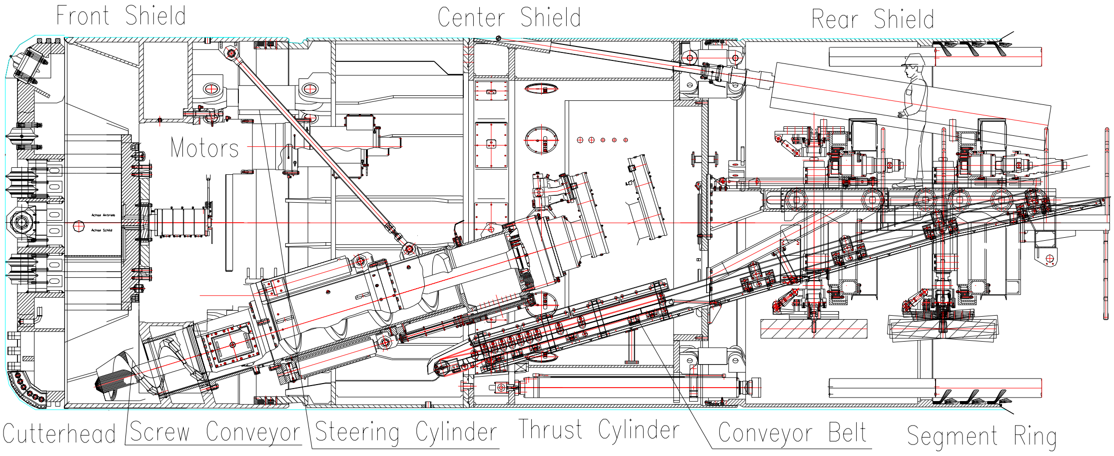

Figure 5.4 Profile of the TBMs used in T05

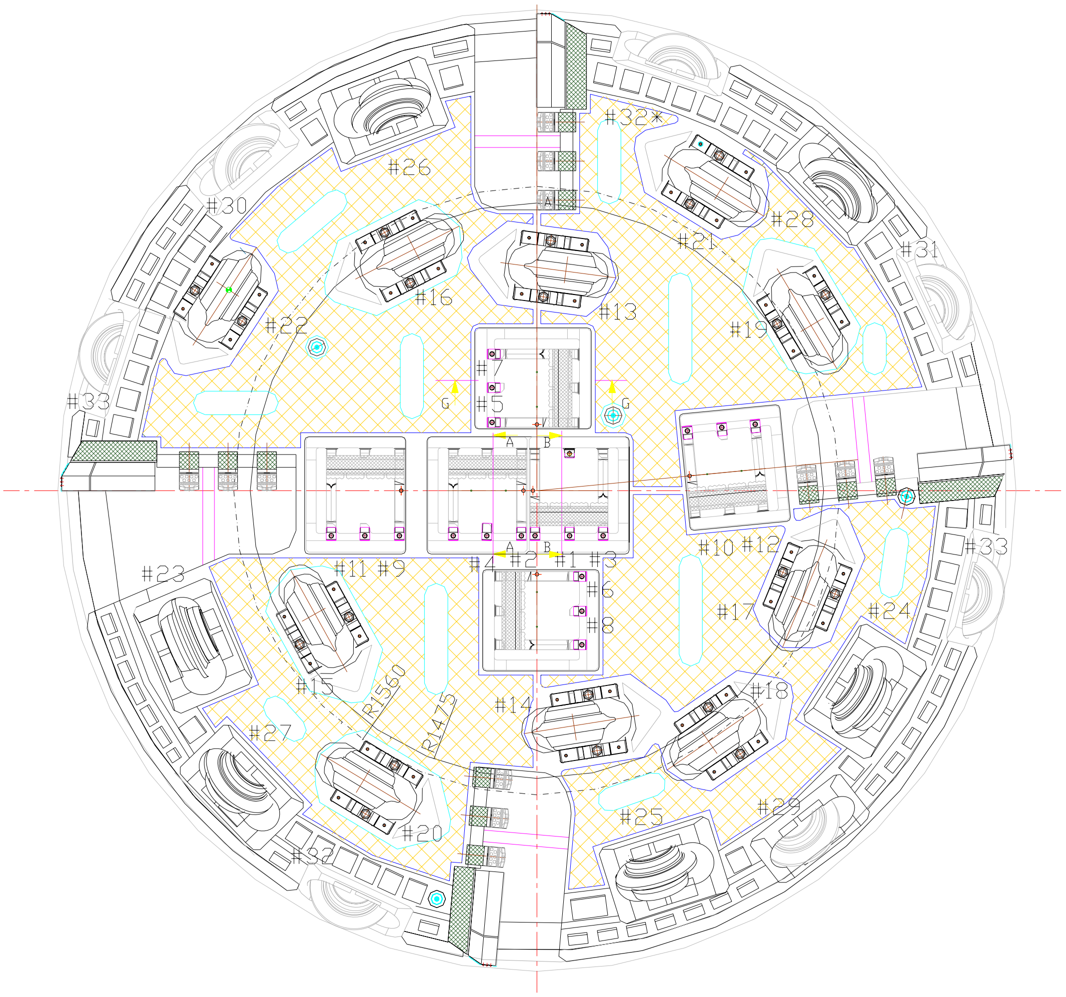

Figure 5.5 TBM Cutterhead used in T05

5.4.2 TBMs for T06

Due to the similarity of the excavated ground conditions with T05, the TBMs used in T06 are similar to these used in T05. The dimensions, components and operating characteristics of those TBMs are summarized in Table 5.7.

Table 5.7 Summary of dimensions, components, and operating characteristics of the T06 S177, S178 TBMs

Manufacturer Model number	Herrenknecht S177, S178	
Tunnelling system	Diameter	4,450 mm
	Overall shield length	12.285 m
	Shield weight	Approx. 200 tons
	Total thrust force	22,608 kN
	Cutterhead torque max.	2,596 kNm
	Max. tunneling speed of the machine	100 mm/min
	Max. operating air pressure	4.5 bar
Cutterhead	Outer diameter (min)	4,500 mm (with new disc cutters)
	Length	Approx. 1,600 mm
	Weight	Approx. 50 tons
	Opening surface	Approx. 12%
	Number of single cutter discs	19 pcs
	Number of double cutter discs	5 pcs
	Track distribution of the cutter discs	29
	Track distance	Approx. 90 mm
	Diameter of cutter discs	431.8 mm
	Width cutter discs	19.0 mm and 24 mm (gauge cutter)
Torque system	Drive motors	5
	Drive motor rating	250 kW
	Nominal torque	1,731 kNm
	Max. torque	2,596 kNm
	Cutterhead speeds	0~9.75
Thrust system	Thrust cylinder numbers	2*12
	Cylinder diameter	200 mm
	Stroke length	2300 mm
	Maximum pressure per cylinder	942 kN
	Steering cylinder numbers	8
	Cylinder diameter	240 mm
	Stroke length	300 mm
	Maximum pressure per cylinder	1, 357 kN

5.5 Rock Mass Joint System

The above sections present the regional geology, general site geotechnical conditions and TBM specifications for tunneling. Due to intensive weathering of the bedrocks, rock exposures are hardly observed except at the rock quarries. The statistics of the joint system (including all discontinuities, such as joints, fissures, factures and cracks and so on) in the rock mass cannot be conducted in the ground surface. Because the joint system within rock masses extensively affects the rock mass fragmentation process, it influences the TBM penetration rate to a large extent. Its effect is analyzed in the Chapter 4. In order to relate the rock mass conditions to the TBM penetration rate, the tunnel face mapping was conducted during tunnel excavation. The purposes of face mapping are as follows:

- To provide accurate geological information for evaluating the rock mass boreability.
- To evaluate the TBM performance in different rock mass conditions.
- With the shield friction tests, penetration tests, and chips sieve tests, to optimize the TBM operation in different rock mass conditions in order to improve TBM penetration rate and reduce cutter wear.
- By comparing information from face mapping with the data from geological investigation, the experience and lessons can be further used for future project planning and construction.

5.5.1 Tunnel Face Mapping

As full observations of the rock mass conditions were not possible due to immediate installation of segmental lining, the tunnel face mapping was carried out in the TBM cutterhead chamber. During the cutter inspection and cutter replacement, the cutterhead chamber is opened. It gives us a chance to survey the rock mass conditions in the tunnel face. Before the observation, the rock powder and fragments at the tunnel face was washed out. Then, the tunnel face can be mapped through the four openings used for the conveyance of the mucks. The tunnel face mapping includes the information as follows.

- Rock name, for example, granite;
- Color;
- Rock weathering grade, for example, fresh, slightly weathered, moderately weathered, and highly weathered;
- Joint descriptions: number of joint sets, approximate joint length in the tunnel face, joint aperture, joint alteration;
- Measurements of joint sets: for each joint set, the joint spacing the angle between the tunnel axis and the joint plane must be estimated for each joint set;
- Estimation of RQD in the tunnel face: one meter rule used for the measurement of RQD at the same tunnel face position and direction, RQD and fracture number are recorded to complement the joint spacing in the face mapping;
- Water inflow from the tunnel face (L/second).

The record of a joint system is explained by Figure 5.6 as an example. There are two joint sets plus one random joint. Joint set 1 includes joints ①, ②, ③, and the spacing is about 100 cm. The average length of the joint set is about 150 cm. The angle α between joint plane and tunnel face is 45°. In a similar way, the second joint set and the random joint can also be described. Then, the photos are taken through the four openings evenly distributed in the cutterhead for further check. Some muck samples are also taken from the cutterhead chamber for rock identification in the site office.

In order to continuously record the various rock mass conditions encountered by TBM, the face mapping and muck sampling were frequently conducted. During the tunnel construction, tunnel face mapping and mucks sampling or rock core sampling at the same tunnel face were carried out about once per 30~50 m or when the TBM performance changes dramatically under the same operation conditions, for example, the thrust suddenly decreases or increases. An example of tunnel face mapping is shown in Figure 5.7. The corresponding photos taken during tunnel face mapping are shown in Figures 5.8 and 5.9.

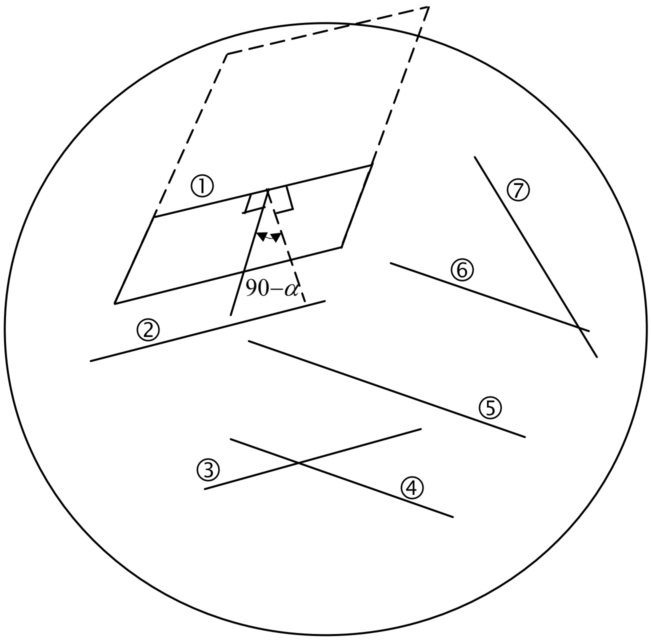

Figure 5.6 Tunnel face mapping requirement

In total, more than 80 tunnel face mappings were taken in T05 and T06 tunnels by the author. The rock mass conditions vary from fresh granite rock mass to very closely fractured and highly weathered rock mass. A few mixed faces were also recorded. Although these face mappings for mixed face ground conditions were not used to set up the rock mass characteristic model for the penetration rate prediction in the study, they would be very useful for further study of the effect of mixed face on the TBM performance. Due to time limit, the rock core samples were not taken for some rings. Thus, the rock mass properties for these rings were not complete for analyzing the TBM penetration rate. At last, about 50 face mapping data were used to establish the rock mass properties database.

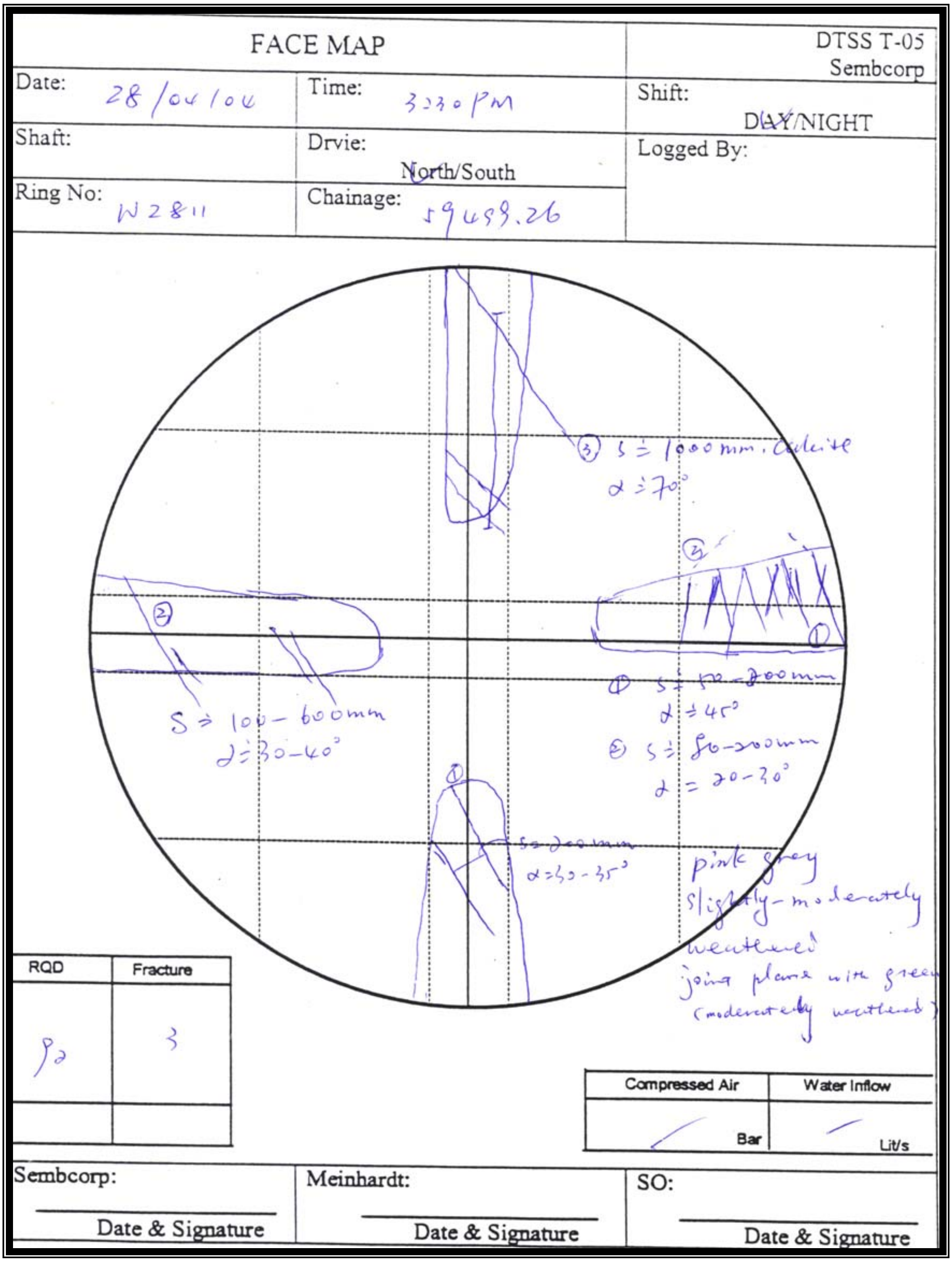

FACE MAP

DTSS T-05
Sembcorp

Date: 28/04/04
Time: 3:30 PM
Shift: ~~DAY~~/NIGHT
Shaft:
Drvie: North/South
Logged By:
Ring No: W2811
Chainage: 59459.26

③ S ≑ 1000 mm. Calcite
α ≑ 70°

②

①

② S ≑ 100 – 600 mm
α ≑ 30 – 40°

① S ≑ 50 – 200 mm
α ≑ 45°
② S ≑ 50 – 200 mm
α = 20 – 30°

①
S = 200 mm
α = 30 – 35°

pink grey
slightly – moderately weathered
joint plane with green (moderately weathered)

RQD	Fracture
90	3

Compressed Air	Water Inflow
Bar	Lit/s

Sembcorp:
Date & Signature

Meinhardt:
Date & Signature

SO:
Date & Signature

Figure 5.7 Tunnel face map of North Ring 2811 in T05

Figure 5.8 Photo taken from the upper left opening of North Ring 2811 in T05

Figure 5.9 Photo taken from the upper right opening of North Ring 2811 in T05

5.5.2 Joint Spacing

Joint spacing is an important rock mass parameter that influences the TBM penetration rate, as analyzed in Chapter 4. Joint spacing is the separation between the adjacent joints. It can be represented by RQD, joint frequency and volumetric joint count. For a particular set of joints, joint normal spacing, the mean perpendicular distance between the adjacent joints, is usually used to express the joint spacing (Brady and Brown, 1985). In practice, joint spacing is measured along a specific direction (scan line) for all discontinuities and represented by the mean spacing of all discontinuities along the scan line. Joint spacing is regarded as a classification parameter in many existing rock mass classification systems (e.g. Barton et al., 1974; Bieniawski, 1973; Palmstrom, 1996a and 1996b).

The rock quality designation (RQD) was first proposed by Deere (1963) to provide a quantitative estimate of rock mass quality from drill core logs. It is defined as the percentage of intact core pieces longer than 100 mm in the total length of core. The core should be at least NX size and should be drilled with a double tube core barrel. RQD is an easy and quick measurement of the degree of jointing along the core drill hole. RQD gives an average degree of jointing along the actual section.

Priest and Hudson (1976) found that an estimate of RQD could be obtained from discontinuity spacing measurements made on core or outcrop exposure using Equation (5.1).

$$RQD = 100e^{-0.1\lambda}(0.1\lambda + 1) \tag{5.1}$$

where λ is the discontinuity frequency, which is the number of fractures per meter, and the reciprocal of the mean spacing. For values of λ in the range 6 to 16/m, a good approximation to measured RQD values was found to be given by the linear relation, as shown in Equation (5.2)

$$RQD = 110.4 - 3.68\lambda \tag{5.2}$$

The volumetric joint count (J_v) is defined as the sum of the number of joints per cubic meter for each joint set present (ISRM, 1981; Palmstrom, 1982). According to this definition, Equation (5.3) is derived. It takes into account all the joints and fractures encountered.

$$J_v = \sum \left(1/J_{si} \right) + N_{r(5)} or N_{r(10)}/5 \tag{5.3}$$

where J_{si} is the joint spacing in meters for the actual joint set; $N_{r(5)}$ or $N_{r(10)}$ is the number of random joints along 5 or 10 m perpendicular sampling lines.

Because the installation of segmental lining prevents the observation of the tunnel wall, the scan line measurement along the tunnel wall is not possible. Only the tunnel face can be surveyed during cutter inspection and replacement. Due to the limited space in the TBM cutterhead chamber, only the joint sets and its spacing are recorded during tunnel face mapping. Thus, the volumetric joint number can be derived from the tunnel face mappings. The joint spacing is hereafter denoted by the volumetric joint number that would be used to set up the TBM penetration rate prediction model.

5.5.3 Joint Orientation

Joint orientation is another important factor affecting the performance of TBM. The penetration rate changes with the angle between the tunnel axis and the joint plane. According to the analysis in Chapter 4, the most favorable angle for TBM excavation is about 60°. The influence of the angle on penetration rate shows a certain tendency.

Usually, a rock mass contains several major sets of joints plus some random joints. Each joint set may have different effects on the TBM penetration rate. The higher the joint density or frequency, the larger the effect of the joint set on the TBM penetration rate. Therefore, the orientation of the most frequent joint or the closest spaced joint set would be considered to set up the penetration rate prediction model.

The angle (α) between the tunnel axis and the joint plane can be determined from the tunnel face mapping.

5.6 Intact Rock Test

Together with the joint spacing and orientation recorded in the tunnel face mapping, rock mechanical property tests were conducted to establish a database in order to evaluate the rock mass boreability. These mechanical tests included rock uniaxial compressive strength (UCS), Brazilian tensile strength (BT) and point load tests. UCS is regarded as an independent parameter in the database. Brazilian tensile strength is used to decide the rock brittleness index. In some rings, the core samples are not available. The point load strength is regarded as a substitute of the UCS. The following section introduces the field rock coring program and experimental procedures.

5.6.1 Field Rock Coring Program

In order to identify the rock mass conditions, the core rock samples at the mapping tunnel face were taken by drilling during the tunnel face mapping period. Due to the limited space in the cutterhead chamber, a drilling machine with a small inner diameter of 34 mm was used for core rock sampling. The drilling process is described as follows:

- Fix the drilling machine in the cutterhead, as shown in Figure 5.10a.
- Rotate the cutterhead to select a suitable location, in order to avoid the joints and its weathered zones, as shown in Figure 5.10b.
- Take the rock sample from the machine, as shown in Figure 5.10c.
- Repeat the above process to obtain enough core samples.

The rock samples must be enough to conduct three uniaxial compressive strength tests and five Brazilian tensile strength tests. Because coring at tunnel face was a time-consuming process, sampling in some rings was carried out in the tunnel wall during the machine maintenance in order not to affect the project progress. Since sampling was designed to conduct in the mapped tunnel face, the frequency of sampling would be the same with the tunnel face mapping. Thus, the rock mass conditions are completely recorded. But, in some rings, core samples were very difficult to obtain due to highly weathered and fractured rock mass conditions. Only hand rock samples were taken from the cutterhead chamber.

(a) Fix the drilling machine (b) choose a suitable position

(c) Retract the machine to get the sample (d) Rock samples

Figure 5.10 Rock sample coring in the tunnel face

5.6.2 Uniaxial Compressive Strength Test

Uniaxial compressive strength is one of the most basic rock strength parameters for rock mass condition evaluation. It is commonly used to assess rock mass boreability. The uniaxial compressive strength tests were performed in accordance with the procedure recommended in ISRM standard (Brown, 1981). The samples were prepared to satisfy the requirements of the standard. A ratio between length, *l*, and diameter, *d*, of the sample is mostly 2.5 and some range from 2 to 2.5 in light of the core sample length. Four strain gauges were attached to the samples with two for measuring radial strain and the other two for axial strain. General procedure was as follows:

- Samples were first measured using vernier caliper.
- Samples were cut to the desired length from a cored sample using an abrasive cutter machine as shown in Figure 5.11.
- Top and bottom of samples were then grinded (Figure 5.12) to achieve a smooth and flat surface for platen loading.
- Four strain gauges, two for axial and two for radial strain measurements were attached to the centre of the samples in the longitudinal direction (Figure 5.12).

Figure 5.11 Sample cutting and grinding

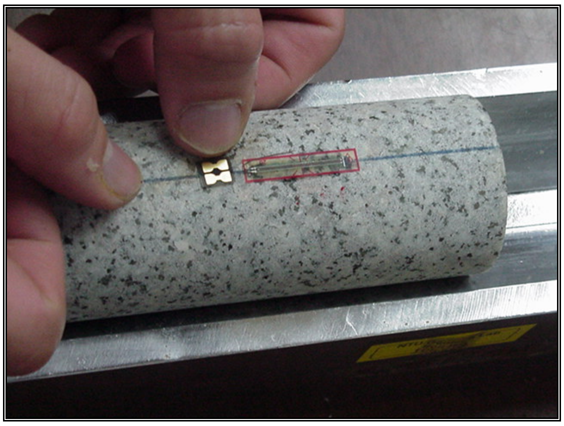

Figure 5.12 Attaching of strain gauge

UCS measurements were made using an electronic servo controlled Stiff Test System STS-1000 with a capacity of 1100 kN. It was manufactured by Structural Behaviour Engineering Laboratories, Inc. (SBEL) in United States. It is designed for static and dynamic closed-loop operation and is capable of performing strain or stress controlled as well as post failure behaviour type test. It comprises a four-columns testing frame, load cell, servo controlled hydraulic actuator and triaxial cell as shown in Figure 5.13. Loading data and other test parameters were recorded with a computer based data acquisition system for further analysis. The loading rate used in the tests is 1.0 MPa per second.

The uniaxial compressive strength of the specimen is calculated by dividing the maximum load carried by the specimen during the test, by the original cross-sectional area.

$$\sigma_c = \frac{P}{A_o} \quad (MPa) \tag{5.4}$$

Because of the limited space in the cutterhead chamber, the rock sample diameter is not the standard size, 50 mm. Thus, the measured UCS is corrected to a diameter 50 mm, using the following equation proposed by Hoek and Brown (1997).

Figure 5.13 STS-1000 machine used for compressive strength testing

$$\sigma_{c50} = \sigma_{cd}\left(\frac{50}{d}\right)^{-0.18} \tag{5.5}$$

where σ_{cd} is the uniaxial compressive strength of a rock specimen with a diameter of d mm, σ_{c50} is the compressive strength of a 50 mm diameter sample.

5.6.3 Rock Brittleness Index

Rock brittleness index was discussed in details in Chapter 4. In this study, the brittleness index is defined to be the ratio of the uniaxial compressive strength to Brazilian tensile strength. It is an indirect test parameter and commonly used to evaluate the rock mass boreability. Together with the above measured uniaxial compressive strength, the Brazilian tensile strength is used to calculate the rock brittleness index. Brazilian tensile strength provides an indirect measurement of rock tensile strength. It is measured according to the procedure recommended by

ISRM in 1981. The tensile strength test was conducted in the same test machine used for the UCS testing as shown in Figure 5.14.

Due to the small diameter samples taken from the site, a new jaw model was designed for the small diameter specimen according to the ISRM standard. In the Brazilian tensile test a rock disk is loaded diametrically between platens. The ratio of diameter d to thickness t of the disk is about 2:1. A loading rate of 200 N per second is adopted according to the ISRM standard. The specimen ruptures usually along a single tensile type fracture aligned with the axis loading. The rupture load P is measured with the help of an automatic recording equipment. The direction of any visible planes of weakness with respect to the applied load must be noted. If the fracture plane deviates significantly from a straight line between platen contacts, the test is considered invalid. The tensile strength of the rock is calculated from the following formula:

$$\sigma_t = \frac{2P}{\pi dt} = \frac{0.636P}{dt} \tag{5.6}$$

where σ_t denotes the Brazilian tensile strength (MPa), P denotes the rupture load (N), d is the diameter of the specimen (mm) and t is the thickness of the specimen (mm).

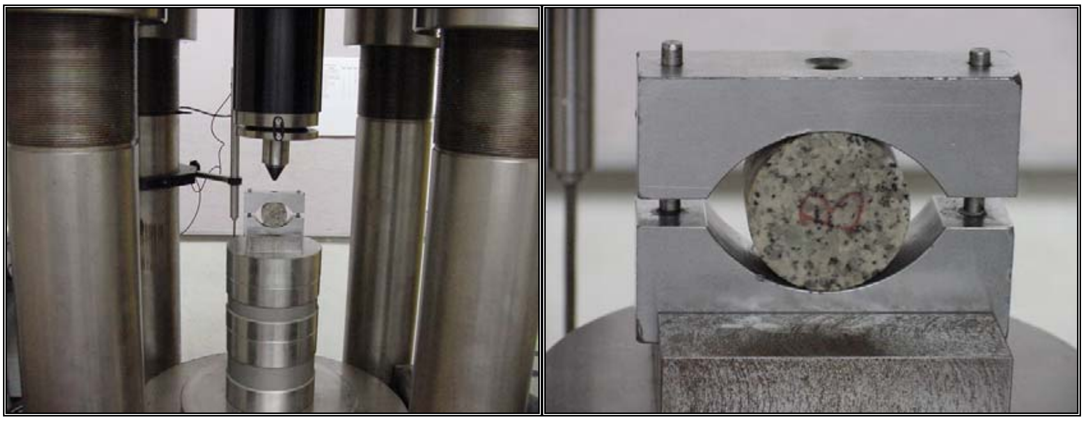

Figure 5.14 Compression machine loaded with sample for Brazilian tensile test

5.6.4 Summary of Laboratory Test Results

The test results including rock uniaxial compressive strength and Brazilian tensile strength performed in the laboratory and the calculated rock brittleness index are listed in Appendix A. Together with the joint parameters, these rock strength parameters would be used to set up the prediction model of TBM penetration rate. In order to obtain the correct intact rock strength that represents the true strength of the rock to be bored, the screening to separate the structural failures from the normal failure is necessary. This is important for granitic rocks found in Singapore, which contained many secondary fractures and filled calcite veins. These experimental strength results that represented the structural failures along the fractures and calcite veins were obviously lower than those of the normal failures. These results were filtered and they cannot be used to develop TBM penetration rate prediction model.

The relationships among the rock unaxial compressive strength, Brazilian tensile strength and rock weathering grades in T05 and T06 were shown respectively in Figures 5.15 and 5.16. As can be seen, the UCS of fresh granite is more than 140 MPa and most of these fall between 160 MPa and 250 MPa. The UCS of slightly weathered granite is between 100 MPa to 170 MPa. The UCS of moderately weathered granite varies from 50 MPa to 120 MPa. The UCS of the highly weathered granite is less than 50 MPa. The relationship between the uniaxial compressive strength and the weathered grade is consistent with the proposed weathering scheme by Zhao et al. (1994a). These experimental results also showed that with higher weathering grade of granite, the brittleness index decreases. The brittleness index of fresh granite varies from 10 to 28; the brittleness index of the slightly weathered granite is from 8 to 20; the brittleness index of the moderately weathered granite locates between 6 and 11 and that of the highly weathered granite is less than 5. The rock brittleness index increases generally with increasing UCS. But, the brittleness index varies in a wide range for the same UCS value.

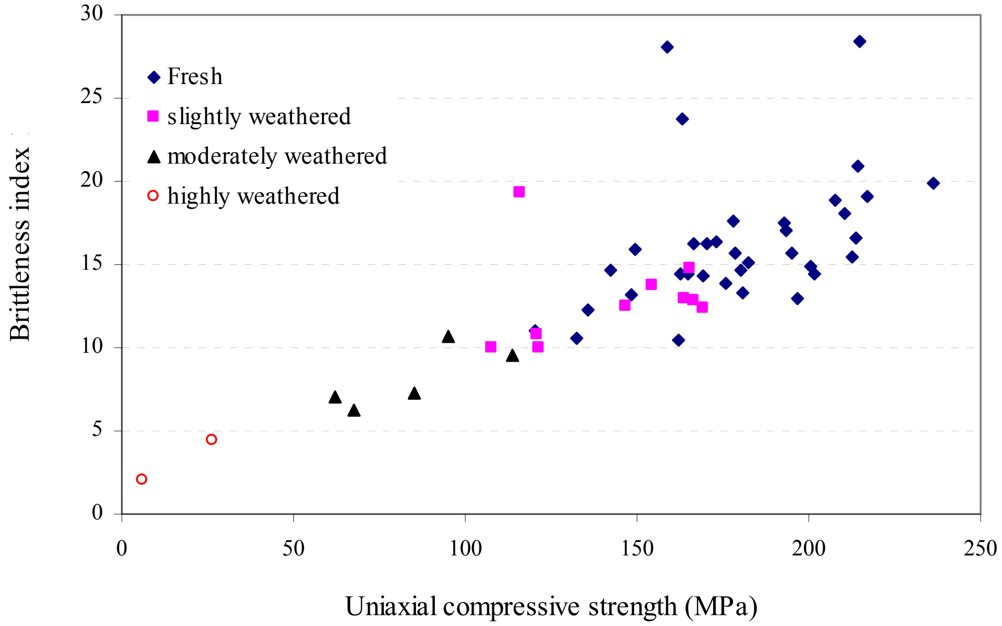

Figure 5.15 Variation of granite brittleness index at different rock compressive strengths and weathered grades in T05

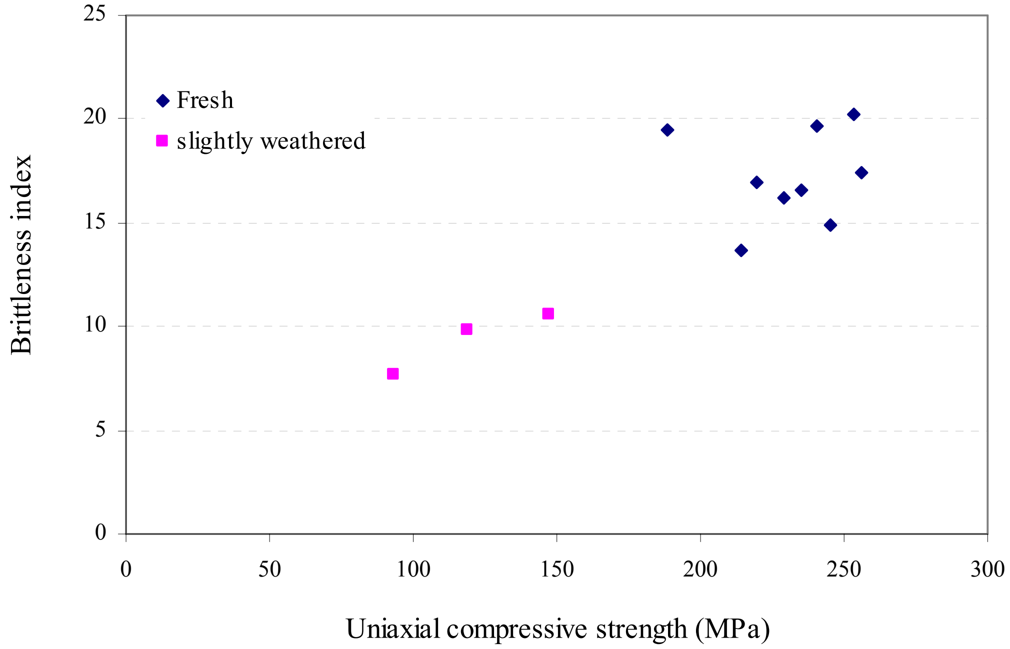

Figure 5.16 Variation of granite brittleness index at different rock compressive strength and weathered grades in T06

5.7 TBM Performance

As stated earlier, the objective of this study is to correlate TBM performance with rock mass conditions. The above sections presented the detailed rock mass conditions. In this section, the corresponding machine performance is evaluated. Generally, TBM is designed based on the given site conditions. It takes into account all possible ground conditions including hard rock, soft ground as well as mixed face ground in some cases. TBMs are well known to run thrust limited status in hard rock formations because it takes more thrust to penetrate the rock. On the contrary, TBMs run power or torque limited status in the soft ground due to the higher rolling force needed for deeper penetration in a given level of thrust (Cheema, 1999). In the mixed face ground, TBMs cannot always operate efficiently due to cutterhead vibration and face instability.

To fully understand the effect of geological conditions on the machine performance, the level of thrust and torque that are used to reach a certain penetration rate has to be measured. In other words, the magnitudes of cutter load, torque, penetration rate have to match the rock mass properties. Clearly, in a given rock mass conditions and for a machine with certain cutterhead design, the penetration rate increases as the thrust increases and then the corresponding torque increases. Due to the variation of the rock mass properties, the TBM operator often changes the cutter load or the torque from one ring to another ring in order to achieve maximum progress. To analyze the effect of variable rock mass conditions on the TBM performance, the operating parameters (thrust force, torque and RPM) of the machine should be monitored at rings where the tunnel face mapping and intact rock strength tests are conducted. In other words, the machine performance matches the rock mass properties. Furthermore, the effect of the rock mass properties on machine performance can be analyzed and evaluated.

Fortunately, the machine operating parameters can be monitored automatically by the TBM acquisition system in T05 and T06. The monitored parameters include thrust force, torque, revolution per minute, penetration rate, and other useful state parameters. These parameters are recorded once per 10 seconds or as an average per ring. The recorded files can be opened in the EXCEL spreadsheet environment.

It is worthy to note that the average cutter force is one of the major parameters for the rock mass boreability evaluation during hard rock excavation. It is the normal force applied on the cutter to penetrate the rock. It is provided by the total thrust generated by the thrust cylinders installed between the rear shield and the segment lining. Based on the machine structure, the force acted on the cutterhead is directly provided by the steering cylinders. The steering cylinders are indirectly pushed by thrust cylinders. Thus, the cutter load is calculated from the steering cylinder monitoring data. It is simply calculated by multiplying the applied steering pressure by the total area of the steering cylinders. Due to existence of the friction force between the front shield and tunnel wall, a part of the gross force is attributed to overcome the friction. Therefore, estimating the friction force is an essential component for evaluating the actual thrust delivered to the cutterhead, as the TBM moves forward to the tunnel face. Friction tests were conducted to determine the magnitude of the friction force in the site that would be presented in Chapter 6. The net thrust force truly acted on the cutterhead is the total steering force minus the friction force. The average cutter load is estimated by the net thrust force divided by the total cutter number. Here, the differentiation of the cutter position in the cutterhead is not taken into consideration, although the force distribution in face cutter and gauge cutter is observed to be different (Nelson, 1983).

The machine operating and performance parameters including the total steering force, torque, revolution per minute and the penetration rate in the corresponding rings were extracted from the machine recorded files. All the TBM performance raw data and analysis results were given in Appendix B. Using these parameters, the effect of rock mass properties on the machine penetration rate would be further analyzed and compared.

5.8 Database

TBM specifications were collected from the documents provided by the manufacturer. TBM operating parameters can be extracted directly and analyzed from the TBM acquisition system. The corresponding rock mass properties can be obtained by tunnel face mapping and laboratory intact rock tests. After extensive data collection in T05 and T06, a database including rock mass properties, TBM specifications and the corresponding TBM operating parameters can be established. The data set is shown in Table 5.8. All of the data are listed in Appendix C. The database is analyzed progressively to set up a function for the prediction of TBM penetration rate in Chapters 6 and 7.

Table 5.8 Database for the prediction model

TBM specifications	TBM operating parameters	Rock mass parameters
TBM diameter	Thrust	Uniaxial compressive strength
Cutter number	Torque	Brittleness index
Cutter spacing	Revolution per minute	Joint spacing
Cutter size and shape	Penetration rate	Joint orientation

Chapter 6 Rock Mass Boreability Analysis

6.1 Introduction

Three terms, namely cuttability, boreability and excavatability, are usually used to describe relative performance of rock cutting tools in a rock mass. Cuttability is mainly applied in coal measures mining and excavatability in the excavation of rock slopes. Boreability is extensively used in rock tunneling. The Commission on Engineering and Technical Systems of USA (1984) defined boreability as a value expressing the boring properties of rock in terms of the penetration rate with certain numbers/types of cutters and amount of pressure applied. It is equivalent to “tunnelability”, the ease or difficulty with which a rock type can be penetrated by a tunnel boring machine. Howarth (1987b) defined boreability as the prediction of the penetration rate of a rock cutting machine in a rock mass. From the above definitions, one can see that the boreability is a comprehensive variable related to the rock mass properties, machine parameters as well as tunnel geometry. It is neither an absolute nor an accurately definable quantity. When rock mass boreability is compared or calculated, a set of conditions must be included or indicated.

Since the rock mass boreability is a comprehensive parameter reflecting the rock mass conditions (rock material properties, joint properties), TBM operation properties (thrust, torque and RPM) and TBM performance (penetration rate, cutter wear) with a certain TBM specifications (cutterhead design, cutter diameter, cutter spacing). It may be described by rock mass conditions and TBM performance respectively. In light of the rock mass properties, the first version of the NTNU model (Blindheim et al., 1983) described the rock mass boreability based on three factors: drilling rate index (DRI), bit wear index (BWI), and the intensity of weakness planes in the rock mass. According to the description, the rock mass boreability takes the penetration rate and cutter wear into consideration. The updated version (Bruland, 1998) of the model included the orientation of weakness plane to describe the rock mass boreability. Sundin and Wenstedt (1994) proposed a boreability index to measure the full face boreability of the rock mass based on the rock mass properties. It is expressed by the result of rock indentation test multiplied by a factor for joint and weakness planes based on the rock mass properties.

Wanner and Aeberli (1979) proposed a specific penetration to denote the rock mass boreability based on the machine performance. The specific penetration is the penetration per revolution, divided by thrust per cutter. Hamilton and Dollinger (1979) used a field penetration index to describe the rock boreability. The field penetration index, defined as the ratio of the applied thrust per cutter to the penetration per revolution, actually is the inverse of the specific penetration. A boreability index (Sundin and Wanstedt, 1994) was proposed to measure the full face boreability of the rock mass in terms of the TBM performance. Its calculation is the same as the specific penetration. In fact, the same parameters are used in these three indexes to describe the rock mass boreability calculated from the machine performance. It is noted that the boreability index is a penetration rate normalized by the design and operation parameters of the machine. Thus, it facilitates the comparison of the performance of different TBMs.

Hamilton and Dollinger (1979) found that the boreability index is a function of the thrust. It decreases with increasing thrust per cutter. This is due to a change in the efficiency of the cutting action at the cutterhead. Borg (1988) and Bruland (1998) found that a critical thrust must be applied to overcome the rock’s inherent resistance against breaking. Below this critical thrust value almost no penetration rate can be achieved and above this value the penetration rate increases rapidly with the increase of thrust force. Therefore, the previously defined boreability index calculated by the TBM performance data cannot accurately represent the rock mass boreability. Only when the thrust force remains constant, can the calculated boreability index be compared for different rock mass conditions.

In this chapter, the results for in situ shield friction tests, which were conducted to decide the shield friction in order to calculate the actual thrust acted on the TBM cutterhead and the thrust force per cutter, are presented. After that, several penetration tests were carried out to assess the rock mass boreability. By analyzing the penetration test results conducted at T05 and T06 sites and other TBM sites in the world, a specific rock mass boreability index that is defined as a boreability index at penetration rate equal to 1 mm per revolution, is proposed to evaluate the rock mass boreability in different rock mass conditions.

6.2 Shield Friction Test

6.2.1 Forces Acting on the Cutterhead

In order to assess the rock mass boreability, the force exerted by TBM cutterhead on the rock mass need to be calculated. The forces acted on the front shield of the TBM are shown in Figure 6.1. In this figure, $F_{steering}$ denotes the total force of steering cylinders (kN), which is adopted to calculate the thrust force per cutter in T05 and T06 based on the specifications of these machines; F_{rock} is equal to the force acted on rock mass by cutterhead (kN); $F_{frontshield}$ represents the friction force of front shield (kN); $W_{frontshield}$ stands for the total weight of front shield (kN); $F_{earthpressure}$ is the force from earth pressure (kN); and $F_{support}$ is the force supporting the shield by the tunnel invert. According to equilibrium of forces in the horizontal direction, the equation is shown as follows:

$$F_{steering} = F_{rock} + F_{earthpressure} + F_{frontshield} \tag{6.1}$$

In Equation (6.1), the steering force and the earth pressure acted on the cutterhead are available from the TBM records. Only if the friction force of the front shield is known, can the force acted on the rock mass be calculated. Therefore, in situ tests were performed to find out the friction force.

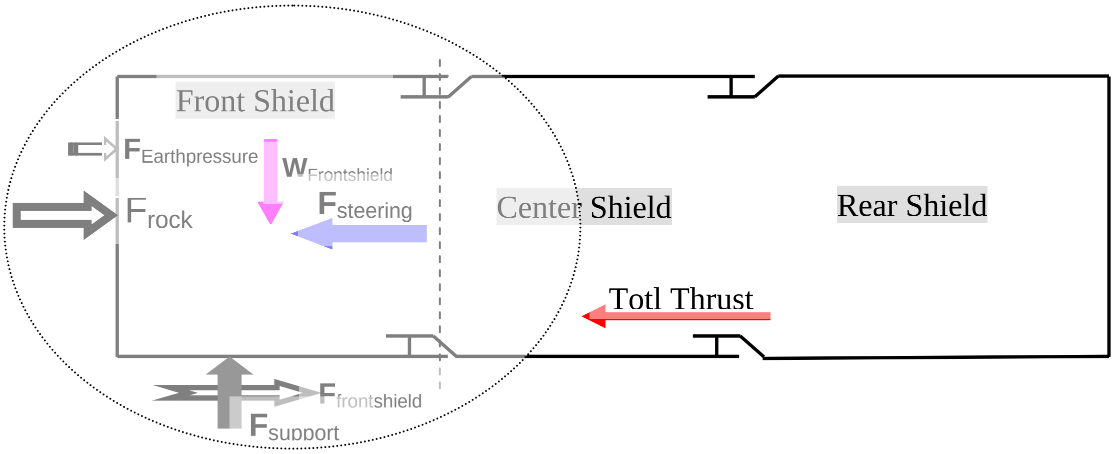

Figure 6.1 Sketch of the forces acting on the TBM front shield

6.2.2 In Situ Tests and Results

When a ring length of the tunnel is excavated, the TBM is stopped to install ring segments in the rear shield. After several rings excavated, the cutters in the cutterhead shall be thoroughly checked. At this moment, the shield friction tests can be carried out without interfering with the normal tunnelling progress. First of all, the mucks in the cutterhead chamber are removed. Then, the cutterhead is extracted from the tunnel face to a distance dependent on the capacity of the steering hydraulic cylinders. After that, the cutterhead is pushed forward to the tunnel face with cutterhead rotation similar to the normal excavation. During the process, the steering cylinders must move in the same pace. The uneven movement of the steering cylinders results in the breakage of the rock mass in the tunnel wall by cutterhead and discs. Particularly the peripheral discs are close to and may easily crush into the tunnel wall, when the cutterhead is pushed forward. The uneven movement among different cylinders may also results in the internal confrontation in these cylinders. During the test, the variations of the total steering force, the positions of the steering cylinders with time were recorded. The position variation of each steering cylinder from the beginning to the end during the test recorded the real movement of the cutterhead. At the beginning, these cylinders may not be located at the same position. Thus, they have different original records, as shown in Figures 6.2, 6.4 and 6.6.

A series of retracting and pushing tests were carried out in T06 north tunnel. The shield friction force is calculated respectively from these retracting tests and pushing tests. Some tests results are deleted due to the uneven movement of the cylinders. The calculated front shield friction forces from the different ring tests are listed in Tables 6.1 and 6.2 and some samples of the data analysis are shown in Figures 6.2-6.7. Some points shown in these Figures are abnormal due to the uneven movement of the steering cylinders. In the calculation of the average value of the friction force, these points are not taken into account.

It can be seen from the Tables 6.1 and 6.2 that the calculated friction forces show quite a large difference between the retracting and pushing tests. The values for retracting the cutterhead are much less than that for pushing. The torque applied during the tests also varies greatly in the retracting and pushing friction tests. The torque for retracting the cutterhead is less than that for pushing. However, the minimum and average values for the two types of friction tests fall within a narrow range.

The results from the friction tests by pushing cutterhead indicate the process of pushing the cutterhead forward is more complicated than the retracting process. In the process of pushing cutterhead, more factors besides the friction force influence the cutterhead movement. The fringe of the shield and the gauge cutters may cause local instability of the tunnel wall. Some rock chips dropped from the tunnel face and tunnel wall may block the clearance between the shield and tunnel wall. It increases greatly the force needed for pushing the cutterhead. Although the TBM is in the condition of pushing the cutterhead during excavation, the above mentioned factors influencing the pushing force do not exist during continuously mining process. Because the cutterhead is in close contact with the tunnel face, it prevents the local instability of the tunnel wall, and the excavated rock blocks and chips from the tunnel face are collected by buckets in time. In addition, the cutterhead vibration helps its movement during boring.

Theoretically, the friction force should be the same both for the pushing and retracting processes, which is the minimum value in each test. Thus, the friction force in the retracting friction tests represents the real friction force between the tunnel wall and the front shield.

Based on the calculation results, the minimum value ranges from 36.0 kN to 87.32 kN and their average is close to 50 kN. Some factors may contribute to the variation of the friction force, namely, the variation of the friction coefficient between shield shell and rock mass, such as the granite weathering grade, ground water condition and some obstacles in front of the cutterhead. Therefore, a friction force of 50 kN is reasonable for the calculation of the boreability index.

Table 6.1 Results for retracting friction tests in T06

Ring No.	Rock mass	Friction force (kN)			Torque (kNm)		
		Min.	Ave.	Max.	Min.	Ave.	Max.
N1690	Fresh to slightly weathered granite	36.0	43.15	72.94	37.66	52.32	64.34
N1988	Fresh to slightly weathered granite	87.32	104.53	111.98	/	/	/
N2014	Fresh to slightly weathered granite	38.0	73.52	200.33	40.45	55.84	74.45
N2129	Fresh to slightly weathered granite	36.0	98.28	266.06	27.33	57.56	97.26

Table 6.2 Results for pushing friction tests in T06

Ring No.	Rock mass	Friction force (kN)			Torque (kNm)		
		Min.	Ave.	Max.	Min.	Ave.	Max.
N1745	Moderately to highly weathered granite (UCS, 20.57 MPa)	962.58	1224.25	1494.73	68.21	79.56	103.5
N2074	Fresh to slightly weathered granite	919.44	1079.70	1355.01	61.75	108.7	154.06
N2124	Fresh to slightly weathered granite	982.1	1053.57	1257.49	160.73	191.29	253.47

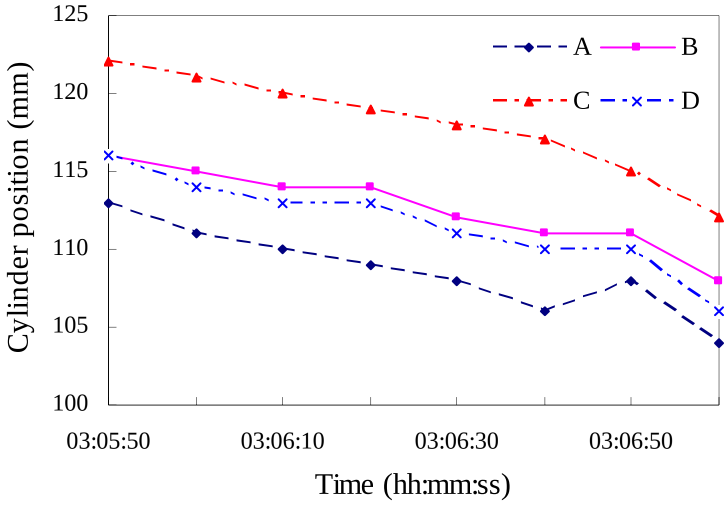

Figure 6.2 The movement of steering cylinders with time at Ring N1690, T06 in retracting front shield friction test (A, B, C and D denote the different set of steering cylinders)

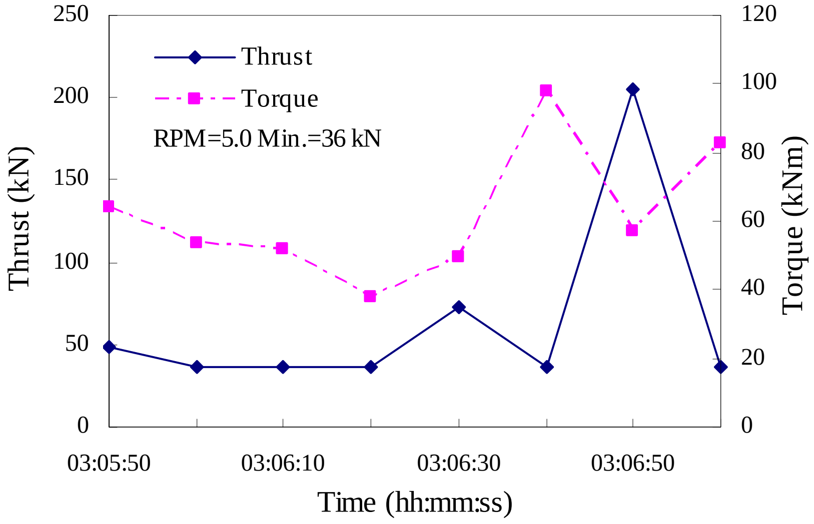

Figure 6.3 Variation of the total steering thrust and torque at Ring N1690, T06 in retracting front friction test

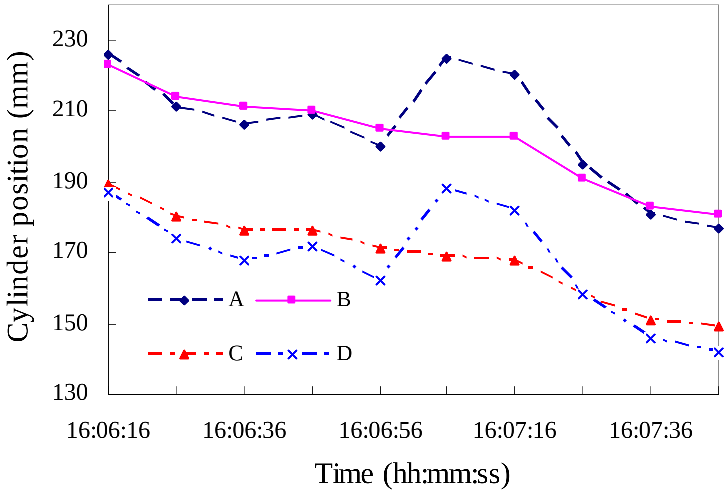

Figure 6.4 The movement of steering cylinders with time at Ring N2014, T06 in retracting front shield friction test (A, B, C and D denote the different set of steering cylinders)

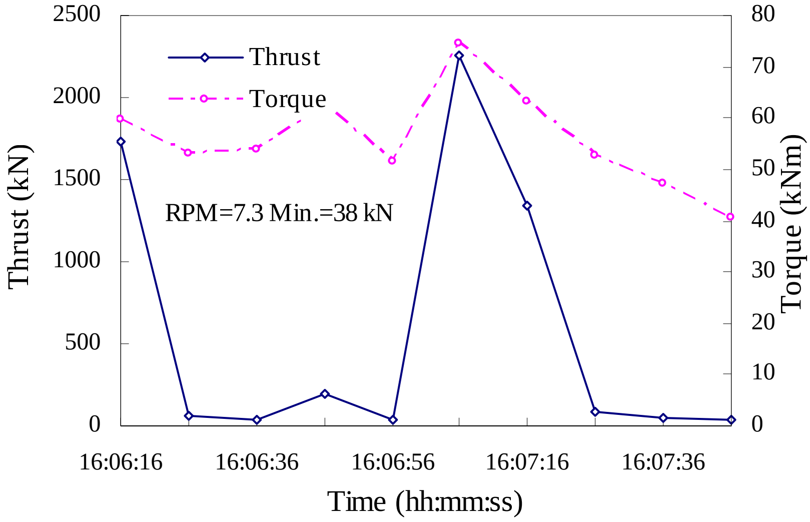

Figure 6.5 Variation of the total steering thrust and torque at Ring N2014, T06 in retracting front friction test

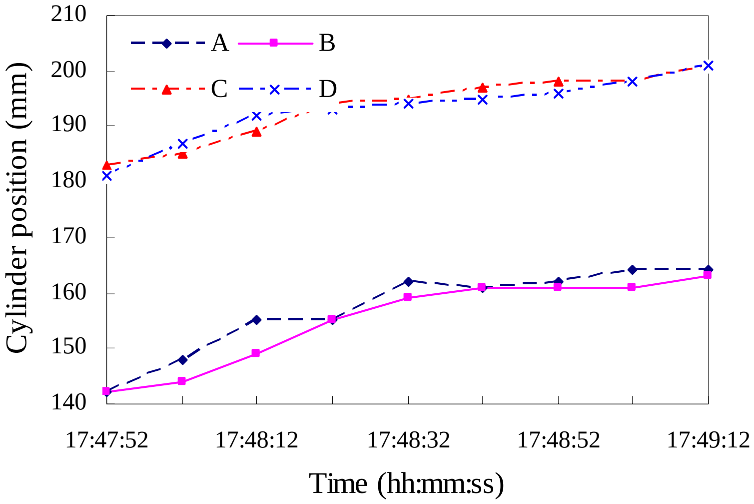

Figure 6.6 The movement of steering cylinders with time at Ring N2124, T06 in pushing front shield friction test (A, B, C and D denote the different set of steering cylinders)

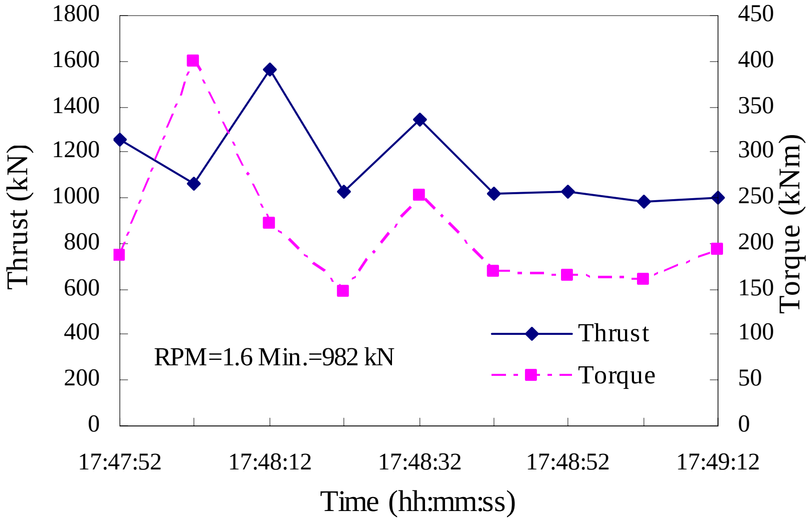

Figure 6.7 Variation of the total steering thrust and torque at Ring N2124, T06 in pushing front friction test

6.3 TBM Penetration Test Conducted in T05

6.3.1 In Situ Test Procedure

A comprehensive TBM penetration test was conducted in the north drive of T05 site. Before the penetration test, the TBM cutters were checked. The cutter wear conditions were recorded and these cutters which satisfied the replacement criterion were replaced. The cutters condition is listed in Table 6.3. The cutterhead chamber was emptied by the screw conveyor. Then, the geological conditions of the tunnel face were mapped.

The test is divided into seven steps, as shown in Table 6.4. Before Step 1, the TBM has been operated for five minutes with full thrust to verify that the TBM is in normal operation condition. It is also useful for the comparison of the test results. The TBM is then operated in different total thrust level, from 40% to 100% of the designed maximum cutter load. According to Bruland (1998), the penetration test duration should correspond to approximately 30 revolutions of the cutterhead at each thrust level. In order to obtain a high quality test result, the test duration at each thrust level is designed to be 10 minutes that include the time used to stabilize the thrust force at the beginning of each step, and the speed, in terms of revolution per minute, is fixed to 10. Due to the extremely low advance rate in the first three steps, the test duration is changed to five minutes. The thrust and torque variations with time are shown in Figures 6.8 to 6.10. From the figures, it can be seen that the thrust is not stable during the first two steps. Thus, these data can not be used to analyze the penetration rate.

In order to study the chipping efficiency in different thrust level, the muck samples were collected for further sieve tests and muck analysis at each step, as shown in Table 6.4. To ensure the muck samples to be representative, the samples were directly taken from the conveyor belt three minutes after the beginning of each step. In this test, due to extremely low advance for the first two steps, the corresponding muck samples were not collected.

Table 6.3 TBM cutter wear conditions

Tool type	Tool position	Tool wear (mm)	Tool type	Tool position	Tool wear (mm)
Double cutters	1/3	10/6	Face single cutters	20	1
	2/4	8/6		21	9
	5/7	5/4	Transition single cutters	22	0
	6/8	10/12		23	15
Face single cutters	9	1		24	0
	10	14		25	10
	11	8		26	1
	12	9		27	0
	13	12		28	5
	14	15		29	8
	15	13		30	10
	16	14	Gauge cutters	31	3
	17	15		32a	4
	18	7		32b	7
	19	7	Remarks: normal		

Table 6.4 Design of the penetration test

TBM penetration test	Thrust level (percentage)	Thrust force in main cylinder (kN)	Thrust force in steering cylinder (average bar)	Test time (minute)	Muck samples (>30 kg)
Step 0	100	9200	165	5	Yes (No. 0)
Step 1	40	3896	95	10	Yes
Step 2	50	4870	100	10	Yes
Step 3	60	5633	103	10	Yes (No. 3)
Step 4	70	6453	108	10	Yes (No. 4)
Step 5	80	7450	121	10	Yes (No. 5)
Step 6	90	8484	142	10	Yes (No. 6)
Step 7	100	9200	165	10	Yes (No. 7)

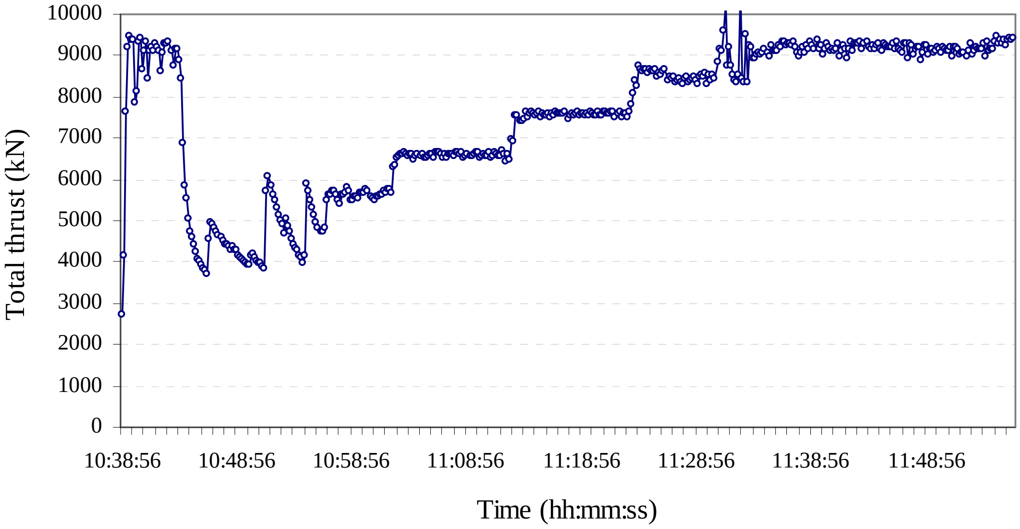

Figure 6.8 Total thrust variation with time

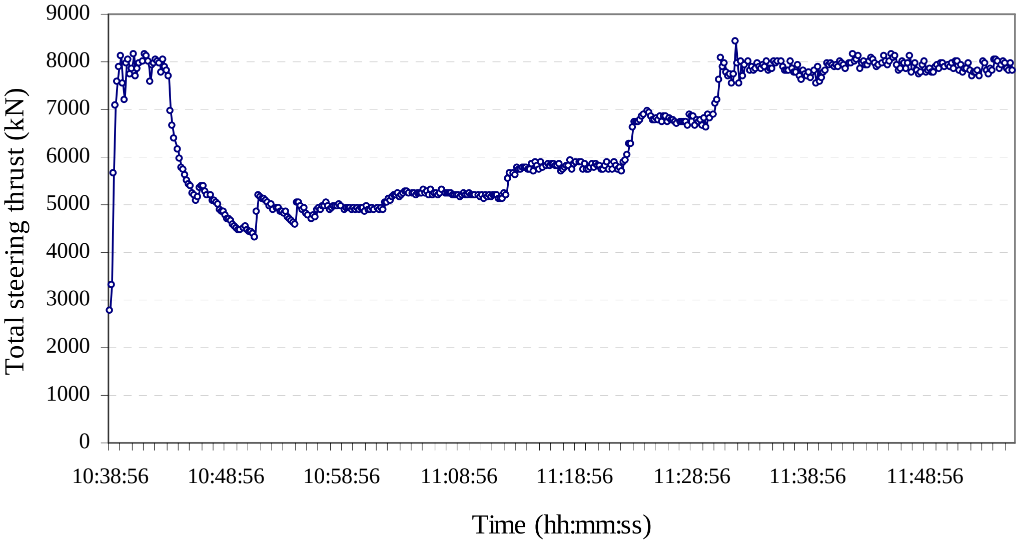

Figure 6.9 Average steering thrust variation with time

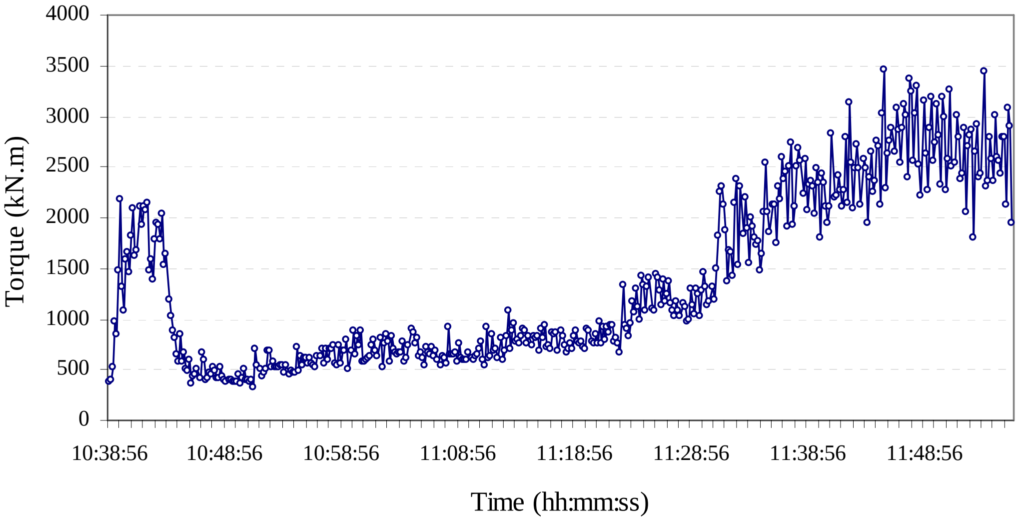

Figure 6.10 Torque variation with time

6.3.2 Rock Mass Conditions

After the cutterhead chamber is emptied, the tunnel face mapping can be carried out through the four buckets in the cutterhead that are designed to collect the mucks. The four buckets are evenly located in the cutterhead. Therefore, the tunnel face can be well observed from the four openings. The tunnel face map of the test ring is shown in Figure 6.11. Photos taken from the cutterhead chamber show the rock mass conditions of the upper right and left openings, as in Figures 6.12 and 6.13 respectively. The rock mass is composed of pink light grey, fresh granite. One joint set is observed in the rock mass. The joint plane is smooth and undulating, and the joint wall is slightly altered with non-softening mineral coating. The joint spacing is about 400 mm. The angle between the tunnel axis and the joint plane is about 30º~40º. The tunnel face is dry during excavation. Some core samples were taken from the tunnel face. The uniaxial compressive strength tests, point load tests and Brazilian tensile strength tests were conducted in the laboratory following the ISRM standards. The rock uniaxial compressive strength corrected to the diameter 50 mm is 172.9 MPa. The point load strength (I_{s50}) is 7.84 MPa. The Brazilian tensile strength is 10.55 MPa.

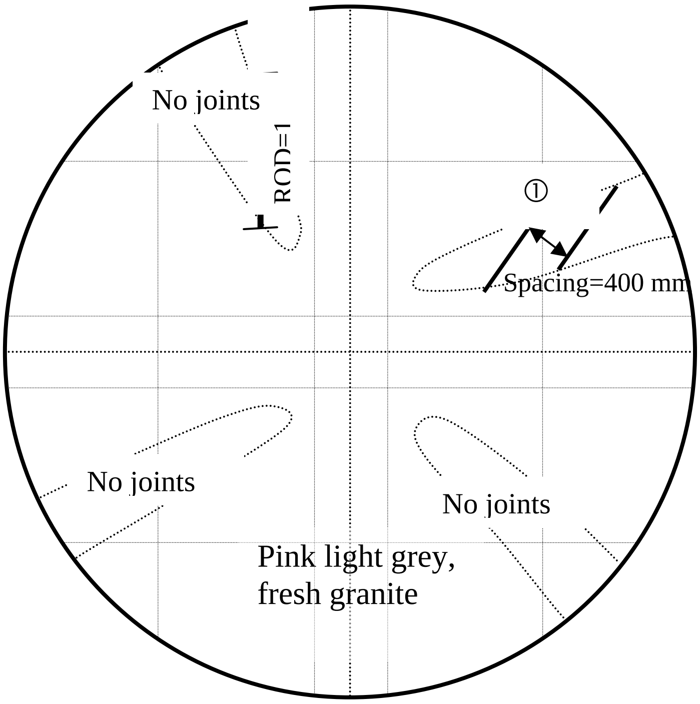

Figure 6.11 Tunnel face map before TBM penetration test

Figure 6.12 Tunnel face at upper right opening (North Ring 2734 in T05)

Figure 6.13 Tunnel face at upper left opening (North Ring 2734 in T05)

6.3.3 Penetration Test Results

The penetration test result is listed in Table 6.5. In each step, the start time, end time, rpm, the total thrust, torque and the steering force are recorded automatically in the TBM acquisition system. The time duration for each step, penetration per revolution, force per cutter and rock mass boreability index were calculated based on the above data. It shall be noted that the number of cutters 33 is the total number of cutters installed in the cutterhead, including the double cutters, face cutters, transition cutters and gauge cutters. The uneven distribution of the force in different sort of cutters was not considered. The friction force between the front shield and the tunnel wall was deducted when the force per cutter and rock mass boreability index were calculated.

The correlations between the total thrust, torque, force per cutter and TBM penetration were shown in Figures 6.14-6.16, respectively. It can be seen that when increasing the total thrust, torque and force per cutter, the penetration increases. From Figures 6.14 and 6.15, it can be seen that there exists a critical point in these curves. Only if the total thrust or force per cutter is more than the critical value, the penetration increases rapidly. It means that the TBM cannot fragment the rock mass effectively until the penetration reaches the critical value. For the tested rock mass, fresh granite with few joints, the critical point is located at the penetration between 0.5 mm/rev and 1.0 mm/rev. With the increase of the torque, the increase of the penetration shows a different tendency. Initially, the penetration increases almost linearly with increasing torque. Then, when the penetration is more than the critical value and the TBM operates efficiently, the torque increases slowly compared with the previous stage. Because the thrust force is more than the critical value, the increase of the thrust force makes the cutter indentation process more effective and the interaction between two cuts is strengthened. The induced lateral cracks under the action of the neighbouring cutters can reach each other and coalesce to form rock chips more frequently. With the increase of the penetration, the rock chipping force acted on the two sides of the cutters has to increase, which also leads the increase of chipping frequency. Thus, the increment rate of the friction force between the cutters and rock grooves is slower than that of the penetration. Correspondingly, the rate required to increase the torque is getting slower with increasing penetration.

The correlation between the boreability index (BI) and the penetration was plotted in Figure 6.17. As can be seen, the boreability index for a rock mass is not a constant. The rock mass boreability index decreases with increasing penetration. The data points can be fitted into a power function as shown in the Figure 6.17. The coefficient R is as high as 0.9996. From this function, it is easy to obtain the boreability index for the penetration of 1 mm per revolution. It is close to the critical point and does not change with the force acted on the tunnel face. So, the boreability index at penetration 1 mm/rev is not relevant to the machine operation conditions (thrust force, RPM and torque) and eliminates the influence of the operation uncertainties on the rock mass boreability. In fact, the index is only dependent on the rock mass conditions and cutterhead design, especially the cutter diameter, cutter spacing and cutter tip width. Consequently, the boreability index at penetration 1 mm/rev, defined as specific rock mass boreability index (SRMBI) hereafter is used to evaluate the rock mass boreability.

Table 6.5 Penetration test results

Test step	Start time (hh:mm:ss)	End time (hh:mm:ss)	Duration (minutes)	Advance (mm)	Penetration (mm/rev)	Thrust force (kN)	Torque (kNm)	Average steering force (bar)	Force per cutter (kN/cutter)	BI ((kN/cutter) /(mm/rev))
0	10:39:36	10:44:06	4.5	70	1.62	9020.43	1696.82	163.05	237.12	146.49
3	10:56:46	11:02:26	5.67	10	0.18	5624.69	667.51	101.94	147.68	817.25
4	11:03:46	11:13:06	9.33	26	0.29	6597.39	673.93	107.81	156.28	543.42
5	11:13:16	11:22:56	9.67	44	0.47	7566.27	810.29	119.69	173.67	368.32
6	11:24:06	11:30:46	6.67	59	0.92	8497.22	1199.27	140.46	204.07	222.40
7	11:31:26	11:56:36	25.17	481	1.98	9153.28	2432.27	163.30	237.50	120.05

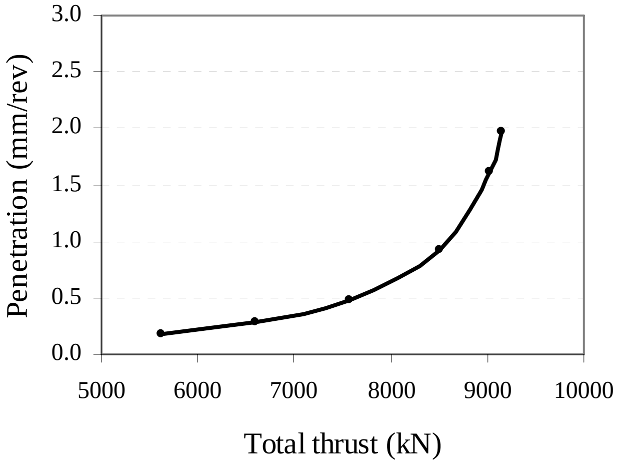

Figure 6.14 Variation of penetration with the total thrust

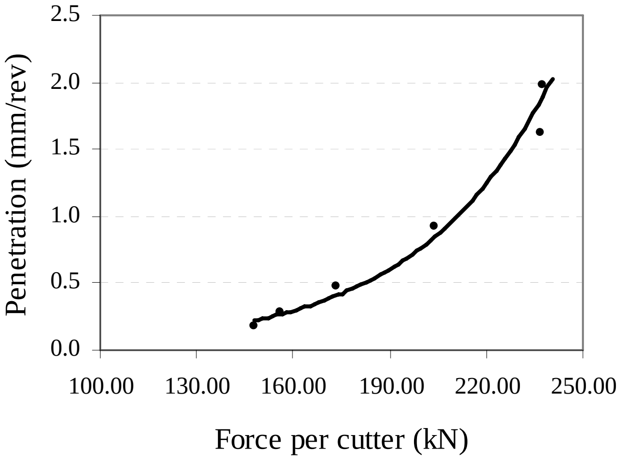

Figure 6.15 Variation of penetration with the force per cutter

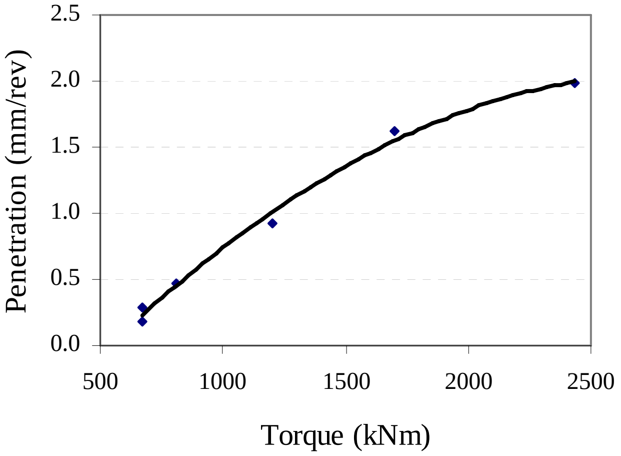

Figure 6.16 Variation of penetration with the torque

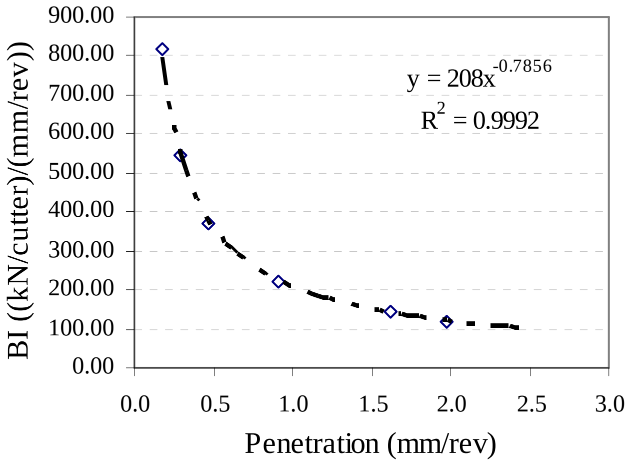

Figure 6.17 Variation of boreability index with the penetration

6.3.4 Muck Sieve Analysis

During the penetration test, rock muck samples more than 30 kg were taken from the conveyor belt at each test step. These samples were then transported to the laboratory in Nanyang Technological Univeristy (NTU) for sieve analysis. The sieve analysis was conducted following the BS code 1377 (1990). Based on the chip shape, as defined in Figure 6.18, the middle axis size distribution can be obtained from the standard sieve analysis. The distribution curves for samples collected from the different test steps are shown in Figure 6.19. With increasing thrust force and consequently increasing penetration per revolution, the chip size increases. Only in Steps 0 (Sample No. 0) and 7 (Sample No. 7), the mucks are well graded. That is to say, any increase of the thrust force will result in the improvement of the TBM efficiency on rock fragmentation. The TBM can efficiently fragment the rock mass only if the force per cutter reaches a critical value. The sieve analysis results verified that there exists a critical point for a rock mass in the TBM penetration curve. When the thrust is more than the critical value, the rock mass can be efficiently fragmented. Otherwise, the rock is crushed into rock powder and small pieces.

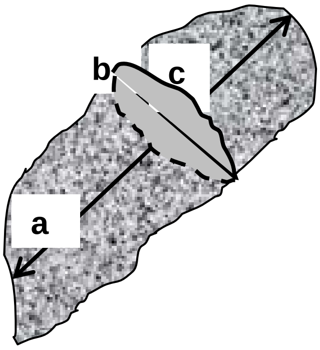

Figure 6.18 Chip shape (a: the longest axis; b: the middle axis; c: the shortest axis)

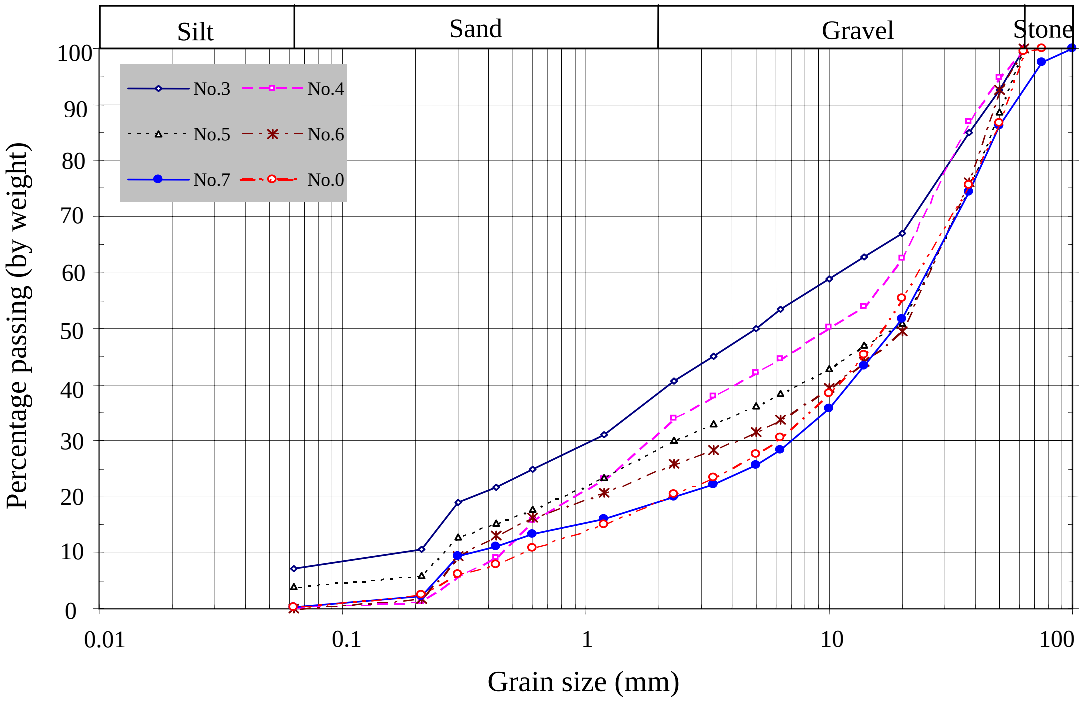

Figure 6.19 Rock chip size distribution for different thrust forces

6.3.5 Muck Shape Analysis

After the sieve analysis, the large chips with longest axis more than 37.5 mm were taken for further shape analysis at each test step. The dimensions of every chip, as defined in Figure 6.18, are measured. The longest axis distribution of the largest 25 rock chips in every step was drawn in Figure 6.20. The length of the large chips increases generally with increasing penetration per revolution. Due to the multi-pass cutting, the large chips also were formed in Steps 5 and 6. The chip shape was also analyzed based on the ratio of the measured three axes. The chip shape can be described in four types, namely flat, elongated and flat, elongated and cubic according to the ratio of the middle axis to the longest axis and the ratio of the shortest axis to the middle axis, as shown in Figure 6.21. In order to find out the shape variation in different steps, the largest 25 chips in the longest and middle axis were selected to obtain the statistical mean value and standard deviation. The results are also shown in Figure 6.21. With increasing penetration per revolution, the chip shape changes slowly from flat to elongated and flat. It also shows the rock breakage efficiency increases with the increasing penetration per revolution.

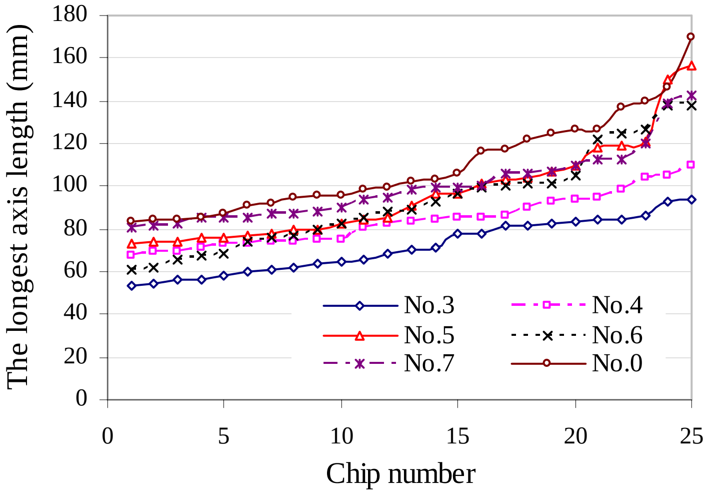

Figure 6.20 The longest axis length distribution of the largest 25 chips

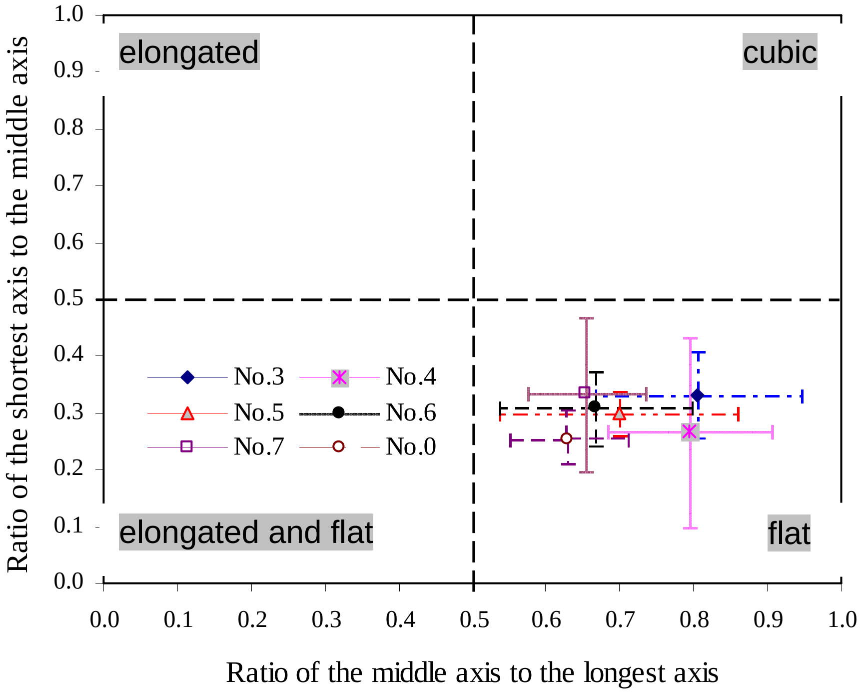

Figure 6.21 Rock chip shape variation for different thrust forces (centre point: mean value; cross: standard deviation)

6.4 Penetration Test Conducted in T06

A simple penetration test slightly different from the one in T05 was performed at ring N1887 in T06. In this test, the force per cutter was increased continuously, and correspondingly the torque was also increased continuously. Then, the TBM penetration per revolution increased continuously. The results were listed in Table 6.6. The rock mass is composed of pink grey granite with rock uniaxial compressive strength close to 122 MPa. The rock mass is slightly to moderately weathered. The RQD is close to 80 in the tunnel face and the joint spacing close to 200mm, as shown in Figure 6.22.

The test results are shown in Figures 6.23 and 6.24. With increasing torque and thrust per cutter, the penetration per revolution increases. The relation between the thrust per cutter and the penetration also shows that there exists a critical value in the curve. Because the rock mass is easily excavated, the critical thrust force is very low. The correlation between torque and the penetration shows the same tendency with the test result in T05. The variation of the rock mass boreability index with penetration per revolution was plotted in Figure 6.25. The correlation can also be fitted with a power function as shown in this figure. The coefficient R is up to 0.9945. The specific rock mass boreability index is 61.21 kN/cutter/mm/rev.

Figure 6.22 Tunnel face in N1877, T06

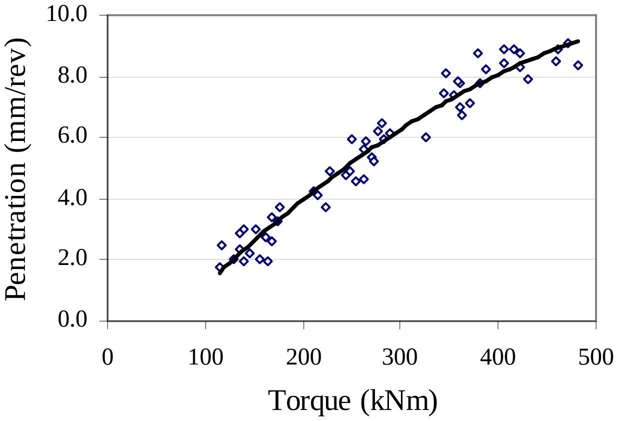

Figure 6.23 Relation between torque and penetration

Table 6.6 Penetration test results in N1877, T06

Time (hh:mm:ss)	Penetration (mm/rev)	Torque (kNm)	Thrust per cutter (kN/cutter)	BI (kN/cutter/mm/rev)
15:28:54	1.998	155.783	77.059	38.568
15:29:04	1.995	129.102	78.972	39.585
15:29:14	1.739	113.825	74.863	43.049
15:29:24	2.366	135.342	79.149	33.453
15:29:34	1.988	140.075	74.473	37.461
15:29:44	1.993	163.314	79.362	39.820
15:29:54	2.606	168.478	79.504	30.508
15:30:04	2.245	145.455	74.260	33.078
15:30:14	2.494	116.837	78.405	31.438
15:30:24	2.860	134.696	82.656	28.901
15:30:34	2.735	161.808	83.931	30.688
15:30:44	2.987	139.215	87.261	29.214
15:30:54	3.367	168.263	83.790	24.886
15:31:04	2.999	151.049	85.879	28.636
15:31:14	3.250	174.933	90.130	27.732
15:31:24	3.738	176.009	90.272	24.150
15:31:34	3.742	223.992	91.264	24.389
15:31:44	4.228	210.221	94.311	22.306
15:31:54	4.117	215.170	90.096	21.884
15:32:04	4.598	254.976	91.689	19.941
15:32:14	4.610	261.646	97.145	21.073
15:32:24	4.743	242.926	96.330	20.310
15:32:34	4.983	245.724	92.965	18.656
15:32:44	4.880	228.080	97.464	19.972
15:32:54	4.876	247.015	103.237	21.173
15:33:04	5.380	270.253	97.287	18.083
15:33:14	5.223	271.974	99.447	19.040
15:33:24	5.969	283.809	101.573	17.017
15:33:34	6.474	280.796	98.455	15.208
15:33:44	6.218	276.923	101.714	16.358
15:33:54	5.860	265.089	98.881	16.874
15:34:04	6.116	288.327	98.030	16.029
15:34:14	5.974	249.166	108.870	18.224
15:34:24	5.614	261.861	105.257	18.749
15:34:34	5.991	326.843	108.091	18.042
15:34:44	6.972	360.839	110.287	15.819
15:34:54	7.483	343.626	109.968	14.696
15:35:04	7.758	359.979	113.192	14.590
15:35:14	8.737	378.698	110.358	12.631
15:35:24	8.119	347.069	111.845	13.776
15:35:34	6.720	362.561	110.712	16.475
15:35:44	7.843	358.903	111.811	14.256
15:35:54	8.220	386.660	115.495	14.050
15:36:04	7.119	371.598	112.590	15.815
15:36:14	7.358	355.030	114.750	15.595
15:36:24	8.743	422.163	121.764	13.927
15:36:34	8.339	481.119	117.832	14.130
15:36:44	7.878	429.909	115.353	14.642
15:36:54	9.112	470.576	112.767	12.376
15:37:04	8.876	406.455	124.138	13.986
15:37:14	7.768	381.926	116.309	14.973
15:37:24	8.862	416.784	120.702	13.620
15:37:34	8.402	405.810	118.612	14.117
15:37:44	8.465	460.033	121.977	14.410
15:37:54	8.876	461.539	116.097	13.080
15:38:04	8.317	421.732	125.449	15.083

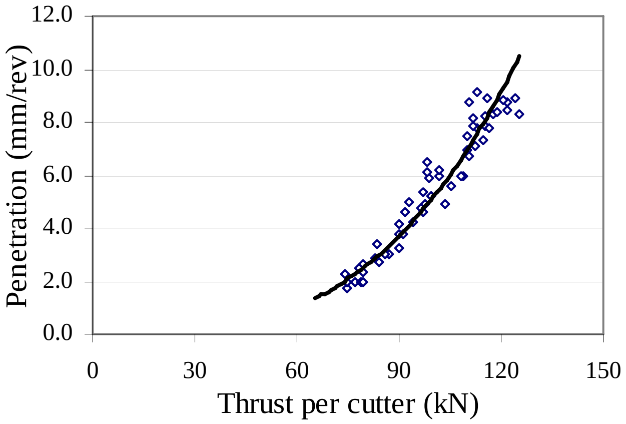

Figure 6.24 Relation between thrust per cutter and penetration

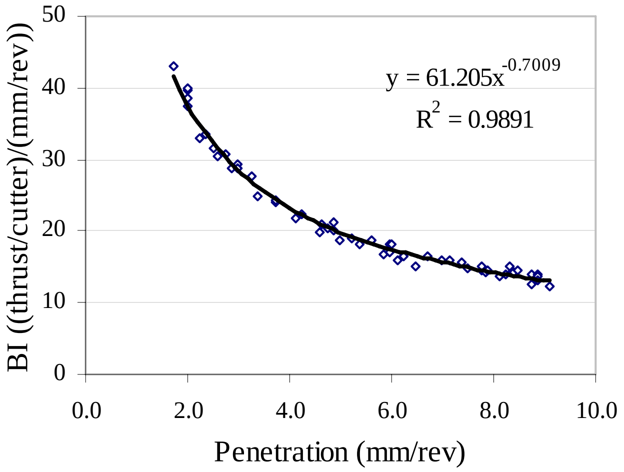

Figure 6.25 Variation of boreability index with penetration

6.5 Evaluation of Rock Mass Boreability

Three penetration test results conducted in granite-gneiss, granite and sandstone with quartzitic matrix outside Singapore are shown in Figures 6.26 to 6.28 respectively (data provided by Buchi, 2004). The relation between rock mass boreability index and penetration is fitted very well by the power function. From these figures, one can see that the critical point is located at the penetration between 0.5 mm/rev to 1.0 mm/rev. The rock mass boreability index increases rapidly with decreasing penetration when the penetration is less than the critical point. On the contrary, the rock mass boreability index decreases slowly with increasing penetration when the penetration is more than the critical value. It is similar to the results of the penetration tests conducted in T05 and T06.

Figure 6.29 shows all the correlation curves between the rock mass boreability index and the penetration per revolution from the test results by Buchi (2004), and the test results conducted in T05 and T06. All curves satisfy power functions. The correlation coefficient is close to 1. Using the power function, one can easily obtain the rock mass boreability index at the penetration per revolution of 1.0 mm/rev ($BI_{(1)}$), the specific rock mass boreability index. Since rock mass boreability index is the force per cutter normalized by the penetration per revolution and the specific rock mass boreability index is the specific BI at penetration per revolution of 1 mm/rev, it is a normalized value and eliminates the influence of the operation uncertainties (thrust force, RPM and torque), especially the influence of thrust force on the boreability index. Because the specific rock mass boreabiltiy index is close to the critical point, it can be used to stand for and differentiate the rock mass boreability. The test results show that the specific rock mass boreability index falls in a wide range from 61.2 kN/cutter/mm/rev to 208 kN/cutter/mm/rev in different rock masses of the above mentioned penetration tests. It is not only related to the rock material strength, but also to the joint system of the rock mass. For example, the rock strength of granite in T05 penetration test is 172.9 MPa and its specific rock mass boreabiltiy index is 208 kN/cutter/mm/rev, while the rock strength of granite-gneiss in Dr. Buchi' test is close to 250 MPa and its rock mass boreability index is only 120.67 kN/cutter/mm/rev. It remains a constant in the same rock mass condition if the same TBM is used, and does not change due to different operating thrust force. Nevertheless, more effort is needed to obtain the specific rock mass boreability index than the boreability index. The boreability index can be calculated directly from the TBM acquisition record, while the specific rock mass boreabiltiy index can only be obtained from the penetration test. However, in practice, the contractors are only concerned with the maximum advance rate. TBM operator usually operates the machine to maximize the largest penetration rate in every stroke. Thus, the penetration test is rarely conducted in tunnel excavations.

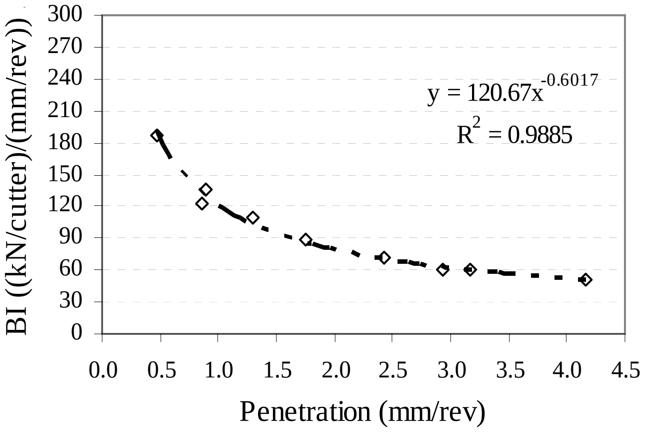

Figure 6.26 Relation between boreability index and penetration in granite-gneiss, Aspo, Sweden (data provided by Dr. Ernst Buchi, GEO 96)

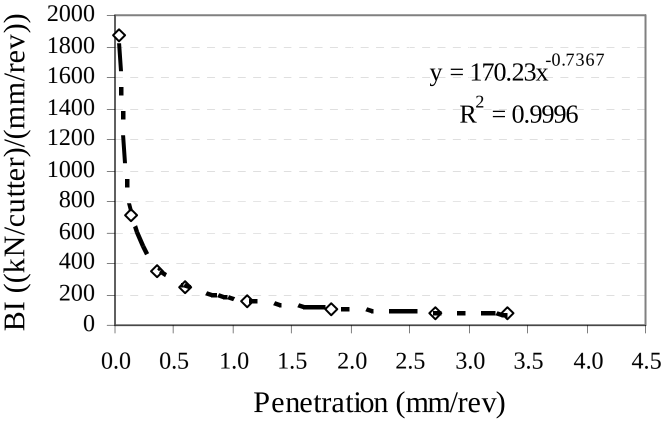

Figure 6.27 Relation between boreability index and penetration in granite, Emolweni tunnel (data provided by Dr. Ernst Buchi, GEO 96)

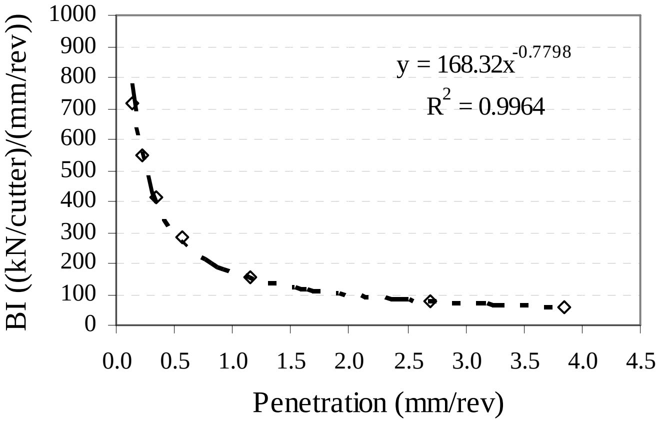

Figure 6.28 Relation between boreability index and penetration in sandstone with quartztic matrix (data provided by Dr. Ernst Buchi, GEO 96)

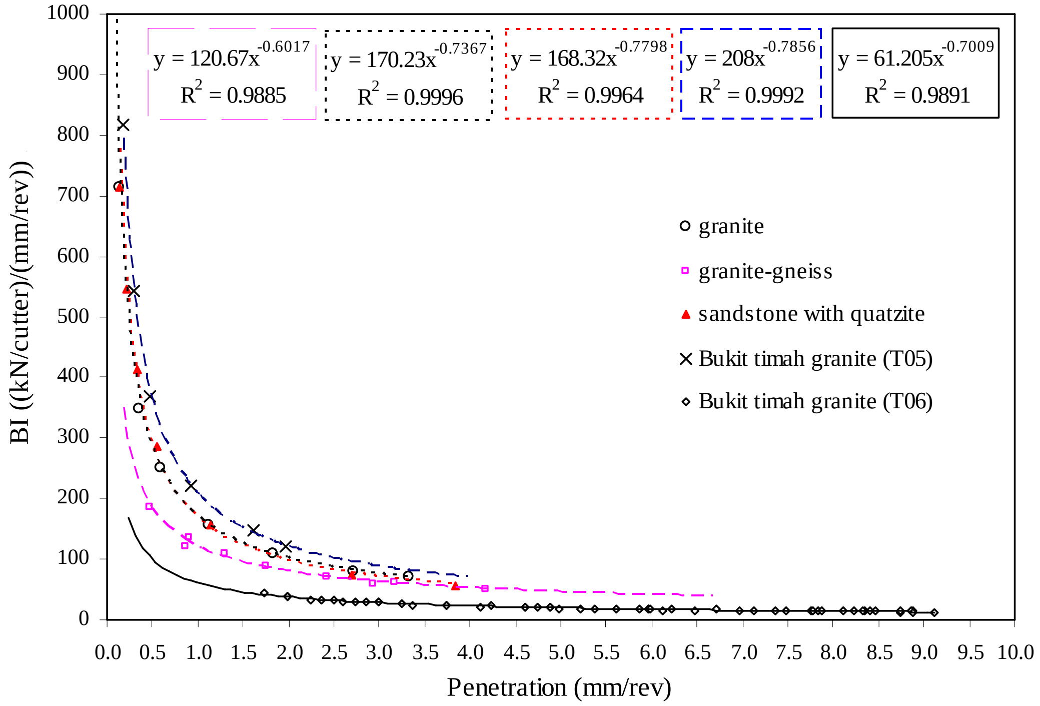

Figure 6.29 Rock mass boreability index variation with different penetrations

All of the listed penetration test results show that the power varies in a narrow range from 0.60 to 0.79 in different rock mass conditions. These curves are proximately offset curves with different specific rock mass boreability index values, as shown in Figure 6.29. If a power is assumed to be 0.75, the deviations at each thrust level in every test are listed in Table 6.7, based on the specific rock mass boreability index and the power function. The maximum deviation of the predicted rock mass boreability index is close to 18%, for the granite-gneiss rock mass. The deviations in other rock masses are less than 10%. Only if the granite rock masses are taken into consideration, the maximum deviation of the predicted rock mass boreability index is less than 8.5%. TBMs are usually operated with a limited thrust force under the hard rock conditions. In most cases, TBMs can efficiently fragment rock mass and the penetration is more than 1 mm per revolution. Generally, the estimated rock mass boreability index is somewhat less than the actual value as the power is taken to be 0.75. On the contrary, the estimated specific rock mass boreability index is somewhat greater than the actual value if the power of 0.75 is used. For the penetration prediction, the estimation is conservative. Hereafter, the specific rock mass boreability index is estimated using the power equal to 0.75 and applied to evaluate the specific rock mass boreability index in T05 and T06.

Table 6.7 Deviation analysis while using the specific rock mass boreability index with a power of 0.75 to calculate the boreabiltiy index

Rock type	Thrust per cutter (kN)	Penetration per revolution (mm)	Boreability index (kN/cutter/mm/rev)	Predicted boreabiltiy index (kN/cutter/mm/rev)	Deviation (%)
Granite-gneiss	175.00	2.93	59.73	53.88	9.79
	87.50	0.47	186.17	212.58	-14.19
	105.00	0.86	122.09	135.12	-10.67
	122.50	0.90	136.11	130.59	4.05
	140.00	1.29	108.53	99.69	8.14
	157.50	1.76	89.49	78.97	11.75
	175.00	2.43	72.02	62.00	13.91
	192.50	3.17	60.73	50.79	16.36
	210.00	4.17	50.36	41.35	17.89
Granite (Emolweni tunnel)	75.00	0.04	1875.00	1903.23	-1.51
	100.00	0.14	714.29	743.77	-4.13
	125.00	0.36	347.22	366.28	-5.49
	150.00	0.60	250.00	249.70	0.12
	175.00	1.12	156.25	156.36	-0.07
	200.00	1.84	108.70	107.75	0.87
	220.00	2.72	80.88	80.37	0.63
	240.00	3.33	72.07	69.06	4.18
Sandstone with quartzitic matrix	100.00	0.14	714.29	735.43	-2.96
	120.00	0.22	545.45	523.98	3.94
	140.00	0.34	411.76	378.03	8.19
	160.00	0.56	285.71	260.01	9.00
	180.00	1.15	156.52	151.57	3.16
	200.00	2.69	74.35	80.13	-7.78
	220.00	3.84	57.29	61.36	-7.10
	100.00	0.14	714.29	735.43	-2.96
Granite (T05, DTSS)	237.12	1.62	146.49	144.94	1.06
	147.68	0.18	817.25	750.48	8.17
	156.28	0.29	543.42	529.65	2.53
	173.67	0.47	368.32	365.54	0.75
	204.07	0.92	222.40	221.86	0.24
	237.50	1.98	120.05	124.70	-3.87
Granite (T06, DTSS)	74.86	1.74	43.05	40.42	6.12
	79.50	2.61	30.51	29.84	2.19
	83.79	3.37	24.89	24.62	1.05
	91.69	4.60	19.94	19.49	2.25
	97.14	4.61	21.07	19.45	7.68
	97.29	5.38	18.08	17.33	4.19
	98.46	6.47	15.21	15.08	0.84
	109.97	7.48	14.70	13.53	7.95
	110.36	8.74	12.63	12.04	4.65
	112.77	9.11	12.38	11.67	5.70

Although the proposed specific rock mass boreability index eliminates the influence of TBM operation (cutter force, RPM and torque), the value of the specific rock mass boreability index is still affected by TBM specifications, such as cutter spacing, cutter diameter and tip width, cutterhead stiffness. As analyzed in Chapters 2 and 3, a stiff cutting system reduces the machine vibration and cutter shock loads, and increases rock fragmentation efficiency. The cutter geometry and cutter spacing directly affect the cutter indentation and rock chipping process. In order to obtain a specific rock mass boreability index not influenced by the TBM specifications and its operational parameters, a large number of TBM penetration tests in different rock mass conditions with different TBMs should be performed in the future. Then, a correction factor is possibly obtained to adjust the specific rock mass boreability index for different TBM specifications. The independent specific rock mass boreability index can be extensively applied to predict and compare the TBM performance.

6.6 Summary

The definition of rock mass boreability is introduced in this chapter. It is a comprehensive variable that is not only relevant to the rock mass conditions, but also to the tunnel boring machine parameters and the operating factors as well. In order to eliminate the influence of the machine factors (cutter number, cutter spacing, thrust force), a normalized parameter, rock mass boreability index is proposed to represent the rock mass boreability. However, the boreability index is not a constant for different operating thrust forces.

In order to accurately assess the rock mass boreability, a series of TBM front shield friction tests were conducted in T06 north drive. It was found that the friction force between the front shield and the tunnel wall is about 50 kN. Then, two kinds of typical TBM penetration tests were conducted in fresh granite with few joints in T05 north drive and in moderately weathered moderately fractured granite in T06 north drive respectively. With the increase of the thrust force per cutter, the penetration per revolution increases. However, a critical point exists in these correlation curves. The penetration per revolution increases rapidly with increasing thrust per cutter when the thrust per cutter is higher than the critical value. The critical point is located at the penetration per revolution between 0.5 mm/rev to 1.0 mm/rev. The muck sieve test results verified that with increasing thrust force, the muck size increases and the rock breakage efficiency also increases. Only if the thrust force is more than the critical value, are the mucks well-graded. The muck shape analysis results also showed that with the increase of the thrust, the chip shape varies from flat to elongated and flat.

Besides the penetration tests conducted in Singapore, some penetration test data by Dr. Ernst Buchi are collected. The correlation between the rock mass boreability index and the penetration per revolution is fitted well to a power function. The correlation coefficient is close to 1. Because the boreability index is a function of the thrust, the boreability index at 1.0 mm/rev close to the critical point, defined as the specific rock mass boreability index, is proposed to evaluate the rock mass boreability. It can be obtained from the correlation curve between the boreability index and the penetration per revolution. The powers of all fitting power functions fall in a narrow range. A constant 0.75 can be used to estimate the specific rock mass boreability index.

Based on the in situ TBM friction and penetration tests, the specific rock mass boreability index in the corresponding rings was obtained. Based on the correlation among the penetration per revolution, rock mass boreability index, specific rock mass boreability index, the specific rock mass boreability index of each ring in the established database in Chapter 5 was obtained. The results were listed in Appendix B. In next chapter, the correlation between the specific rock mass boreability index and rock mass properties would be progressively analyzed.

Chapter 7 Rock Mass Characteristics (RMC) Model

7.1 Introduction

The database of rock mass parameters and TBM performance has been established in Chapter 5. The rock mass boreability was analyzed in Chapter 6. In this chapter, a prediction model is set up based on the established database and rock mass boreability analysis. Firstly, the statistical method is described and the distribution characteristics of these parameters in the database are revealed. Then, the statistical model is obtained by performing a nonlinear statistical analysis using a commercial nonlinear regression software, NLREG. After that, the effect of each rock mass parameter on TBM penetration rate is analyzed. Finally, the limitations of this rock mass characteristics (RMC) model are discussed. Compared with other commonly used models, the advantages and shortcomings of this model are identified.

7.2 Development of Prediction Equation

7.2.1 Statistical Method

Nonlinear Regression Analysis

The goal of nonlinear regression is to fit a model to these given data. The program finds the best-fit values of the variables in the model which can be interpret scientifically. Choosing a model is a scientific decision. The model choice should not be based solely on the shape of the graph. It should be based on the understanding of the physical process. The nonlinear regression follows the below steps: a) Start with an initial estimated value for each variable in the equation. b) Generate the curve defined by the initial values. Calculate the sum of the squared residuals. c) Adjust the variables to make the curve come closer to the data points. d) Adjust the variables again so that the curve comes even closer to the points. Repeat many times. e) Stop the calculations when the adjustments make virtually no difference in the sum-of-squares. f) Report the best-fit results.

Estimating Parameters

NLREG uses a model/trust-region technique along with an adaptive choice of the model Hessian. The algorithm is essentially a combination of Gauss-Newton and Levenberg-Marquardt methods (Sherrod, 1996). The basis for the minimization technique is to compute the sum of the squared residuals for one set of parameter values and then slightly alter each parameter value and re-compute the sum of squared residuals to see how the parameter value change affects the sum of the squared residuals. If the function being modeled is well behaved, and the starting value for the parameter is not too far from the optimum value, the procedure will eventually converge to the best estimate for the parameter.

Parameters’ *t* Statistic and *Prob(t)*

The *t* statistic is computed by dividing the estimated value of the parameter by its standard error. This statistic is a measure of the likelihood that the actual value of the parameter is not zero. The larger the absolute value of *t*, the less likely that the actual value of the parameter could be zero. The *Prob(t)* value is the probability of obtaining the estimated value of the parameter if the actual parameter value is zero. The smaller the value of *Prob(t)*, the more significant the parameter and the less likely that the actual parameter value is zero.

Model Quality

The *proportion of variance explained* (R^2) indicates how much better the function predicts the dependent variable than just using the mean value of the dependent variable. This is also known as the *coefficient of multiple determination*. It can be calculated as follows:

$$\left.\begin{aligned} R^2 &= 1 - SSE/SST \\ SSE &= \sum (y_j - \hat{y}_j)^2 \\ SST &= \sum (y_i - \bar{y})^2 \end{aligned}\right\} \tag{7.1}$$

Because the objective of regression analysis is to find a model that is simple and provides a good fit to the data, usually the *adjusted coefficient of multiple determination* is also given to evaluate the model quality. R^2 is often adjusted for the number of parameters in the model and the number of data observations by Equation (7.2). It is a more conservative estimate of the percentage of variance explained, especially when the sample size is small compared to the number of parameters.

$$R_a^2 = 1 - \frac{n-1}{n-k} \times (1 - R^2) \tag{7.2}$$

where n is the number of observations; k is the number of parameters.

F-test for the Model Utility

F-test tests the null hypothesis that all of the regression coefficients are equal to zero. This tests the full model against a model with no variables and with the estimate of the dependent variable being the mean of the values of the dependent variable. The *F* value is the ratio of the mean regression sum of squares divided by the mean error sum of squares. The value of *Prob(F)* is the probability that the null hypothesis for the full model is true. A low value would imply that at least some of the regression parameters are nonzero and that the regression equation does have some validity in fitting the data.

Assessing Model Adequacy

A normal probability plot of the residuals is used as a basis for validating the normality assumption. The correlation between the residuals and their expected values is plotted in the graph. If the residuals are normally distributed, the correlation value should be close to 1.00. A correlation coefficient (r) less than 0.94 suggests that the residuals are not normally distributed (Sherrod, 1996).

7.2.2 Database Properties

Based on the extensive rock material strength experiments and tunnel face mappings, the parameters that characterize the rock mass boreability were obtained. The corresponding TBM performance data were collected and analyzed to calculate the specific rock mass boreability index (SRMBI). The data collection process was discussed in details in Chapter 5. Although many tunnel face mappings have been conducted during tunnel construction, only part of these were used to establish the database, because no corresponding core rock samples were obtained in some locations due to the time-consuming coring process. Some rock experiment results were not used either, because these samples failed along certain structural weak planes. Only a total of 47 data sets were used for the correlation analysis.

Figures 7.1 to 7.5 show histograms of the variables in the established database. These graphs present the range and cumulative distribution curve of each parameter. Figure 7.1 shows the range of the angle between the tunnel axis and the joint plane, which is mainly distributed between 0º and 80º. As the angle is close to 90º, it is difficult to be observed at the tunnel face. Generally the angle is evenly distributed from 0º to 80º except the range between 20º and 30º. Figure 7.2 shows the range of the volumetric joint count (J_v), which is between 0 and 30. In most cases, the volumetric joint count is less than 15 in the mapped granitic rock masses. The results are consistent with the joint investigation in Mandai granite (Zhao et al., 1995; Zhao, 1996). Figure 7.3 shows the range of the rock uniaxial compressive strength, which is between 100 MPa and 260 MPa. The UCS mainly concentrates between 160 MPa and 200 MPa, which is the normal compressive strength of fresh granite found in Singapore. Figure 7.4 shows the range of the rock brittleness index which ranges from 8 to 22. The high frequency zone is from 14 to 16. Figure 7.5 shows the range of the specific rock mass boreability index, which varies from 110 kN/cutter/mm/rev to more than 210 kN/cutter/mm/rev. It mainly distributes in the range between 130 kN/cutter/mm/rev and 210 kN/cutter/mm/rev.

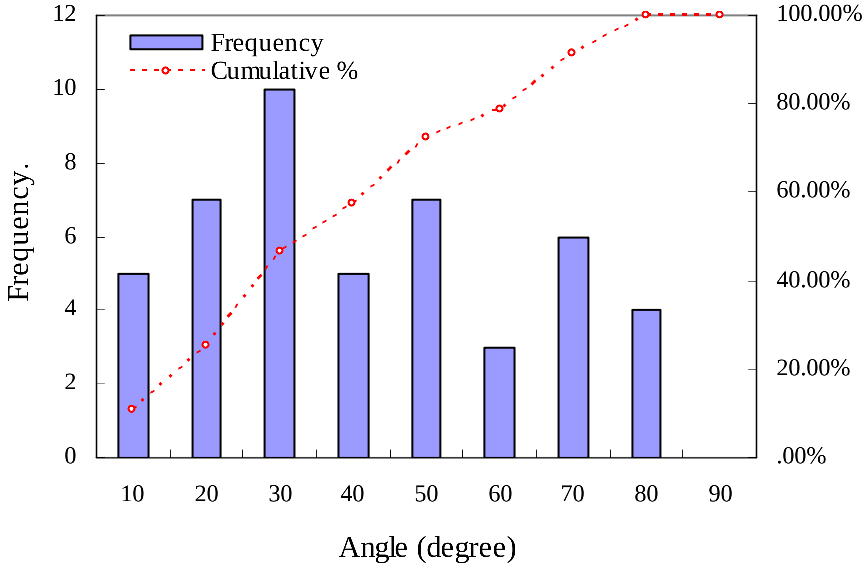

Figure 7.1 Histogram of variation of the angle between tunnel axis and joint plane in the database

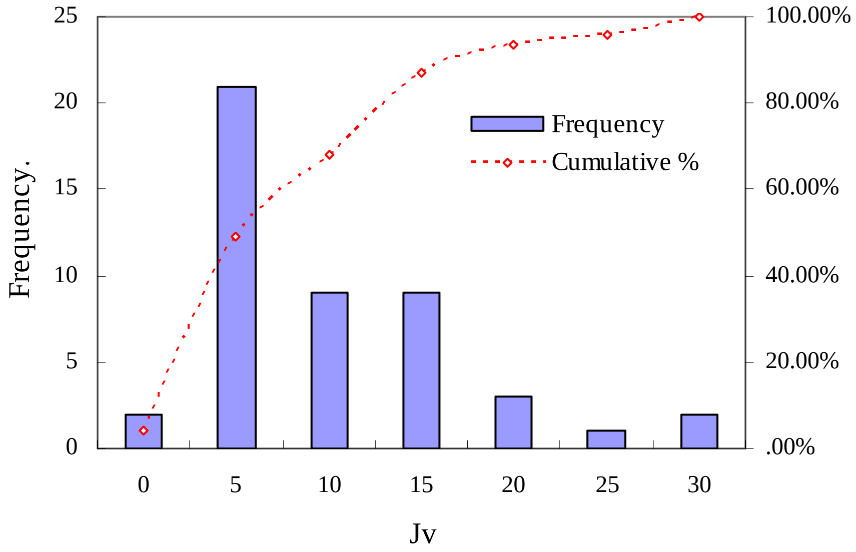

Figure 7.2 Histogram of Jv variation in the database

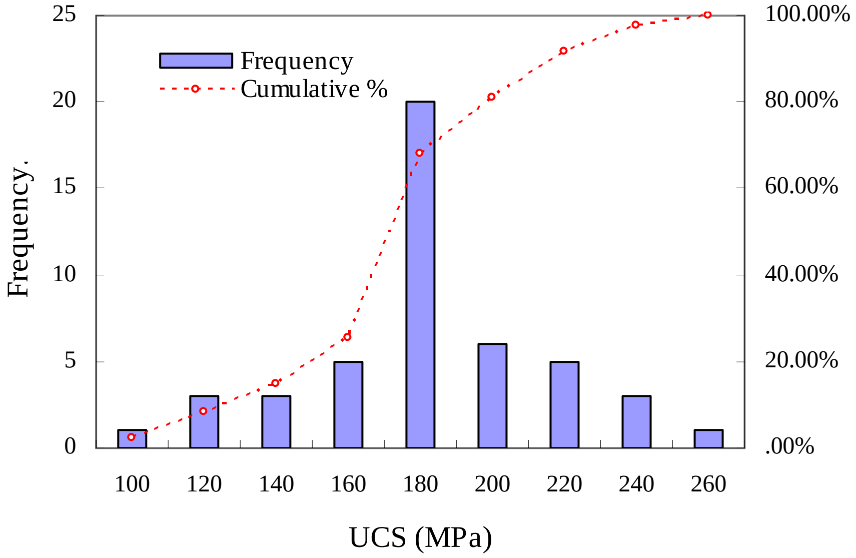

Figure 7.3 Histogram of UCS variation in the database

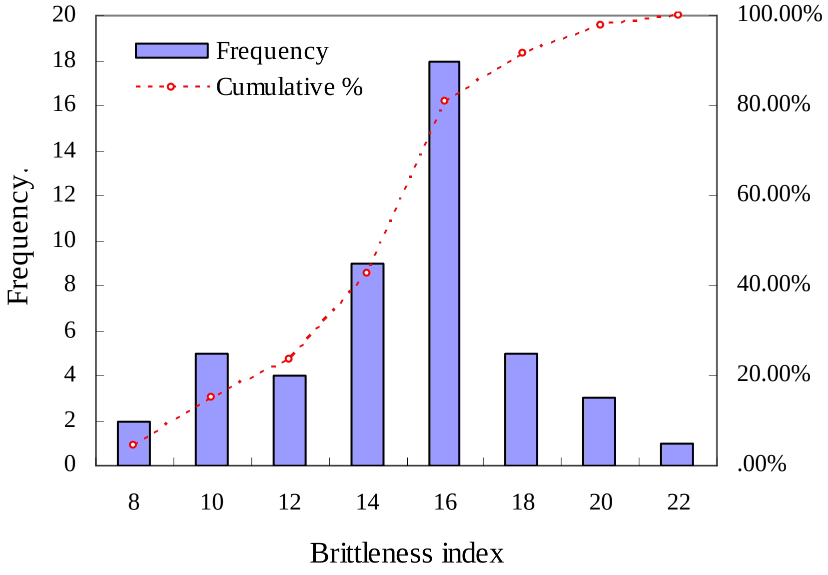

Figure 7.4 Histogram of brittleness index variation in the database

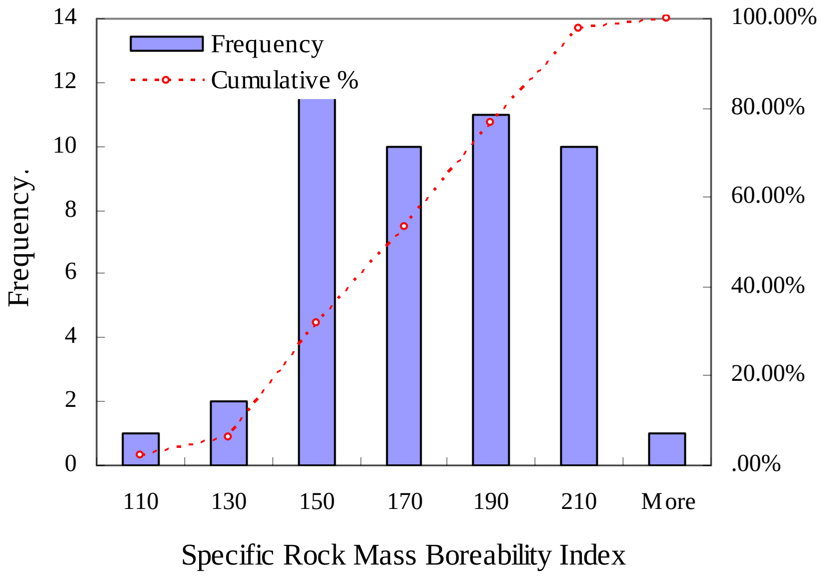

Figure 7.5 Histogram of the specific rock mass boreability index variation in the database

7.2.3 Regression Analysis Results

A nonlinear regression analysis was carried out to set up a relationship between the rock mass parameters and the specific rock mass boreability index (SRMBI), using the previous proposed statistical method based on the obtained database. Nonlinear Regression Analysis Program (NLREG) was used for the regression analysis to find out the best combination of parameters to express the relationship between the rock mass parameters and the specific rock mass boreability index. After a series of modeling of parameters combination, the best model found is as follows:

$$BI_{(1)} = 37.0588 \cdot UCS^{0.2617} \cdot Bi^{-0.1001} \cdot (0.8384 e^{-0.05455 \cdot Jv} + e^{-0.087 \cdot \sin(\alpha+30)}) \tag{7.3}$$

where $BI_{(1)}$ is the specific rock mass boreability index; UCS is rock uniaxial compressive strength (MPa); *Bi* is rock brittleness index; Jv is the volumetric joint count and α is the angle between tunnel axis and joint plane.

The *F*-test related to the utility of the overall regression model was carried out. The model statistic value *F* and *Prob(F)* are 24.53 and 0.00001 respectively. The null hypothesis can be rejected. That means at least one of the independent variables,

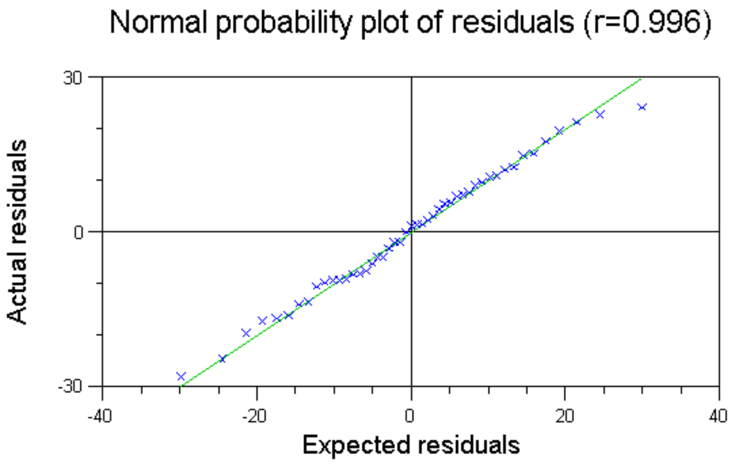

Figure 7.6 Correlation between the actual residuals and the expected residuals

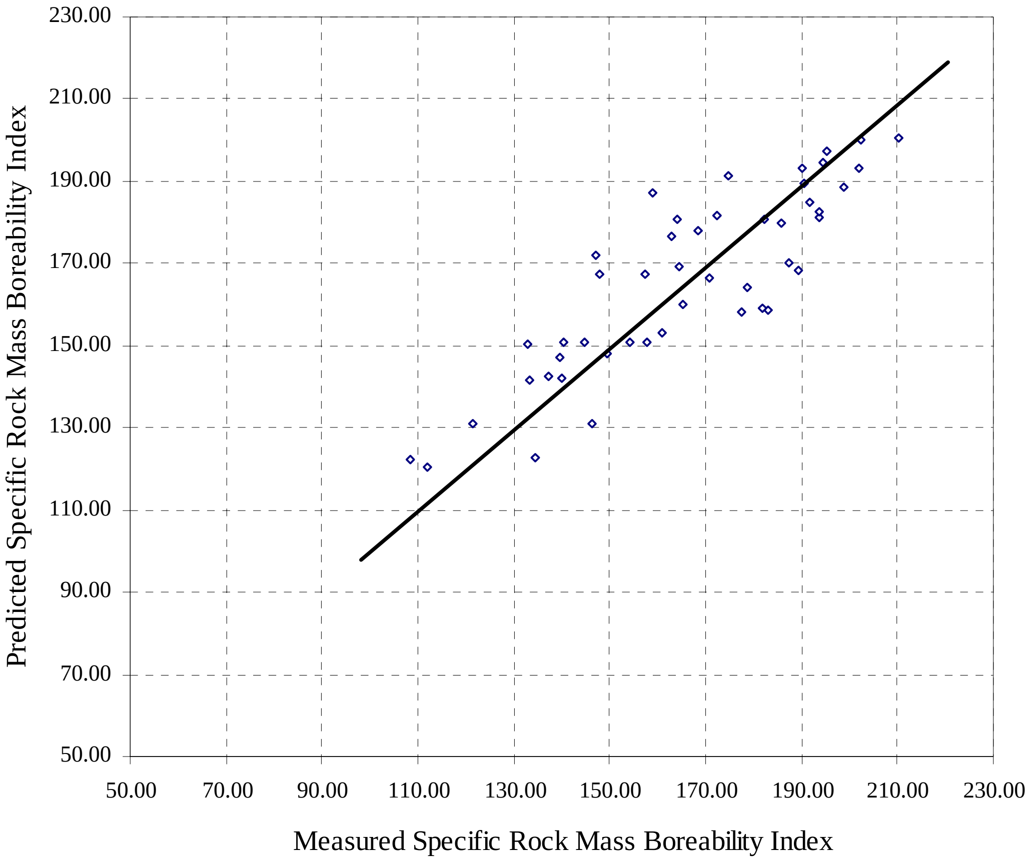

Figure 7.7 Comparison between the measured and predicted specific rock mass boreability index

namely the four rock mass parameters significantly affects the specific rock mass boreability index.

Based on the statistical results, the proportion of variance explained (R^2) is 74.94% and the adjusted coefficient of multiple determination ($R_a{}^2$) is 71.89%. It indicates that the above regression model explains 74.94% of the total variance of the 47 data sets. The model adequacy was also assessed. The relationship between the residuals and their expected values was plotted in Figure 7.6. The correlation coefficient (r) is 0.996, which is very close to 1.

The measured specific rock mass boreability index is compared with the predicted one, as shown in Figure 7.7. Most of the residuals are less than 10 kN/cutter/mm/rev. The statistical results are listed in Appendix D.

7.3 Effect of Rock Mass Parameters on Specific Rock Mass Boreability Index

Based on the rock mass properties, the statistical model to predict the specific rock mass boreability index was established and its utility, quality and adequacy were assessed in the above section. To study the behavior of these parameters that govern the specific rock mass boreability index equation, and then the effect on the performance of tunnel boring machine, four parametric studies are performed. When the effect of one parameter on specific rock mass boreability index is in study, the other three remain constant, so that the correlation between the studied parameter and the specific rock mass boreability index can be obtained.

7.3.1 Effect of Rock Uniaxial Compressive Strength

When the angle between tunnel axis and joint plane, rock brittleness index and volumetric joint count were held constant, the effect of rock uniaxial compressive strength on the specific rock mass boreability index was studied. Figure 7.8 shows the relationship between rock uniaxial compressive strength and specific rock mass boreability index. In the graph, the values for UCS are varied from 20 MPa to 360

MPa. The specific rock mass boreability index increases with increasing UCS. With the change of UCS, the specific rock mass boreability index varies in a great range. The analysis shows that UCS has a significant effect on the specific rock mass boreability index. The curve can be divided into two sections. One is that for UCS less than 100 MPa, the specific rock mass boreability index increases rapidly with increasing UCS. It means the specific rock mass boreability index is mainly controlled by the rock uniaxial compressive strength. The other is that for UCS more than 100 MPa, the specific rock mass boreability index increases approximately linearly with the increase of UCS. But, the slope of the curve decreases with the increase of the volumetric joint count from 5 to 20, as shown in Figure 7.8. It means the effect of UCS on the specific rock mass boreability index is less significant at higher value of volumetric joint count.

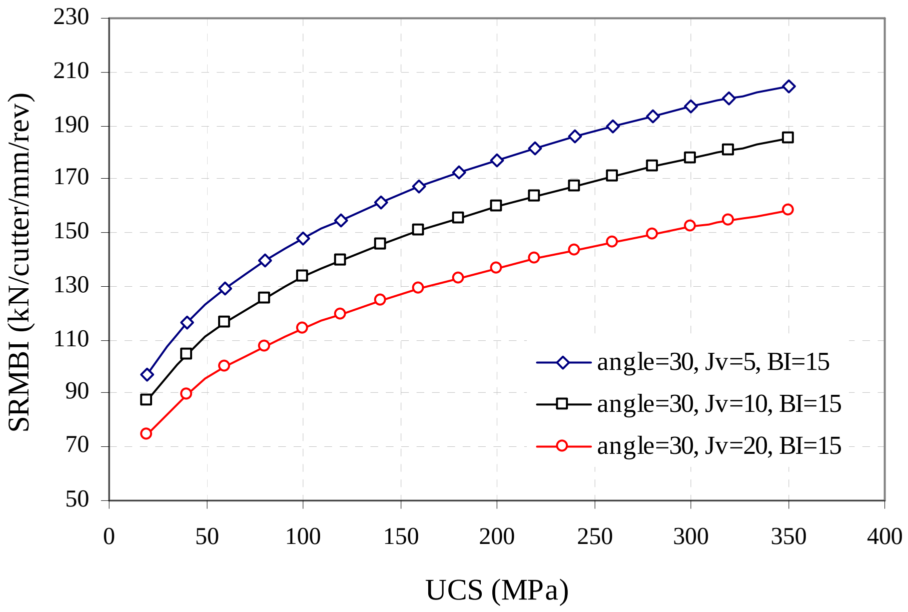

Figure 7.8 Effect of UCS on specific rock mass boreability index

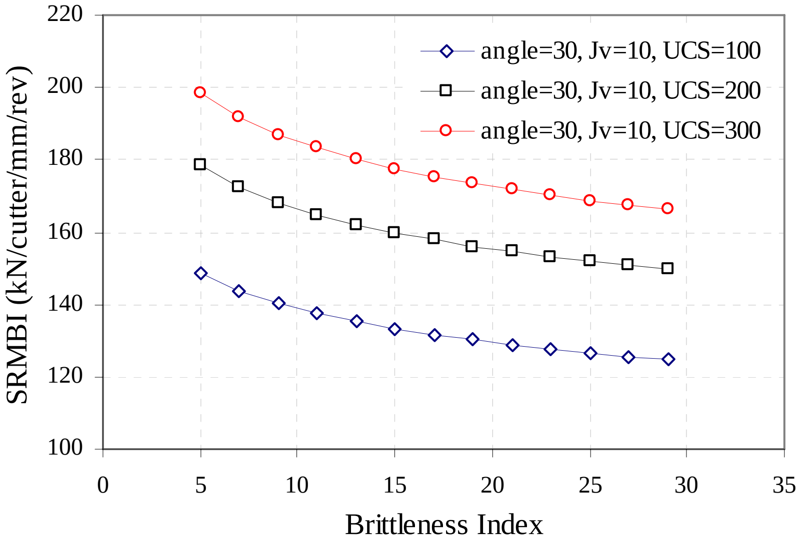

Figure 7.9 Effect of Brittleness index on specific rock mass boreability index

7.3.2 Effect of Rock Brittleness Index

In order to analyze the effect of rock brittleness index on specific rock mass boreability index, the angle between tunnel axis and joint plane, volumetric joint count and UCS were held constant. The values for rock brittleness index vary from 5 to 29. The relationship between brittleness index and specific rock mass boreability index is shown in Figure 7.9. With increasing rock brittleness index, the specific rock mass boreability index decreases. The analysis shows that the brittleness index has a greater effect on the specific rock mass boreability index at higher values of UCS.

7.3.3 Effect of Joint Spacing

Figure 7.10 shows the relationship between volumetric joint count and specific rock mass boreability index, when the angle between tunnel axial and joint plane, rock brittleness index and UCS were held constant. The analysis reveals that the volumetric joint count has a significant effect on the specific rock mass boreability index. When J_v varies from 0 to 45, the specific rock mass boreability index varies in a large range. As J_v is less than 5, the specific rock mass boreability index decreases approximately linearly with increasing J_v. With J_v more than 30, the effect of J_v on the specific rock mass boreability index decreases. At higher values of UCS, the effect of J_v on the specific rock mass boreability index increases. As shown in

Figure 7.10, the distance between the two curves of UCS 100 MPa and UCS 200 MPa is more than that between the two curves of UCS equal to 200 MPa and 300 MPa.

7.3.4 Effect of Joint Orientation

When rock uniaxial compressive strength, rock brittleness index and volumetric joint count were held constant, the effect of the angle between tunnel axis and joint plane on the specific rock mass boreability index was analyzed. Figure 7.11 shows the relationship. With the increase of the angle from 0º to 90º, the specific rock mass boreability index decreases at the beginning and then increases. It reaches the minimum value as the angle is equal to 60º. It can be seen from Figure 7.11 that the distance between the two curves at J_v equal to 15 and 10 is less than the distance between the two curves at J_v equal to 10 and 5. So, the angle has a greater effect on the specific rock mass boreabiltiy index at higher values of J_v. The specific rock mass boreability index varies in a narrow range with variation of the angle. Compared with the effects of rock uniaxial compressive strength, brittleness index and volumetric joint count, the angle has less significant effect on the specific rock mass boreability index.

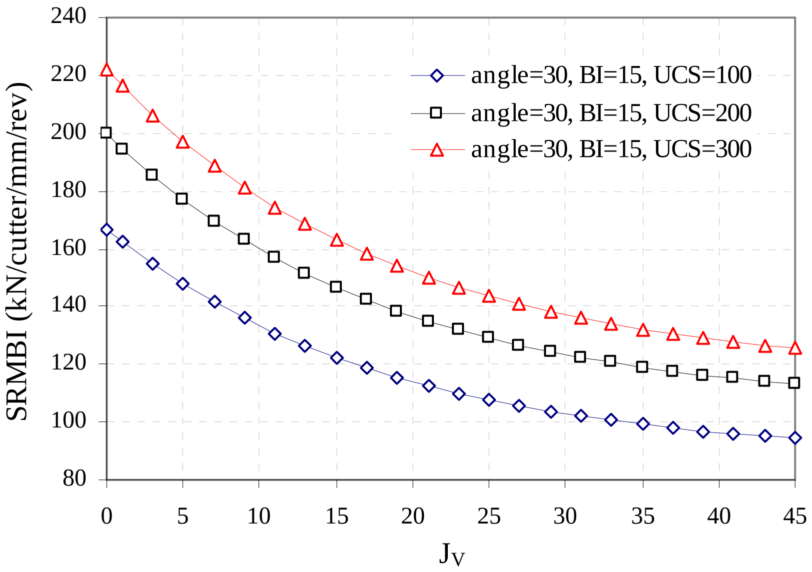

Figure 7.10 Effect of Jv on specific rock mass boreability index

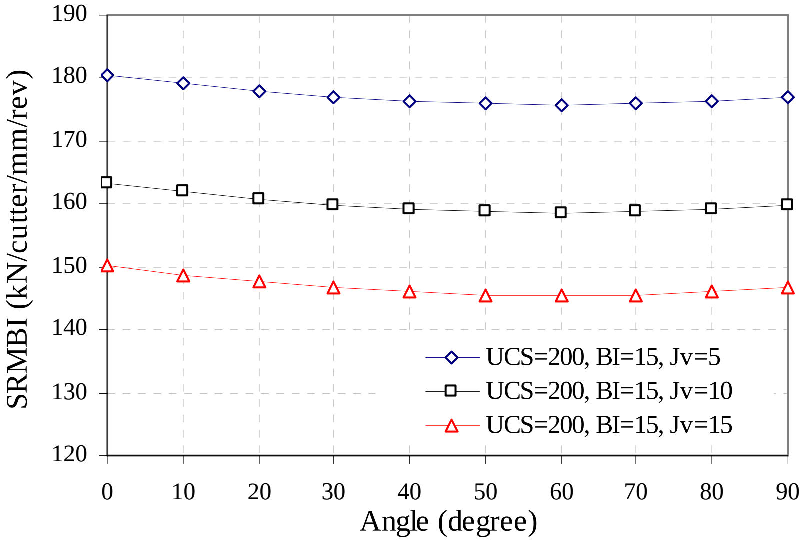

Figure 7.11 Effect of joint orientation on specific rock mass boreability index

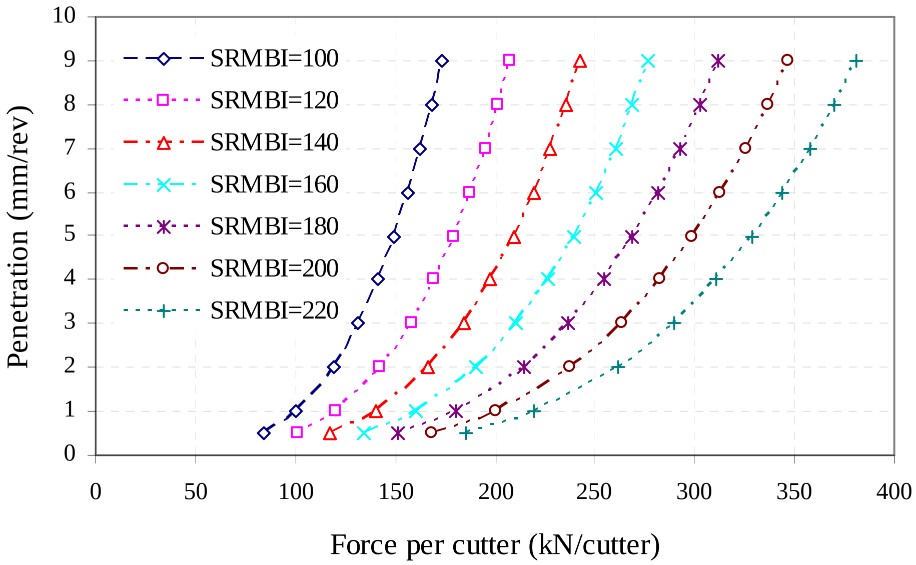

Figure 7.12 Penetration variation with thrust forces at different specific rock mass boreability indices

7.4 Relationships among Penetration, Specific Rock Mass Boreability Index and Thrust Force

In light of the results of penetration tests conducted in T05 and T06, the relationships among the rock mass boreability index, the specific rock mass boreability index and TBM penetration are estimated as follows:

$$BI \approx BI_{(1)} \cdot P^{-0.75} \tag{7.4}$$

where BI is the rock mass boreability index; $BI_{(1)}$ is the specific rock mass boreability index and P is the penetration per revolution.

According to the above correlation function, the relationships among the penetration rate, specific rock mass boreability index and thrust force are shown in Figure 7.12. When the specific rock mass boreability index is constant, the penetration rate increases with increasing machine thrust force. As can be seen, when the thrust force is more than a critical value, the penetration rate almost increases rapidly with the increase of the thrust force. With the increase of the specific rock mass boreability index, the corresponding thrust force to reach a certain penetration per revolution increases and as the thrust force is more than the critical value the slope of the curve decreases. For a given rock mass, the thrust force range that is required to fragment the rock mass efficiently can be decided. The results can help TBM design and optimize TBM efficient operation.

7.5 Effect of Rock Mass Parameters on Penetration Rate and Comparison with the Numerical Modelling Results

Combined the regression model and the relationships among rock mass boreability index, specific rock mass boreability index and thrust force, the effect of rock mass parameters on the penetration rate are revealed in this section. The results are compared with that of the numerical modeling obtained in Chapters 3 and 4. Since the regression model is based on the TBM performance in T05 and T06, DTSS, Singapore, the thrust force per cutter is assumed to be 200 kN in order to reflect the real TBM operation state. The rock mass conditions are also selected to stand for the typical rock mass conditions found in T05 and T06.

7.5.1 Rock Uniaxial Compressive Strength

As the thrust force was held at 200 kN/cutter, the relationship between UCS and penetration per revolution is shown in Figure 7.13. In the graph, the maximum penetration rate is taken as 12 mm/rev, because of the limits of the machine torque and muck removal capacity. Generally, the penetration rate decreases with increasing UCS. The penetration rate distributes in a large range from less than 1 mm/rev to more than 12 mm/rev due to the effect of UCS. It shows the UCS has a decisive influence on TBM penetration rate. It agrees with the theoretical analysis in Chapters 3 and 4. When the rolling cutter indents the rock mass, it is pressed at first into the rock surface, then forms a crushed zone in rock surface. Thus, the rolling cutter must overcome the rock strength.

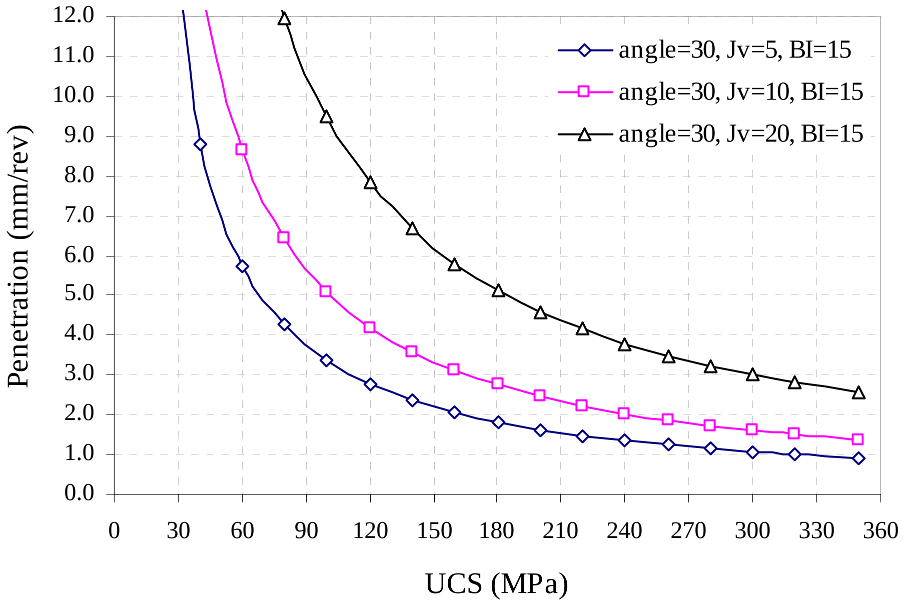

Figure 7.13 Penetration variation with different rock strengths at thrust force of 200 kN/cutter

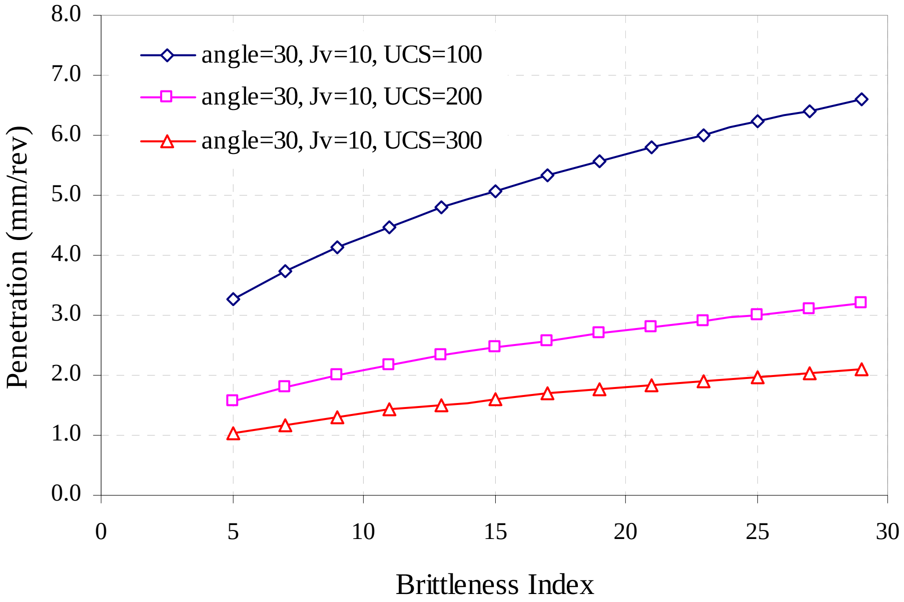

Figure 7.14 Penetration variation with different rock brittleness indexes at thrust force of 200 kN/cutter

7.5.2 Rock Brittleness Index

Figure 7.14 shows the relationship between rock brittleness index and penetration per revolution, as the thrust force was fixed at 200 kN/cutter and the other parameters were held constant. The penetration rate almost increases linearly with increasing rock brittleness index. The result coincides with the numerical simulation result. The numerical simulation shows that with the increase of the brittleness index, the crushed zone increases and the number and length of the main cracks outside the crushed zone also increase. It is obvious that with the increase of the rock brittleness index the cutter indentation process is getting easier. With increasing brittleness index, the failure elements increase linearly.

7.5.3 Volumetric Joint Count

The effect of volumetric joint count on the penetration rate is shown in Figure 7.15, as the thrust force was fixed to 200 kN/cutter and the other rock mass parameters were held constant. The penetration rate increases with increasing volumetric joint count. The curve can be divided into three sections as follows: the first section is when J_v is less than 5, the penetration rate almost increases linearly with increasing J_v; the second section is when J_v between 6 to 15, the penetration rate is sensitive to J_v and the incremental rate of the penetration rate increases with increasing J_v; the third section is when J_v is more than 15, the penetration rate almost increases linearly, but the incremental rate is higher than that in the first section. The results verify the rock breakage mechanisms in different joint spacings by numerical simulations in Chapter 4 are correct. When the joint spacing is within 80 mm, the side cracks can propagate to the joint plane and improve the yield of rock chipping. With the joint spacing more than 200 mm, the median crack cannot reach the joint plane. The joint spacings of 80 mm and 200 mm are two critical points in the graph. While the volumetric joint count is transferred into the equivalent joint spacing, the effect of joint spacing on the penetration rate are shown in Figure 7.16, together with the results of the numerical modeling conducted in Chapter 4 and the in situ measurements by Bruland (1998). All of the results reveal that due to the influence of the joint spacing, the penetration rate may increase more than nine times. The trend of the four curves shows very good agreement. The statistical model result is almost consistent with that of the numerical modeling, and slightly smaller than the in situ measurements by Bruland.

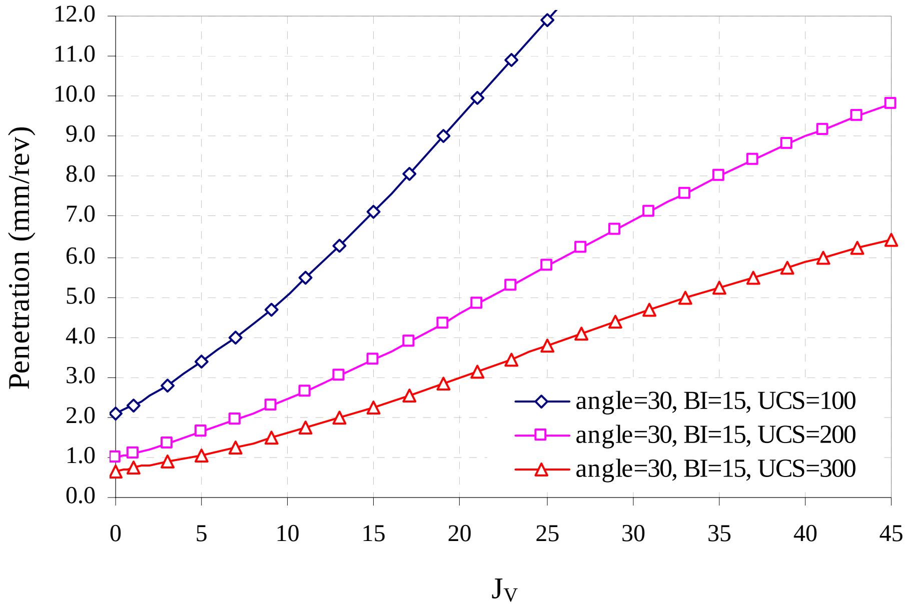

Figure 7.15 Penetration variation with different volumetric joint counts at thrust force of 200 kN/cutter

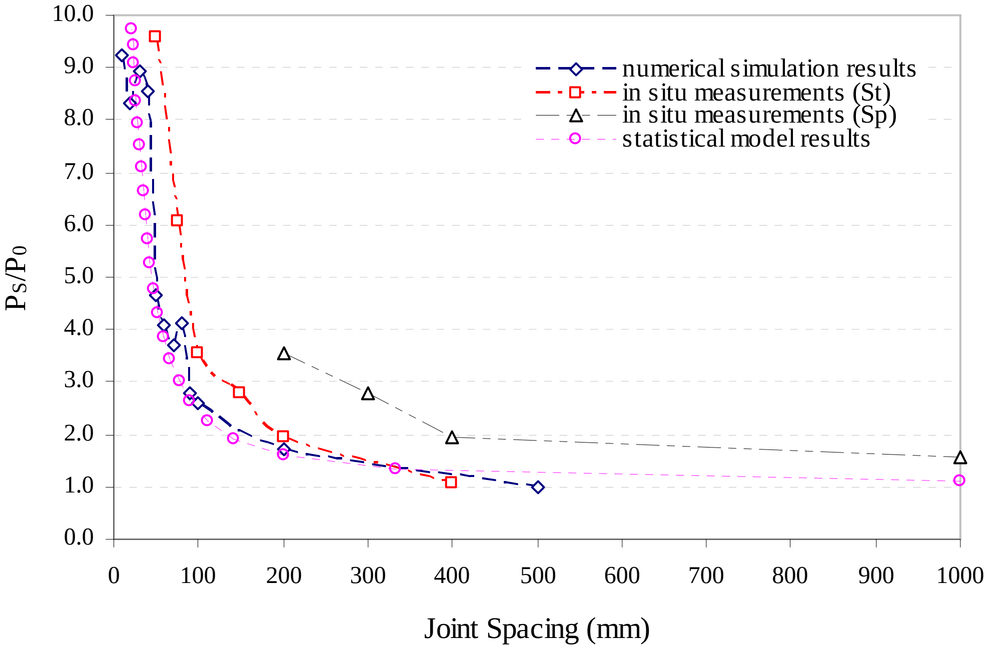

Figure 7.16 Effect of joint spacing on penetration rate

The difference between the statistical results and the in situ measurements may be derived from the joint classification. As described in Chapter 4, Bruland's (1998) results were based on the field observations and statistical analysis of over 250 km of TBM excavated tunnels in hard rock conditions for more than twenty years. The discontinuities are divided into two types in NTNU model, namely joints (Sp) and fissures (St), and five classes. These two types of discontinuities were independently measured and taken into account. The effect of each discontinuity class and its orientation on the TBM penetration rate was obtained. In this model, all discontinuities were regarded as joints and measured at the same time. In addition, during the tunnel face mapping, the joint properties such as the weathering grade, fillings and aperture were not recorded in details due to the time limit in the cutterhead chamber. The joint length can not be measured due to the small openings in the cutterhead and thus not taken into consideration in the model. In most cases, the joints in the granitic rock mass are tight and well matched, and the joint planes are fresh. These joint properties, which are the same with the numerical simulation, may also be the main reasons why the influence of joint spacing on the penetration rate in this model is less significant than that of the in situ measurements by Bruland (1998).

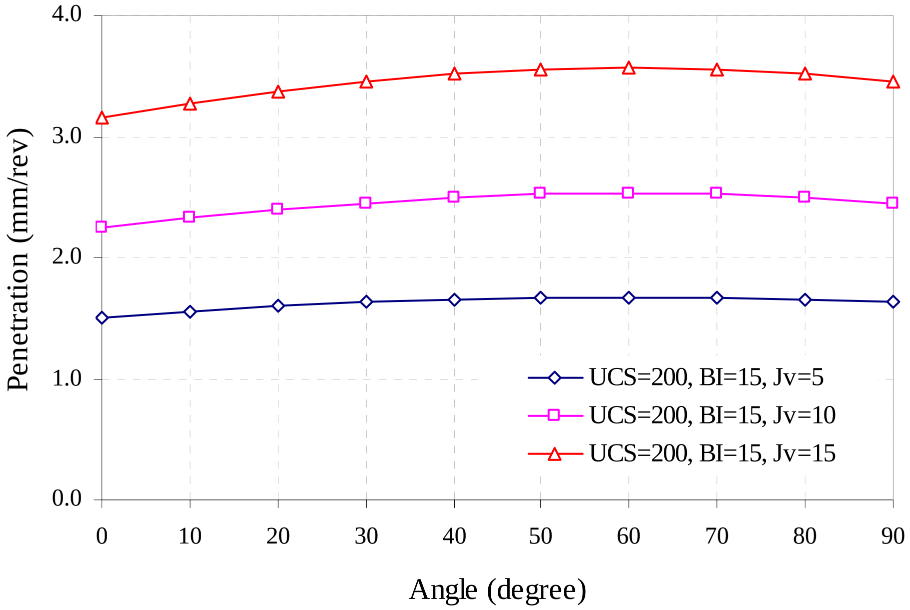

Figure 7.17 Penetration variation with different joint orientations at thrust force of 200 kN/cutter

7.5.4 Joint Orientation

Figure 7.17 shows the relationship between joint orientation and penetration per revolution, as the thrust force was fixed to 200 kN/cutter and the other rock mass parameters were held constant. The statistical model results present the same trend with the numerical simulation and the in situ measurements by Bruland (1998). The penetration rate increases with increasing angle between tunnel axis and joint plane as the angle is less than 60º, and then decreases with increasing angle. The penetration rate reaches the maximum value as the angle is equal to 60º. The influence of the angle on the penetration rate is smaller than that of the numerical simulation and the in situ measurements shown in Chapter 4. In the statistical data, the angle adopted is the angle between tunnel axis and the minimum spacing joint set. It does not take the angle of the other joint sets and random joints into consideration because it is very difficult to obtain the equivalent angle from several joint sets theoretically. The influence of these angles between tunnel axis and other larger spacing joint sets and random joints is neglected in this model. Another reason may be the error of the measurements during the tunnel face mapping. Due to the small openings in the cutterhead and time limit for surveying, it is very difficult to measure the angle directly. In most cases, the angle was estimated visually.

7.6 Model Limitations

7.6.1 Parameters of Tunnel Boring Machine

Although the thrust force per cutter is a normalized value by the cutter number in the statistical model, the stress level acting on the rock face is still greatly affected by the cutter diameter and cutter tip width even if the force per cutter is the same. In fact, it is the stress that influences the rock fragmentation process, as analyzed in Chapter 3. The linear cutting machine experiments performed by Snowdon et al. (1981, 1982) and the numerical simulation in Chapter 3 verified that there exists an optimal cutter spacing for different rocks in a certain penetration. The optimal cutter spacing in different rock mass also affects the machine efficiency significantly. In this model, the machine parameters are held constant. The cutter diameter is 432 mm and the cutter tip width 19 mm and the cutter spacing in the face cutters is 90 to 100 mm in T05 and T06. When the machine parameters are changed, especially cutter diameter, cutter tip width and cutter spacing, the model should be modified to consider the effects of these parameters.

7.6.2 Parameters of Rock Mass

All of the statistical data are based on the granitic rock masses found in Singapore in this statistical model. Although these rock mass parameters vary in a large range, as discussed in Section 7.2, the rock type is only granite formation. Lower values of rock strength and brittleness index are relevant to the weathering grades. The properties of joints are also affected by the weathering grades. So, the model really reflects the effects of the granitic rock masses with different weathering grades on TBM penetration rate. When the model is applied to rock masses other than granite, special attention must be paid due to the singularity of the original data of the statistical model.

7.6.3 Boundary Conditions

The boundary conditions of rock masses mainly include the in situ stress and ground water. The ground water may primarily impact the advance rate (Nelson, 1983; Laughton and Nelson, 1996). Tunnel instability accidents always occur with inflow of ground water. However, it has little effect on the penetration rate. The in situ stress impacts both the penetration rate and advance rate. If the in situ stress is not enough to promote stress slabbing at the face, the stress that acts on TBM cutters to form and propagate cracks increases with increasing confining stress (Cook et al., 1984; Liu et al., 2002) and the corresponding penetration rate decreases. If the in situ stress is high relative to rock strength to yield stress slabbing and the rock is not greatly overstressed or susceptible to bursting, the penetration rate may result in an increase (U. S. Army Corps of Engineers, 1997). Myrvang et al. (1998) and Boniface (2000) observed that the suitable in situ stress increases TBM penetration rate in actual tunneling projects. As the in situ stress is high and the rock is overstressed, the stress slabbing and spalling, raveling, face overbreak and ground squeezing may occur, which must be controlled with shield or cutterhead modifications and rock supports (Phien-wej and Cording, 1990; Myrvang et al. 1998). In this case, the penetration rate and advance rate are greatly affected.

In this model, the statistical data are collected from T05 and T06. The in situ stress in these tunnel sites is low relative to the rock strength. So, the model does not take the in situ stress into consideration. The effects of in situ stress on penetration rate should be further studied based on this model.

7.7 Comparison between the Rock Mass Characteristics (RMC) Model and Other Models

As mentioned earlier, over the years, researchers have made a great progress and models have been developed to predict the TBM penetration rate. The recent commonly used models include NTNU model (Bruland et al., 1995; Bruland, 1998), CSM model (Rostami and Ozdemir, 1993; Rostami et al., 1996; Cheema, 1999), and Q_{TBM} (Barton, 1999 and 2000; Barton and Jhun, 2000). CSM model is based on the cutting forces acting on the individual cutter that is obtained by laboratory linear cutting tests in various rock types with different cutting geometry. The basic principle is to start from the individual cutter forces and determine the overall thrust, torque and power requirement in terms of the cutterhead design. The estimated values are then compared with the machine installed thrust and power. The penetration rate of the machine is the maximum penetration per revolution that can be achieved with the available machine parameters. NTNU model and Q_{TBM} are empirical performance prediction models. They are based on the historical field performance of machines in different rock mass types with different cutters and cutterhead layouts. Then, a set of correlation graphs and empirical equations are proposed by correlation analyses between rock mass properties, machine parameters, and the penetration rate.

Because the philosophy behind each model is different and these models are originated from different data bases, the different input parameters are required in order to predict the penetration rate. The input and output of these models are listed in Table 7.1. Of course, the input parameters are also determined by these researchers' understanding on the rock cutting process. Due to the very complex nature of the problem, various parameters in different models are proposed to explain and correlate the penetration rate. CSM model is based on the laboratory tests. The cutting geometry can be fully controlled and explained. The cutting process and mechanisms by single cutter can be observed clearly. The cutting forces can be monitored by an acquisition system. The rock material properties can be obtained by experiments. Nilsen and Ozdemir (1993) stated "a great of advantage of the CSM model is that new and 'unexpected' rock conditions may be easily taken into account and machine optimization can easily be accomplished". But, the rock mass structure can not be modeled due to the experimental limitation and the variation of TBM operating parameters not taken into account. Moreover, the penetration rate predicted by this model is theoretically the maximum attainable penetration rate. Although this model is modified by Cheema (1999), it only indirectly takes joint conditions into consideration.

NTNU model originated from the achieved performance of the machine in the field. It naturally incorporates the effects of the ground, machine parameters and operating parameters into a whole system. The main advantage is the generally very comprehensive empirical data basis, where the important influence of rock jointing can be easily taken into account (Nilsen and Ozdemir, 1993). In this model, the input parameters, as shown in Table 7.1, include rock mass properties, machine parameters and TBM operating parameters. As can be seen, a drilling rate index (DRI) that expresses the resistance against impact load for prediction of percussive drilling (Bruland et al., 1995; Blindheim, 2004) is included in the rock mass properties. It is calculated from some special rock test results which are the brittleness value S_{20} and Siever's J-value (Blindheim and Bruland, 1998; Bruland, 1998). But, Kahraman (2001) found that the correlation between the penetration rate of rotary drilling, TBM excavation and rock brittleness defined by the impact test does not exist based on the correlation analysis, because the rock breakage process in TBM boring and rotary drilling is dominated by thrust and crushing. Furthermore, it is not convenient to perform this kind of tests outside Norway, which increases difficulties for the model users.

Q_{TBM} is modified from the Q-system, which originally was developed for rock support design. The input parameters for the penetration rate prediction are also listed in Table 7.1. The rock mass properties cover all of the parameters used for rock mass support assessment and additional factors influencing TBM performance. Among these parameters, CLI and quartz content are considered to mainly relate to cutter wear (Bruland, 1998). In the Q system, J_r/J_a represents the roughness and friction characteristics of the weakest significant joint or clay filled discontinuity that might pose instability. J_w/SRF indicates the stress levels in the tunnel that might result in the tunnel instability. Sundaram et al. (1998) concluded that the boreability of the rock mass does not depend on the properties that are selected for the purpose of stability assessment based on the correlation analysis between the field penetration index and J_r/J_a, J_w/SRF. In this model, some of the confirmed important machine parameters, such as cutter diameter and cutter spacing are not taken into account. Furthermore, the model includes a great number of parameters, and is quite complex (Blindheim, 2004).

Table 7.1 Input and output parameters of some models for TBM penetration rate prediction

Model	**Input parameters**			**Output parameters**
	Rock mass properties	**TBM parameters**	**Operating parameters**	
CSM model	Rock UCS(1) (psi) Rock tensile strength (psi)	TBM diameter (ft) Cutter radius (in) Cutter Tip width (in) Cutter spacing (in) Num. of cutters RPM (rev/min) Thrust (lbs) Torque (ft-lbs) Power (hp)		Basic penetration (in/rev.) Penetration rate (ft/hr)
NTNU model	Fracture frequency(2) Fracture orientation Drilling rate index (DRI)(3) Porosity (%)	Cutter diameter (mm) Cutter spacing (mm) TBM diameter (m) Num. of cutters RPM (rev/min)	Cutter load (Ton) Torque (kN-m)	Basic penetration (mm/rev.) Penetration rate (m/hr)
Q_{TBM}	RQD_o Joint set number Joint roughness Joint alteration Joint water reduction factor Stress reduction factor Cutter life index (CLI)(3) Quartz content (%) Rock mass strength (MPa) Induced biaxial stress (MPa)	TBM diameter (m)	Cutter load (Ton)	Penetration rate (m/hr)
RMC model	Rock UCS (MPa) Rock brittleness index Volumetric joint count Joint orientation	TBM diameter (m) Cutter diameter (mm) Cutter spacing (mm) Cutter tip width (mm) Num. of cutters RPM (rev/min)	Cutter load (kN) Torque (kN-m)	Basic penetration (mm/rev.) Penetration rate (m/hr)

(1) The modified CSM model uses a rock mass boreability index (RMBI) to replace the original rock UCS. RMBI is a function of the mass size reduction factor, rock elasticity modulus and Poisson's ratio (Cheema, 1999).

(2) Fractures are divided into joints and fissures which are progressively classified into five classes (Bruland, 1998).

(3) DRI is derived from the brittleness value S_{20} and Sievers' J-value. CLI is assessed on the basis of Sievers' J-value and the Abrasion Value Steel. The impact brittleness test, Sievers' miniature drill test and steel abrasion test consist of a set of NTNU special tests for TBM performance (Bruland, 1998).

The newly developed rock mass characteristics (RMC) model for the penetration rate prediction is based on the rock breakage process analysis. The parametric analysis of rock mass properties indicates that rock uniaxial compressive strength, rock brittleness index, joint spacing and joint orientation are the main factors influencing TBM penetration rate. A specific rock mass boreability index is proposed to express the rock mass boreability. Using the specific rock mass boreability index, the thrust force is normalized by the cutter number and the influence of the thrust force variation in operation is eliminated. It combines the cutting force analysis and correlation analysis between the actual penetration rate and rock mass parameters. But, more research works are needed to fine-tune and update the new model so that it can be applicable for more rock mass types excavated by different TBMs.

Based on the philosophy behind these models, each one has its advantages and shortcomings. For the potential users, two or more models may be used in order to take advantages of these models and get a more reasonable and comparable prediction value.

7.8 Conclusions

Based on the established database in Chapter 5 and the rock mass boreability analysis in Chapter 6, the prediction model for TBM penetration rate was set up in this chapter using multiple nonlinear regression analysis method. The effect of each rock mass parameter on the penetration rate was analyzed based on the new model. Of the four rock mass parameters, rock unaxial compressive strength and volumetric joint count have predominant effects on the penetration rate. With the increase of rock uniaxial compressive strength, the penetration rate decreases. The result coincides with the theoretical analysis. The penetration rate increases approximately linearly with increasing rock brittleness index. It reveals that the formation of rock chips is mainly caused by the tensile failure of rock, which is consistent with the numerical modeling. The penetration rate increases with increasing volumetric joint count. The penetration rate is sensitive to the variation of the volumetric joint count as it varies from 5 to 15. The model result shows a good agreement with the numerical simulation. The tendency is also consistent with the in situ measurements by Bruland (1998). The penetration rate increases with the increase of the angle between tunnel axis and joint plane, when the angle is less 60º, then decreases with increasing angle. The tendency is consistent with the numerical simulation and the in situ measurements by Bruland (1998). But, the effect of the angle on penetration rate is much less significant than that in the numerical modeling and the in situ measurements. The main reason is that in the model, only the angle of the minimum spacing joint set is taken into consideration. The statistical data are only collected from granitic rock masses in T05 and T06, Singapore. The machine parameters are fixed in these TBMs used in these two tunnels. Based on the above reasons, special attention must be paid when the model is used to predict the penetration rate in other rock masses or using different machine types. In this model, the effect of the in situ stress on the penetration rate is not taken into account.

Chapter 8 Conclusions and Recommendations

8.1 Conclusions

A rock mass characteristics (RMC) model for TBM penetration rate prediction in granite rock mass was developed in this study. The prediction model is based on rock mass properties and machine parameters. Especially, these parameters of rock mass properties used in the model are well defined in rock engineering and easily obtained in the site investigation or during the tunnel construction by geological mapping and normal rock mechanical experiments. These parameters include rock compressive strength, rock brittleness index, joint spacing and joint orientation. Its potential application on tunnel project planning and scheduling, choice of tunneling methods and TBM performance evaluation is promising.

The model was developed in four stages. At the first stage, the relevant literature was reviewed. The main factors influencing the TBM penetration rate were identified. Then, the rock breakage process was analyzed by numerical modeling. The rock fragmentation mechanism was revealed. The effect of each rock mass parameter on the penetration was analyzed based on the rock mass fragmentation process. Due to the existence of joints in rock masses, it changes the rock fragmentation mode, and furthermore, affects the penetration rate. At the third stage, an extensive field and laboratory test program was performed to develop a database of rock mass properties and TBM performance in various rock mass conditions. The work includes the collection of the site investigation data, the tunnel face mapping for joint spacing and orientation survey, rock coring in the tunnel face, rock strength tests in the laboratory, collection of TBM data, and TBM penetration data analysis. Finally, the established database was subsequently utilized to develop an equation between rock mass characteristics and the specific rock mass boreability index in order to predict the TBM penetration rate. The effect of each rock mass parameter on the penetration rate was analyzed and the results were compared with those of the numerical modeling.

The findings from the study can be summarized as follows:

1. The rock breakage process by TBM cutters is divided into two stages, namely rock indentation process and rock chipping process by two neighboring cutters. Rock indentation process by a TBM cutter is composed of the formation of a crushed zone, formation of minor cracks zone and major cracks propagation. Based on the above process, the side cracks, initiated from the crushed zone under the neighboring cutters, propagate to each other, and then coalesce to form rock chips. The crack initiation and propagation mainly follow the frontier of the tensile failure zones.

2. The main rock mass properties that influence TBM penetration process are rock compressive strength, rock brittleness, joint spacing and joint orientation. The rock compressive strength affects the formation of crushed zone. The higher the rock strength, the more load is required on the cutter. The rock brittleness affects the crushed zone size and cracks initiation and propagation in the rock indentation and chip formation. The higher rock brittleness results in easier rock fragmentation. Due to the existence of joints, the principal stress field is changed and the rock chipping process is affected. Two modes of crack initiation and propagation are observed to break the rock mass. One is that the crack initiates from the joint plane and propagates upward to the free surface. The other is that the crack initiates from the crushed zone and propagates downward to the joint plane. The increase of joint spacing results in the decrease of the penetration rate. The favorite joint angle between tunnel axis and joint plane for the penetration rate is 60º. With the increase or decrease of the angle from 60º, the penetration rate decreases.

3. The main machine parameters that directly influence rock fragmentation process and the penetration rate are cutter diameter and tip width, and cutter line spacing. The cutter force, torque, revolution per minute and other operational parameters also greatly influence the machine efficiency, and then the penetration rate.

4. By the in situ TBM penetration tests, the relations among the penetration per revolution, the cutter thrust and torque were analyzed. A specific rock mass boreability index was proposed to express the rock mass boreability. The specific rock mass boreability index is the normal cutter force over the penetration per revolution of 1 mm/rev. The mucks in different cutter thrust level were studied by sieve analysis. With increasing thrust force, the muck size increases and becomes well-graded, and the chip shape varies from flat to elongated and flat.

5. A database including TBM specifications, rock mass properties and the relevant TBM performance was established through extensive site data collection and laboratory experiments. The approaches to obtain these parameters were described in details. The database was then used to develop the RMC model for TBM penetration rate.

6. The RMC model for TBM penetration rate was set up based on the statistical analysis of the established database. It is determined by rock compressive strength, rock brittleness, joint spacing and joint orientation. The parametric analysis showed that of the four rock mass parameters, rock uniaxial compressive strength and volumetric joint count have a predominant effect on the penetration rate. With the increase of rock uniaxial compressive strength, the penetration rate decreases. The penetration rate increases approximate linearly with increasing rock brittleness index. It reveals that the formation of rock chips is mainly caused by the tensile failure of rock, which is consistent with the numerical modeling. The penetration rate increases with increasing volumetric joint count. The correlation curve between the penetration rate and the volumetric joint count can be divided into three sections. In the first section, the

penetration rate increases almost linearly with increasing volumetric joint count when the volumetric joint count is less than 5. But the increasing rate is smaller than that in the second and third sections. In the second section, the penetration rate increases nonlinearly with increasing volumetric joint count. In the third section, the penetration rate also increases almost linearly with increasing volumetric joint count, when the volumetric joint count is more than 15. The increasing rate is more than that in the first and second sections. The penetration rate is sensitive when the volumetric joint count varies from 5 to 15. It is in good agreement with the numerical simulations. The penetration rate increases with the increase of the angle between tunnel axis and joint plane, when the angle is less 60º, then decreases with increasing angle. The tendency is consistent with the numerical modeling. But the effect of joint orientation on the penetration rate in the new model is less significant than that in the numerical simulation.

8.2 Recommendations for Future Research

1. The RMC model is a statistical model based on the established database, which is only composed of granite rock masses along the alignment of T05, T06 tunnels of DTSS project. An extensive variety of rock mass types and rock mass properties from other TBM tunnel projects should be added to the database to update and fine-tune the model in the future.

2. The rock breakage mechanism induced by TBM cutters is the fundamental factor of the TBM cutterhead design, especially for the cutter spacing in different rock mass properties. Due to the limitations of UDEC, only the optimal cutter spacing of double cutters was simulated. If possible, the rock failure process under the action of two single TBM cutters with time spacing should be further studied using other numerical simulation methods. The influence of earth (confining) pressure on TBM cutter configuration should be also analyzed.

3. The in situ TBM penetration test directly presents the rock fragmentation efficiency by TBM cutterhead at different thrust level. During the tunnel

construction, the penetration test is not a time-consuming test if the test program is well designed. It is recommended to perform the penetration test for every rock type in every tunnel project. It will provide a better understanding of the fragmentation process of different rocks and rock masses under the action of different machines.

4. Although the proposed specific rock mass boreability index eliminates the influence of TBM operation (cutter force, RPM and torque), the value of the specific rock mass boreability index is still affected by TBM specifications. In order to progressively obtain a specific rock mass boreability index independent of the TBM specifications, a large number of TBM penetration tests in different rock mass conditions with different TBMs should be performed or collected in the future. Then, it is possible to obtain a correction factor for different TBM specifications. The independent specific rock mass boreability index can be extensively applied to predict and compare the TBM performance.

5. The penetration rate is determined by machine parameters and rock mass properties. The accuracy of rock mass properties obtained from the site investigation greatly influences the prediction result. The site geological background, such as geological structures, geological history, should be well understood. The outcrops near tunnel alignment should be surveyed. The joint system in the outcrops should be statistically analyzed. The geological data, such as RQD, joint spacing, joint orientation and other existing foliation in the rock core should be recorded in each borehole log. Especially, the rock test results in the laboratory should be carefully screened to exclude rock structural failures. During the construction stage, the geological mapping of tunnel face and wall and rock core strength tests should be performed in various rock mass types or evenly along the tunnel alignment to improve the accuracy of the prediction model.

6. Cutter wear is an important factor that influences the economy of TBM tunneling and TBM selection. The correlation between rock mass properties

including rock compressive strength, rock brittleness index, rock abrasive index, joint spacing and joint orientation, and cutter wear should be analyzed in the future study.

Appendix B

Summary of TBM Performance Data

TBM performance data in T05 north drive

Ring No.	Penetration (mm/rev.)	Torque cutting wheel (kNm)	Cutting wheel rotation speed	Pressure steering cylinder 01 (bar)	Pressure steering cylinder 04 (bar)	Pressure steering cylinder 05 (bar)	Pressure steering cylinder 08 (bar)	steering force (kN)	force per cutter (kN/cutter)	BI (kN/cutter /mm/rev)	SRMBI (kN/cutter /mm/rev)
N1638	3.47	2836.39	7.49	101.86	144.75	189.96	43.14	5361.87	164.07	47.35	120.25
N1819	3.64	3937.75	8.85	331.72	116.44	160.67	39.37	7458.26	222.19	61.13	160.92
N1845	4.53	3859.09	8.87	127.83	163.67	47.45	138.51	4199.78	163.29	36.09	111.96
N2006	2.79	2515.01	9.56	140.37	160.34	192.17	95.30	6066.81	201.49	72.35	155.97
N2014	2.21	2515.04	9.60	177.60	185.30	234.70	98.66	7331.72	238.77	108.29	195.95
N2022	2.10	2809.30	9.60	152.42	188.58	213.87	94.63	6815.94	222.65	106.02	184.95
N2023	3.16	3038.63	9.63	146.75	147.10	178.02	71.33	5814.08	185.97	58.85	139.49
N2057	2.09	2513.85	9.57	185.68	161.19	207.08	97.48	6804.35	223.31	106.85	185.72
N2065	2.23	2880.43	9.55	97.55	204.80	119.21	88.30	5205.56	174.47	78.24	142.77
N2071	2.30	3077.90	9.58	153.56	113.20	143.67	156.00	5071.53	193.99	84.34	157.52
N2097	3.08	3337.29	9.06	169.11	155.14	120.12	133.75	5474.96	198.02	64.40	149.54
N2103	2.30	2472.01	9.59	115.54	184.09	175.96	115.38	5858.33	202.45	88.02	164.39
N2118	3.56	3268.27	9.62	122.27	167.73	155.46	135.56	5494.94	199.02	55.90	144.89
N2127	2.55	3119.73	9.62	124.84	213.95	171.45	119.40	6277.09	215.79	84.62	170.76
N2131	3.25	3033.87	9.67	94.27	193.29	154.68	78.68	5456.72	178.28	54.86	132.78
N2136	3.12	3965.72	9.56	155.64	146.01	191.45	80.04	6069.53	196.30	62.92	147.70
N2264	3.32	3147.77	8.58	171.14	190.81	129.76	134.01	6040.79	214.44	64.69	158.92
N2335	2.44	2893.49	9.64	173.85	145.43	74.90	143.35	4875.92	184.01	75.42	147.23
N2346	3.86	3595.78	9.11	150.62	104.13	140.41	49.14	4881.35	151.85	39.34	108.33
N2375	1.94	2718.38	9.64	122.29	96.54	203.45	178.88	5215.28	205.97	106.44	174.63
N2382	1.74	1790.13	9.64	136.13	202.37	199.01	99.92	6606.68	218.48	125.93	190.36
N2493	1.05	1148.51	9.60	157.68	183.46	183.07	179.79	6445.72	241.45	229.95	238.52
N2496	2.51	3607.44	9.60	123.35	196.47	196.97	139.72	6356.12	225.07	89.67	178.81
N2533	4.78	2281.46	8.74	28.26	161.20	102.46	36.14	3630.33	111.75	23.40	75.60
N2552	4.96	3907.76	8.94	131.80	188.82	129.85	94.01	5547.16	186.41	37.58	124.91
N2572	2.16	2450.45	9.60	177.19	121.23	148.09	130.58	5507.38	197.66	91.51	163.05
N2612	3.91	3157.38	9.63	85.82	188.73	152.04	73.33	5267.15	171.04	43.74	121.63

TBM performance data in T05 north drive

Ring No.	Penetration (mm/rev.)	Torque cutting wheel (kNm)	Cutting wheel rotation speed	Pressure steering cylinder 01 (bar)	Pressure steering cylinder 04 (bar)	Pressure steering cylinder 05 (bar)	Pressure steering cylinder 08 (bar)	steering force (kN)	force per cutter (kN/cutter)	BI (kN/cutter /mm/rev)	SRMBI (kN/cutter /mm/rev)
N2639	3.48	3952.83	8.52	119.22	175.06	186.31	79.19	5905.93	191.69	55.08	140.35
N2728	1.81	2291.20	9.63	154.13	200.27	191.83	111.06	6711.73	225.33	124.84	194.40
N2735	1.58	1991.63	9.61	125.98	205.25	162.83	139.68	6081.66	217.21	137.47	193.74
N2759	1.88	2307.35	9.39	81.64	257.10	131.37	184.32	5789.81	224.35	119.33	191.59
N2762	1.79	2155.54	9.60	135.87	195.30	182.99	127.09	6324.25	219.80	122.79	190.02
N2811	3.64	3202.47	9.55	119.62	166.30	187.86	80.39	5836.12	189.76	52.20	137.43
N2829	3.74	3165.29	9.60	129.28	176.21	184.63	77.63	6034.03	194.44	52.06	139.87
N2841	3.75	3308.93	9.54	185.33	128.01	255.56	56.51	6984.50	214.33	57.16	154.02
N2870	3.49	3294.33	9.61	153.90	185.20	198.87	79.86	6611.99	211.72	60.67	154.90
N2876	4.10	2622.79	9.18	72.65	169.16	199.92	71.22	5444.65	175.53	42.87	123.40
N2882	1.88	2308.00	9.61	166.48	177.82	215.06	97.03	6870.27	225.02	119.69	192.17
N2886	1.78	2006.01	9.52	110.68	199.61	211.74	130.20	6418.25	223.59	125.61	193.57
N2888	1.98	2595.96	9.59	93.45	216.78	184.81	160.51	6093.19	224.73	113.50	189.45
N2890	2.71	3059.93	9.57	131.21	183.59	204.58	125.27	6386.85	220.97	81.69	172.30
N2894	2.74	2514.73	9.10	131.39	195.19	186.31	123.62	6302.87	218.16	79.77	169.65
N2898	2.22	2251.69	9.62	143.08	167.41	224.27	107.83	6573.17	220.26	99.44	180.55
N2902	1.35	2046.34	9.64	154.16	185.32	187.46	108.21	6478.99	217.69	161.25	201.96
N2906	1.70	2352.26	9.63	105.32	227.45	180.60	148.63	6315.07	226.96	133.90	198.91
N2911	1.37	1853.78	9.70	65.18	270.11	130.75	197.31	5744.35	227.42	166.61	210.40
N2914	1.32	2191.51	9.64	191.38	158.96	246.59	57.45	7324.17	224.33	170.59	209.48
N2917	3.58	2817.98	9.49	118.88	146.95	201.15	68.10	5753.22	183.17	51.16	133.16
N2920	3.06	2905.26	9.54	148.45	160.09	194.80	100.72	6192.93	206.97	67.75	156.55
N2925	3.28	3258.72	9.52	131.23	186.66	201.12	130.54	6381.78	222.66	67.88	165.45
N2929	3.62	3021.31	9.58	112.69	155.92	176.25	89.91	5487.21	183.06	50.64	132.76
N3003	6.59	2435.51	8.08	59.37	151.55	129.65	19.20	4209.86	122.69	18.63	76.59
N3017	3.89	3195.31	9.62	148.04	201.14	196.91	100.17	6710.04	221.53	56.95	157.74
N3024	3.82	3489.27	9.33	122.74	204.02	191.76	121.64	6373.69	219.42	57.44	156.95

TBM performance data in T05 north drive

Ring No.	Penetration (mm/rev.)	Torque cutting wheel (kNm)	Cutting wheel rotation speed	Pressure steering cylinder 01 (bar)	Pressure steering cylinder 04 (bar)	Pressure steering cylinder 05 (bar)	Pressure steering cylinder 08 (bar)	steering force (kN)	force per cutter (kN/cutter)	BI (kN/cutter /mm/rev)	SRMBI (kN/cutter /mm/rev)
N3028	4.29	3633.52	9.38	169.67	167.61	226.98	71.14	6926.54	217.78	50.82	151.37
N3033	3.63	3311.95	9.38	104.76	204.85	162.63	151.76	5815.41	213.85	58.99	154.98
N3041	3.62	3376.00	9.50	104.48	205.55	183.94	115.57	6079.25	208.86	57.77	151.47
N3050	2.65	2775.24	9.56	87.61	234.61	168.17	170.36	6036.62	226.52	85.64	177.62
N3055	2.81	2811.29	9.37	155.24	173.88	233.37	85.70	6904.99	222.19	79.07	171.61
N3068	2.73	2596.37	9.44	126.04	173.77	189.71	103.12	6024.79	203.03	74.37	157.95
N3074	2.63	2657.01	9.60	139.27	170.13	217.83	91.57	6482.07	212.05	80.63	166.52
N3082	1.78	1971.97	9.68	142.98	177.03	224.67	87.42	6693.62	216.64	121.71	187.56
N3091	3.16	2713.87	9.67	61.53	208.12	160.05	92.00	5305.36	178.56	56.51	133.92
N3094	2.05	2221.76	9.63	128.57	198.45	193.66	126.65	6403.46	221.90	108.24	185.45
N3100	1.51	1751.81	6.65	110.80	115.11	147.10	64.21	4584.19	149.41	98.95	134.78
N3103	1.92	2225.08	9.29	145.62	174.30	227.43	81.34	6721.39	215.47	112.22	183.05
N3107	1.77	1905.17	9.50	119.84	205.84	203.07	112.62	6499.09	219.84	124.55	190.73
N3115	1.90	2038.81	9.51	196.20	124.71	229.31	76.49	6758.46	214.78	113.34	183.06
N3119	1.74	1944.71	9.33	161.66	173.87	242.95	74.14	7097.77	223.72	128.58	194.79
N3127	1.91	2017.81	9.47	181.42	145.81	261.68	50.38	7225.28	219.12	115.03	186.52
N3135	1.44	1570.74	9.40	171.32	141.31	246.41	87.55	6863.69	221.64	153.92	202.33
N3141	2.43	2940.01	9.60	149.70	181.02	218.54	87.54	6748.02	218.26	90.01	174.90
N3164	3.19	2686.50	9.54	89.49	133.84	163.27	46.44	4783.18	147.97	46.38	110.72
N3171	2.45	2772.77	9.54	134.52	173.94	210.00	96.93	6375.50	210.88	86.07	168.55
N3174	1.89	2225.58	9.42	128.31	174.92	202.92	101.33	6225.29	208.15	110.13	177.52
N3180	2.20	2343.08	9.45	158.41	155.83	239.49	75.49	6800.30	215.65	98.24	177.17
N3189	1.96	2292.23	9.47	140.42	175.48	211.00	101.27	6476.45	215.29	109.84	181.95
N3193	1.92	1997.47	9.18	148.26	154.83	226.44	82.63	6504.89	209.77	109.25	178.20
N3196	2.48	2238.74	9.59	157.83	164.92	228.45	83.70	6771.44	217.61	87.75	173.41
N3200	2.70	2403.19	8.54	189.44	131.06	257.65	57.86	7084.06	217.99	80.89	170.14
N3211	2.15	2172.59	8.52	154.98	164.30	229.87	87.62	6733.71	218.25	101.75	180.34

TBM performance data in T05 north drive

Ring No.	Penetration (mm/rev.)	Torque cutting wheel (kNm)	Cutting wheel rotation speed	Pressure steering cylinder 01 (bar)	Pressure steering cylinder 04 (bar)	Pressure steering cylinder 05 (bar)	Pressure steering cylinder 08 (bar)	steering force (kN)	force per cutter (kN/cutter)	BI (kN/cutter /mm/rev)	SRMBI (kN/cutter /mm/rev)
N3214	2.03	2141.22	9.07	155.39	164.53	235.52	81.61	6816.24	218.35	107.56	182.93
N3219	2.22	2210.85	8.94	171.31	155.34	231.17	79.63	6843.47	218.49	98.64	179.09
N3230	2.27	2393.51	9.34	157.10	163.22	236.96	92.53	6841.78	222.75	98.34	181.57
N3234	2.30	2234.72	9.64	142.24	167.11	222.44	77.39	6537.55	208.73	90.95	169.59
N3245	2.55	1961.92	9.66	105.49	138.53	170.69	65.45	5124.18	164.22	64.53	130.02
N3257	2.37	2391.29	9.38	163.80	141.57	191.64	113.92	6114.44	209.34	88.33	168.72
N3262	3.12	3109.91	9.28	155.06	131.21	211.36	74.61	6120.72	195.99	62.92	147.52
N3270	2.83	2989.33	9.54	108.33	194.06	198.10	122.30	6158.34	213.43	75.55	164.62
N3272	3.08	2518.50	9.40	37.15	238.24	154.21	170.11	5300.90	205.47	66.71	155.10
N3281	1.60	1673.50	9.57	145.42	169.63	222.00	88.05	6600.22	214.23	134.31	190.63
N3289	2.09	2204.33	9.48	130.53	186.08	199.06	97.77	6341.03	210.21	100.58	174.83
N3297	2.13	2214.25	9.34	123.29	194.91	198.47	120.49	6351.41	218.39	102.77	180.88
N3305	1.69	1785.57	9.50	147.92	181.70	221.03	86.47	6763.65	218.37	129.60	191.67
N3314	1.94	2117.15	9.59	133.38	195.98	217.27	115.95	6716.32	227.16	117.09	192.48
N3322	2.10	2369.24	9.56	122.89	184.84	211.32	108.82	6382.75	215.18	102.71	178.86
N3326	2.05	2422.24	9.68	109.05	202.48	199.55	124.21	6288.02	217.74	106.22	181.97
N3344	2.70	2691.30	9.59	149.31	159.04	220.77	88.45	6504.83	211.63	78.38	165.09
N3356	1.97	2404.31	9.46	151.31	181.76	213.98	101.87	6719.64	222.44	112.91	187.76
N3372	3.56	3416.50	9.60	148.08	161.83	209.27	81.02	6384.80	205.63	57.76	149.70
N3389	3.68	2805.95	9.57	107.72	146.32	184.67	62.93	5412.83	171.63	46.70	123.96
N3414	3.53	3267.37	9.37	148.08	124.57	223.95	49.87	6109.49	187.10	53.00	136.50
N3431	3.95	3060.57	9.39	88.39	216.55	171.40	92.83	5865.04	194.93	49.41	138.31
N3443	4.86	3310.44	8.57	94.36	182.26	164.89	67.97	5434.57	174.34	35.87	117.42
N3455	4.25	2672.80	9.63	120.15	117.02	182.59	33.13	5184.67	154.81	36.43	107.82
N3468	3.13	3253.81	9.48	164.34	135.34	221.14	58.79	6403.28	198.53	63.53	149.32
N3477	2.63	2507.57	9.34	156.43	153.02	217.41	74.70	6474.52	206.11	78.52	161.92
N3481	2.55	2791.22	9.62	125.39	177.15	206.45	97.86	6262.12	207.93	81.70	164.63

TBM performance data in T05 north drive

Ring No.	Penetration (mm/rev.)	Torque cutting wheel (kNm)	Cutting wheel rotation speed	Pressure steering cylinder 01 (bar)	Pressure steering cylinder 04 (bar)	Pressure steering cylinder 05 (bar)	Pressure steering cylinder 08 (bar)	steering force (kN)	force per cutter (kN/cutter)	BI (kN/cutter /mm/rev)	SRMBI (kN/cutter /mm/rev)
N3486	2.62	2722.08	9.65	123.85	159.97	204.03	77.34	6007.22	193.56	74.02	152.21
N3492	2.60	2820.08	9.58	148.64	164.08	210.71	94.93	6435.94	211.90	81.66	166.95
N3495	1.98	2606.43	9.61	164.34	155.26	246.35	73.20	6949.61	219.07	110.92	184.80
N3498	2.05	2337.39	9.62	92.92	203.53	172.89	123.68	5783.35	203.16	99.10	169.79
N3508	3.39	3076.16	9.62	85.81	148.91	178.22	43.81	5102.26	156.14	46.06	115.07
N3514	2.65	2866.38	9.51	159.72	183.60	208.44	81.82	6777.12	217.15	81.94	170.20
N3518	1.50	1939.26	9.49	158.67	181.27	237.00	86.87	7080.98	227.58	151.72	205.64
N3520	1.66	2427.44	9.67	156.96	167.36	248.14	85.26	7029.00	225.48	136.24	198.80
N3522	1.53	2581.10	9.66	140.61	150.68	249.30	73.18	6644.23	210.32	137.46	189.11
N3524	3.43	3354.77	9.30	96.08	203.09	207.35	109.65	6228.43	211.15	61.56	155.15
N3549	1.49	1877.54	9.70	114.66	207.96	205.68	123.84	6496.31	223.56	150.04	202.35
N3593	2.81	2904.13	9.54	97.84	193.31	208.98	119.74	6154.05	212.42	75.59	164.07
N3609	3.33	4086.97	9.22	141.46	129.91	227.60	37.27	6136.36	183.57	55.13	135.89
N3635	3.36	3013.54	9.64	105.58	166.20	207.82	52.80	5907.36	182.24	54.32	134.66

TBM performance data in T05 south drive

Ring No.	Penetration (mm/rev.)	Torque cutting wheel (kNm)	Cutting wheel rotation speed	Pressure steering cylinder 01 (bar)	Pressure steering cylinder 04 (bar)	Pressure steering cylinder 05 (bar)	Pressure steering cylinder 08 (bar)	steering force (kN)	force per cutter (kN/cutter)	BI (kN/cutter /mm/rev)	SRMBI (kN/cutter /mm/rev)
S1989	3.51	4081.39	8.37	127.81	172.66	138.79	120.08	6753.87	191.54	54.57	139.94
S2001	2.91	3750.51	9.15	114.42	217.64	112.81	170.56	7431.22	210.89	72.60	161.54
S2003	2.90	3852.09	9.91	117.33	228.96	124.09	170.87	7742.99	219.80	75.79	168.43
S2010	2.63	3638.45	9.92	86.75	260.26	92.02	209.16	7826.67	222.19	84.48	174.48
S2025	3.92	3653.77	9.12	81.80	260.83	55.59	202.81	7257.22	205.92	52.53	146.35
S2033	4.86	1288.48	6.80	29.91	183.93	8.97	132.98	4296.02	121.31	24.99	81.73
S2052	1.89	2254.38	9.91	72.01	279.12	81.66	234.68	8059.47	228.84	121.08	195.17
S2088	2.55	2899.78	9.94	81.46	290.73	42.87	277.01	8356.70	237.33	93.07	187.81
S2092	4.13	2761.73	9.94	88.97	162.19	6.45	119.40	4552.37	128.64	31.15	90.24
S2095	4.51	1862.96	9.31	77.67	104.26	97.65	76.37	4298.01	121.37	26.94	83.31
S2104	2.36	2739.81	9.90	176.71	154.87	179.53	147.20	7948.99	225.69	95.83	182.18
S2111	1.52	2085.17	9.95	91.69	274.47	62.65	272.77	8471.53	240.62	158.30	216.70
S2729	5.33	1212.12	8.66	35.79	123.00	39.42	127.31	3930.45	110.87	20.80	72.97
S2779	6.26	838.92	7.98	91.75	46.72	70.40	34.08	2933.54	82.39	13.17	52.10
S3007	5.51	609.36	6.74	19.94	125.62	62.74	89.75	3598.93	101.40	18.40	66.18
S3265	5.77	1500.41	8.08	60.61	90.36	57.51	65.78	3311.61	93.19	16.16	60.14
S3283	5.51	1754.68	8.15	40.35	127.92	55.61	42.88	3221.11	90.60	16.44	59.14
S3284	5.78	1948.23	8.09	65.44	87.97	61.44	81.29	3575.75	100.74	17.43	64.97

TBM performance data in T06 north drive

Ring No.	Penetration (mm/rev.)	Torque cutting wheel (kNm)	Cutting wheel rotation speed	Pressure steering cylinder 01 (bar)	Pressure steering cylinder 04 (bar)	Pressure steering cylinder 05 (bar)	Pressure steering cylinder 08 (bar)	steering force (kN)	force per cutter (kN/cutter)	BI (kN/cutter /mm/rev)	SRMBI (kN/cutter /mm/rev)
N755	3.18	352.71	5.58	102.29	132.91	84.02	89.48	3627.57	125.09	40.59	93.27
N1204	6.62	713.89	8.12	156.06	198.73	184.82	106.98	5738.97	197.90	30.67	124.05
N1540	7.10	731.05	8.28	145.50	156.91	177.45	73.02	4907.21	169.21	23.85	103.68
N1649	5.68	781.10	8.79	160.06	235.45	141.65	135.44	5969.92	205.86	36.24	133.35
N1650	6.70	621.95	8.51	91.36	163.88	101.12	69.77	3782.19	130.42	19.44	81.03
N1690	4.32	684.77	9.03	168.24	217.22	201.95	185.69	6861.85	236.62	54.90	164.17
N1712	7.25	324.19	9.08	53.84	111.68	117.60	0.48	2517.15	86.80	12.22	53.11
N1750	9.87	505.46	8.42	32.39	139.37	65.68	23.47	2315.76	79.85	8.12	45.09
N1761	5.82	383.78	8.19	13.02	138.56	75.25	24.31	2228.96	76.86	13.32	49.58
N1865	7.75	376.75	8.47	65.41	118.61	116.47	21.78	2860.32	98.63	12.72	59.10
N2016	7.97	467.09	7.84	96.34	127.56	130.23	44.04	3534.08	121.86	15.29	72.44
N2045	8.07	648.82	7.95	186.99	139.05	208.45	30.36	5013.45	172.88	21.44	102.59

Appendix C

Database of Rock Mass Properties and Specific Rock Mass Boreability Index

Database of rock mass properties and specific rock mass boreability index

T05 north drive					
Ring No.	**Jv**	**Jo (°)**	**UCS (MPa)**	**Bi**	**SRMBI ((kN/cutter/(mm/rev))**
N1819	13.3	20	196.5	12.96	160.92
N1845	29.3	35	172.76	13.56	111.96
N2023	12.2	75	148.6	10	139.49
N2057	3	20	178.37	15.72	185.72
N2071	5	70	165	14.95	157.52
N2097	11.2	80	170.17	16.24	149.54
N2103	1.5	62.5	107.92	9.99	164.39
N2118	7	20	107.59	10	144.89
N2127	5	75	166.33	16.31	170.76
N2131	10.4	60	165.6	14.72	132.78
N2136	6	20	169	14.31	147.7
N2264	3	60	236.51	19.94	158.92
N2335	5	20	172.93	14.48	147.23
N2346	23.3	60	146.82	12.51	108.33
N2375	0.4	35	175.83	14.52	174.63
N2382	1.2	5	163.94	12.91	190.36
N2495	4.5	25	121.6	10.03	178.81
N2572	2.7	45	162.43	14.39	163.05
N2612	18	27	132.37	10.52	121.63
N2639	9.6	20	130.7	10	140.35
N2728	0.7	70	217.27	19.13	194.4
N2734	2	30	172.9	16.39	193.74
N2759	1.1	40	178.02	17.61	191.59
N2762	0.2	70	193.27	17.09	190.02
N2811	16.1	45	195.34	15.11	137.43
N2829	6	35	67.39	6.23	139.87
N2841	12.3	25	162.06	10.45	154.02
N2886	2.5	30	175.63	13.91	193.57
N2888	4.6	35	154.6	13.7	189.45
N2890	3.3	10	169.47	12.36	172.3
N2902	0.4	50	177.2	13.15	201.96
N2906	1.7	30	214.34	20.93	198.91
N2911	0	0	194.86	15.73	210.4
N2925	8.3	67	180.27	14.69	165.45
N3068	10.3	45	164.97	14.42	157.95
N3082	6.2	30	180.53	13.31	187.56
N3135	0.4	10	200.57	14.93	202.33
N3174	10.6	45	201.44	14.45	177.52
N3214	6	45	149.35	15.87	182.93
N3326	10.9	30	212.54	15.43	181.97
N3635	20	30	103.95	8	134.66
T05 south drive					
S2003	6.7	30	228.95	14.12	168.43
S2025	26.7	45	236.79	15.7	146.35
S2052	0	0	176.86	14.57	195.17
S2104	4.5	65	177.04	9.29	182.18
T06 north drive					
N1649	14	75	147.02	10.56	133.35
N1690	5.3	20	240.3	19.68	164.17

Appendix D

Nonlinear Statistical Results

```
   1: Title "rock mass properties for TBM penetration rate prediction";
   2: variable No;
   3: Variable Jv;          // The volumetric joint count
   4: Variable angle;     // the angle between the tunnel axis and joint plane
   5: Variable UCS;       // Rock material uniaxial compressive strength
   6: Variable Bi;        // Rock material brittleness index
   7: Variable Boreability;       // Rock mass boreability index at 1 mm/rev
   8: Parameter a=1;          // Constant
   9: Parameter b=1;
  10: Parameter c=-1.5;
  11: Parameter d=1;
  12: Parameter e=-0.1;
  13: Parameter f=1;
  14: Parameter g=0.8;
  15: Correlate Jv, angle, UCS, BI, Boreability;
  16: Confidence 95;
  17: Iterations 100;
  18: tolerance 1E-4;
  19: Output OBS, predicted, residual;
  20: Function Boreability = a*ucs^b*(Bi)^c*(d*EXP(e*Jv)+EXP(f*(sin(angle+30))));
  21: SPlot xvar=boreability, yvar=predicted;
  22: Rplot xvar=boreability;
  23: Nplot;
  24: Data;

Beginning computation...
Stopped due to: Relative function convergence.


   ----  Final Results  ----

NLREG version 4.2
Copyright (c) 1992-1999 Phillip H. Sherrod.  All rights reserved.
This is a registered copy of NLREG that may not be redistributed.

rock mass properties for TBM penetration prediction
Number of observations = 47
Maximum allowed number of iterations = 100
Convergence tolerance factor = 1.000000E-004
Stopped due to: Relative function convergence.
Number of iterations performed = 94
Final sum of squared deviations = 7.4452420E+003
Final sum of deviations = -5.8453765E-001
Standard error of estimate = 13.4756
Average deviation = 10.4954
Maximum deviation for any observation = 28.1101
Proportion of variance explained (R^2) = 0.7494  (74.94%)
Adjusted coefficient of multiple determination (Ra^2) = 0.7189  (71.89%)
Durbin-Watson test for autocorrelation = 0.967
```

```
          ----  Descriptive Statistics for Variables  ----

 Variable    Minimum value  Maximum value    Mean value      Standard dev.
----------  --------------  --------------  --------------  --------------
       No            1            47            24       13.71131
       Jv            0          29.3       7.497872       7.102464
    angle            0            80       39.18085       21.71841
      UCS        67.39         240.3       171.5723          35.687
       BI         6.23         20.93        13.9334       3.106038
Boreability        108.33          210.4        165.8864        25.41527


         ----  Correlation Matrix  ----

 Variable       Jv       angle       UCS        Bi     Boreability
----------   ----------  ----------  ----------  ----------  ----------
       Jv:     1.000      0.162     -0.095     -0.290     -0.790
    angle:     0.162      1.000     -0.013      0.084     -0.255
      UCS:    -0.095     -0.013      1.000      0.796      0.374
       Bi:    -0.290      0.084      0.796      1.000      0.422
Boreability:    -0.790     -0.255      0.374      0.422      1.000


              ----  Calculated Parameter Values  ----

 Parameter  Initial guess  Final estimate  Standard error     t      Prob(t)
----------  -------------  ----------------  --------------  ---------  -------
        a            1       37.0587757        16.7468       2.21  0.03253
        b            1      0.261743789     0.09621404       2.72  0.00952
        c         -1.5      -0.10009314     0.09637825      -1.04  0.30510
        d            1      0.838363524      0.4434991       1.89  0.06580
        e         -0.1    -0.0545549976     0.02744078      -1.99  0.05351
        f            1    -0.0870252085      0.1618515      -0.54  0.59370


              ----  Analysis of Variance  ----

  Source     DF   Sum of Squares    Mean Square    F value   Prob(F)
----------  ----  --------------  --------------  ---------  -------
Regression     5       22267.82       4453.563      24.53  0.00001
Error         41       7445.242       181.5913
Total         46       29713.06


         ----  95.000% Confidence Intervals  ----

 Parameter     Lower limit      Best estimate      Upper limit
----------  ----------------  ----------------  ----------------
        a       3.23758172       37.0587757       70.8799697
        b     0.0674335869      0.261743789      0.456053991
        c     -0.294734976      -0.10009314     0.0945486957
        d    -0.0573103855      0.838363524       1.73403743
```

```
      e     -0.109973341     -0.0545549976    0.000863345824
      f     -0.413894403     -0.0870252085     0.239843986

  ---   Output Data   ---
 1  153.22523    7.69477
 2  120.25067   -8.29067
 3  147.14098   -7.65098
 4  179.96037    5.75963
 5  167.40286   -9.88286
 6  148.05683    1.48317
 7  169.30877   -4.91877
 8  150.98432   -6.09432
 9  166.46072    4.29928
10  150.12792  -17.34792
11  167.42887  -19.72887
12  187.03006  -28.11006
13  171.94258  -24.71258
14  122.34687  -14.01687
15  191.37171  -16.74171
16  189.26116    1.09884
17  164.05115   14.75885
18  176.69335  -13.64335
19  130.81357   -9.18357
20  150.89909  -10.54909
21  194.55332   -0.15332
22  181.18717   12.55283
23  184.71320    6.87680
24  193.29350   -3.27350
25  142.38679   -4.95679
26  141.98884   -2.11884
27  150.90835    3.11165
28  182.71600   10.85400
29  168.19251   21.25749
30  181.72933   -9.42933
31  192.97402    8.98598
32  188.41602   10.49398
33  200.76201    9.63799
34  159.96186    5.48814
35  150.86230    7.08770
36  169.95210   17.60790
37  199.95709    2.37291
38  158.04327   19.47673
39  158.74781   24.18219
40  159.27376   22.69624
41  122.68832   11.97168
42  177.89491   -9.46491
43  131.17041   15.17959
44  197.23952   -2.06952
45  180.75806    1.42194
46  141.57604   -8.22604
47  180.54093  -16.37093
```

Appendix A

Summary of Intact Rock Strength Test Results

Test results in T05 north drive

Ring No.	Diameter (mm)	Length (mm)	UCS (Mpa)	Corrected UCS (Mpa)	BT (Mpa)	BI	I_{50} (axial, Mpa)	I_{s50} (irr.)	E (Gpa)	Poisson's ratio	Remarks
BH9001	51.65	124.10	6.02	6.05	2.02	3.00	1.11				greenish pink grey, HW
BHESR	63.30	159.38	152.29	158.89	5.67	28.02	9.42		61.24	0.24	pink grey, SW
BHEZMN3	63.18	159.35	156.52	163.25	6.89	23.69	9.31		69.78	0.24	pink grey, F-SW
BHEZMS4	76.03	168.30	199.44	215.07	7.57	28.41	9.18		90.34	0.27	dark grey, fresh
BHIU2A	63.30	158.50	25.29	26.39	4.42	5.97	2.22				greenish grey, MW-HW
BHTPW12-2	75.98	168.90	107.38	115.78	5.98	19.36	7.33				grey, SW
N1819	33.30	84.40	211.42	196.50	15.16	12.96	11.30	9.53	57.31	0.25	grey,fresh
Shaft U2								11.52			grey, fresh
N1845	33.80	84.20	67.81	63.20	12.74	4.96	8.69	9.49			grey, SW-F, failure along with joint plane, angle 45
N2003								5.19			dark green grey, MW-HW
N2006	33.68	83.05	66.82	62.26	8.88	7.01	2.10		34.13	0.18	greenish grey, MW
N2014	33.65	79.70	129.82	120.89	11.14	10.85		7.93	66.02	0.23	pink grey, SW
N2022	33.45	77.79	91.63	85.23	11.75	7.25			60.41	0.17	pink grey, MW
N2023							7.82				pink grey, fresh
N2057	33.55	75.45	191.65	178.37	11.35	15.72	10.22	7.40			grey, fresh
N2065	33.20	82.85	179.36	166.62	12.95	12.87					dark pink grey, SW
N2071	33.63	84.53	103.67	96.52	11.04	8.74			64.81	0.23	grey,fresh, shear failure
N2097	33.50	74.06	183.21	170.17	10.48	16.24			74.42	0.26	grey, fresh
N2103-1	33.45	84.10	116.02	107.92	10.80	9.99	8.97		56.38	0.16	pink grey, SW
N2118	33.53	82.40	115.62	107.59							slightly grey, fresh, along with joint plane, 70 degree
N2127	33.45	83.10	178.81	166.33	10.20	16.31	8.74		63.08	0.23	grey, fresh
N2131					11.25			8.72			dark grey, F-SW
N2136	33.48	83.73	181.66	169.00	11.81	14.31		9.15			pink grey, fresh
N2263								9.16			pink grey, fresh
N2264	33.25	84.00	254.53	236.51	11.86	19.94	8.37	10.31	68.79	0.24	grey, fresh

Test results in T05 north drive

Ring No.	Diameter (mm)	Length (mm)	UCS (Mpa)	Corrected UCS (Mpa)	BT (Mpa)	BI	I_{50} (axial, Mpa)	I_{s50} (irr.)	E (Gpa)	Poisson's ratio	Remarks
N2265								5.89			pink grey
N2335	33.45	84.30	98.96	92.05	11.94	7.71	9.39	8.81			pink grey, F-SW, along with joint plane
N2342								9.43			pink grey
N2346	33.15	82.58	158.09	146.82	11.74	12.51	6.40	8.94	59.36	0.27	pink grey, SW
N2375	33.43	84.73	87.49	81.37	12.11	6.72	9.25				pink grey, SW, along with joint plane
N2382	33.58	83.99	176.10	163.94	12.70	12.91	10.72		62.03	0.33	pink grey, SW
N2495	33.35	83.95	130.79	121.60	12.12	10.03	2.29		64.13	0.30	pink grey, SW
N2552	33.30	79.08	122.24	113.61	11.85	9.59	7.00	7.00	52.73	0.23	greenish grey, MW
N2553					8.94			5.00			greenish pink grey,SW-MW
N2572	33.64	81.16	174.44	162.43	11.29	14.39			62.95	0.20	pink grey,fresh
N2591								7.17			greenish pink grey, SW
N2612	33.63	84.70	142.17	132.37	12.58	10.52		9.62	74.65	0.24	pink grey, fresh
N2613								8.64			
N2639								6.88			pink grey
N2728	33.59	84.34	233.40	217.27	11.36	19.13	9.29		69.55	0.25	grey, fresh
N2734	33.54	84.15	185.80	172.90	10.55	16.39	7.84		62.60	0.24	grey, fresh
N2759	33.28	81.75	191.56	178.02	10.11	17.61	8.65		65.30	0.29	pink grey, fresh
N2761				207.81	11.01	18.87	7.63		64.81	0.27	grey, fresh
N2762	33.37	84.53	207.86	193.27	11.31	17.09	7.79		57.79	0.24	pink grey, fresh
N2811	33.30	76.20	97.79	90.89	12.93	7.03	10.28		76.28	0.28	pink grey, SW, partly along with joint plane
N2829	33.16	83.64	72.56	67.39	10.82	6.23			52.90	0.16	pink grey, MW
N2841	33.83	82.85	173.87	162.06	15.51	10.45					pink grey, fresh
N2870	33.90	84.90	176.47	164.55							grey, discolored, SW
N2882	33.85	71.83	196.62	183.29							grey, discolored, SW

Test results in T05 north drive

Ring No.	Diameter (mm)	Length (mm)	UCS (Mpa)	Corrected UCS (Mpa)	BT (Mpa)	BI	I_{50} (axial, Mpa)	I_{s50} (irr.)	E (Gpa)	Poisson's ratio	Remarks
N2886	33.85	82.80	188.41	175.63	12.63	13.91					grey, fresh
N2888					11.29		8.14				pink grey, SW-MW
N2890	33.85	80.45	181.80	169.47	13.71	12.36					pink grey, F-SW
N2903	33.90	81.20	190.04	177.20	13.48	13.15			74.24	0.26	pink grey, SW
N2906	33.85	86.00	229.93	214.34	10.24	20.93			69.33	0.19	grey, discolored, SW
N2911	33.90	81.90	208.98	194.86	12.39	15.73			63.40	0.28	greenish pink grey, discolored, SW-MW
N2914	33.90	83.60	195.69	182.47	12.04	15.16			64.74	0.27	pink grey, SW
N2925	33.78	83.60	193.46	180.27	12.27	14.69			64.76	0.26	grey, fresh
N3068	32.60	84.40	178.17	164.97	11.44	14.42					grey, fresh
N3082	33.15	73.35	194.39	180.53	13.56	13.31					pink grey, fresh
N3094	33.23	84.68	207.69	192.96	11.01	17.53					grey, fresh
N3103	33.35	80.90	159.83	148.59	11.31	13.14					pink grey, fresh
N3119					10.90		6.34				grey, fresh
N3135	33.05	84.85	216.09	200.57	13.43	14.93					grey, fresh
N3174	33.33	84.48	216.70	201.44	13.94	14.45					pink grey, F-SW
N3193	33.23	84.83	153.46	142.58	9.74	14.64					pink grey, fresh, failure along joint plane (SW)
N3214	33.43	82.65	160.58	149.35	9.41	15.87					grey, fresh
N3277	33.10	84.20	146.02	135.57	11.01	12.31					grey, fresh
N3314					12.35						pink grey, fresh
N3326	33.35	84.35	228.61	212.54	13.77	15.43					grey, fresh
N3522	32.78	84.63	230.68	213.79	12.85	16.64	8.35		71.55	0.23	grey, fresh
N3549	33.38	84.35	226.51	210.61	11.66	18.06					grey, fresh
N3608							9.73				grey, fresh
N3635								5.47			pink light grey, SW-MW

Test results in T05 South drive

Ring No.	Diameter (mm)	Length (mm)	UCS (Mpa)	Corrected UCS (Mpa)	BT (Mpa)	BI	I_{50} (axial, Mpa)	I_{s50} (irr.)	E (Gpa)	Poisson's ratio	Remarks
S2001								6.61			black grey, fresh, fine grain
S2003	33.65	80.75	99.47	92.63	16.21	5.71	10.71	13.39	69.38	0.22	Dark grey, fresh, invisible joint plane
S2010	33.40	84.30	157.78	146.73	18.82	7.80			84.63	0.28	Dark grey, SW, original crack
S2025	33.53	82.30	254.45	236.79	15.08	15.70		11.51	82.50	0.28	dark grey, fresh
S2052	33.45	83.45	48.70	45.30	12.07	3.75		9.26			greenish dark grey, MW, failure along original crack
S2088	33.40	82.30	157.14	146.13				9.91			Dark grey, fresh, original crack in the end
S2092	33.21	84.68	199.46	185.29	17.98	10.31	10.42	10.46	85.97	0.30	dark grey, fresh
S2095								8.09			greenish dark grey, SW
S2104	33.42	82.15	190.36	177.04	19.06	9.29	11.23		82.77	0.30	dark grey, SW
S2111								11.02			deep dark grey, fresh, fine grain
S2729								0.57			pink grey, HW
S2779								3.61			lightly grey, HW
S3264								5.01			greenish pink grey, SW
S3265								4.88			greenish pink grey, SW-MW
S3283								7.81			greenish grey, SW
S3284								1.70			greenish grey, MW-HW

Test results in T06 north drive

Ring No.	Diameter (mm)	Length (mm)	UCS (Mpa)	Corrected UCS (Mpa)	BT (Mpa)	BI	I_{50} (axial, Mpa)	I_{s50} (irr.)	E (Gpa)	Poisson's ratio	Remarks
N755	51	125	213.15	213.91	15.64	13.68					Calcium dyke; load perpendicular to dyke; very fine grain
N1206	51				8.70						Reddish brown grain, calcium veins
N1540	51	104	228.25	229.27	14.18	16.17					Small, medium grain; calcium vein perpendicular to load
N1649	51	125	146.5	147.02	13.92	10.56					Small, medium grain, SW
N1650	51	104		256.12	14.73	17.39					Fine, medium grain
N1690	51			240.30	12.21	19.68					Small medium grain, Redish brown
N1712	51				2.02						Medium, large grain; Reddish brown
N1750	51	104		219.37	12.95	16.94					Medium, Large grains
N1761	51	126	233.99	234.83	14.20	16.54					Reddish brown, small grain
N1863	51	102		188.50	9.68	19.47					Fine grain, calcium vein, load perpendicular to calcium vein
N1864	48	118	255.21	253.34	12.52	20.23					veins
N2010	51	128	118.61	119.03	12.13	9.81					Fine, medium grain; partial calcium vein; load perpendicular to calcium vein, SW
N2011	52	125	92.49	93.15	12.13	7.68					Small, medium grain; fine cracks perpendicular to load, SW
N2045	51			245.05	16.47	14.88					Reddish brown, small medium grains

References

Adler L. and Krishnan G. V. 1983. A unified rock classification for drilling and boring. *RETC Proceedings,* Vol. 1, pp.157-174.

Aeberli U. and Wanner W. J. 1978. On the influence of discontinuities at the application of tunnelling machines. *Proc. Third Int. Congr. IAEG*, Section III, Madrid, Vol. 2, pp.7-14.

Alber M. 1996a. Prediction of penetration and utilization for hard rock TBMs. Barla G. (ed.), *Eurock'96,* Balkema, Rotterdam, pp.721-725.

Alber M. 1996b. Classifying TBM contracts. *Tunnels and Tunnelling*. 38(12):41-43.

Alber M. 2000. Advance Rates of Hard Rock TBMs and Their Effects on Project Economics. *Tunnelling And Underground Space Technology*, 15(1):55-64.

Altindag R. 2002. The evaluation of rock brittleness concept on rotary blast hole drills. *Journal of South African Institution of Mining and Metallurgy*, 102(1):61-66.

Askilsrud O. G. 1998. Development of TBM technology for hard rock conditions. *Norwegian TBM Tunnelling*, 30 Years of Experience with TBMs in Norwegian Tunnelling, Norwegian Soil and Rock Engineering Association, No.11, pp.35-42.

Barla G. 2000. Lessons learnt from the excavation of a large diameter TBM tunnel in complex hydrogeololgical conditions. *Geo2000 – An International Conference on Geotechnical & Geological Engineering*, Melbourne, Australia, pp.938-996.

Barton N., Lien R. and Lunde J 1974. Engineering classification of rock mass for the design of tunnel support. *Norwegian Geotechnical Institute*, 106:1-48.

Barton N. 1987. Rock Mass Classification and Tunnel Reinforcement Selection Using the Q-system. Kirkaldia L. (ed.), *Rock Classification Systems for Engineering Purpose*, pp.59-88.

Barton N. 1999. TBM performance estimation in rock using Q_{TBM}. *Tunnels and Tunnelling International*, (9):30-34.

Barton N. 2000. *TBM Tunnelling in jointed and faulted rock*. A. A. Balkema, Rotterdam, Brookfield, pp.172.

Barton N. and Jhun I. 2000. TBM performance estimation in rock using Q_{TBM}. Fuji Research Institute Corporation, *Http://www.fuji.ric.co.jp/crab/geo/SR005.pdf*.

Benardos A. G. and Kaliampakos D. C. 2004. Modelling TBM performance with artificial neural networks. *Tunnelling and Underground Space Technology*, 19(6):597-605.

Benjumea R. and Sikarskie D. L. 1969. A note on the penetration of a rigid wedge into a nonisotropic brittle material. *Int. J. of Rock Mech. & Mining Sci & Geomech. Abs.*, 6(4):343-352.

Bickel J. O., Kuesel T. R. and King E. H. (eds) 1994. *Tunnel Engineering Handbook*. Chapman & Hall, second edition.

Bieniawski Z. T. 1973. Engineering classification of jointed rock masses. *The Civil Engineer in South Africa*, pp.335-343.

Bieniawski Z. T. 1989. *Engineering rock mass classifications – A complete manual for engineers and Geologists in mining, civil, and petroleum engineering*. John Wiley & Sons.

Blindheim O. T., Johansen E. D. and Johannessen O. 1983. Criteria for the selection of full face tunnel boring or conventional tunneling. *Norwegian Tunnelling Technology*, Norwegian Soil and Rock Engineering Association, Norwegian Tunnelling Society, NFF, 2:33-38.

Blindheim O. T. and Bruland A. 1998. Boreability testing. *Norwegian TBM Tunnelling*, 30 Years of Experience with TBMs in Norwegian Tunnelling, Norwegian Soil and Rock Engineering Association, 11:21-28.

Blindheim O. T. 2004. TBM performance prediction models. *Tunnels & Tunnelling International*, December 2004, pp.23-27.

Boniface A. 2000. Tunnel boring machine performance in basalts of the Lesotho formation. *Tunnelling and Underground Space Technology*, 15(1):49-54.

Borg A. 1988. Hard rock tunnel boring in Norway. *Norwegian Tunnelling Today*, Norwegian Soil and Rock Engineering Association, 5:109-112.

Brady B. H. G. and Brown E.T. 1985. *Rock mechanics for underground mining*. George Allen & Unwin, pp.48-84.

Broch E. and Franklin J. A. 1972. The point-load strength test. *Int. J. Rock Mech. Min. Sci.*, 9:669-697.

Brown E. T. (ed.) 1981. *Rock characterization testing and monitoring*. ISRM suggested methods.

Bruines P. A. 2001. The use of neurofuzzy modeling for performance prediction of tunnel boring machines. Adachi, Swets & Zeitlinger (eds), *Modern Tunnelling Science and Technology*, pp.583-588.

Bruland A., Dahlo T. S. and Nilsen B. 1995. Tunneling performance estimation based on drillabiltiy testing. *Proceedings 8th International Congress on Rock Mechanics*, Tokyo, Japan.

Bruland A. 1998. Hard rock tunnel boring. *Doctoral thesis*, Norwegian University of Science and Technology, Trondheim.

BS code 1377:1990. *Method of test for soils for civil engineering purpose*.

Buchi E. 2004. Paper on reuse of TBM much with sieve curves and 3 pages of penetration test results. *Private communications*.

Cheema S. 1999. Development of a rock mass boreability index for the performance of tunnel boring machines. *Doctoral dissertation*, Dept. of Mining Engineering, Colorado School of Mines, Golden, Colorado, USA, p.262.

Chen S.G. and Zhao J. 1998. A study of UDEC modeling for blast wave propagation in jointed rock masses. *Int. J Rock Mech. Min. Sci.*, 35:93-99

Chiaia B. 2001. Fracture mechanisms induced in a brittle material by a hard cutting indenter. *International Journal of Solids and Structure*, 38:7747-7768.

Clark G. B. 1987. *Principles of rock fragmentation*. John Wiley & Sons, pp.243-294.

Coates D. F. 1964. Classification of rock for rock mechanics. *Int. J. Rock Mech. Min. Sci.*, 1:421-429.

Commission on Engineering and Technical Systems of USA 1984. *Geotechnical site investigation for underground projects*, Volume 1 and Volume 2, pp.182.

Cook N. G. W., Hood M. and Tsai F. 1984. Observations of crack growth in hard rock loaded by an indenter. *Int. J. Rock Mech. Min. Sci. & Geomech. Abstr.*, 21(2):97-107.

Cundall PA. 1971. A computer model for simulating progressive large scale movements in blocky rock systems. *Proc. Symp. Int. Soc. Rock Mech.*, Nancy, France; Vol.1: paper II-8.

Deere D. U. and Deere D. W. 1988. The Rock Quality Designation (RQD) Index in Practice. Kirkaldia L. (ed.), *Rock Classification Systems for Engineering Purpose*, pp.91-101.

Deere D.U. 1963. Technical description of rock cores for engineering purposes. *Felsmechanik und Ingenieurgeologie*, 1(1):16–22.

Deere D. U and Miller R. P. 1966. Engineering classification and index properties of intact rock. *Air Force Laboratory Technical Report*, Albuquerque, NM.

ED. Zublin AG, Singapore Branch, Meinhardt Singapore Pte Ltd and Geoconsult Asia Singapore Pte Ltd, 2001. *Geotechnical interpretative report of DTSS contract T06, Queensway Tunnel*, p.99.

Fan S.C., Jiao Y.Y., Zhao J. 2004. On modeling of incident boundary for wave propagation in jointed rock masses using discrete element method. *Computers and Geotechnics*, 31(1):57-66.

Farmer I. W., Hignett H. J. and Hudson J. A. 1979. The Role of Geotechnical Factors in the Cutting Performance of Tunnelling Machines in Rocks. *Proceedings of the 4th International Congress on Rock Mechanics*, Montreux (Suisse), pp.371-377,.

Farmer I. W. and Glossop N. H. 1980. Mechanics of Disc Cutter Penetration. *Tunnels and Tunnelling International*, 12(6):22-25.

Franklin J. A., Louis C. and Masure P. 1974. Rock material classification. *Proc. 2nd Int. Cong. Rock Mech.*, ISRM, Belgrade, Vol.1, pp.1-3.

Franklin J. A. 1986. Size-strength system for rock characterization. Karmis M. (ed.), *Application of rock characterization techniques in mine design*, AIME, Now York, pp.11-16.

Frobenius P. 1989. Tunnelling technologies for the collider ring tunnels. *Proceedings of 1st International Industrial Symposium on the Supercollider*, New Orlesns, LS, pp.93-110.

Fukui K. and Okubo S. 1999. Rock-properties estimation by TBM cutting force. Vouille G. and Berest P. (eds), *Proceedings of the 9th International Congress on Rock Mechanics*, Paris, Vol. 2, pp.1217-1220.

Gehring K. 1994. Experience with TBM-application under extreme rock condition in a South-African project leads to development of high-performance disk cutters. *7th International IAEG Congress*, Balkema, Rotterdam, pp.4243-4252.

Geological society 1970. Report on the logging of rock cores for engineering purposes. *Q. J. Eng. Geol.*, 3:1-24.

George E. A. 1995. *Brittle Failure of rock material – Test results and constitutive models*. A.A. Balkema/Rotterdam/Brolkfield, pp.123-128.

Girmscheid G. and Schexnayder C. 2003. Tunnel boring machine. *Practice Periodical on Structural Design and Construction*, ASCE, 8(3):150-163.

Graham P. C. 1976. Rock Exploration for Machine Manufacturers, in Exploration for Rock Engineering. Bieniawski Z. T. (ed.), *Proceedings of the Symposium, Johannesburg, Balkema*, Vol. 1, pp.173-180.

Grandori R., Lembo-Fazio A. and Ribacchi R. 1990. Excavation of the Ridracoli hydraulic tunnels using a double-shield TBM. *Rock Mechanics and Rock Engineering*, 23:141-165.

Grandori R., Sem M., Lembo-Fazio A. and Ribacchi R. 1995. Tunnelling by Double shield TBM in the Hong Kong granite. *Proceedings of 8th Int. Cong. for Rock Mechanics*, Vol.1, pp.569-574.

Grima M. A., Bruines P. A. and Verhoef P. N. W. 2000. Modeling tunnel boring machine performance by Neuro-fuzzy methods. *Tunnelling and Underground Space Technology*, 15(3):259-269.

Hamilton W. H. and Dollinger G. L. 1979. Optimizing tunnel boring machine and cutter design for greater boreability. *RETC Proceedings*, Atlanta, Vol.1, pp.280-296.

Hanamura T. 1995. State of the art of the Japanese TBM technology – New development. Wagner H. and Schulter A. (eds), Tunnel Boring Machines –

Trends in Design & Construction of Mechanized Tunnelling, *Proceedings of the international lecture series TBM Tunnelling Trends*, Hagenberg, Austria, A. A. Balkema, Rotterdam, pp.199-212.

Herrenknecht M. and Bappler K. 2002. Update on mixshields and hard rock TBMs. *Proceedings of 28th ITA General Assembly and World Tunnel Congress*, Sydney, Australia, p.6.

Hoek E. and Brown E. T. 1997. Practical estimates of rock mass strength. *Int. J. Rock. Mech. Min. Sci.*, 34(8):1165-1186.

Howarth D. F. 1981. The effect of jointed and fissured rock on the performance of tunnel boring machines. *Proceedings of the International Symposium on Weak Rock*, Tokyo, A.A.Balkema, pp.1069-1074.

Howarth D. F. and Rowlands J. C. 1987a. Quantitative assessment of rock texture and correlation with drillability and strength properties. *Rock Mechanics and Rock Engineering*, 20:57-85.

Howarth D. F. 1987b, Mechanical rock excavation – assessment of cuttability and boreability. *RETC proceedings*, volume 1, pp.145-164.

Hucka V. and Das B. 1974. Brittleness determination of rocks by different methods. *Int. J. rock Mech. Min. Sci. & Geomech. Abstrs*, 11:383-392.

Hughes H. M. 1986. The Relative Cuttability of Coal Measures Rock. *Mining Science and Technology*, 3:95-109.

Hulme T. W. and Burchell A. J. 1999. Tunnelling projects in Singapore: an overview. *Tunnelling and Underground Space Technology*, 14(4):409-418.

Hwong T. C. 1978. Classification of the rock mass structures and determination of rock mass quality. *Bulletin of the International Association of Engineering Geology*, 18:139-142.

Imai K., Hanaoka Y. and Tanaka Y. 2002. *New* technologies of shield tunnelling boring machines. *Proceedings of 28th ITA General Assembly and World Tunnel Congress*, Sydney, Australia, p.10.

Innaurato N., Mancini R., Rondena E. and Zaninetti A. 1991. Forcasting and effective TBM performance in a rapid excavation of a tunnel in Italy. Wittke W. (ed.), *Proceedings of the 7th International Congress on Rock Mechanics*, Aachen, pp.1009-1014.

International Society for Rock Mechanics (ISRM) 1979. Suggested methods for the quantitative description of discontinuities in rock masses. *Int. J. Rock Mech. Min. Sci.*, 15(6):319-368.

International Society for Rock Mechanics 1981. Basic geotechnical description of rock Masses. *International Journal of Rock Mechanics and Mining Sciences*, 18:85-110.

Ishii G. 2000. Current issues regarding mechanized and automated tunnelling. Zhao J., Shirlaw J. N. and Krishnan R (eds), Tunnels and Underground Structures, *Proc. of the international conference on tunnels and underground structures*, Singapore, A. A. Balkma, Rotterdam, pp.75-86.

Itasca Consulting Group 1996. *UDEC reference manual*, Version 3.0, Minneapolis, Minnesota, USA.

Jennings J. E. B., Brink A. B. A and Williams A. A. B. 1973. Revised guide to soil profiling for civil engineering purposes in Southern Africa. *Civil Engineer in South Africa*, 15(1):3-12.

Jiao Y.Y., Zhao J. and Ge X.R. 2004. New formulation and validation of the three-dimensional extension of a static relaxation method. *Advances in Engineering Software*, 35(6):317-323

Johannessen S., Askilsrud O. G. and Bruland A. 1998. The Meraker project – 10 KM of tunnel in 12 months. *Norwegian TBM Tunnelling, 30 Years of Experience with TBMs in Norwegian Tunnelling*, Norwegian Soil and Rock Engineering Association, No. 11, pp.85-90.

Kahraman S. 2002. Correlation of TBM and drilling machine performances with rock brittleness. *Engineering Geology*, 65(4):269-283.

Kahraman S. and Altindag R. 2004. A brittleness index to estimate fracture toughness. *International Journal of Rock Mechanics & Mining Sciences*, 41:343-348.

Kirsten H. A. D. 1988. Case histories of groundmass characterization for excavatability. In L. Kirkakdie (ed.), *Rock Classification Systems for Engineering Purposes*, Philadelphia, pp.102-120.

Kou S. Q., Huang Y., Tan X. C. and Lindqvist P. A. 1998. Identification of the governing parameters related to rock indentation depth by using similarity analysis. *Engineering Geology*, 49:261-269.

Kutter H. K. and Sanio H. P. 1982. Comparative study of performance of new and worn disc cutters on a full-face tunnelling machine. *Tunnelling'82*, IMM, London, pp.127-133.

Laughton C. and Nelson P. P. 1996. The development of rock mass parameters for use in the prediction of tunnel boring machine performance. Barla G. (ed.), *Eurock'96*, Balkema, Rotterdam, pp.727-733.

Laughton C., Nelson P. P. and AI-Jalil Y. A. 1994. Use of sedimentary rock impact indices in evaluation of tunnel boring machine performance. *Tunnelling*, Institute of Mining and Metallergy, London, UK, pp.200-209.

Laughton C. 1998. Evaluation and prediction of tunnel boring machine performance in variable rock masses. *Doctoral dissertation*, the Graduate School of the University of Texas at Austin, USA, p.313.

Lawn B. R. and Swain M. V. 1975. Microfracture beneath point indentation in brittle solids. *Journal of Materials Science*, 10(1):113-122.

Lindquist P. and Ranman K. E. 1980. Mechanical rock fragmentation chipping under a disk cutter. *Technical Report*, University of Lulea.

Lindquist P. –A. and Lai H. H. 1983. Behavior of the crushed zone in rock indentation. *Rock Mech. Rock Engng*, 16:199-207.

Liu H. Y., Kou S. Q., Lindqvist C. A. and Tang C. A. 2002. Numerical simulation of the rock fragmentation process induced by indenters. *International Journal of Rock Mechanics & Mining Science*, 39:491-505.

Liu P. and Liang W. H. 2000. Design considerations for construction of the Qinling Tunnel using TBM. *Tunnelling and Underground Space Technology*, 15(2):139-146.

Lundberg B. 1974. Penetration of rock by conical indenters. *Int. J. rock Mech. Min. Sci. and Geomech. Abstr.*, 4:269-272.

Lauffer H. 1958. Gebirgsklassifizierung fur den stollenbau. *Geol. Bauwesen,* 74:46-51.

McFeat-Smith I. and Askilsrud O. G. 1993. Tunnel boring Machines in Hong Kong. *RECT Proceedings*, pp.401-413.

McFeat-Smith I., Nieuwenhuijs G. K. and Lai W. C. 1986. Application of seismic surveying, oriented drilling and rock classification for site investigation of rock tunnels. *Rock Engineering and Excavation in an Urban Environment*, pp.249-260.

McFeat-Smith I. 1999. Mechanised tunnelling for Asia. *Workshop Mannal*, Organized by IMS Tunnel Consultancy LTD.

Miller R. P. 1965. Engineering classification and index properties for intact rock. *Ph. D dissertation*, University of Illinois, Urbana, Illinois, p.333.

Mishnaevshy JR L. L. 1995. Physical mechanisms of hard rock fragmentation under mechanical loading: a review. *Int. J. Rock Mech. Sci. & Geomech. Abstr.*, 32(8):763-766.

Morimoto T. and Hori M. 1986. Performance Characteristics of a Tunnel Boring Machine from the Geomechanical Viewpoint. *Int. J. Rock Mech. Sci. & Geomech. Abstr.*, 23(1):55-66.

Movinkel S. T. and Johannessen O. 1986. Geological parameters for hard rock tunnel boring. *Tunnels & Tunnelling International*, (4):45-48.

Muller L. 1978. Removing misconceptions on the New Austrian Tunnelling Method. *Tunnels and Tunneling*, 10:667-671.

Myrvang A., Blindheim O. T. and Johansen E. D. 1998. Rock stress problems in bored tunnels. *Norwegian Soil and Rock Engineering Association*, No. 11, pp.56-62.

Nelson P. P. 1983. Tunnel boring machine performance in sedimentary rock. *Doctoral dissertation*, the Graduate School of Cornelll University, USA, p.438.

Nelson P. P. and Kulhawy F. H. 1984. Cutter wear and its influence on tunnel boring machine performance. Brown E. T. and Hudson J. A. (eds.), *Design and Performance of Underground Excavations, ISRM Symposium*, Cambridge, UK, pp.239-246.

Nelson P. P., Ingraffea A. R. and O'rourke T. D. 1985a. TBM performance prediction using rock fracture parameters. *Int. J. Rock Mech. Min. Sci. & Geomech. Abstr.*, 22(3):189-192.

Nelson P. P., O'Rourke T. D. and Glaser S. D. 1985b. TBM system downtime – causes, frequency, and duration of six tunnel projects. *RETC Proceedings*, New York, NY, pp.751-770.

Nelson P. P. 1993. TBM performance analysis with reference to rock properties. Hudson J. A. (eds), *Comprehensive Rock Engineering*, UK: Pergamon, pp.261-291.

Nelson P. P., Yousof A. Al-Jalil and Laughton C. 1999. Improved strategies for TBM performance prediction and project management. *RETC Proceedings*, pp.963-979.

Nilsen B. and Ozdemir L. 1993.Hard rock tunnel boring prediction and field performance. *RETC proceedings*, pp. 833-852.

Nishimatsu Y. 1972. The mechanics of rock cutting. *Int. J. Rock Mech. Min. Sci. & Geomech. Abstr.*, 9(2):261-270.

O'Rourke J. E., Spring J. E. and Coudray S. V. 1994. Geotechnical parameters and tunnel boring machine performance at Goodwill Tunnel, California. Nelson & Laubach (eds), Rock Mechanics Models and Measurements Challenges from Industry, *Proc. of the 1st North American Rock Mechanics Symposium*, The University of Texas at Austin, A. A. Balkema, Rotterdam.

Ouchterlony F. 1974. Fracture mechanics applied to rock blasting. *Proc. 3rd Congr. ISRM*, Denver, Vol. 2, pp.1377-1383.

Ozdemir L., Miller R. S. and Wang F. D. 1977. *Mechanical tunnel boring prediction and machine design*. Report to National Science Foundation, Colorado School of Mines, Golden, p.313.

Palmstrom A. 1982. The volumetric joint count – a useful and simple measure of the degree of rock mass jointing. *Proceedings of 4th International Congress of International Association of Engineering Geology*,India, A. A Balkema /Rotterdam, Vol. 2, pp.221-228.

Palmstrom A. 1995. Rmi – a rock mass characterization system for rock engineering purposes. *Ph. D dissertation*, Oslo University, Norway.

Palmstrom A. 1996a. Characterizing rock masses by the Rmi for use in practical rock engineering, Part 1: The development of the rock mass index (RMi). *Tunnelling and Underground Space Technology*, 11(2):175-188.

Palmstrom A. 1996b. Characterizing rock masses by the Rmi for use in practical rock engineering, Part 2: Some practical applications of the rock mass index (RMi). *Tunnelling and Underground Space Technology*, 11(3):287-303.

Pang S. S., Goldsmith W. and Hood M. 1989. A force-indentation model for brittle rocks. *Rock Mechanics and Rock Engineering*, 22:127-148.

Pang S. S. and Goldsmith W. 1990. Investigation of crack formation during loading of brittle rock. *Rock Mechanics and Rock Engineering*, 23:53-63.

Paul B. and Sikarskie D. L. 1965. A preliminary theory of static penetration by a rigid wedge into brittle material. *Transactions*, Society of Mining Engineers, AIME, 232:372-383.

Phien-wej N. and Cording E. J. 1990. Sheared shale response to deep TBM excavation. *Engineering Geology*, 30:371-391.

Philipp Holzmann – Sembcorp Joint Venture 2001. *Geotechnical interpretative report of DTSS contract T05, Kranji Tunnel*, p.49.

Phillips H. R. 1975. *The mechanical cutting characteristics and properties of selected rock formations*. Reports to T.R.R.L., Univ. of N'cle, U.K.

Pitts J. 1984a. A survey of engineering geology in Singapore. *Geotechnical Engineering*, 15:1-20.

Pitts J. 1984b. A review of geology and engineering geology in Singapore. *Quarterly Jounal of Engineering Geology*, 17:93-101.

Priest S. D. and Hudson J. A. 1976. Discontinuity spacings in rock. *Int. J. Rock Mech. Min. Sci. & Geomech. Abstr.*, 13:135-148.

Protodyakonov M. M. 1963. Mechanical properties and drillability of rocks. *Proc. 5th Symp. Rock Mech.*, University of Minnesota, pp.103-118.

Public Works Department of Singapore 1976. *Geology of The Republic of Singapore*, p.79.

Rabcewicz L. and Golser T. 1972. Application of the NATM to the underground works at Tarbela. *Water Power*, pp.88-93.

Reichmuth D. R. 1963. Correlation of force displacement data with physical properties of rock for percussive drilling systems. Fairhurst C. (ed.), *Proc. 5th Symp. Rock Mechanics*, Univ. of Minnesota, pp.33-60.

Ribacchi R. and A. Lembo F. 2005. Influence of rock mass parameters on the performance of a TBM in a gneissic formation (Varzo Tunnel). Rock *Mechanics and Rock Engineering*, 38(2):105-127.

Robbins R. J. 1982. The application of tunnel boring machines to bad rock conditions. Wittke W. (ed.), *Rock Mechanics: Caverns and Pressure Shafts, ISRM Symposium*, Aachen, A. A. Balkema, Rotterdam, pp.827-836.

Rostami J. and Ozdemir L. 1993. A new model for performance perdiction of hard rock TBMs. *RETC Proceedings*, pp.793-809.

Rostami J., Ozdemir L and Nilson B. 1996. Comparison between CSM and NTH hard rock TBM performance prediction models. *Proceedings of Annual Technical Meeting of the Institute of Shaft Drilling and Technology (ISDT)*, Las vegas NV, p.11.

Rostami J. 1997. Development of a force estimation model for rock fragmentation with disc cutters through theoretical modeling and physical measurement of crushed zone pressure. *Doctoral dissertation*, Dept. of Mining Engineering, Colorado School of Mines, Golden, Colorado, USA, P.382.

Roxborough F. F. and Phillips H. R. 1975. Rock excavation by disc cutter. *Int. J. Rock Mech. Min. Sci. & Geomech. Abstr.*, 12:361.

Roxborough F. F. 1978. Fundamental studies on the mechanics of cutting rock with dics. *Third Australian Tunnelling Conference*, Sydney, pp.43-47.

Sanio H. P. 1985. Prediction of the performance of disc cutters in anisotropic rock. *Int. J. Rock Mech. Min. Sci. & Geomech. Abstr.*, 22(3):153-161.

Sapigni M., Berti M., Bethaz E., Busillo A. and Cardone G. 2002. TBM performance estimation using rock mass classifications. *International Journal of Rock Mechanics & Mining Sciences*, 39:771-788.

Sharma J. S., Chu J. and Zhao J. 1999. Geological and geotechnical features of Singapore: an overview. *Tunnelling and Underground Space Technology*, 14(4):419-431.

Sherrod H. P. 1996. Nonlinear regression analysis program. *NLERG Manual*, p70.

Shinji M, Akagi W., Shiroma H., Yamada A. and Nakagawa K. 2002. JH method of rock mass classification for tunneling. ISRM International Symposium on Rock Engineering for Mountainous Regions, *EUROCK2002*, Funchal, Portugal, pp.375-383.

Skinner E. H. 1988. A Ground Support Prediction Concept: The Rock Structure Rating (RSR) Model. Kirkaldia L. (ed.), *Rock Classification Systems for Engineering Purpose*, pp.35-49.

Shirlaw J. N., Hencher S. R. and Zhao J. 2000. Design and construction issues for excavation and tunnelling in some tropically weathered rocks and soils. *GeoEng2000 - An International Conference on Geotechnical & Geological Engineering*, Melbourne, Australia, pp.1286-1329.

Snowdon R. A., Temporal J. and Hignett H. J. 1981. *A linear rock cutting rig--supplementary report 588*. Tunnels and Underground Pipes Division, Structures Department, Transport and Road Research Laboratory, Crowthorne, Berkshire.

Snowdon R. A., Ryley M. D. and Temporal J. 1982. A study of disc cutting in selected British rocks. *Int. J. Rock Mech. Min. Sci. & Geomech. Abstr.*, 19:107-121.

Snowdon R. A., Ryley M. D., Temporal J. and Crabb G. L. 1983a. The effect of Hydraulic stiffness on tunnel boring machine performance. *Int. J. Rock Mech. Min. Sci. & Geomech. Abstr.*, 20(5):203-214.

Snowdon R. A., Ryley M. D. and Temporal J. 1983b. Reply to the discussion by H. K. Kutter and H. P. Sanio of the paper by R. A. Snowdon, M. D. Ryley and J. Temporal, “A study of disc cutting in selected British rocks”, *Int. J. Rock Mech. Min. Sci. & Geomech. Abstr.*, 20(2):105.

Stacey T. R. 1981. A simple extension strain criterion for fracture of brittle rock. *Int. J. Rock Mech. Min. Sci. and Geomech. Abstr.*, 18:469-471.

Sundaram N. M., Rafek A. G. and Komoo I. 1998. The influence of rock mass properties in the assessment of TBM performance. *Proceedings of 8th International IAEG Congress*, Balkema, Rotterdam, pp.3353-3359.

Sundin N. O. and Wanstedt S. 1994. A boreability model for TBM’s. Nelson & Laubach (eds), *Rock Mechanics*, Balkema, Rotterdam, p.8.

Tarkoy P. J. 1973. A study of rock properties and tunnel boring machine advance rates in two mica schist formations. *Proceedings of 15th Symp. Rock Mech.*, Custer State Park, South Dakota.

Terzaghi K. 1946. Rock Defects and Loads on Tunnel Support. Proctor R. V. and White T. (eds), *Rock Tunnelling with Steel Supports*, Commercial Shearing Co., Youngstown, OH, pp.15-99.

Thuro K. 1997. Drillability prediction: geological influences in hard rock drill and blast tunneling. *Geol Rundsch*, 86:426-438.

Thuro K. and Plinninger R. J. 2003. Hard rock tunnel boring, cutting, drilling and blasting: rock parameters for excavatability. *ISRM 2003-Technology roadmap for rock mechanics, South African Institute of Mining and Metallurgy*, pp.1-7.

Tseng Y. Y., Wong S. I., Chu B. and Wong C. H. 1998. The Pinglin mechanized tunneling in difficult ground. *Proceedings of 8th Congr. of IAEG*, Vancouver, Canada, p.6.

U. S. Army Corps of Engineers 1997. *Engineering and Design – Tunnels and Shafts in Rock, CECW-EG Engineer Manual.* Appendix C: Tunnel boring machine performance concepts and performance prediction, pp.C1-14.

Valle N. D. 2001. Boring through a rock-soil interface in Singapore. *RETC proceedings*, pp.633-645.

Vihtuk A. A. 1998. Determination of strength of solid porous body. *Acta Phys. Pol. A 93 Supplement*, S71.

Wagner H. and Schumann E. R. H. 1971. The stamp-load bearing strength of rock – an experimental and theoretical investigation. *Rock Mech.*, 4(3):185-207.

Wallace J. C., Ho C. E., Bergh C. J., Zhao J., Zhou Y. X. and Choa V. 1995. A proposed warehouse-shelter cavern scheme in Singapore granite. *Tunnelling and Underground Space Technology*, 10(2):163-167.

Wanner H. and Aeberli U. 1979. Tunnelling machine performance in jointed rock. *Proceedings of 4th Congress of the International Society for Rock Mechanics*, Montreux, Vol. 1, pp.573-580.

Whittaker B. N., Singh R. N. and Sun G. 1992. Rock facture mechanics: Principles, Design and Applications. *Developments in Geotechnical Engineering*, Vol. 71, Elsevier.

Williamson D. A. and Kuhn C. R. 1988. The unified rock classification system. Kirkaldie L. (ed.), *rock engineering systems for engineering purpose*, ASTM STP 984, American Society for Testing Material, Philadelphia, pp.7-16.

Yasar E. 2001. A new rock mass classification for coal measures rocks. *Engineering Geology*, 62:393-300.

Zhao J., Broms B. B., Zhou Y. and Choa V. 1994a. A study of the weathering of the Bukit Timah granite, Part A: review, field observations and geophysical survey. *Bulletin of the International Association of Engineering Geology*, (49):97-106.

Zhao J., Broms B. B., Zhou Y. and Choa V. 1994b. A study of the weathering of the Bukit Timah granite, Part B: field and laboratory investigation. *Bulletin of the International Association of Engineering Geology*, (50):105-111.

Zhao J., Zhou Y., Sun J., Low B. K., and Choa V. 1995. Engineering geology of the Bukit Timah granite for cavern construction in Singapore. *Quarterly Journal of Engineering Geology*, 28:153-162.

Zhao J. 1996. Construction and utilization of rock caverns in Singapore, Part A: the Bukit Timah granite bedrock resource. *Tunnelling and Underground Space Technology*, 11(1):65-72.

Zhao J., Liu Q., Lee K. W., Choa V. and Teh C. I. 1999. Underground cavern development in the Jurong sedimentary rock formation. *Tunnelling and Underground Space Technology*, 14(4):449-459.

Zhao J., Hefny A. M. and Zhou Y. 2005. Hydrofracturing in situ stress measurements in Singapore granite. *International Journal of Rock Mechanics and Mining Sciences*, 42(4):577-583.

Publications produced/prepared by author through this research work

Journal papers

1. Zhao J, Gong QM, and Eisenstein Z (2006). Tunnelling through a frequently changing ground: A case history in Singapore. *Tunnelling and Underground Space Technology* (Submitted).

2. Zhao J and Gong QM (2006). Development of a rock mass characteristics model for TBM penetration rate prediction, Part A: rock breakage process and factor analysis. *International Journal of Rock Mechanics and Mining Sciences* (submitted).

3. Gong QM and Zhao J (2006). Development of a rock mass characteristics model for TBM penetration rate prediction, Part B: Database, Statistical model and parameter study. *International Journal of Rock Mechanics and Mining Sciences* (submitted).

4. Gong QM, Zhao J and Jiang YS (2006). In Situ TBM Penetration Tests and Rock Mass Boreability Analysis in Hard Rock Tunnels. *Tunnelling and Underground Space Technology* (accepted).

5. Gong QM and Zhao J (2005). Influence of Rock Brittleness on TBM penetration rate in Singapore Granite. *Tunnelling and Underground Space Technology* (accepted).

6. Gong QM and Zhao J (2006). Numerical simulation of rock fragmentation process induced by two TBM cutters and cutter spacing optimization. *Tunnelling and Underground Space Technology*, 21(3-4): 263.

7. Gong QM, Zhao J, Bian HY, Wang SJ and Liu G (2006). Classification and applicability of full-face TBMs. *Chinese Journal of Engineering Geology*, 14(1): 101-106.

8. Gong QM, Jiao YY and Zhao J (2006). Numerical modeling of the effects of joint spacing on rock fragmentation by TBM cutters. *Tunnelling and Underground Spacing Technology*, Vol. 21(1):46-55.

9. Gong QM, Zhao J, Jiao YY (2005). Numerical modelling of the effects of joint orientation on rock fragmentation by TBM cutters. *Tunnelling and Underground Space Technology*, Vol. 20(2): 183-191.

10. Gong QM, Zhao J, Zhang XH (2004). Performance prediction of hard rock TBM tunneling. *Chinese Journal of Rock Mechanics and Engineering*, Vol. 23, Supplement Issue 2, pp.4709-4714. (in Chinese)

Conference papers

11. Gong QM and Zhao J (2006). Numerical simulation of rock fragmentation process induced by two TBM cutters and cutter spacing optimization. *AITES-ITA 2006*, Seoul, South Korea.

12. Dong AA, Ma GW, Gong QM and Zhao J (2006). Numerical simulation on rock cutter performance in mixed face ground, *GeoShanghai2006*, China.

13. Gong QM, Zhao J and Bian HY (2005). Numerical simulation of influence of joint orientation on rock fragmentation process induced by a TBM cutter, *Eurook 2005*, pp.173-178.

14. Zhang XH, Gong QM, Zhao J, Bian HY (2003). TBM Performance under weathering influence. *Proc. Underground Singapore 2003 Conference, Singapore*, pp.177-186.

15. Gong QM, Zhang XH, Zhao J and Cai JG (2003). A Review of the Rock Mass Classification System and Applicability to Machine Tunnelling. *Proc Underground Singapore 2003 Conference,* Singapore, pp.276-284.

Others

16. Gong QM, Zhao J (2005). Effect of Rock Mass Properties on Tunnel Boring Machine Excavation, *CE Bulletin*, Nanyang Technological University.